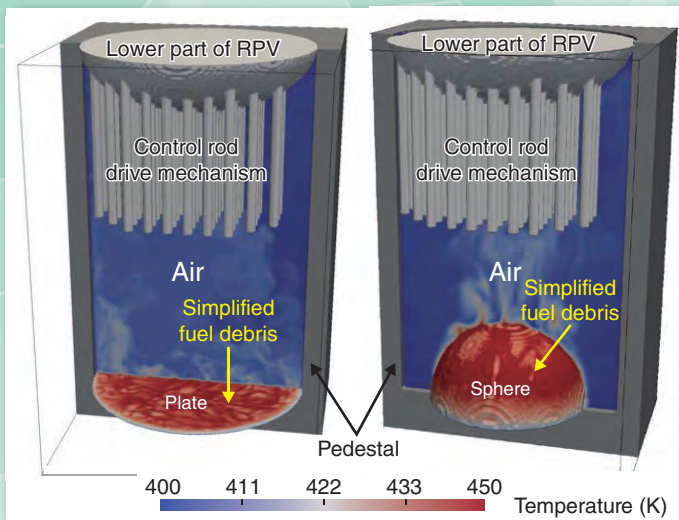


JAEA R&D Review

2017-18



Results of the Air Cooling Simulation for Simplified Debris (Topic 1-5)



Drilling Machine for Large Diameter Pit (Topic 8-5)



Message from the President

児玉 敏雄

President Toshio KODAMA

We sincerely thank you for your understanding and continued support of our research and development (R&D) activities.

The Japan Atomic Energy Agency (JAEA) is the sole comprehensive R&D institute dedicated to nuclear energy in Japan, and our mission is to contribute to the welfare and prosperity of society through nuclear science and technology. JAEA aims to contribute to this field through active cooperation with industries and universities, maximizing our R&D achievements with a focus on certain priorities. JAEA is concentrating on issues such as the response to the accident at the Fukushima Daiichi Nuclear Power Station operated by the Tokyo Electric Power Company Holdings, Inc., research on safety improvement in the field of nuclear energy, R&D toward the establishment of nuclear fuel recycling technology such as fast reactors and reprocessing, and the development of technology for the treatment and disposal of radioactive waste. Furthermore, to support these R&D activities and create new technologies, we have implemented nuclear science and engineering research and human resources development.

Regarding the accident at the Fukushima Daiichi Nuclear Power Station, we are using our scientific and technical expertise and are working on the R&D necessary for the restoration of the environment and the decommissioning of the plant's reactor facilities. On the other hand, based on the Japanese Government's final decision and policy, we will implement tasks toward the decommissioning of the fast breeder reactor Monju safely and steadily and will contribute to fast reactor R&D using our knowledge. In addition, we will decommission the nuclear fuel reprocessing plants safely and steadily and contribute to further R&D activities by acquiring useful data.

We are undertaking these activities, with safety being the topmost priority. However, a contamination accident occurred at the Plutonium Fuel Research Facility of JAEA's Oarai Research and Development Center on June 6, 2017. We take this incident with the utmost seriousness and will take steps to prevent recurrence and determine the cause.

This publication has been issued annually since the foundation of JAEA with the intention of keeping you updated with the agency's day-to-day accomplishments. For your reference, we are also publishing the annual report *Japan Atomic Energy Agency 2017*, which describes the activity status of the whole agency.

We are pleased that you will gain further understanding of JAEA's accomplishments through this publication, and we expect your continued encouragement and guidance in our R&D activities.

About This Publication and the Outline of the Organization of JAEA-----	8
---	---

1 *Research and Development Related to the Accident at TEPCO's Fukushima Daiichi NPS*

Decommissioning and Environmental Recovery -----	10
1. Observation of Core Melting and Relocation Behavior under Severe-Accident Conditions -----	11
– Plasma-Heating Tests with a Simulated Fuel Assembly –	
2. Predicting the Location of Melt Leakage from the Reactor Pressure Vessel during Severe Accidents --	12
– Development of a Failure-Evaluation Method Based on Thermal-Hydraulics and Structural Analyses –	
3. Toward Estimating Characteristics of Radioactive Material Released in Severe Accidents -----	13
– Experimental and Analytical Technologies for Evaluating Fission Product Chemistry in a Reactor –	
4. Thermodynamic Estimation of Fuel Debris Characteristics-----	14
– Thermodynamic Evaluation of High-Temperature-Reaction Products between Molten Core and Concrete –	
5. Can Fuel Debris be Retrieved without Water?-----	15
– Development of a Numerical-Simulation Method for Air Cooling of Fuel Debris –	
6. Investigating the Effect of Seawater and Concrete Components upon Nuclear-Fuel-Reprocessing-Plant Materials --	16
– Effect of Sulfate Ions upon Corrosion of a Highly Active Liquid-Waste Tank –	
7. Estimation of the Amount of Radioactivity in Water-Treatment Waste -----	17
– Calculation of Radionuclide Concentration in Contaminated Water –	
8. Development of a Small, Portable Position-Sensitive Alpha-Particle Detector -----	18
– Direct Measurement of Plutonium Contamination in Narrow Spaces of Solid-Waste Material and Equipment –	
9. Study of the Contamination State inside the Reactor Building-----	19
– Detailed Radiochemical Analysis to Accelerate Disposal of Waste –	
10. Development of an Analytical Method to Determine ⁹³ Zr, ⁹⁴ Nb, and ⁹³ Mo Concentrations in Contaminated Water and Rubble Waste --	20
– Radiochemical Separation of Difficult-to-Measure Nuclides –	
11. Development of a Test Method for Remotely Operated Robots for Decommissioning-----	21
– Design of Testing Fields for Robot-Performance Evaluation and Operator-Proficiency Training –	
12. Fiber Detector for Monitoring of Contaminated Water -----	22
– Demonstration Experiment at the TEPCO's Fukushima Daiichi NPS –	
13. Estimation of Doses to Residents with Consideration of Behavioral Patterns -----	23
– Is Decontamination of Residential Areas Based on a Guide Value of 0.23 μSv/h Effective? –	
14. How Long Does Radiocesium Remain in Forest-Surface Litter? -----	24
– Radiocesium Transfer from Litter to Mineral Soil in Two Forest Types –	
15. Mechanism of Vertical Migration of Radiocesium into Soils -----	25
– Effect of Sorption Kinetics upon Vertical Migration of Radiocesium into Soils –	
16. Redeposition Mechanism of Radiocesium on River Flood Plains-----	26
– Heterogeneous Distribution of Radiocesium Depending on Weather, Topography and Vegetation –	
17. Prediction of the Amount of Radiocesium Discharge during Typhoons and Heavy-Rainfall Events-----	27
– Simulation of the Amount of Radiocesium Discharge between Several River Basins –	
18. Reproduction of the Soil using Salt-----	28
– Synchrotron X-rays Reveal the Mechanism of Cesium Removal from Soil –	
19. Observation of Atomic-Scale Edge Structure via Supercomputers -----	29
– Towards an Understanding of the High Cesium Affinity of Clay Minerals –	
20. Prevention of Radioactive Cesium Accumulation in Shiitake Mushrooms Cultured with Contaminated Wood Logs ----	30
– Reduction of Cesium Absorption using Minerals –	

2 Nuclear Safety Research

Implementing Continuous Improvements in Safety	31
1. Estimating Hydrogen-Gas Behavior during Nuclear Power Plant Accidents	32
– Influence of Mesh Shape upon Computational Fluid Dynamics Analysis of Buoyant Flows –	
2. Evaluating Molten-Core-Debris Formation in Reactor Containment Vessels	33
– Evaluation of Molten-Core Coolability in Severe Accidents –	
3. Refinement of Crack Growth Evaluation in the Reactor Internals of Light Water Reactors	34
– Analyses of Locally Deformed Structures and Strain in Highly Irradiated Stainless Steels –	
4. Deterioration Rate of Buffer Material in Geological-Disposal Sites	35
– Alteration Rate of Compacted Montmorillonite under Highly Alkaline Conditions –	
5. Evaluating the Effect of Seismic Activity upon Geological Disposal	36
– Evaluation of the Influence of Splay-Fault Growth upon Groundwater Flow around a Geological-Disposal System –	
6. Determination of Plutonium-Isotope Ratios in Individual U/Pu Mixed Particles	37
– Novel Approach using Alpha and Mass Spectrometry for Nuclear Non-Proliferation –	

3 Advanced Scientific Research

Advanced Science Pioneers the Future	38
1. New Experimental Method for Obtaining Nuclear-Fission Data	39
– Opening-Up Fission Studies for Neutron-Rich Nuclei –	
2. A New Form of Atomic Nuclei with a “Strange Particle”	40
– An Antikaon and Two Nucleons Make a Bound State through the Strong Interaction –	
3. Magnetic Order of Non-Magnetic Ions	41
– Theoretical Investigation of Higher-Order Magnetic Order of Non-Kramers Ions –	
4. High-Speed Rotation Turns an Ordinary Metal into a Magnet	42
– Exploring the Relationship between Magnetism and Rotation that Fascinated Einstein –	
5. Asymmetric Structure of the New “Germanene” Material	43
– Possible New Germanene Properties –	

4 Nuclear Science and Engineering Research

An Interface Bridge between Nuclear-Energy R&D and Fundamental Research	44
1. Prevention of Severe-Accident Progression by Delaying Core Overheating and Melting	45
– Development of FEMAXI-ATF Code for Accident-Tolerant Fuel-Behavior Analysis –	
2. Efficient Partition of Nuclides in High-Level Waste	46
– High-Efficiency Separation of Americium and Curium –	
3. Reliability Evaluation of Nuclear Data Required for Core Design of Nuclear Transmutation Systems ...	47
– Verification of Trans-Uranium(TRU) Cross-Sections Based on Critical Experiments using FCA –	
4. Real-Time Measurement of Heavy-Liquid-Metal Flow under a Severe Environment	48
– Development of an Ultrasonic Flowmeter for a Lead-Bismuth Target –	
5. Interface of Nuclear Data and Transport Codes	49
– Development of Nuclear Data Processing System FRENDY –	

6. Research on the Material-Degradation Behavior by Radiolytic-Hydrogen Absorption-----	50
– Hydrogen-Absorption Behavior on Zirconium under γ -ray Irradiation –	
7. Predicting Mechanical Properties of Alloys -----	51
– Computational Approach for Modeling the Strengthening/Softening Mechanism –	
8. Quantitation of the Difficult-to-Measure Nuclide Palladium-107 -----	52
– Measurement of Palladium Obtained by Laser Irradiation of Spent Nuclear Fuel –	
9. Forecast of Radionuclide Dispersion in the Ocean -----	53
– Development of an Emergency-Assessment System for Marine-Environmental Radioactivity –	
10. Development of Neutron Calibration Fields for Improving the Reliability of Neutron-Dose Estimation ---	54
– Moderated Neutron Calibration Fields Considering Energy Distributions in Actual Workplaces –	

5 Applied Neutron and Synchrotron-Radiation Research and Development

Contributing to Developments in Science and Technology, and Academic Research

using Neutron and Synchrotron Radiation -----	55
1. Magnetic-Structure Analysis of a Highly Neutron-Absorbent Material with Pulsed-Neutron Diffraction----	56
– Magnetic Structure of EuGa_4 Studied by Single-Crystal Neutron Diffraction –	
2. Towards a Comprehensive Understanding of the Unique Magnetic Properties of Layered Systems----	57
– An Application of Polarized Neutron Scattering under Grazing-Incidence Geometry to Analysis of In-Plane Magnetic Structure –	
3. Realization of High-Intensity Proton Beams -----	58
– Beam-Instability Issues and the Measure at the 3-GeV RCS in J-PARC –	
4. Exploring the Structural Materials Frontier using Neutron Diffraction -----	59
– Development of the Bulk Texture Measurement Technique at the Rapidest Level –	
5. Nanoscopic-Structural Investigation of Nanoparticles for Drug-Delivery Carriers -----	60
– Small-Angle Neutron Scattering Reveals the Internal Structure of Nanogels –	
6. Aiming for the Development of Stronger Stainless Steel-----	61
– First Observation of an Intermediate ϵ -phase at Room Temperature using High-Intensity Synchrotron Radiation –	
7. Electronic Structure of Actinide Compounds Studied by Synchrotron Radiation -----	62
– Electronic Structures of Uranium Compounds that Show the Coexistence of Superconductivity and Magnetism –	

6 HTGR Hydrogen and Heat Application Research

Research and Development of HTGR, Hydrogen Production, and Heat Application Technologies-----	63
1. Toward a Demonstration of the HTGR Cogeneration System -----	64
– Completion of Component Design and Preliminary Safety Assessment for the HTTR-GT/ H_2 Plant –	
2. Development of High-Temperature Equipment for Heat Utilization of a High-Temperature Gas Furnace----	65
– Proposal for a Low-Cost, Long-Lived Intermediate Heat Exchanger –	
3. Toward Practical Load-Following Operation of HTGRs Connected to Heat-Application Systems -----	66
– Elucidation of Thermal-Load-Fluctuation Absorption at Various Coolant Pressures –	
4. Safety Enhancement of High-Temperature Gas-Cooled Reactors -----	67
– Nuclear and Thermal Design of an Oxidation-Resistant Fuel-Loaded Reactor Core –	
5. R&D on CO_2 -Free H_2 Production by the IS Process -----	68
– Progress from Lab Stage to Industrial-Material-Facility Stage –	

6. Clarifying the Core Temperature in High-Temperature Gas-Cooled Reactors 69
 – Development of Measurement Technology Based on Melt Wires for Control-Rod Temperature to Estimate Core Temperature –

7 *Research and Development of Fast Reactors*

Research and Development of Fast Reactor Cycle Technology 70

1. Sophisticated Structural-Integrity Assessment of Fast-Reactor Components 71
 – A Proposal of Procedure for Assessing Leaks before Breakage of Fast-Reactor Pipes –
2. Development of a Thermal-Hydraulic-Evaluation Method for a Straight-Tube Steam Generator 72
 – Establishing a Three-Dimensional Simulation Model and Comparing it with Test Data –
3. Improvement of Maintenance Technology for Sodium-Cooled Fast Reactors 73
 – Development of a Visual-Inspection Device under Opaque Sodium –
4. Progress in Reactor Modeling during Natural-Circulation Cooling 74
 – Validation of a Reactor Analytical Model using Measured Data –
5. Advancing the Separation Process for Spent Nuclear Fuel Reprocessing 75
 – Development of a Sludge-Cleaning Method in a Centrifugal Contactor –

8 *Research and Development on Fuel Reprocessing, Decommissioning, and Radioactive Waste Management*

Decommissioning of Nuclear Facilities and Radioactive Waste Management 76

1. Quantifying the Radioactivity of Waste Products 78
 – Accuracy Improvement of a Quantitative Method Focused on Scattering γ -rays –
2. Radioactivity-Confirmation Method for the Disposal of Low-Level Waste 79
 – Evaluation Method to Determine the Radioactivity Concentration in Radioactive Waste Generated from Post-Irradiation Examination Facilities –
3. Understanding the Self-Sealing Function of the Underground Environment 80
 – Study of the Long-Term Behavior of Hydrogeological Structures Related to Faulting –
4. Micropores Retarding Mass Transport in Granitic Rock 81
 – Visualization and Observation of Matrix-Diffusion Pathways –
5. Demonstration of Geological Disposal Technology in a Real Underground Environment 82
 – Technological Development for an In situ Experiment to Confirm the Performance of an Engineered Barrier System at the Horonobe Underground Research Laboratory (URL) –
6. Investigation of the Fault Distribution in Sedimentary Rocks 83
 – Relationship between Faults Oriented Parallel and Oblique to Bedding in Neogene Massive Siliceous Mudstones –
7. Dating of Minerals in Rocks 84
 – Technical Development of a Rapid CHIME Dating Procedure –
8. Mechanistic Modeling of Nuclide Migration in Rock 85
 – Clay-Based Modeling Approaches for Diffusion and Sorption in Mudstone –
9. Evaluation of the Long-Term Mechanical Behavior of a TRU Waste Repository 86
 – Development of a Mechanical Analysis Method Considering the Chemical Evolution of Engineered Barrier Materials –
10. Improvement of the Uncertainty and Rapidity of the Measurement Technique for a Plutonium Nitrate Solution Sample 87
 – Improvement of Neutron Nondestructive Assay –
11. Understanding the Characteristics of Insoluble Sludge in the Reprocessing of Fast Reactor Fuels 88
 – Evaluating the Characteristics of Insoluble Sludge from the Dissolution of Irradiated Fast Reactor Fuel –

9 *Computational Science and E-Systems Research*

Computational Science for Nuclear Research and Development -----	89
1. Acceleration-Flow Analysis in a Nuclear Reactor-----	90
– Development of Massively Parallel Communication-Avoiding Matrix Solvers –	
2. Development of a Low-Power-Consumption Computing Technology Based on Accelerators-----	91
– Optimization of Nuclear-Fluid-Simulation Kernels on Accelerators –	
3. High-Temperature Properties of Nuclear-Fuel Materials-----	92
– First-Principles Molecular-Dynamics Simulation of Thorium Dioxide –	
4. Solving the Mystery of Irradiation-Resistant Alloys-----	93
– Simulation of Interstitial Atoms’ Migration Based on First-Principles Calculation –	

10 *Development of Science & Technology for Nuclear Nonproliferation*

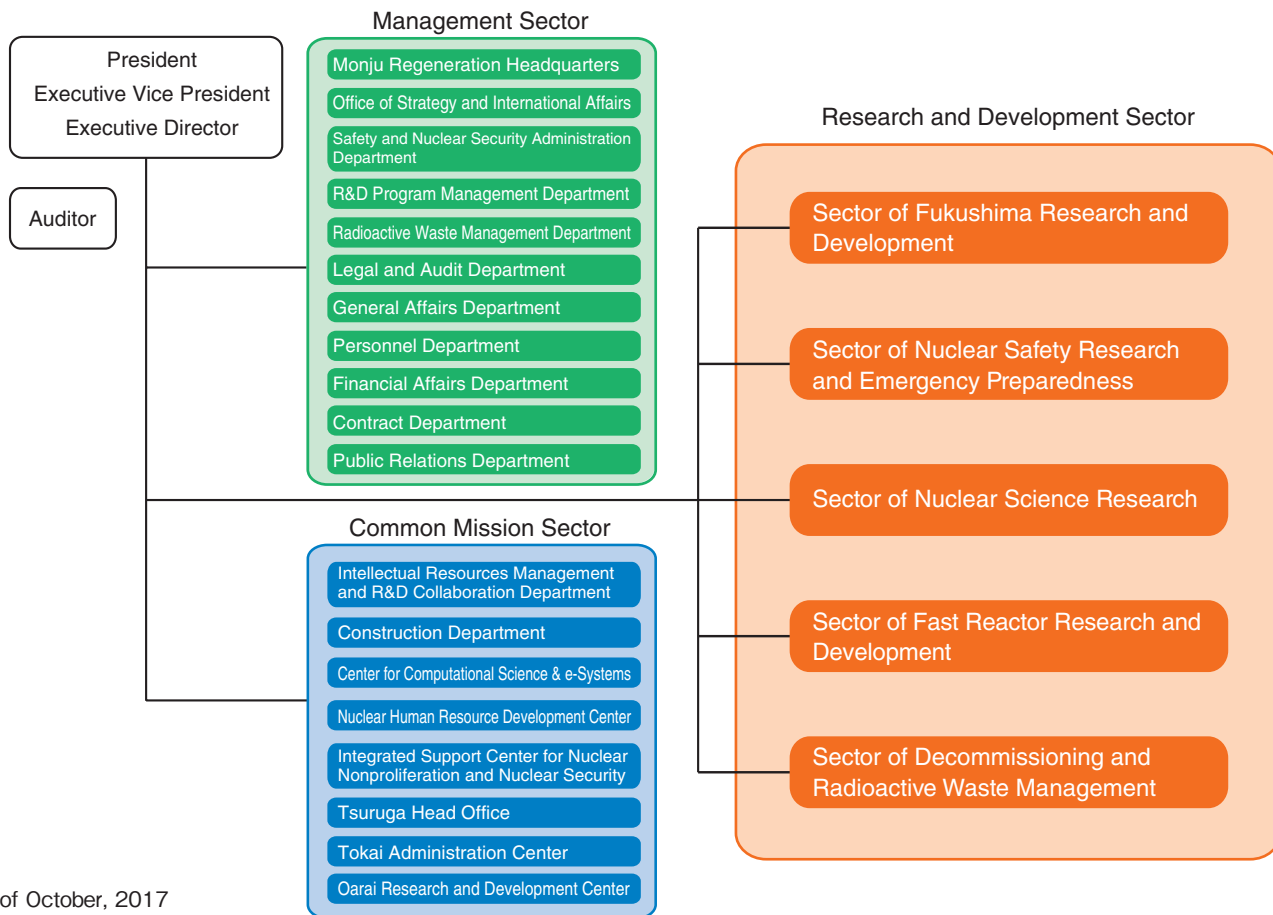
Development of Technology and Human Capacity Building in the Nuclear Nonproliferation and Nuclear Security Fields to Support the Peaceful Use of Nuclear Energy -----	94
1. Toward Enhancement of Monitoring Capability for Nuclear Tests-----	95
– Evaluating the Impact of MIPF on Observational Results at CTBT Radionuclide Stations –	
 Promotion of Collaboration – Intellectual Property Held by JAEA –-----	 96

About This Publication and the Outline of the Organization of JAEA

This publication introduces our latest research and development (R&D) results in each field. Each chapter presents the activities of one R&D Sector. The various R&D Sectors perform their activities through R&D centers or institutes. Depending on the R&D activities, some of these centers or institutes comprise only one site, whereas others comprise two or more sites. The R&D centers and institutes are located throughout Japan, as shown on the map below. The following brief introduction outlines the research undertaken by each R&D Sector at various R&D centers and institutes.

1. **The Sector of Fukushima Research and Development** is engaged in R&D, aimed at promote the decommissioning of the Fukushima Daiichi Nuclear Power Station (1F) of Tokyo Electric Power Company Holdings, Inc. (TEPCO) and environmental recovery after the 1F accident.
2. **The Nuclear Safety Research Center, Sector of Nuclear Safety Research and Emergency Preparedness**, is in charge of safety research that supports the national nuclear safety bodies that regulate nuclear power plants, nuclear fuel cycle facilities, and radioactive waste-disposal facilities. This work is being conducted at the Nuclear Science Research Institute.
3. **The Advanced Science Research Center, Sector of Nuclear Science Research**, explores yet-undiscovered disciplines and studies advanced atomic energy sciences via the Nuclear Science Research Institute to develop new theories and investigate novel phenomena, materials, and technologies. In particular, six research themes have been organized under the two divisions “advanced actinides science” and “advanced nuclear materials science”.
4. **The Nuclear Science and Engineering Center, Sector of Nuclear Science Research**, is engaged in key and basic research on various fundamental technologies that support nuclear power use. These efforts are being conducted mainly at the Nuclear Science Research Institute and the Oarai Research and Development Center.
5. **The Materials Sciences Research Center, Sector of Nuclear Science Research**, is engaged in research using neutrons at the Nuclear Science Research Institute and Japan Proton Accelerator Research Complex (J-PARC). Research using synchrotron radiation is being performed at the Harima Area.

Japan Atomic Energy Agency -Outline of Organization-



As of October, 2017

6. **The HTGR Hydrogen and Heat Application Research Center, Sector of Nuclear Science Research**, conducts R&D on technologies for high-temperature gas-cooled reactors (HTGRs) and thermochemical hydrogen production at the Oarai Research and Development Center.
7. **The Sector of Fast Reactor Research and Development** is conducting R&D toward the establishment of fast reactor (FR) cycles to address long-term energy security and global environmental issues. In Tsuruga, staff at the Prototype Fast Breeder Reactor Monju and the Monju Project Management and Engineering Center are conducting R&D on “MONJU” and preparation toward decommissioning of “MONJU”. R&D activities are also aimed at enhancing the safety of the FR system at the Oarai Research and Development Center and at manufacturing plutonium fuel and reprocessing spent FBR fuel at the Nuclear Fuel Cycle Engineering Laboratories.
8. **The Sector of Decommissioning and Radioactive Waste Management** develops technologies for the safe and rational decommissioning of nuclear power facilities as well as measures for processing and disposing of radioactive waste in their R&D centers or institutes. This sector also conducts multidisciplinary R&D aimed at improving the reliability of geological disposal of high-level radioactive waste in Japan. A particular focus involves establishing techniques for investigating the deep geological environment through R&D at the Tono Geoscience Center and the Horonobe Underground Research Center. At the Nuclear Fuel Cycle Engineering Laboratories, the focus is on improving the technologies for disposal facility design and safety assessment. Furthermore, the development of nuclear fuel cycle technology for light water reactors (LWRs) is in progress at the Nuclear Fuel Cycle Engineering Laboratories.
9. **The Center for Computational Science & e-Systems** performs research on advanced simulation technology and on basic technology in computational science, and also operates and maintains computer systems. These efforts are mainly conducted at the Nuclear Science Research Institute and the Kashiwa Office.
10. **The Integrated Support Center for Nuclear Nonproliferation and Nuclear Security (ISCN)** plays an active role in technology development in the field of nuclear nonproliferation and nuclear security in international organizations, such as the International Atomic Energy Agency (IAEA), and each country, activities to contribute nuclear material management and peaceful uses on ensuring transparency, and policy research. And ISCN continues human capacity development support projects which contribute the capacity building in Asian countries. These efforts are carried out mainly at the Head Office and the Nuclear Science Research Institute.

R&D Institutes/Centers of JAEA



Decommissioning and Environmental Recovery

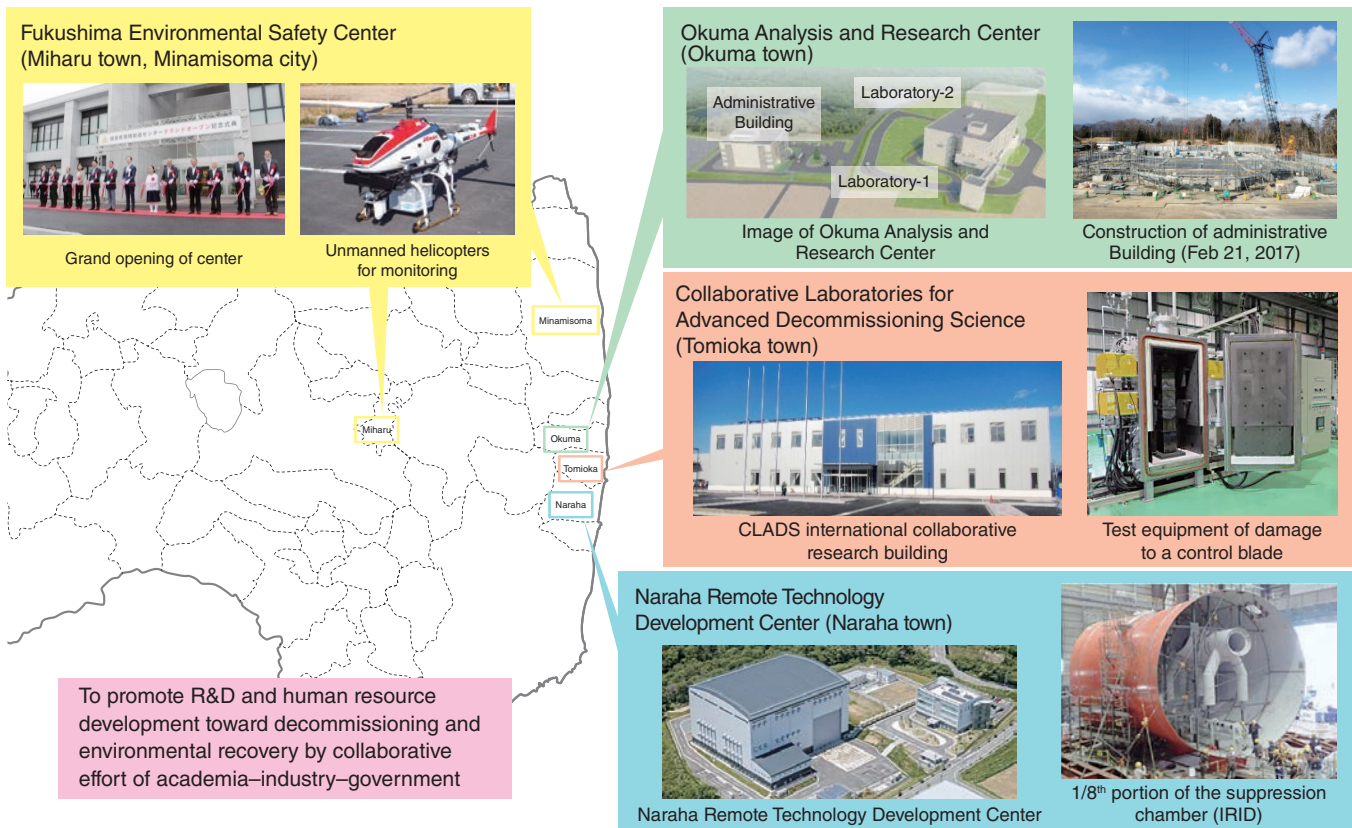


Fig.1-1 Location of activity bases of the Sector of Fukushima Research and Development

We are proceeding with research and development toward decommissioning of 1F and the environmental recovery and reconstruction of areas affected by the 1F accident.

We are Japan's sole comprehensive research and development institute in the field of nuclear energy and are conducting R&D to promote the decommissioning of the TEPCO's Fukushima Daiichi NPS (1F), as well as environmental recovery after the 1F accident. Other sectors and bases also conduct ambitious research in this field (Fig.1-1). Our full results are described below.

For decommissioning of 1F, research is being promoted to clarify the 1F-accident progression (Topics 1-1, 1-2, and 1-3), remove spent debris from nuclear reactors (Topics 1-4 and 1-5), treat and dispose of radioactive wastes generated by the decommissioning work (Topics 1-6, 1-7, 1-8, 1-9, and 1-10), and develop technologies for remote-controlled instruments (Topic 1-11) based on the Mid- and Long-Term Roadmap formulated by the Inter-Ministerial Council for Contaminated Water and Decommissioning Issues. In addition, we have monitored the leakage of the contaminated water at 1F using a fiber detector developed for environmental-radiation monitoring (Topic 1-12).

As an international research and development base, the Collaborative Laboratories for Advanced Decommissioning Science (CLADS) International Collaborative Research Building was opened in March 2017 in Tomioka town (Fig.1-1, center right). A network will be established by which competent people from universities, research institutes, and companies in and outside of Japan can interact to promote R&D and human-resource development towards decommissioning by a collaborative effort of academia, industry, and government. At the Naraha Remote Technology Development Center, the International Research Institute for Nuclear Decommissioning (IRID) conducts actual-

scale tests for repairing sections of the containment vessel from which cooling water is leaking (Fig.1-1, bottom right). The Okuma Analysis and Research Center studies the radioactive materials generated from 1F, such as radioactive-waste and debris samples obtained after the removal of fuel debris from nuclear reactors. Construction of the Administrative building started in FY2016 (Fig.1-1, top right).

The Fukushima Environmental Safety Center has researched and developed technologies related to environmental recovery for the safety and security of residents based on the Fukushima Prefectural Centre for Environmental Creation Policy for Medium- and Long-term Initiatives, as formulated by the Fukushima Prefectural Center for Environmental Creation's Management Strategy Conference.

In the field of environmental recovery, evaluating the exposure doses to residents (Topic 1-13) and research on the migration behavior of radiocesium in the environment in watershed areas from forests to the ocean (Topics 1-14, 1-15, 1-16, and 1-17) are also being promoted. In basic research on environmental radioactivity, efforts are underway to determine the adsorption/desorption mechanism of radiocesium to clay minerals (Topics 1-18 and 1-19) and develop technologies to suppress migration of radiocesium to mushrooms using clay minerals (Topic 1-20).

The Fukushima Prefectural Center for Environmental Creation became fully operational at Miharu town in July 2016 (Fig.1-1, top left). We are performing R&D in cooperation with Fukushima Prefecture and the National Institute for Environmental Studies (NIES) through this Center.

1-1 Observation of Core Melting and Relocation Behavior under Severe-Accident Conditions — Plasma-Heating Tests with a Simulated Fuel Assembly —

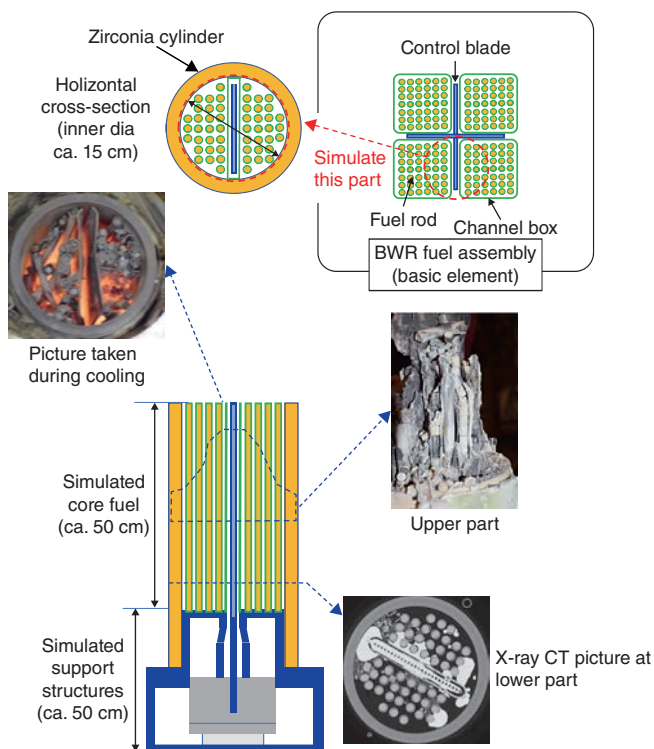


Fig.1-2 Example of a plasma-heating-test piece and observation after heating

A test piece, comprising a single control blade surrounded by two channel-box surfaces and fuel rods is heated from above with a non-transfer-type plasma torch.

We are studying core-melting and relocation behavior under severe-accidental conditions in boiling-water reactors for a better understanding of accident progression and the present core status of the TEPCO's Fukushima Daiichi NPS (1F).

BWRs such as 1F have cross-shaped control blades comprising boron carbide (B_4C) and stainless steel (SS) surrounded by four fuel assemblies (Fig.1-2). B_4C and SS can form eutectics, allowing melting and relocation starting at around 1200 °C. After this relocation, the remaining fuel columns may collapse and relocate down to the fuel bottom through the possibly voided space provided by relocation of control-blade materials. Such BWR-specific core-degradation and relocation behavior is simulated by plasma-heating technology. The test piece as presented in Fig.1-3 uses zirconia (ZrO_2) pellets to simulate real UO_2 fuel, while all other materials are basically the same as actually used in BWRs. The test piece, made of a 50-cm-high fuel part and a 50-cm-high support-structure part, is heated at the top so that

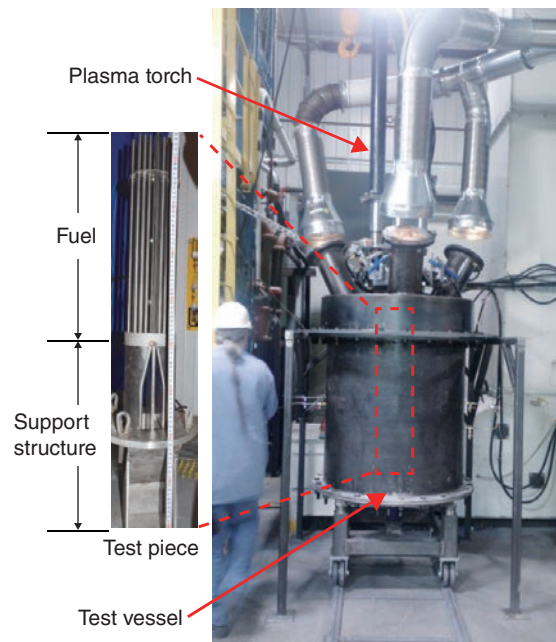


Fig.1-3 Plasma-heating-test apparatus

A 1-m-high test piece simulating part of a BWR core and lower-support structure is set into a vessel and heated from above with a plasma torch.

the large axial temperature gradient thought to have existed in the 1F accident (ca. 2000 K/m) could be realized. As is shown in Fig.1-2, the control blade is lost in the upper region, but fuel columns remain. X-ray CT reveals that such relocated material fills the space between the control blade and the channel box or between fuel rods in the lower part. The test piece after heating comprises ceramics, including boron, and is quite hard; a water jet is used to cut this piece. Precise material tests such as analyses with x-rays and chemical methods are underway.

We are presently conducting this test program as a member of the International Research Institute for Nuclear Decommissioning (IRID), with financial support from the Ministry of Economy, Trade and Industry, Japan (METI) subsidy for the Project of Decommissioning and Contaminated Water Management. The outcomes will also be reflected in evaluation of BWR-core-melting and relocation behavior and improvement of evaluation technology.

Reference

Abe, Y., Sato, I. et al., Preparation for a New Experimental Program Addressing Core-Material-Relocation Behavior during Severe Accident with BWR Design Conditions –Conduction of Preparatory Tests Applying Non-Transfer-Type Plasma Heating Technology–, Proceedings of 24th International Conference on Nuclear Engineering (ICONE 24), Charlotte, North Carolina, USA, 2016, ICONE24-60249, 7p., in DVD-ROM.

1-2 Predicting the Location of Melt Leakage from the Reactor Pressure Vessel during Severe Accidents

— Development of a Failure-Evaluation Method Based on Thermal-Hydraulics and Structural Analyses —

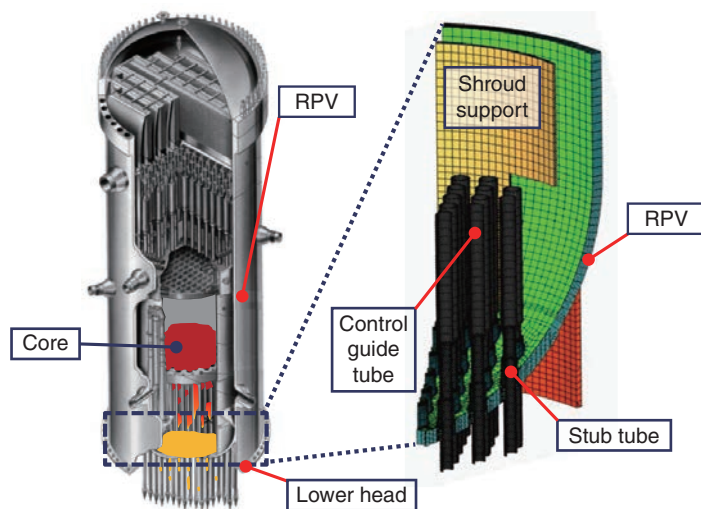


Fig.1-4 Analytical model of the RPV lower head

The RPV lower head of a BWR similar to 1F has a complicated geometry since there are many penetrations and welds for connecting the control-rod-guide tubes. Considering this complicated geometry is important in order to predict where the lower head will rupture after relocation of molten fuel. We have developed a detailed 3D model to assess the failure behavior of the lower head during accidents.

To support estimates of the distribution of molten materials (fuel and melted core materials) inside and outside of the reactor pressure vessels (RPVs) of the TEPCO's Fukushima Daiichi NPS (1F), we are researching assessment of the failure behavior of the RPV's lower head due to relocation of molten materials. Since severe accidents may include a large uncertainty, the amount of molten materials to be relocated to the lower head and their states differ depending on the accidental scenario. Therefore, developing an analytical method applicable for several conditions is important. In addition, developing a method for estimating local failure by considering geometrically complicated structures is necessary because there are many penetrations and welds for connecting the control-rod-guide tubes in boiling-water reactors (BWRs) such as 1F.

In this study, we are developing a coupled-analysis method for thermal-hydraulics (TH) and structural analyses, which can be applied to the behavior of molten materials and to the thermal-elastic-plastic-creep behavior of the structures,

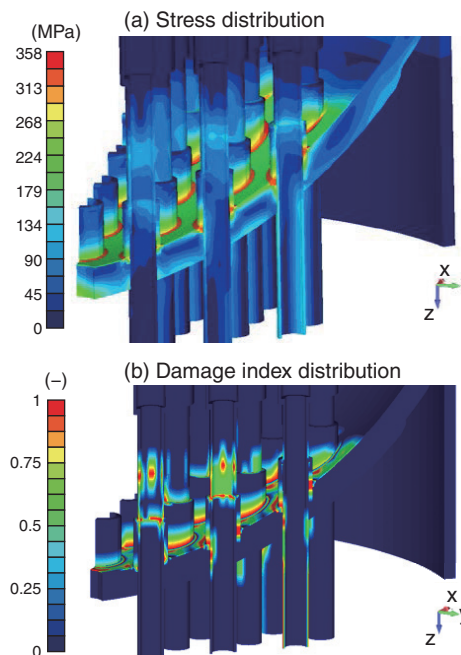


Fig.1-5 An example of the stress and damage-index distributions

This figure illustrates an example of the distribution of stress (a) and damage index (b) obtained by structural analysis. Due to the heating of relocated molten materials, it can be seen that creep deformation and stress occur in the control-rod-guide tubes or stub tubes and that it is possible that failure may occur in such locations, where the damage index reaches unity.

respectively. Using this method, failure location and time are estimated by evaluating the damage index of materials due to creep deformation.

Fig.1-5 illustrates an example of analytical results obtained using a three-dimensional (3D) model that considers penetration of a BWR (Fig.1-4). As an initial condition, we assumed that 10% of the reactor core has been melted and relocated to the lower head and that the coolant water in the reactor completely evaporates. Here, this scenario differs from the 1F accident. Due to heating of relocated molten materials, deformation and stress are generated due to creep. Using a damage criterion that considers creep deformation, it is shown that molten materials may leak from penetrations such as control-rod-guide tubes or stub tubes where the calculated damage index showed high values (red regions in Fig.1-5(b)).

In the future, by comparison with experiments, we will improve the failure-evaluation methods and prediction of molten materials outside of the RPV in 1F.

Reference

Katsuyama, J. et al., Creep Damage Evaluations for BWR Lower Head in Severe Accident, Transactions of 24th International Conference on Structural Mechanics in Reactor Technology (SMIRT-24), Busan, Korea, 2017, 11p., in USB Flash Drive.

1-3 Toward Estimating Characteristics of Radioactive Material Released in Severe Accidents

— Experimental and Analytical Technologies for Evaluating Fission Product Chemistry in a Reactor —

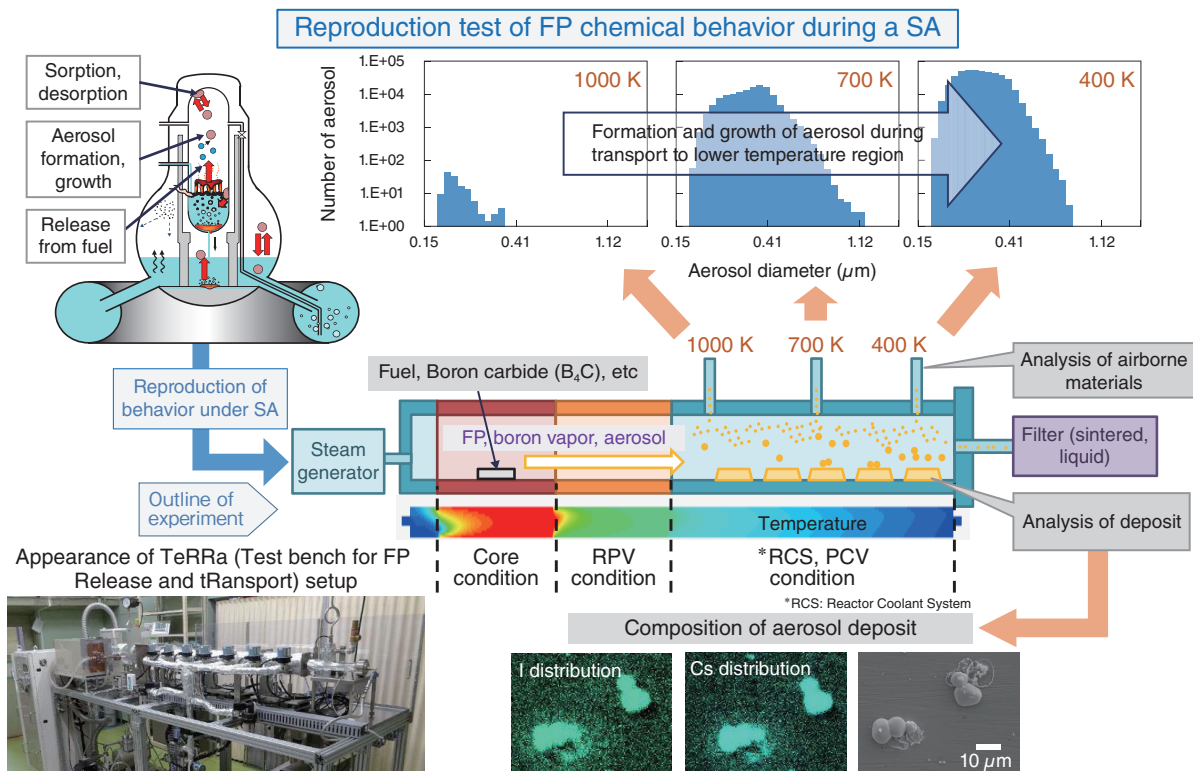


Fig.1-6 Technological development for reproductive experiments of FP chemical behaviors under SA conditions

We have developed an experimental setup to reproduce cesium (Cs) chemical behaviors during transport in a high-temperature region of a reactor during a SA. We confirmed the performance of the setup for the measurement of chemistry-related phenomena such as Cs-containing aerosol formation and growth during transport and adhesion of Cs compounds to the structural material of a reactor. In the near future, we will acquire data concerning FP chemical behaviors and improve chemical behavior models based on analysis of the experimental data.

One of the most important and urgent issues for the decommissioning of the TEPCO's Fukushima Daiichi NPS is to decide the method of fuel debris removal. The distribution of cesium (Cs), which is the main radiation source in the reactor, is critical for this issue, and its characteristics such as chemical form and properties are required information for the evaluation of changes in the distribution over the course of years. In a severe accident (SA), Cs is released from fuel and reaches the primary containment vessel (PCV) through high-temperature regions such as the reactor pressure vessel (RPV). Therefore, the chemical reaction and physical behavior under such a high-temperature condition should be identified for the evaluation of the Cs distribution and characteristics. However, there are difficulties facing this evaluation because Cs reacts with various materials such as other fission products (FPs) and structural materials in a non-steady way in the high-temperature region.

We started a basic study to evaluate Cs chemical behavior systematically and improve the model in the high-temperature region of the reactor. The model will be used to improve the SA analysis code, which will lead to a more accurate evaluation of the Cs distribution and characteristics around the PCV.

Our setup was designed to reproduce the contiguous chemical behaviors of Cs during transport in a reactor. The condition in the high-temperature region of a reactor during a SA would be a

complex one where the changes in thermal-hydraulic condition, formation and growth of the aerosol, as well as the high-temperature chemical reaction, would occur simultaneously. Therefore, we designed this setup to have a simple path for FP transport to minimize thermal-hydraulic impacts upon the chemical behavior of Cs, and to measure changes in the aerosol size during transport for the estimation of its effects upon such behavior (Fig.1-6). Furthermore, the furnace used in this setup can reach a temperature up to 2500 K, enabling consistent reproduction of the chemical behaviors from fuel melting to transport in a reactor; this is an advantage of this setup compared with other similar setups.

We have previously confirmed that our setup can reproduce the formation and growth of Cs-containing aerosol under a SA condition by a heating test of a non-radioactive Cs-containing specimen. We also confirmed by chemical analysis of deposits that temperature where the Cs-containing aerosol was deposited is similar to the previous results under similar setups. From these results, we confirmed our setup's reliability for evaluating the chemical behavior of Cs during transport in a SA (Fig.1-6).

In the future, we will proceed with acquiring data concerning the chemical behavior of Cs by the heating a Cs-containing specimen under various conditions. Modeling will be conducted based on analysis of the experimental data.

Reference

Miyahara, N., Miwa, S. et al., Development of Experimental and Analytical Technologies for Fission Product Chemistry under LWR Severe Accident Condition, Proceedings of 2017 Water Reactor Fuel Performance Meeting (WRFPM 2017), Jeju Island, Korea, 2017, 9p., in USB Flash Drive.

1-4 Thermodynamic Estimation of Fuel Debris Characteristics

— Thermodynamic Evaluation of High-Temperature-Reaction Products between Molten Core and Concrete —

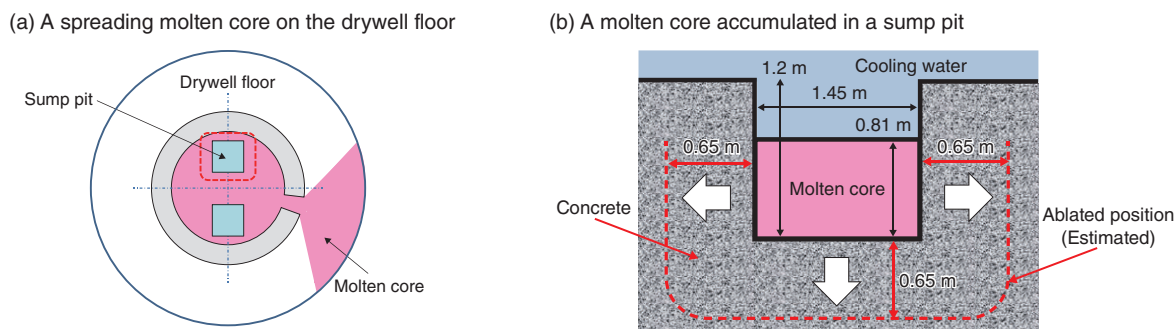


Fig.1-7 Image of a spreading molten core on the drywell floor of a containment vessel

(a) The molten core spreading on the concrete floor of the containment vessel melts and ablates concretes through its heat. (b) Its temperature decreases with the mixture of concrete components and concrete ablation, then finishes.

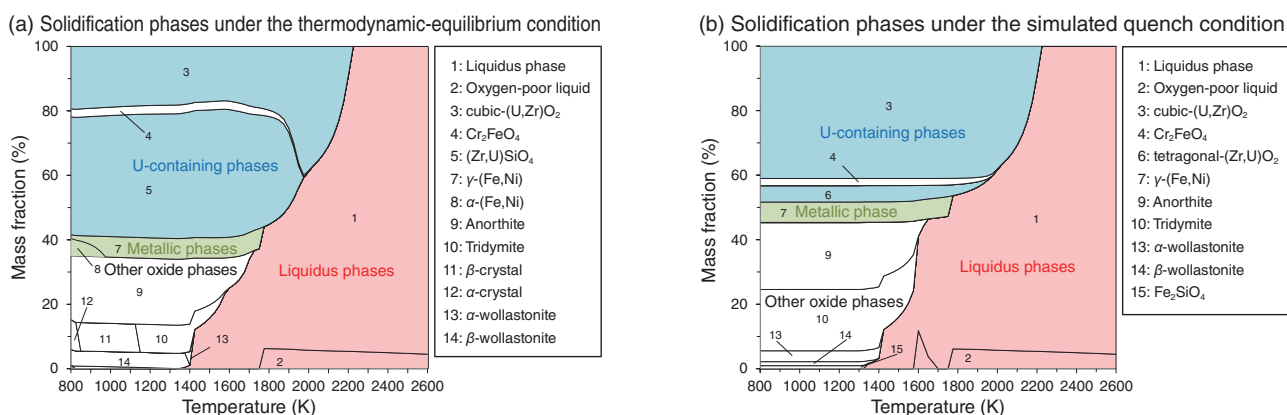


Fig.1-8 Thermodynamically estimated solidification phases of mixed molten-core-concrete material

(a) The oxide phases containing uranium (U) and zirconium (Zr), which have high liquidus temperatures, solidify during the cooling process of the liquidus phases composed of molten core and concrete. Metallic and oxide phases composed of concrete components then solidify. (b) The formation of a tetragonal solid solution of U and Zr in the place of zirconium silicate was predicted.

The TEPCO estimated that molten-core material penetrated the bottom of the pressure vessel and spread on the concrete floor in the containment vessel during the Fukushima Daiichi NPS (1F) accident, as shown in Fig.1-7. Core material at temperatures above 2000 °C melts and ablates the concrete. The liquidus temperature of the molten core decreased and the ratio of solid phases increased due to mixture of concrete components, and concrete ablation is then completed. The solidified material is called fuel debris and consists of complex materials composed of uranium (U) dioxide fuel, structural materials such as iron and zirconium (Zr), and concrete components. Estimation of the chemical phases and properties of fuel debris is important for fuel debris removal. We have evaluated phases using the experimental and computational approaches. This paper shows the part of our results obtained by the computational approach.

In this study, FactSage6.4 was used as thermodynamic-equilibrium software and NUCLEA was used as a thermodynamic database. The initial condition was decided with analytical results for concrete picked up from the 1F building and simulation results of the 1F-accident progression.

Under the thermodynamic-equilibrium condition, the

solidification phases in regions under long-term cooling, such as the inside of molten materials, can be estimated. In this condition, U is expected to form a cubic solid solution with Zr ((U,Zr)O₂) and zirconium silicate ((Zr,U)SiO₄), as shown in Fig.1-8(a). The formation of a metallic phase made of stainless steel and oxide phases composed of concrete components were also estimated. It seems that (U,Zr)O₂ and (Zr,U)SiO₄ solidify in a low-liquidus-temperature oxide liquid composed of concrete components during the cooling process.

On the contrary, in regions under the quench condition simulated with the Scheil model, such as near the boundary of the cooling water, we estimate that most of the U solidifies into cubic (U,Zr)O₂ and tetragonal Zr rich solid solution ((Zr,U)O₂) forms, as shown in Fig.1-8(b).

In conclusion, it was estimated that main phases of fuel debris are (U,Zr)O₂ and (Zr,U)SiO₄ and that the formation behavior depends on the cooling conditions. These results, together with the actual fuel debris characteristics, will be useful for fuel debris removal and clarification of the progression of the 1F accident. We will estimate the fuel debris characteristics in more detail using experimental data and computational prediction.

Reference

Kitagaki, T. et al., Thermodynamic Evaluation of the Solidification Phase of Molten Core-Concrete under Estimated Fukushima Daiichi Nuclear Power Plant Accident Conditions, Journal of Nuclear Materials, vol.486, 2017, p.206-215.

1-5 Can Fuel Debris be Retrieved without Water?

— Development of a Numerical-Simulation Method for Air Cooling of Fuel Debris —

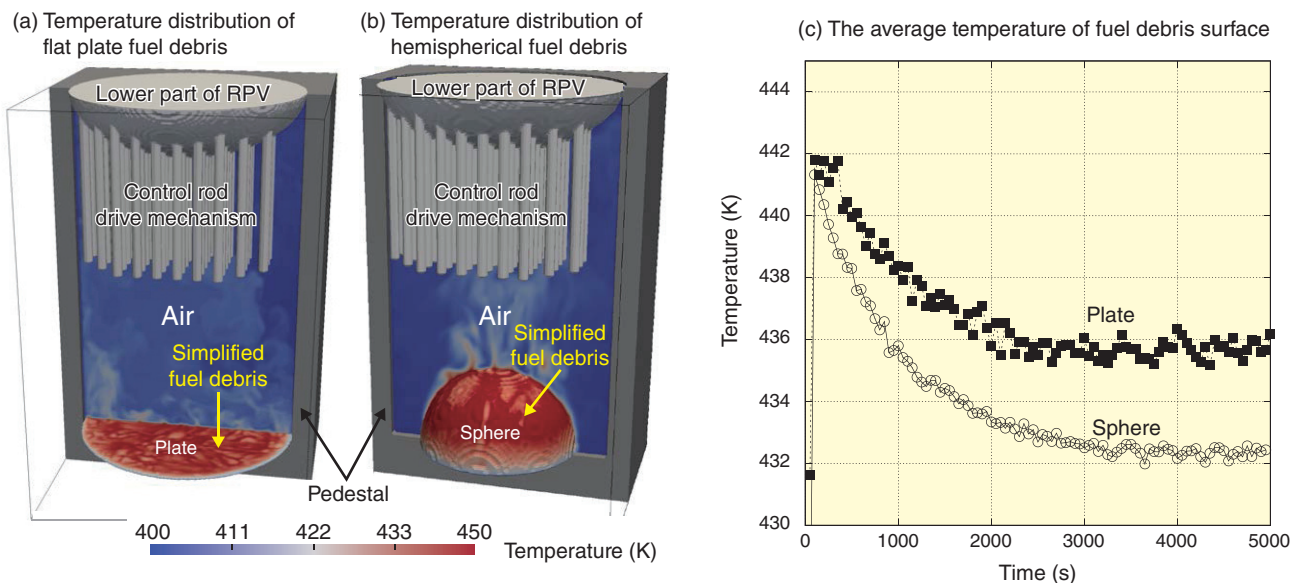


Fig.1-9 Exemplary numerical-simulation results

We performed air-cooling simulation for simplified fuel debris, which is cooled by a natural convection induced by its decay heat, assuming that this debris accumulates at the lower part of a pedestal in some part of the primary containment vessel. The color of fuel debris and gas indicates its temperature. From Figs.1-9(a) and (b), we found that the heat of fuel debris is transferred by a complicated flow around it, and also that the surface-temperature distribution of a spherically shaped case becomes more uniform than the plate case. From Fig.1-9(c), the average temperature of fuel debris is varies slightly with difference in the shape.

It is estimated that solidified fuel and structures (fuel debris) have accumulated at the lower part of the primary containment vessel (PCV) of the TEPCO's Fukushima Daiichi NPS (1F). As possible retrieval methods, full submersion (fuel debris is retrieved inside water) and a dry method (fuel debris is retrieved without water) are reviewed. Although the full-submersion method allows cooling fuel debris to be retrieved perfectly, some problems remain, such as water leakage and generation of contaminated water. On the contrary, dry methods have the merit not generating contaminated water (which therefore cannot leak). However, a mechanism for air cooling of fuel debris, including its decay heat, has yet to be elucidated. Thus, such a method must be developed.

To evaluate the cooling performance of fuel debris, we have to calculate not only the heat and flow around this debris, but also to estimate its shape and position. Such an evaluation is very difficult in 1F in its current state. Therefore, we are developing a computational-fluid-dynamics code called JUPITER for elucidating the melt behavior of fuels and structures, and we investigate the air-cooling performance by applying JUPITER to this problem.

To use JUPITER to investigate the air-cooling performance and the influence of debris shape (one major source of uncertainty) upon the temperature field, as shown in Figs.1-9(a) and (b), we

performed preliminary simulation for plate and spherical debris in a simplified lower part of the PCV including the control-rod drive mechanism. In the simulation, we consider heat generation by decay and set the temperature of fuel debris higher than that of the surrounding air. As a result, as shown Figs.1-9(a) and (b) the air heated by fuel debris moves to the top of the reactor vessel, becoming lighter than the other part of the air. This phenomenon makes the flow pattern very complicated and causes the surface temperature of the fuel debris to change intricately. In the case of spherical debris, the streamlined shape causes the flow in the debris' vicinity to flow more easily than in the plate case, meaning heat transfer becomes large and the amount of heat transfer to the air phase increases; this causes the surface temperature of the spherical debris to tend to be lower than that of plate shape, as shown in Fig.1-9(c). From these results, we found that evaluating debris shape and air flow is important because this shape affects to air-cooling performance. Therefore, JUPITER can be used to investigate air-cooling performance in the dry condition.

In the near future, we will perform a validation simulation with some experiments, as well as simulation under several fuel shapes and location conditions based on estimated accident scenarios. These results will be used to help select a fuel-retrieval method.

Reference

Yamashita, S. et al., Development of a Numerical Simulation Method to Evaluate Molten Material Behavior in Nuclear Reactors, Proceedings of 2017 International Congress on Advances in Nuclear Power Plants (ICAPP 2017), Fukui and Kyoto, Japan, 2017, paper 17640, 10p., in DVD-ROM.

1-6 Investigating the Effect of Seawater and Concrete Components upon Nuclear-Fuel-Reprocessing-Plant Materials

— Effect of Sulfate Ions upon Corrosion of a Highly Active Liquid-Waste Tank —

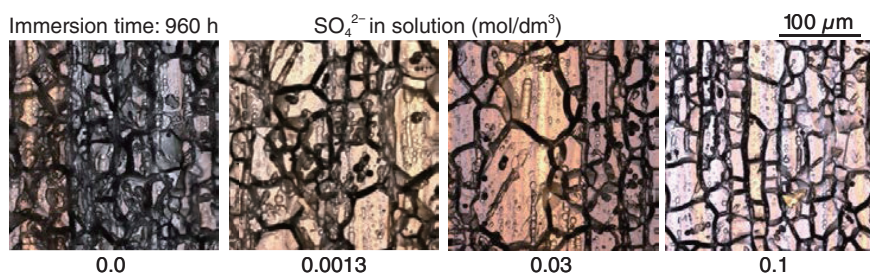


Fig.1-10 Corrosion morphology of SUS316L specimens in HAW with sulfate ions

We conducted an immersion test for 960 h and confirmed the progress of uniformly intergranular corrosion under all conditions.

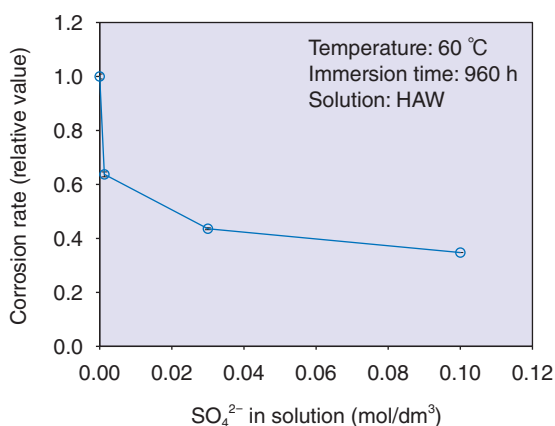


Fig.1-11 Relation between the corrosion rate of SUS316L specimens and sulfate-ion concentration in HAW

The corrosion rate was calculated from the weight loss and is shown as a value relative to that in HAW without sulfate ions. The corrosion rate decreased with increasing sulfate-ion concentration.

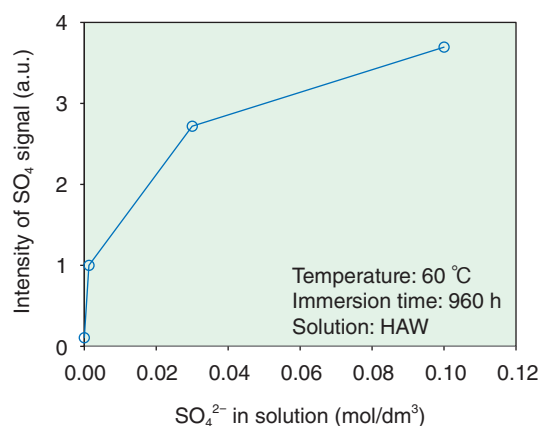


Fig.1-12 Relation between the intensity of the SO₄ signal and the sulfate-ion concentration in HAW

The intensity of the SO₄ signal increased with increasing sulfate-ion concentration. There was a correlation between this signal and the corrosion-rate behavior, suggesting that the protective film inhibited the corrosion of SUS316L.

The spent fuel stored in the pools at the TEPCO's Fukushima Daiichi NPS was exposed to injected seawater and may contain concrete fragments yielded from the explosion. Therefore, the influence of these impurities upon reprocessing needs to be investigated. It was reported that these impurities will move to the waste solution during the separation process. We have been investigating the effect of these impurities upon the corrosion of a high-activity-liquid-waste tank. In this study, the effect of sulfate ions, which are components of seawater and concrete, upon the corrosion behavior was investigated.

An immersion test in surrogate highly active liquid waste (HAW) was performed using SUS316L as a representative tank material. HAW contained nitric acid and surrogate fission products (ruthenium (Ru), cerium (Ce), neodymium (Nd), and vanadium (V) as a substitute for neptunium (Np).

Under all conditions, intergranular corrosion took place (Fig.1-10) and the corrosion rate was suppressed with increasing sulfate-ion concentration (Fig.1-11); the inhibition ratio also decreased. The result of X-ray photoelectron spectroscopy

(XPS) indicated a sulfate on the surface of the specimens after the immersion test. The relationship between the intensity of the SO₄ signal of the XPS spectrum and the concentration of sulfate ions in the solution is shown in Fig.1-12. With increasing sulfate-ion concentration, the intensity of the SO₄ signal increased, but the rate of this increase tended to decrease.

The main factor affecting intergranular corrosion was thought to be Ru, which can have a high valance (+VIII). It has been reported that Ru has a significant effect upon corrosion; however, the slight addition of sulfate ions (approximately 1/100 of Ru concentration (0.1 mol/dm³)) drastically decreased the corrosion rate. This result implies that the contribution of direct interaction between Ru and sulfate ions is small. On the other hand, the correlation between the sulfate ions in HAW and the SO₄ signal of XPS indicates that the dissolution reaction is suppressed by some compounds derived from sulfate ions. Inhibitions caused by sulfate ions were reported in pitting corrosion of stainless steel in NaCl solution, and a similar mechanism also seems to be working in this system.

Reference

Ambai, H. et al., Effect of Sulfate Ion on Corrosion Behavior of SUS316L in High Active Liquid Waste, Zairyo to Kankyo (Corrosion Engineering of Japan), vol.66, no.5, 2017, p.169-172 (in Japanese).

1-7 Estimation of the Amount of Radioactivity in Water-Treatment Waste

— Calculation of Radionuclide Concentration in Contaminated Water —

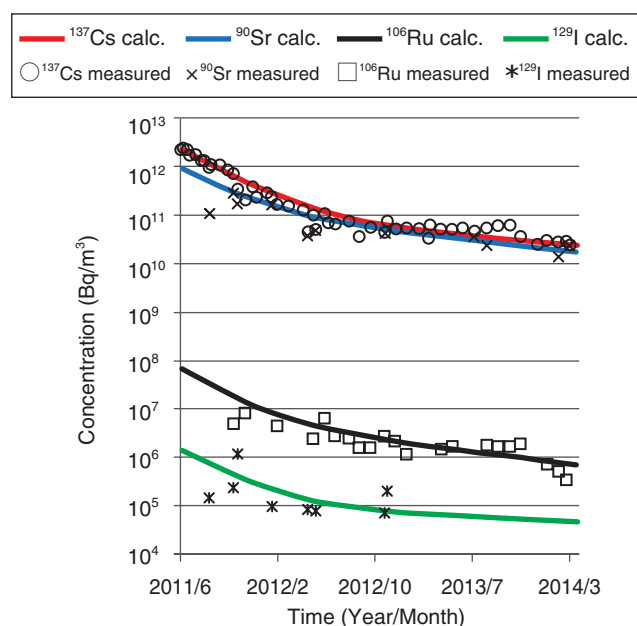


Fig.1-13 Time dependence of the radionuclide concentration in contaminated water

The high initial concentration of radioactivity decreased due to dilution by a continuous cooling water supply. Since middle of 2012, this decrease in concentration has slowed down, suggesting that radionuclides are released from the fuel debris continuously. Lines indicate calculation results with the analytical data.

At the TEPCO's Fukushima Daiichi NPS (1F), a water-treatment system consisting of cesium (Cs)-adsorption devices and other components is being operated to remove radionuclides from the contaminated water. Some secondary wastes, such as sludge and spent adsorbents, are generated from water treatment. These wastes have never been generated in normal operation of the NPS; therefore, investigating new methodologies for their storage, processing, and disposal is necessary. To establish such methodologies, waste composition and radioactive inventory are essential information.

The cooling water for the damaged fuels in 1F1, 1F2, and 1F3 is routed from the reactor buildings by way of turbine buildings to the Centralized Radiation Waste Treatment Facility, and fed to the water-treatment system. The radionuclide concentration in this contaminated water, as fed to Cs-adsorption devices, is useful for estimating the total amount of radioactivity in the waste from the water-treatment system.

^{134}Cs and ^{137}Cs concentrations in the contaminated water are so high that it is rather easy to estimate the ^{134}Cs and ^{137}Cs inventories. On the contrary, few data are available for the other radionuclides due to low concentrations of radioactivity or a lot of time and effort being necessary for analysis. A calculation model has therefore been developed to estimate the

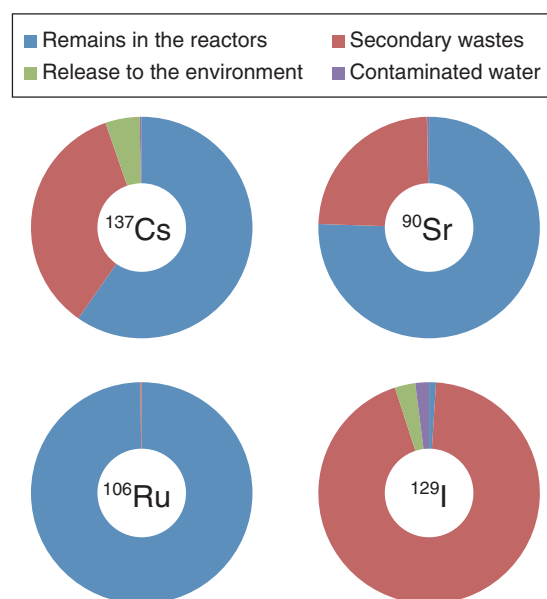


Fig.1-14 Estimated fractions of the inventory of ^{137}Cs , ^{90}Sr , ^{106}Ru , and ^{129}I on 13 March 2014, when water-treatment-system operation commenced

When the total radioactive inventories of the three reactors just before the accident were at 100%, the inventories of secondary wastes from the water-treatment systems were at approximately 35% for ^{137}Cs , approximately 24% for ^{90}Sr , less than 1% for ^{106}Ru , and approximately 94% for ^{129}I . This indicates some differences between radionuclides.

concentrations of various nuclides in the contaminated water.

Since the ^{137}Cs concentration initially decreased at a constant rate with this decrease slowing after the middle of 2012, the calculation model assumes two source terms for radionuclides; the initial release and the continuous release of radioactivity to the cooling water. The concentrations of some nuclides including ^{90}Sr , ^{106}Ru , and ^{129}I were calculated by an equation derived from fitting with the analytical data (Fig.1-13).

Differences in radionuclide behavior were observed; for example, the initial concentration of ^{90}Sr was lower than that of ^{137}Cs , although the concentrations of both nuclides became gradually closer owing to similar continuous release rates. The ^{106}Ru concentration remained at a low value because both the initial concentration and continuous release of ^{106}Ru are relatively low.

The radionuclide inventories in the secondary wastes from the water-treatment system and the inventories of remains in the reactors were estimated with the calculated concentrations (Fig.1-14). The fractions of ^{137}Cs and ^{129}I , which are volatile and water-soluble, were indicated to be greater in the secondary wastes. Conversely, insoluble elements like Ru were suggested to mostly remain in the reactors.

Reference

Shibata, A. et al., Estimation of the Inventory of the Radioactive Wastes in Fukushima Daiichi NPS with a Radionuclide Transport Model in the Contaminated Water, Journal of Nuclear Science and Technology, vol.53, issue 12, 2016, p.1933-1942.

1-8 Development of a Small, Portable Position-Sensitive Alpha-Particle Detector

— Direct Measurement of Plutonium Contamination in Narrow Spaces of Solid-Waste Material and Equipment —

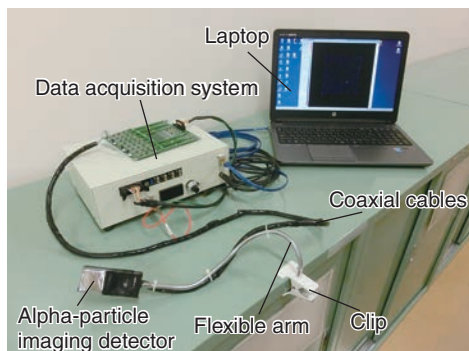


Fig.1-15 The developed small and portable position-sensitive α -particle detector

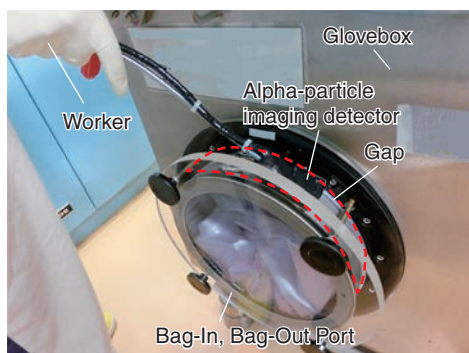


Fig.1-16 Appearance of measurement by the equipment

When decommissioning nuclear facilities such as the TEPCO's Fukushima Daiichi NPS, a lot of solid wastes will be produced. Surface contamination on these wastes should be measured for disposal. It is necessary to measure not only β and γ radionuclides, but also α radionuclides such as plutonium (Pu) isotopes. Since the range of α particles in air is approximately 4 cm, a ZnS(Ag) survey meter, which is an α -particle detector, should be brought as close as possible to the contaminated area. However, it is difficult to measure the surface contamination in narrow spaces of solid waste and equipment using a ZnS(Ag) survey meter. Such materials must be cut for measurement, but certain materials can be impossible to cut. moreover, radon (Rn) progeny exist and emit α particles such that Pu and Rn progeny should be distinguished.

Therefore, we developed a small and portable position-sensitive α -particle detector (Fig.1-15). The detector part comprises a ZnS(Ag) scintillator with a thickness of 10 mg/cm², a light guide, and a photosensor (silicon photomultiplier array). The size of the detector part was 26 mm × 26 mm × 15 mm, and its thickness was ~1/5 that of the ZnS(Ag) survey meter. Fig.1-16

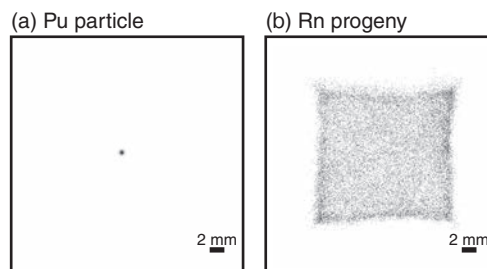


Fig.1-17 Measured 2-dimensional distributions of α particles: Pu sample (a) and Rn progeny (b)

For the Pu sample, α particles were distributed as a spot, whereas for the Rn progeny, they were uniformly distributed.

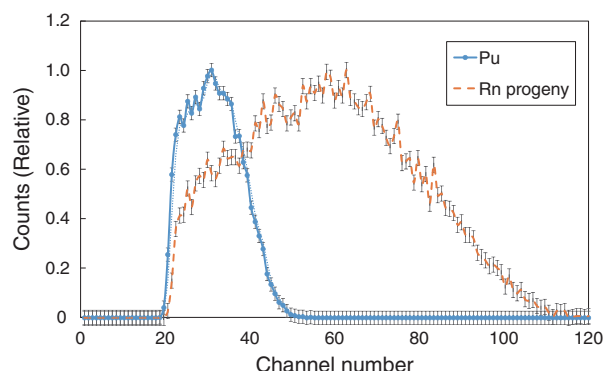


Fig.1-18 Energy spectra of the Pu sample and the filter of Rn progeny (the horizontal axis corresponds to α -particle energy)

The count of the Pu sample was confirmed in fewer than 60 channels, whereas that of the Rn progeny used more than 60 channels. Therefore, both quantities could be distinguished.

shows the appearance of the measurement of equipment (Bag-In/ Bag-Out Port) using our developed detector. Our detector was confirmed to be able to perform direct measurement within a narrow space.

Our developed detector obtained the 2-dimensional distribution and energy spectra of α particles for discrimination of Rn progeny. Fig.1-17 shows the measured 2-dimensional distribution of α particles and Fig.1-18 shows the energy spectra of the Pu sample and the Rn-progeny filter. The α particles for Pu were distributed as a spot, whereas they were uniformly distributed for Rn progeny. In Fig.1-18, both spectra confirmed different channels. This is because the α -particle energies are 5.5 MeV from ²³⁸Pu and 5.15 MeV from ²³⁹Pu, whereas ²¹⁴Po, which is dominant among Rn progeny, emits 5.5-MeV α particles. From these results, Pu and Rn progeny should be distinguished by our developed detector.

This work was supported by the Japan Society for the Promotion of Science (JSPS) KAKENHI Grant-in-Aid for Young Scientists (B) (No.15K21618).

Reference

Morishita, Y. et al., Flexible Alpha Camera for Detecting Plutonium Contamination, Radiation Measurements, vol.103, 2017, p.33-38.

1-9 Study of the Contamination State inside the Reactor Building

— Detailed Radiochemical Analysis to Accelerate Disposal of Waste —

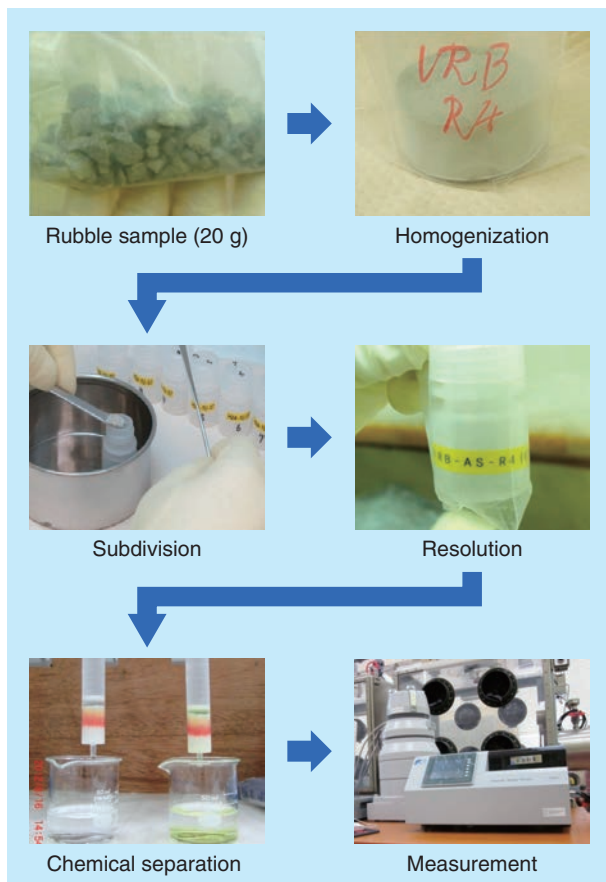


Fig.1-19 Flow of radiochemical-analysis operation

Rubble samples are pulverized using a ball mill for homogenization. The homogenized samples are subdivided and a pretreatment / separation method is carried out suitable for each nuclide.

For the decommissioning of the TEPCO's Fukushima Daiichi NPS (1F), the establishment of disposal policies for the waste (including rubble) that will be generated is an urgent task. To accelerate waste treatment and subsequent disposal, it is first important to clarify information such as the radionuclide and radioactivity concentrations of waste generated by the accident. Therefore, we conducted radiochemical analysis of rubble collected in the reactor buildings (Fig.1-19).

Fig.1-20 shows an example of the nuclides detected among the acquired data for radioactivity concentration. The ^{90}Sr concentration tended to be proportional to that of ^{137}Cs with a correlation coefficient of 0.89. Thus, there is a possibility of estimating ^{90}Sr concentration, which is difficult to directly measure, based on radioactivity from ^{137}Cs (which is easy to measure). On the contrary, it was not clear that the ^{238}Pu concentration was proportional to the ^{137}Cs concentration with a correlation coefficient of 0.51, and further accumulation of radioactivity-concentration data is necessary.

The $^{90}\text{Sr}/^{137}\text{Cs}$ ratio of Units 1, 2, and 3 obtained by radiochemical analysis were $(3.2 \pm 1.5) \times 10^{-3}$, 1.9×10^{-2} ,

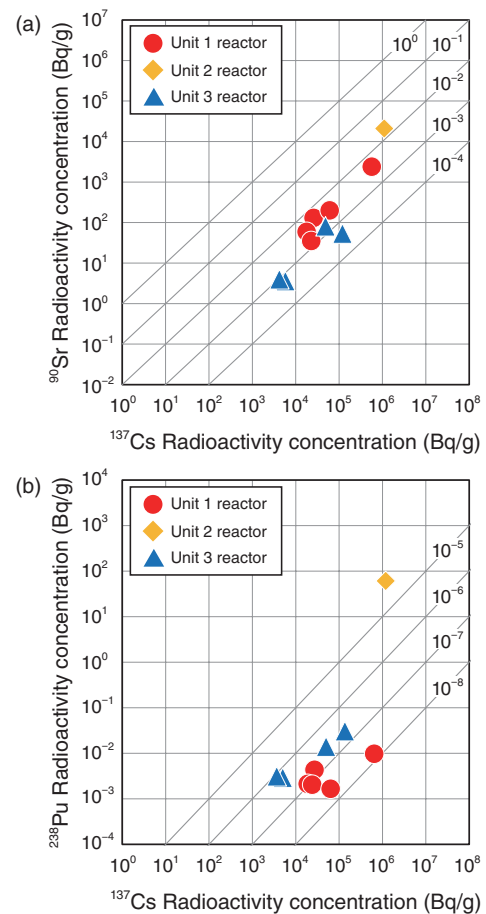


Fig.1-20 Measured radioactivity-concentration results

Concentrations of (a) ^{90}Sr and (b) ^{238}Pu as functions of that of ^{137}Cs (Corrected on March 11, 2011).

and $(8.1 \pm 4.6) \times 10^{-4}$, respectively. These values were 1 to 3 orders of magnitude smaller than the $^{90}\text{Sr}/^{137}\text{Cs}$ ratio in fuel in the nuclear reactor calculated by computer code (ORIGEN2). The analytically obtained $^{238}\text{Pu}/^{137}\text{Cs}$ ratios of Units 1, 2, and 3 were $(6.0 \pm 6.4) \times 10^{-8}$, 5.5×10^{-5} , and $(3.9 \pm 1.9) \times 10^{-7}$, respectively. These values were 3 to 6 orders of magnitude smaller than the $^{238}\text{Pu}/^{137}\text{Cs}$ ratio calculated by the computer code. Therefore, the extent of transport from fuel to the reactor building is suggested to occur in the order $^{238}\text{Pu} < ^{90}\text{Sr} < ^{137}\text{Cs}$.

Results obtained by radiochemical analysis are expected to be used not only for estimating the amount of radioactivity inside the reactor building, but also to evaluate the radiation exposure to workers and the environment. We will continue to analyze radioactive waste from 1F and accumulate radioactivity-concentration data for treatment and subsequent disposal.

This achievement was supported by the Subsidy Project of Decommissioning and Contaminated Water Management by the Agency for Natural Resources and Energy, Ministry of Economy, Trade and Industry, Japan (METI).

Reference

Sato, Y. et al., Radiochemical Analysis of Rubble Collected from Fukushima Daiichi Nuclear Power Station, Hoken Butsuri, vol.51, no.4, 2016, p.209-217 (in Japanese).

1-10 Development of an Analytical Method to Determine ^{93}Zr , ^{94}Nb , and ^{93}Mo Concentrations in Contaminated Water and Rubble Waste

— Radiochemical Separation of Difficult-to-Measure Nuclides —

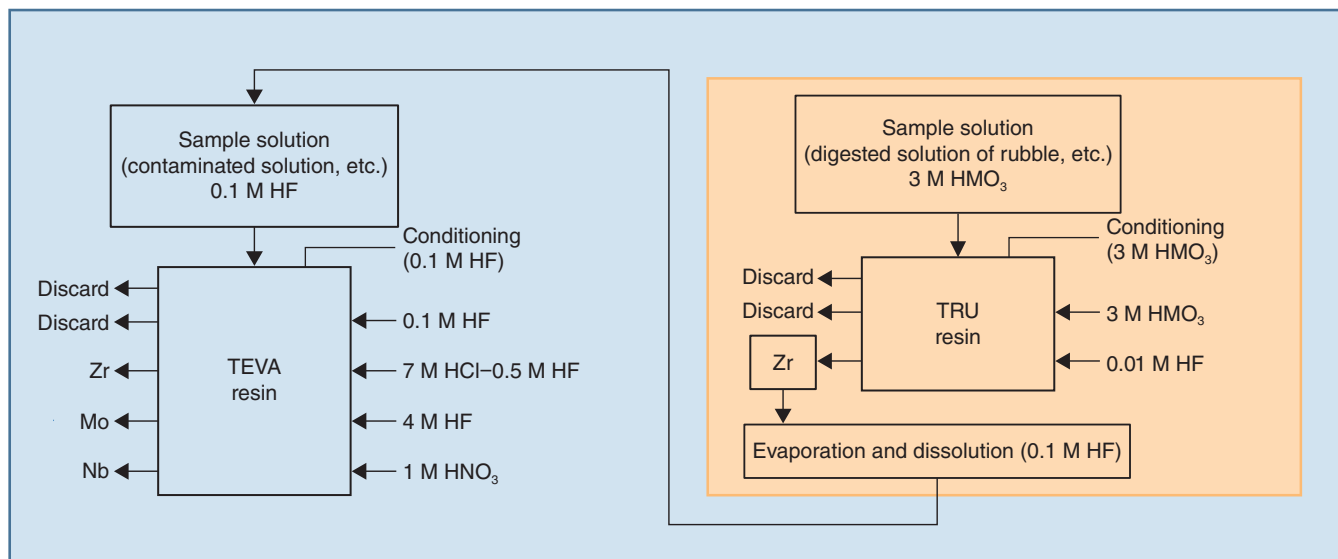


Fig.1-21 Separation method of ^{93}Zr , ^{94}Nb , and ^{93}Mo in contaminated water (left) and in rubble waste (right and left)

Chemical separation of ^{93}Zr , ^{94}Nb , and ^{93}Mo from major elements, radiocesium, and so on, and mutual separation from one another are indispensable for measuring the nuclides contained in contaminated water and rubble waste. We developed separation methods using TEVA and TRU resin.

There are large quantities of highly contaminated water and rubble waste in the TEPCO's Fukushima Daiichi NPS. Although contaminated water is being decontaminated at the water-processing facility, secondary waste, such as sludge, is being generated by this process. To treat the secondary and rubble waste, the radioactivity concentrations of important nuclides, which have a high impact upon safety, have to be evaluated. Because JAEA had scant experience in the measurement of zirconium-93 (^{93}Zr), niobium-94 (^{94}Nb), and molybdenum-93 (^{93}Mo), which are examples of important nuclides, it was necessary to develop an analytical method for such isotopes. To analyze these nuclides, they have to be separated from highly radioactive cesium-137 (^{137}Cs) and major elements of sea water and rubble (crude separation); furthermore, they have to be separated from each other (mutual separation).

Cs and most of major elements of sea water and rubble waste exist as cations in solutions, whereas Zr, Nb, and Mo tend to be anions in solutions. Focusing on the difference, we developed a chromatographic-separation technique using

TEVA resin, which shows anion-exchanger performance. This method is advantageous in that operation is simpler and more rapid than existing techniques, such as the precipitation method. First, the quantities of Zr, Nb, and Mo extracted on the TEVA resin from various acid solutions were studied to find a suitable solution condition. Consequently, as shown in Fig.1-21, crude separation is possible using 0.1 M HF as a sample solution because major cations are eluted; by contrast, Zr, Nb, and Mo are extracted on the TEVA resin in this condition. Furthermore, Zr, Mo, and Nb were eluted sequentially with 0.5 M HF/7 M HCl, 4 M HF, and 1 M HNO₃, respectively. Thus, ^{93}Zr , ^{94}Nb , and ^{93}Mo in the contaminated water were analyzed using this method.

However, preparing a 0.1 M HF sample solution when rubble waste is dissolved by acid is difficult. In such a case, as shown on the right-hand side of Fig.1-21, Zr was separated using TRU resin with a higher concentration of acid; then, it was purified using the same method as the contaminated water.

References

- Shimada, A. et al., Development of an Extraction Chromatography Method for the Analysis of ^{93}Zr , ^{94}Nb , and ^{93}Mo in Radioactive Contaminated Water Generated at the Fukushima Daiichi Nuclear Power Station, *Journal of Radioanalytical and Nuclear Chemistry*, vol.310, issue 3, 2016, p.1317-1323.
- Shimada, A. et al., Separation of Zr in the Rubble Waste Generated at the Fukushima Daiichi Nuclear Power Station, *Journal of Radioanalytical and Nuclear Chemistry*, vol.311, issue 3, 2017, p.1613-1618.

1-11 Development of a Test Method for Remotely Operated Robots for Decommissioning

— Design of Testing Fields for Robot-Performance Evaluation and Operator-Proficiency Training —

(a) Pillar-shape test field with steps (b) Staircase-type test field



(c) Checkered iron slope test field (d) Grating floor test field

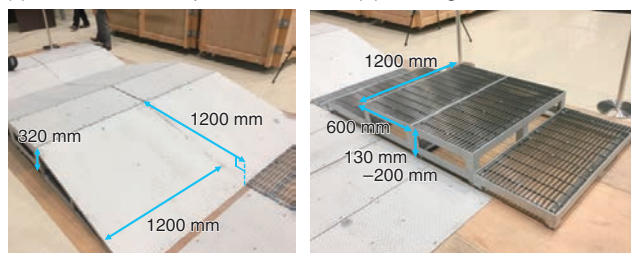


Fig.1-22 Developed test fields

Cable troubles, recognition ability of the working environment, running performance on uneven terrain, and the material properties of the floor were selected as major challenges facing remotely operated robots; to evaluate these problems, we devised four types of testing fields (a)–(d).

Inside the reactor buildings at the TEPCO's Fukushima Daiichi NPS (1F), remotely operated technologies including robots are being deployed for decommissioning tasks. However, some troubles with robot operations have occurred on account of the hazardous working environment. Therefore, it is crucial to execute prior performance evaluation of the robots and operator-proficiency training according to the mission and task. As a pioneering work by the National Institute of Standards and Technology (NIST), a series of standard test methods for response robots (STM) have been developed to measure robot mobility and operability in hazardous environments and to facilitate quantitative evaluation. It is reasonable to introduce a similar STM concept to remote operations for smooth decommissioning of 1F. Most STMs simulate ground surfaces such as rubble utilizing wood; however three-dimensional structures and metal properties that existed in the reactor building have not been prepared. The aim of this research is to develop test methods and test fields for decommissioning tasks that introduce the characteristics and properties of the working environment in the reactor building.

First, we reviewed video data related to robotic operation that is available from the TEPCO website and used a time-analysis approach to study the robot's behavior. The results revealed that traveling, traveling over steps, angular adjustment of sub-crawler tracks, and stopping account for a large percentage of the robot's time allocation. Also, classification and functional

(a) Reproduction of the effect of cable twining around developed test field



(b) Reproduction of blind region in the view by developed test field



Fig.1-23 Verification of the remotely operated robot by test runs

Test runs of the remotely operated robot showed that our testing fields reproduced the problems in remote operations.

analysis of operational troubles demonstrated that the major concerns include structures interfering with the cable connected to the robot and difficulty in recognizing the surrounding environment and the status of the robot.

Based on these results, we designed and developed a test field with three mutually perpendicular elements to reproduce cable interference and low surroundings recognition (Fig.1-22(a)). By conducting tests with a remotely operated robot, this setup is confirmed to reproduce the effect by which the cable can become entwined around a pillar-shaped part (Fig.1-23(a)). This pillar also became an obstacle, generating a blind spot in the operator's view (Fig.1-23(b)). When the robot moves in the reactor building, travel over the steps made of checkered iron and a grating is required. Therefore, we developed a staircase-type test field capable of changing the properties of the thread (Fig.1-22(b)). We also developed checkered-iron slopes and grating floors (Figs.1-22(c) and (d)). We could reproduce situations causing major trouble for remote operation and simulate the properties of the working environment. Developed fields have a size compatible with STM, as developed by NIST.

In a future study, we will design and develop a test field modeling the part accessible to the inside of the primary containment vessel (PCV) and arrange various test environments based on a combination of the test fields developed for promoting robot development and operator training to contribute to the decommissioning of 1F.

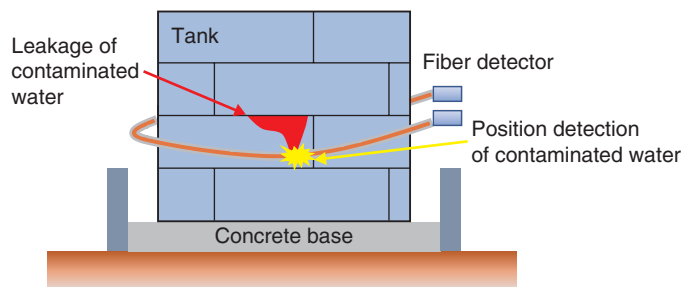
Reference

Kawabata, K. et al., Design of Test Methods for Remotely Operated Robots Utilized for Decommissioning Tasks, Proceedings of 2017 International Congress on Advances in Nuclear Power Plants (ICAPP 2017), Fukui and Kyoto, Japan, 2017, paper 17476, 4p., in DVD-ROM.

1-12 Fiber Detector for Monitoring of Contaminated Water

— Demonstration Experiment at the TEPCO's Fukushima Daiichi NPS —

(a) Image for monitoring contaminated water



(b) Demonstration experiment at the nuclear power station

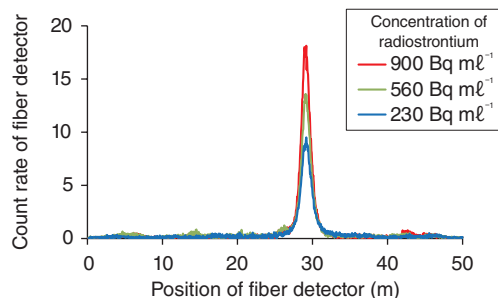

Fig.1-24 Image of the developed fiber detector for use in monitoring contaminated-water leakage

(a) Leakage of contaminated water from the tank was monitored by a fiber detector. (b) Demonstration examination was conducted at the tank.

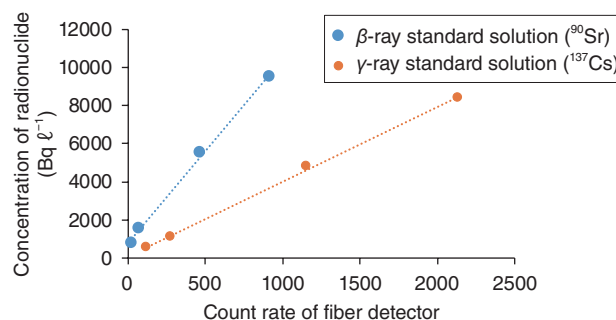
We have been measuring environmental radiation using a plastic-scintillation-fiber-type radiation detector since the accident at the TEPCO's Fukushima Daiichi NPS (1F). The fiber detector used in this study comprises a bundle of optical fibers with a plastic scintillator at its core. The photomultiplier tubes were placed at both ends of the optical-fiber bundle. The position at which radioactive emissions took place was pinpointed on the basis of the difference between the times at which two sensors at each end of the photomultiplier tube counted emissions. The advantage of a fiber detector, which is shaped like a string, is its ability to measure objects of various shapes with close contact. Moreover, the cost and labor needed for radiation monitoring can be reduced because the measurable area of the fiber detector is wider than that of a general radiation detector.

In 1F, various countermeasures have been taken against the risk of contaminated water leaking into the ocean. Thus, the frequency of leakage accidents from a contaminated-water tank has decreased. However, establishment of a leakage-monitoring technique is necessary because detection of contaminated water in the drainage has occurred several times under the present configuration. Therefore, we have conducted

(a) Position spectrum using contaminated water sample



(b) Calibration line of fiber detector using contaminated water sample


Fig.1-25 Calibration of the fiber detector using a contaminated water sample

(a) The peak count rate was observed by immersing the fiber detector in contaminated water. (b) The radionuclide concentration and count rate were related to positive correlation.

demonstration experiments to monitor contaminated-water leakage at 1F using a fiber detector developed for environmental-radiation monitoring.

A fiber detector of 50-m length was developed for monitoring leakage from the contaminated-water tank, as shown in Fig.1-24(a). Ten fiber detectors were gathered into a thin plastic tube with little shielding against β -rays emitted from ^{90}Sr . In the laboratory at 1F, the fiber detectors are able to monitor the contaminated water because the peak count rate was observed by immersing a fiber detector therein (Figs.1-24(b) and 1-25(a)). A demonstration examination using the fiber detector has been in advance of installation around the actual tank (Fig.1-24(b)).

To determine the concentration of contaminants in water from the count rate of the fiber detector, this detector was calibrated using contaminated-water samples of a certain concentration. The radionuclide concentration and count rate were related to positive correlation (Fig.1-25(b)).

This fiber detector was adopted by TEPCO to monitor contaminated water on the basis of our examination results. We wish to contribute to decommissioning work at 1F using a relevant technical support, such as new radiation-detection technology.

Reference

Sanada, Y. et al., Application to Contaminated Water Management in the Fukushima Daiichi Nuclear Power Station using the Plastic Scintillation Fiber, JAEA-Research 2016-011, 2016, 52p. (in Japanese).

1-13 Estimation of Doses to Residents with Consideration of Behavioral Patterns

— Is Decontamination of Residential Areas Based on a Guide Value of 0.23 $\mu\text{Sv/h}$ Effective? —

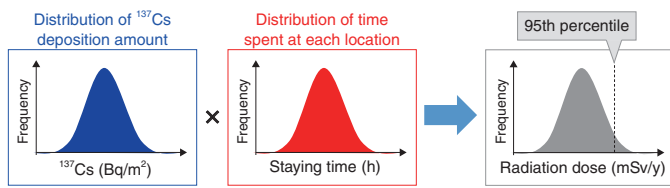


Fig.1-26 Dose assessment using a probabilistic approach
 10000 sets of input values comprising ^{137}Cs -deposition amounts and time spent by residents in the house, workplace, and other places were generated at random from distributions of those measured values. Annual doses were calculated 10000 times. Dose assessments were conducted by comparing the 95th percentiles of the dose distributions to 1 mSv/y. ^{137}Cs -deposition amounts equivalent to 0.23 $\mu\text{Sv/h}$ were applied to contamination of the residential area.

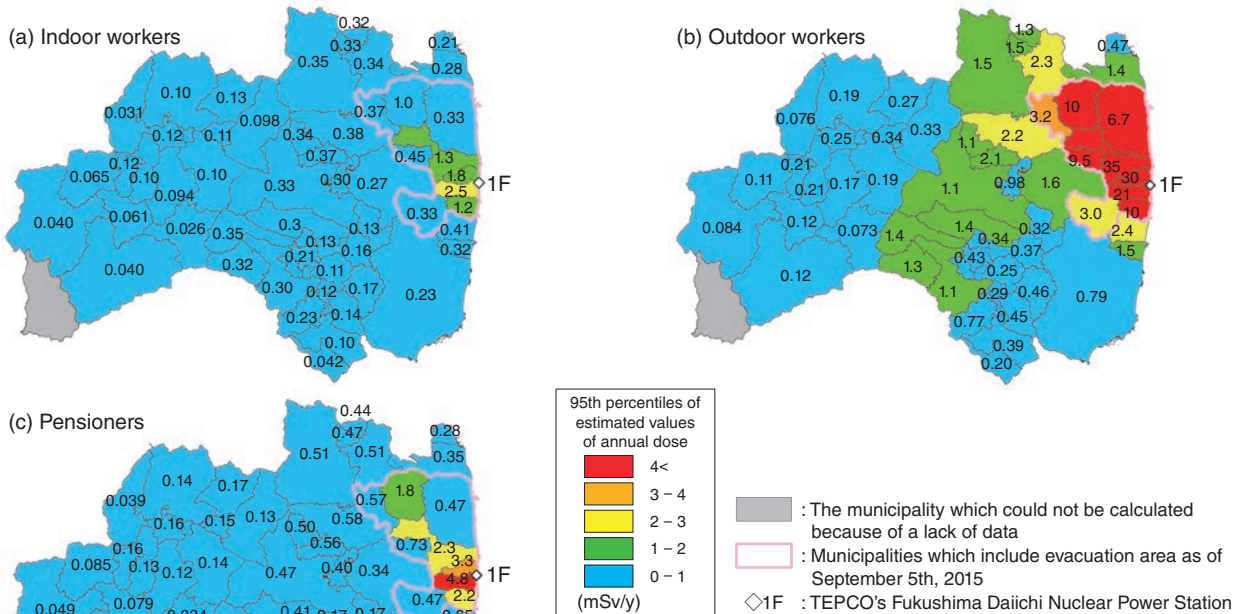


Fig.1-27 95th percentiles of the estimated values of annual doses from March 2016

In approximately two thirds of municipalities, the 95th percentile of all population groups were exposed to doses less than 1 mSv/y. In approximately one-third of municipalities, the 95th percentile of outdoor workers were exposed to doses of more than 1 mSv/y.

Large quantities of radioactive materials were released by the accident at the TEPCO's Fukushima Daiichi NPS (1F), and the influence of the accident still continues in affected areas. In terms of radiation protection, the Japanese government has adopted annual additional doses of 1 mSv as a long-term dosimetric target. According to the Ministry of the Environment, an additional dose of 1 mSv/y corresponds to an air-dose rate of 0.23 $\mu\text{Sv/h}$. We calculated annual doses to residents under the assumption that the air dose outside of their house is 0.23 $\mu\text{Sv/h}$ to assess the effectiveness of decontamination based on this value.

Radiation doses can be calculated from the degree of contamination at a living location and the time spent at these locations. The surface-deposition amounts of cesium 137 (^{137}Cs) in each municipality (as measured by airborne-monitoring survey) and actual survey data for time spent in houses, workplaces, and the other locations were used in this calculation. The probability distributions of deposition amounts of ^{137}Cs and staying times were generated based on these actual data. Numerical values were chosen from those distributions at random as input values for our probabilistic dose-assessment model (Fig.1-26). Residents were divided into three groups, i.e., indoor workers, outdoor workers, and pensioners, by differences in their behavioral patterns.

Calculations were conducted for all municipalities in Fukushima Prefecture. The radiation-dose distributions of each population group in each municipality were derived by 10000 repetitions of the calculation, and the 95th percentiles of these distributions (Figs.1-27(a), (b), and (c)) were compared with 1 mSv/y.

The radiation doses of indoor workers were found to be lowest, and those of outdoor workers were highest. The doses to the 95th percentile of indoor workers and pensioners were less than 1 mSv/y in all municipalities except for 5 in the former evacuation area. On the contrary, the doses to the 95th percentile of outdoor workers were more than 1 mSv/y in one-third of municipalities. These results indicate that (1) radiation doses to all population group in two-thirds of municipalities were adequately reduced by decontamination of residential districts; (2) dose management is needed for outdoor workers in one-third of municipalities; and (3) dose management for all population groups and decontamination in other areas besides residential districts is also necessary in 5 municipalities in the former evacuation area.

We estimated doses to working people and pensioners in this study, and we are going to develop a model for assessment of doses to children returning to the evacuation areas in the future.

Reference

Mori, A. et al., Assessment of Residual Doses to Population after Decontamination in Fukushima Prefecture, Journal of Environmental Radioactivity, vol.166, part 1, 2017, p.74-82.

1-14 How Long Does Radiocesium Remain in Forest-Surface Litter?

— Radiocesium Transfer from Litter to Mineral Soil in Two Forest Types —

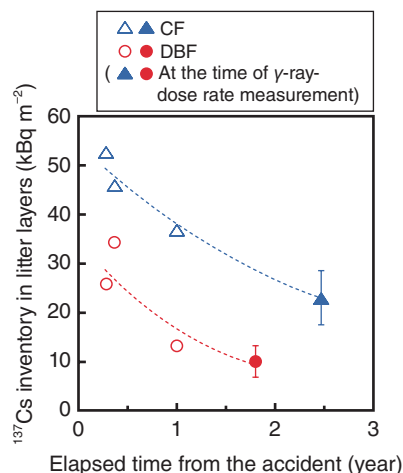


Fig.1-28 Temporal changes in the cesium-137 (¹³⁷Cs) inventory in litter layers

The ¹³⁷Cs inventory in the litter layer of cedar forests (CF) was bigger than that in deciduous broad-leaf forests (DBF), although the total ¹³⁷Cs inventory (litter + soil) was similar between these two contrasting forest types. The ecological half-life of ¹³⁷Cs in CF was 2.1 years, while that in DBF it was 0.95 years (closed symbols indicate spatial-distribution data).

Radiocesium released by the accident at the TEPCO's Fukushima Daiichi NPS (1F) contaminated a broad area of the surrounding forest. The dominant forest types in this area are deciduous broad-leaf forests (DBF) and various evergreen species, such as cedar forests (CF). In DBF, trees were leafless when the 1F accident occurred; thus, most of the radiocesium was deposited onto the forest floor, whereas in CF, part of the radiocesium was attached to the leaves and then transferred to the forest floor when they fell. We investigated the transfer of radiocesium from litter to soil in these two contrasting forest types. Furthermore, we conducted a detailed plot-scale investigation in both forests to estimate the spatial distribution of the retention of radiocesium in litter and the γ -ray-dose rate on the ground surface.

Litter and soil were collected from CF and DBF, and their radiocesium concentrations were measured 3, 5, and 12 months after the 1F accident. In these forests, radiocesium-deposition levels were similar. A 20 m \times 20 m plot was demarcated in each forest. The radiocesium inventory in litter and soil was measured at 25 points in each plot, and the γ -ray-dose-rate distribution was measured using a plastic-

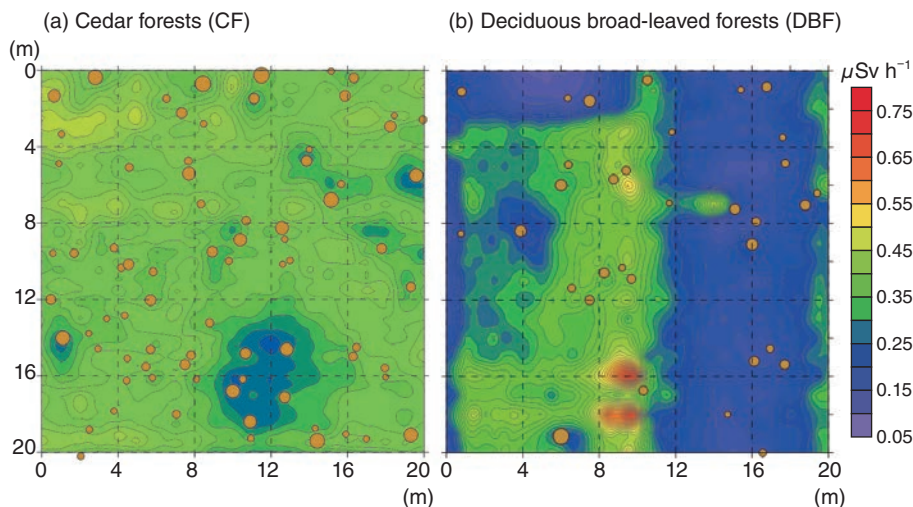


Fig.1-29 Spatial-distribution map of the γ -ray-dose rate at the ground surface in a 20 m \times 20 m plot area of CF (a) and DBF (b)

Circles in the panels indicate standing trees, and the diameters of the circles show the diameter at breast height (DBH). The γ -ray-dose rate had high spatial heterogeneity, and the distributions had no relation with the position or size of the standing trees. CF (a), in which more than half of the deposited radiocesium remained in the surface-litter layer, had a higher γ -ray-dose rate than DBF (b), in which more than 80% of radiocesium was transferred to the mineral soil.

scintillation-fiber (PSF)-detection system 1.8 and 2.4 years after the accident in DBF and CF, respectively.

The radiocesium inventory in the litter layer in CF was larger than that in DBF just after the accident, and the transfer rate to the soil in CF was slower than that in DBF (Fig.1-28). This was because the litter mass in CF was larger than that in DBF and radiocesium attached to the leaves was gradually transferred to the ground as leaves fell over several years. The radiocesium distributions in both forest types displayed high spatial variability, even over small areas (Fig.1-29). The spatial patterns of γ -ray-dose rates depended on the retention characteristics. These rates had a similar spatial distribution to the radiocesium inventory in the litter in CF, whereas the distribution of the γ -ray-dose rate in DBF was similar to that of the total radiocesium inventory (litter + soil). Therefore, it was clear that the forest type affected the dynamics of radiocesium on the forest floor. Radiocesium remaining in the litter is more readily available for vegetation than that in soil, which would be fixed strongly to soil minerals. There is probably less radiocesium recycling in DBF ecosystems than in CF ecosystems.

Reference

Koarashi, J., Atarashi-Andoh, M. et al., Forest Type Effects on the Retention of Radiocesium in Organic Layers of Forest Ecosystems Affected by the Fukushima Nuclear Accident, Scientific Reports, vol.6, 2016, p.38591-1-38591-11.

1-15 Mechanism of Vertical Migration of Radiocesium into Soils

— Effect of Sorption Kinetics upon Vertical Migration of Radiocesium into Soils —

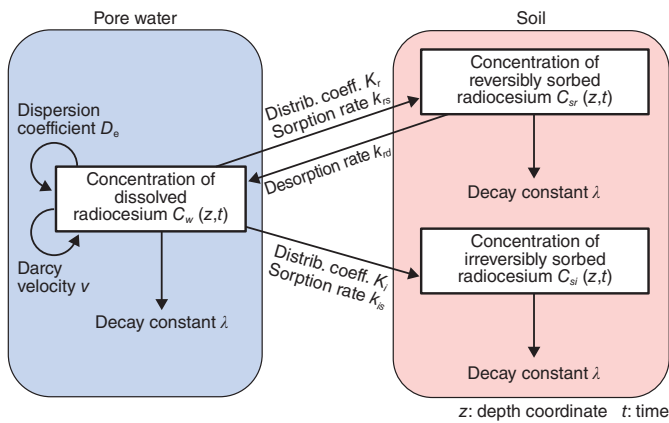


Fig.1-30 Schematic of the developed model

Soil comprises solid, liquid, and gaseous components. Radiocesium migrates in liquid by advection and dispersion. During the migration, sorption and desorption happen back and forth according to the chemical condition. While instantaneous equilibrium is often assumed for sorption, our model introduced fully kinetic terms for both reversible and irreversible sorption sites of the soil matrix.

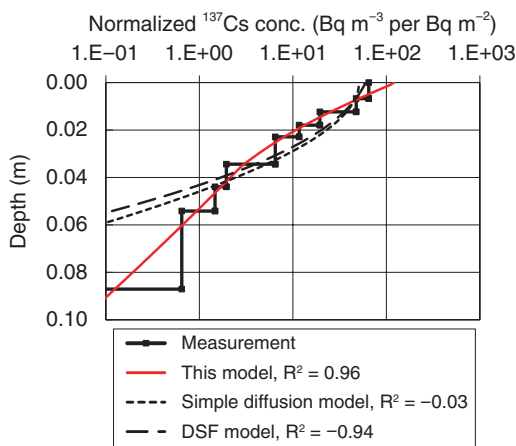


Fig.1-31 Comparison between the model results and the measurements

Our model successfully reproduced the exponential-shape profiles with long tails at large depth that the previous models could not express. The profiles in the figure represent the vertical distribution of radiocesium nine months after the fallout.

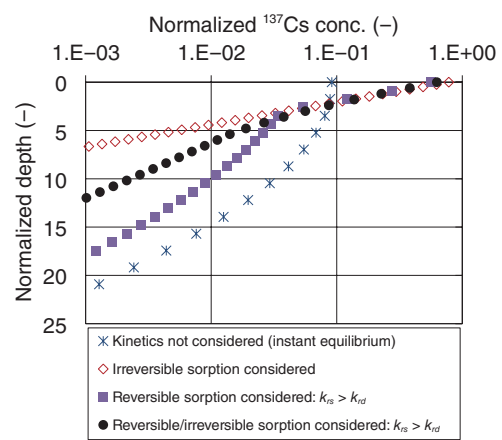


Fig.1-32 Results of the parameter-exploration analysis

Parameter-exploration analysis revealed that the sorption kinetics give rise to the initial exponential shape and that different rates of kinetic sorption and desorption cause the long tail in the depth distribution.

Despite radiocesium's affinity for binding to soil, it gradually migrates deeper into the ground over time. This results in a faster rate of reduction of air-dose rates than would otherwise be expected by radioactive decay. The depth profile and fixation of radiocesium in soil affects its uptake by vegetation and its redistribution by soil erosion and sediment transport. Therefore, it is important to understand the physicochemical processes that alter radiocesium-depth distributions in soil.

The profiles of radiocesium activity measured with depth in the soil often show exponential shapes with long-tails at large depth. However, previous models, such as the simple diffusion model, have been unable to express such profiles. Based on investigations of radiocesium adsorbed by soil minerals, desorption experiments, and field monitoring, we assumed such vertical distributions were affected by sorption kinetics at reversible and irreversible sites. Therefore, we developed

an advection-dispersion equation with fully kinetic reversible/irreversible sorption terms (Fig.1-30).

We compared the model results against the measured depth profile in Fukushima Prefecture (Fig.1-31). The previous models such as the simple diffusion model and the DSF model were unable to express the exponential shapes with long-tails, while our model agreed well with the measured profile.

Then, we conducted a set of analyses to examine the effect of reversible/irreversible sorption kinetics upon the depth distributions (Fig.1-32). The results revealed that the sorption kinetics give rise to the initial exponential shape and that different rates of kinetic sorption and desorption cause the long tail in the depth distribution. We will predict how dose-rate evolution is affected by the migration of radiocesium into soils as the next step of our research.

Reference

Kurikami, H. et al., Coupling the Advection-Dispersion Equation with Fully Kinetic Reversible/Irreversible Sorption Terms to Model Radiocesium Soil Profiles in Fukushima Prefecture, Journal of Environmental Radioactivity, vol.171, 2017, p.99-109.

1-16 Redeposition Mechanism of Radiocesium on River Flood Plains

— Heterogeneous Distribution of Radiocesium Depending on Weather, Topography and Vegetation —

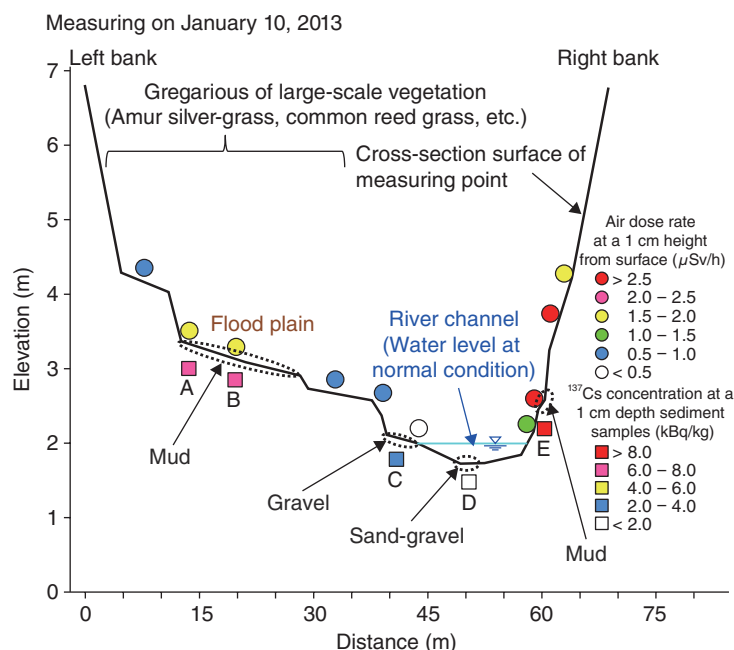


Fig.1-33 The results of field investigation around a river channel
The air dose rate has a heterogeneous distribution. The concentration of radiocesium in the sediment at points with muddy sediment (A, B, and E) was over one order of magnitude higher than that at the edge/bottom of the river channel with sands and gravels (C and D).

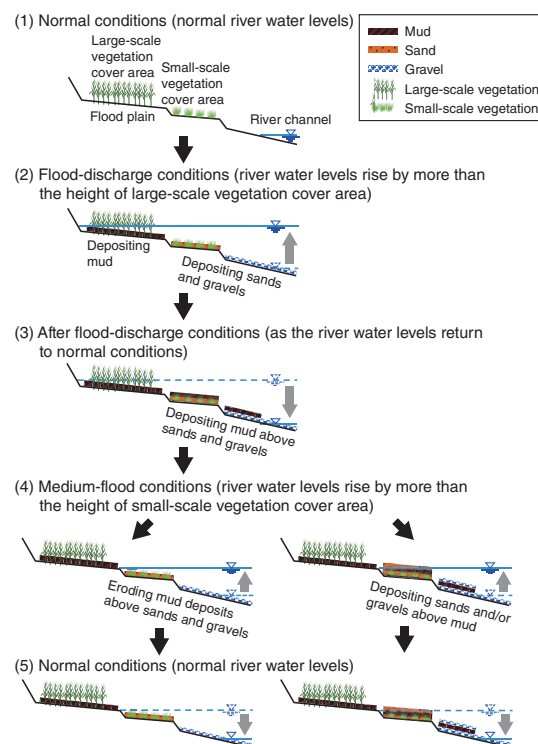


Fig.1-34 Conceptual model for the redeposition and transport mechanisms of radiocesium
According to rainfall and river-water-level-monitoring data, condition (2) occurred about once a year and condition (4) also occurred about 10 times a year.

Since forest covers approximately 70% of the area of Fukushima Prefecture, it is presumed that the radiocesium (Cs) released into the atmosphere by the accident at the TEPCO's Fukushima Daiichi NPS (1F) was widely deposited in forests. As decontamination in mountain forests is not feasible, soil particles containing Cs transported from forests to the flood plains by river flow can potentially increase the local radiation dose around rivers. Prediction of the transportation and deposition behavior of Cs by the river flow using numerical analysis will be helpful for eliminating or reducing movement routes for Cs, leading to a reduction in the future exposure dose. To apply numerical analysis to this prediction, it is necessary to clarify the phenomenon by field investigation and to construct a conceptual model capable of explaining its mechanism. We conducted field investigations at 130 measurement points at 5 rivers around 1F.

From the results of field investigations, it was observed that muddy sediments deposited on the flood plain have high concentration of Cs, while the sand and gravel sediments deposited at the edges or bottoms of river channels have low concentrations of Cs. The spatial distribution of Cs is heterogeneous around river channels (Fig.1-33).

Based on the results of field investigations and rainfall and

river-water-level-fluctuation data in Fukushima Prefecture, a conceptual model for the redeposition and transport mechanisms of Cs in rivers was constructed (Fig.1-34).

This mechanism is as follows.

- (1) Under normal conditions: Cs does not move and the distribution of Cs does not change.
- (2) Under flood-discharge conditions (during typhoons): mud can be deposited in the flood plain, because the water depth there is shallow and river-flow velocity decreases due to friction with large-scale vegetation.
- (3) After flood-discharge conditions: suspended mud is deposited in a wide range of flood plains.
- (4) Under the medium-flood condition: mud deposited at the edges of the river channel is eroded by the river flow with a medium water level. Another possibility is deposition of sands and/or gravels above the contaminated mud, thereby shielding against radiation.
- (5) Return to normal conditions.

Based on this conceptual model, we will continue research to establish analytical-prediction methods for the transport and deposition of Cs due to water discharge in rivers.

Reference

Saegusa, H., Ohyama, T. et al., Deposition of Radiocesium on the River Flood Plains around Fukushima, Journal of Environmental Radioactivity, vol.164, 2016, p.36-46.

1-17 Prediction of the Amount of Radiocesium Discharge during Typhoons and Heavy-Rainfall Events

— Simulation of the Amount of Radiocesium Discharge between Several River Basins —

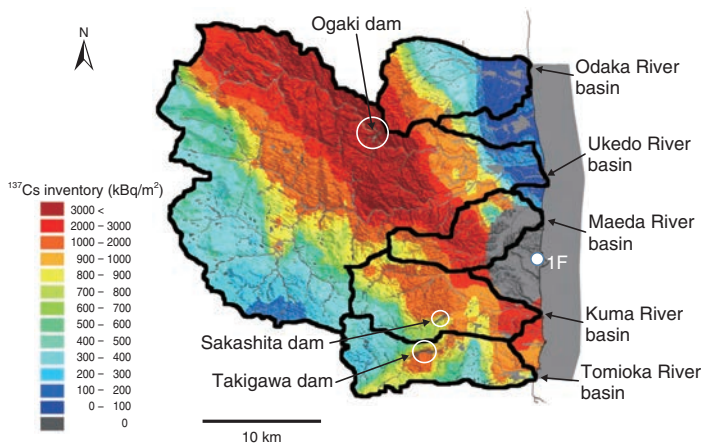


Fig.1-35 A spatial distribution of the ^{137}Cs inventory between five river basins (Odaka River, Ukedo River, Maeda River, Kuma River, and Tomioka River) near the 1F (data from the Second Airborne Monitoring Survey, May 2011)

Radiocesium inventories differ between basins. Some river basins have a dam reservoir that decreases sediment-sorbed radiocesium discharge (Odaka River basin: Without; Ukedo River basin: With; Maeda River basin: Without; Kuma River basin: With; Tomioka River basin: With). Bold black lines indicate borders between basins.

A large amount of radiocesium derived from the TEPCO's Fukushima Daiichi NPS (1F) accident remains in the top surface-soil layer due to strong absorption to soil particles including clay minerals. Therefore, some radiocesium is discharged into rivers and oceans through rainfall events such as typhoons due to water flow and sediment transport. By understanding the characteristics of radiocesium discharge, it is possible to predict the amount of this discharge in the future.

In this study, we extended an existing watershed model of water flow and sediment transport to calculate the migration of cesium-137 (^{137}Cs) into the environment. We simulated water, sediment, and ^{137}Cs discharge during heavy-rainfall events such as typhoons in five contaminated river basins near to 1F (Fig.1-35).

In the simulation, the amount of ^{137}Cs discharge and the ^{137}Cs -discharge ratio (fraction of the amount of discharge against the initial fallout) are calculated in each river basin. The quantities for each basin are considered to differ due to the amount of sediment supplied to the river by precipitation,

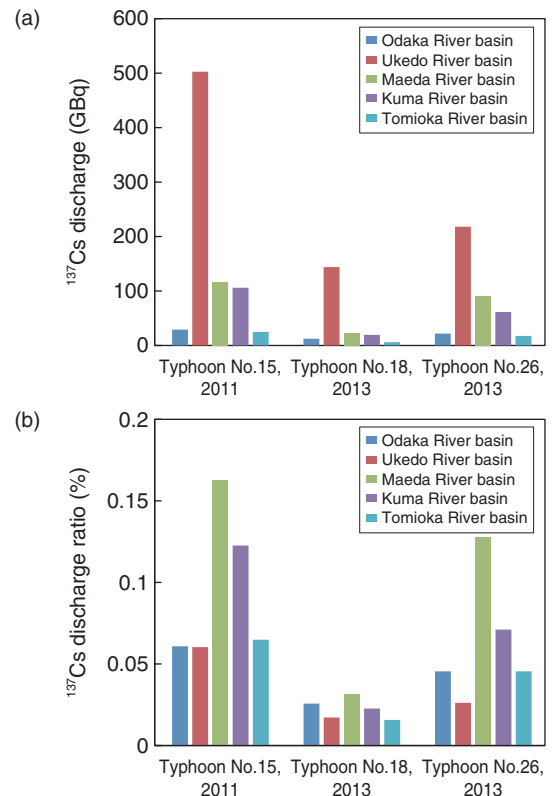


Fig.1-36 Amount of ^{137}Cs discharge (a) and discharge ratio (b) from five river basins under heavy-rainfall events such as typhoons

The amount of radiocesium discharge and the discharge ratio differ according to precipitation, initial inventory, presence of a dam reservoir, and land use.

the initial ^{137}Cs inventory, the presence of a dam reservoir, and the land use.

Our results appear in Fig.1-36. The Ukedo River basin has a large amount of ^{137}Cs discharge due to a high initial ^{137}Cs inventory; however, its discharge ratio was low. The dam reservoir, which served to trap sediment discharge from the upper part of the river, may reduce discharge of radiocesium attached to the suspended sediment downstream. In addition, forested areas can reduce the amount of sediment discharge because surface-water flow does not occur much. Therefore, the Ukedo River basin had low ^{137}Cs discharge because the area upstream of the dam reservoir was forested. The Maeda River basin have no dam reservoir and a highly ^{137}Cs -contaminated paddy-field area, which supplied significant quantities of sediment discharge, thus resulting in a high ^{137}Cs -discharge ratio.

Verification and improvement of this study can be used to predict the amounts of sediment and ^{137}Cs discharge from basins in future.

Reference

Sakuma, K. et al., Characteristics of Radio-Cesium Transport and Discharge between Different Basins near to the Fukushima Dai-Ichi Nuclear Power Plant after Heavy Rainfall Events, *Journal of Environmental Radioactivity*, vols.169-170, 2017, p.137-150.

1-18 Reproduction of the Soil using Salt

— Synchrotron X-rays Reveal the Mechanism of Cesium Removal from Soil —

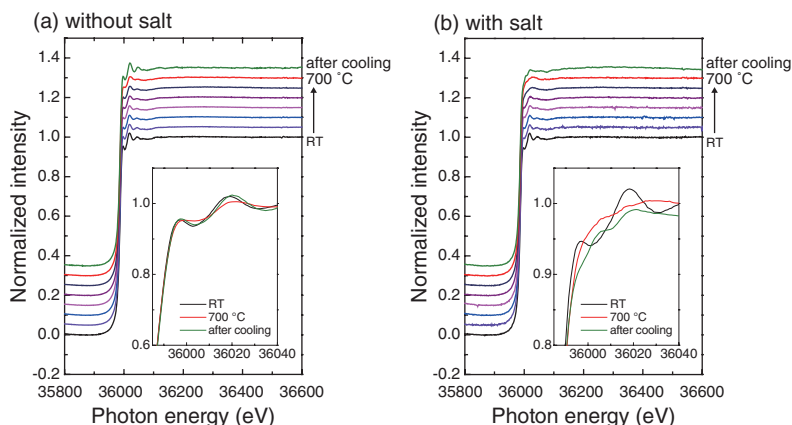


Fig. 1-37 Cs K edge XAFS spectra of WB samples using synchrotron x-rays (a) without and (b) with NaCl–CaCl₂ mixed salts. Different colors correspond to results at different temperatures: RT (black), 200 °C (lilac), 300 °C (blue), 400 °C (pink), 500 °C (purple), 600 °C (indigo), 700 °C (red), and RT at after cooling (green). These results indicate that the local structure of Cs was drastically changed.

A large quantity of radioactive material was scattered by the TEPCO's Fukushima Daiichi NPS accident six years ago. Most of these materials were deposited in the soil around Fukushima. More than 2000 million m³ of radioactive contaminated soil has been placed in a temporary storage facility. Therefore, reducing the volume of the contaminated soil is important. Among the scattered radioactive materials, ¹³⁷Cs (Cs) is the main radioisotope. It has been reported that most Cs is strongly fixed to clay minerals (especially weathered biotite, WB) in the soil. We investigate the mechanism of the Cs-removal process and develop an effective Cs-removal method. Heat treatment is one soil-decontamination method with high efficiency. However, heating to more than 1000 °C is necessary to melt clay minerals, and it is necessary to reduce the processing cost. In this study, an *in situ* extended X-ray-absorption fine structure (*in situ* EXAFS) spectroscopic analysis at high temperature was conducted to investigate the mechanism of Cs removal from WB from Fukushima, as induced by heating with a mixture of NaCl and CaCl₂ salts.

In the experiment, we chose WB derived from Abukuma, where granite forms an interbed with vermiculite by weathering. This clay mineral is known to be representative of the soil in Fukushima. To investigate the effect of molten alkali salts upon clay minerals, we added a NaCl–CaCl₂ mixed salt to the studied samples, conducted *in situ* EXAFS measurements at 200 °C–700 °C, and compared the differences in the spectra with and without the alkali salt. This indicated that most Cs

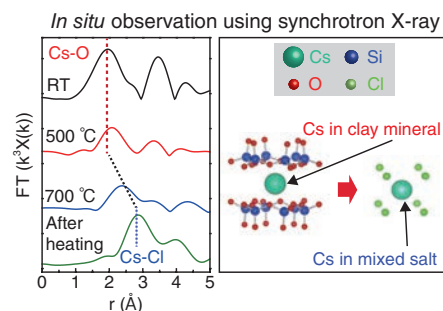


Fig. 1-38 Mechanism of Cs removal from WB Synchrotron x-rays can determine the local structure of Cs. It is known that Cs first bonds to O and then to Cl under heat treatment with mixed salt.

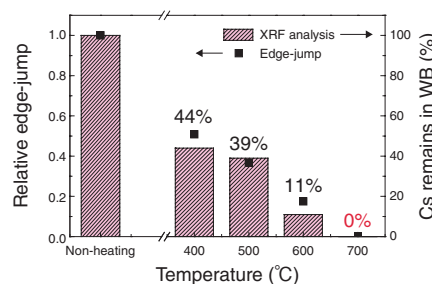


Fig. 1-39 Cs remaining in WB after heat treatment with mixed salt, as determined by XRF analysis We confirmed that almost all Cs was released from WB at 700 °C.

remained in WB during heating at 200 °C–700 °C. In addition, the *in situ* EXAFS spectra gradually changed upon heating with mixed salt and a completely different spectrum was observed for the sample after cooling from 700 °C to room temperature (RT) (Fig. 1-37). This means that the local structure around Cs was modified by the influence of the salt at high temperatures on the basis of the results for the radial-structure-function analysis obtained from *in situ* EXAFS. As the result, Cs formed Cs–Cl bonds after cooling to RT from 700 °C (Fig. 1-38).

If Cs is taken in a chloride phase, it is expected that Cs may be removed effectively from a sample after heating by washing it with water. Therefore, quantum analysis using fluorescence X-rays was performed to estimate the Cs content after washing of the salt from the sample. As the result, we concluded that almost all of the Cs was removed from the WB by heating at 700 °C with mixed salt (Fig. 1-39).

This study was performed under the JAEA project, “Cs sorption-desorption mechanism on clay minerals,” based on the special account for Fukushima environmental recovery from the Ministry of Education, Culture, Sports, Science and Technology, Japan (MEXT). This work was supported by the Japan Society for the Promotion of Science (JSPS) KAKENHI Grants-in-Aid for Scientific Research (A) (No.16H02437) and (C) (No.16K06965). The synchrotron radiation experiments were performed using the BL11XU of SPring-8 (Proposal No.2015B-3504).

Reference

Honda, M. et al., Mechanism of Cs Removal from Fukushima Weathered Biotite by Heat Treatment with a NaCl–CaCl₂ Mixed Salt, ACS Omega, vol.2, no.2, 2017, p.721-727.

1-19 Observation of Atomic-Scale Edge Structure via Supercomputers

— Towards an Understanding of the High Cesium Affinity of Clay Minerals —

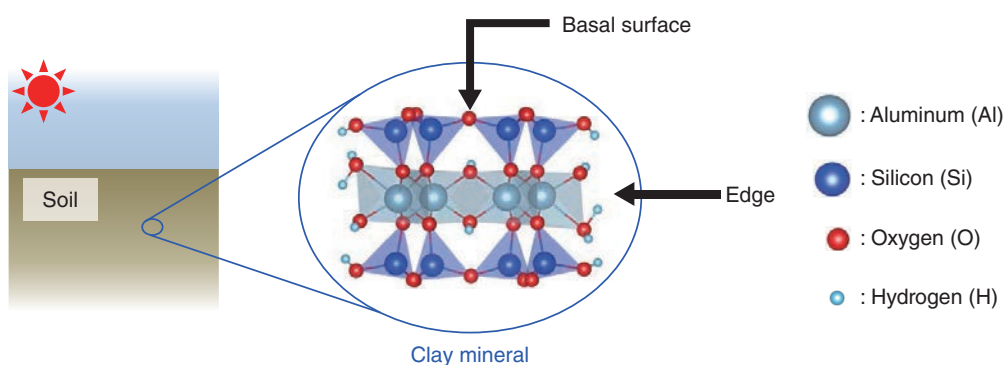


Fig.1-40 Edge structure of clay minerals

The central figure represents a model of pyrophyllite, a clay mineral. Clay minerals have two types of surfaces; one is the “basal plane,” whose surface is flat. The other is the “edge,” which has a complex structure.

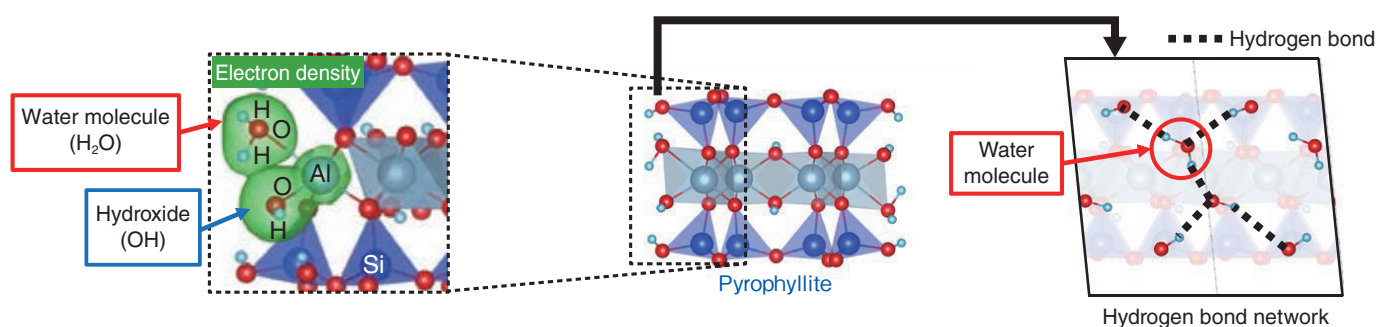


Fig.1-41 Difference in bonds between water molecules and edge Al atoms and between hydroxides and Al atoms

It is known that bonding between hydroxides and Al atoms is covalent (left figure). We revealed that bonding between water molecules and Al atoms forms a hydrogen-bond network (right figure).

Huge quantities of radionuclides were released into the environment by the accident at the TEPCO's Fukushima Daiichi NPS (1F). Radiocesium caused evacuation of residents near 1F because it remains on surface soil as a long-lived γ -ray emitter due to its long half-life and strong adsorptive properties. The Japanese Government has performed large-scale decontamination in Fukushima. These activities have been shown to be effective, i.e., the air-dose rate has been reduced. Another issue, however, has arisen: huge amounts of waste are being produced by decontamination. Volume reduction and safe storage of the waste soil is required to reduce the burden to residents of Fukushima. Therefore, extensive research on the development of effective volume-reduction techniques is ongoing.

It is known that radiocesium is mainly adsorbed by clay minerals in soil. If it were possible to remove radiocesium from clay minerals, the waste volume would drastically reduce. However, we lack effective techniques for volume reduction; one reason for this is lack of scientific knowledge concerning cesium (Cs) adsorption to clay minerals. It is believed that radiocesium falls onto the ground surface in raindrops as ions, which are finally adsorbed by clay minerals via organic/inorganic materials in the surface soil. However,

the details of the process, particularly at the atomic scale, remain unknown. If the details are clarified, development of waste-soil-volume-reduction techniques should advance.

Long-term study of Cs adsorption to clay minerals has revealed that the edges of such minerals (Fig.1-40) are good sites for adsorption of Cs. However, the detailed atomic-scale structure of the edge has yet to be revealed, because it is difficult to observe its non-crystalline structure even using recent advanced experimental apparatuses. In particular, some numerical simulations have predicted that water molecules exist stably at the edge (Fig.1-40); however, the mechanism behind this phenomenon is not understood. The structures of the edge, including water molecules, are thought to affect the affinity of Cs directly. Therefore, we study chemical bonding between the water molecule and the edge of pyrophyllite, which is the simplest clay mineral, using density functional theory.

We observed that the water molecule bonds to the edge by forming a hydrogen-bond network, although the bond between the hydroxides and aluminum (Al) atoms in the edge is covalent (Fig.1-41). We plan to study the dynamics of the water molecule when Cs comes to the edge. We are continuing our study to develop a technique for waste-volume reduction, which contributes to the reduction of environmental damage.

Reference

Okumura, M. et al., Origin of 6-Fold Coordinated Aluminum at (010)-Type Pyrophyllite Edges, AIP Advances, vol.7, issue 5, 2017, p.055211-1-055211-9.

1-20 Prevention of Radioactive Cesium Accumulation in Shiitake Mushrooms Cultured with Contaminated Wood Logs

— Reduction of Cesium Absorption using Minerals —

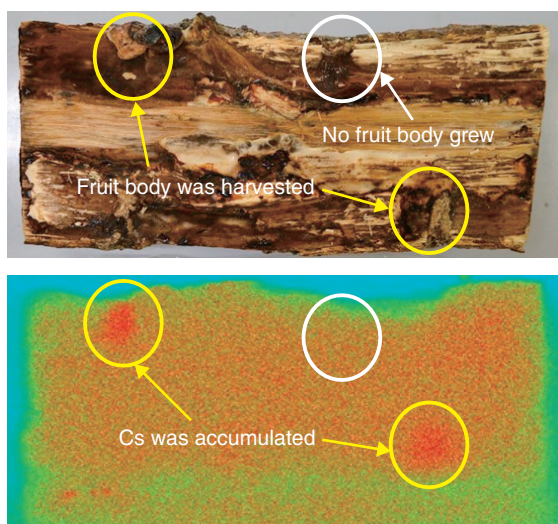


Fig.1-42 Distribution of Cs in a wood log after shiitake mushrooms were cultured and harvested

The top figure is a photograph of a wood log. Sawdust spawns were inoculated in three places. The shiitake fruit bodies were grown and harvested at two places, shown in yellow circles, while mushrooms did not grow within the white circle. The bottom figure shows the distribution of Cs in the wood-log section, as measured with a two-dimensional radiation-distribution detector. Darker regions indicate a higher concentration of Cs.

Wood-log cultivation of shiitake mushrooms is thriving in Fukushima. After the accident at the TEPCO's Fukushima Daiichi NPS (1F), the production of shiitake mushrooms cultured with wood logs was restricted due to the contamination of such logs by radioactive cesium (Cs). It is known that mushrooms accumulate Cs from contaminated litter and wood logs; however, there is no available research for preventing the accumulation of Cs in the fruit bodies (caps and stems) of mushrooms. In this research, we challenged ourselves to reducing Cs accumulation in mushrooms grown on a contaminated wooden log.

We first grew Shiitake by inoculating the sawdust spawn (mixtures of saw dust shiitake spawn) in a wooden log contaminated with Cs from the 1F to examine the absorption of Cs by mushrooms. The concentration of Cs in the fruit body of the mushrooms was approximately 160 Bq/kg in average, which was almost the same as the Cs concentration, approximately 160 Bq/kg, in the wooden log. Next, we prepared sawdust spawn containing 5 or 10wt% of vermiculite powder with a high sorption capacity for Cs and inoculated it in a wooden log to grow shiitake mushrooms. The concentration

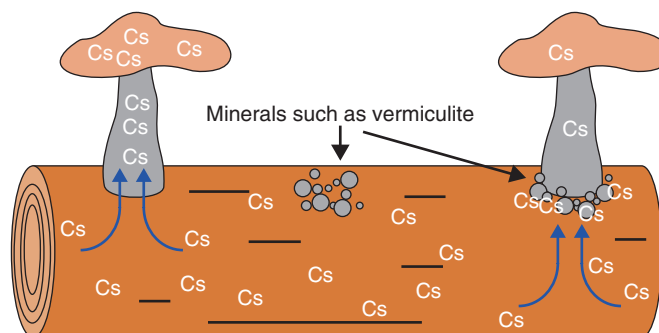


Fig.1-43 Behavior of Cs during culturing of shiitake mushrooms with wood logs

Left: Shiitake mushrooms absorb Cs from wood logs and accumulate it in the fruit body. Middle: when minerals such as vermiculite are embedded in wood logs, Cs is not accumulated on the minerals. Right: when the fruit body of a mushroom grows from sawdust-spawn-containing minerals, the accumulation of Cs in the fruit body decreases due to adsorption of Cs onto those minerals.

of Cs in the fruit body decreased to approximately 80% or 60% of the Cs concentration in the wooden log when the vermiculite content was 5% or 10%, respectively. When zeolite powder was used instead of vermiculite, the Cs concentrations in the fruit body decreased similarly or more. These results demonstrate that the use of vermiculite and zeolite in sawdust spawn reduced the absorption of Cs by the fruit body. After harvesting the fruit body cultured from the vermiculite-containing sawdust spawn, the distribution of Cs in the wooden log was analyzed (Fig.1-42). We observed that Cs was accumulated in the sawdust spawn (shown with yellow circles in Fig.1-42, top figure). On the contrary, Cs did not accumulate in the sawdust spawn from which no fruit body grew (white circle). These results suggest that the Cs dissolved in water in the wood log migrated along with this water when absorbed by the shiitake mushrooms, with a fraction of the Cs being adsorbed on the vermiculite beforehand (Fig.1-43).

These results suggest that reduction of the accumulation of Cs in the fruit body of a shiitake mushroom may be possible by selecting appropriate minerals and adjusting their mixing ratios.

Reference

Ohnuki, T., Kozai, N. et al., Direct Accumulation Pathway of Radioactive Cesium to Fruit-Bodies of Edible Mushroom from Contaminated Wood Logs, Scientific Reports, vol.6, 2016, p.29866-1-29866-6.

Implementing Continuous Improvements in Safety

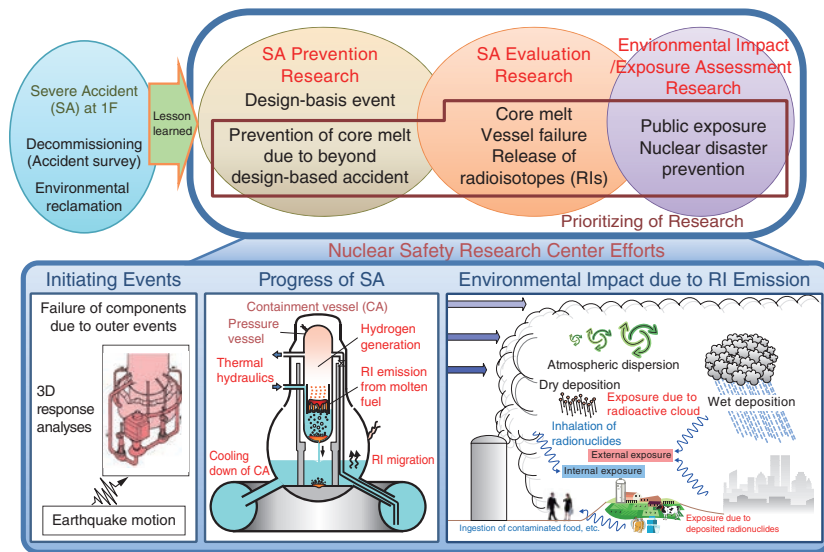


Fig.2-1 Directions of research at the Nuclear Safety Research Center

In accordance with the lessons learned from the accident at 1F, we have promoted studies on severe-accident prevention efforts and nuclear-emergency-preparedness activities such as environmental-impact assessments as well as safety assessments for design-basis events.

The Nuclear Safety Research Center (NSRC) performs advanced safety research to provide a technical basis for nuclear regulation authorities in terms of nuclear-safety assessment as well as offer a long-term viewpoint through calculations, experiments, and measurement techniques. Through such research, we contribute to the development of safety criteria and support the creation of safety regulations with continuous improvement aimed at the highest level of safety.

We reviewed our previous research on design-based events prior to the accident at the TEPCO's Fukushima Daiichi NPS (1F) in accordance with the lessons learned from the disaster, as shown in Fig.2-1. To reduce the risks of operating nuclear facilities, we have expanded research on prevention and mitigation during the progression of severe accidents (SAs), on preparation for and response to emergency situations, on the consequences of radiation and the management of radioactive waste, and on nuclear criticality safety assessment of fuel debris related to the 1F accident.

With regards to SA research, we intend to clarify thermal-hydraulic phenomena during SAs and develop effective measures to mitigate them. Therefore, we have conducted experiments with a large-scale containment-vessel test facility called CIGMA (Containment Integral Measurement Apparatus), as shown in Fig.2-2. The experiments have focused upon the gas-phase behaviors at high temperatures and the thermal-hydraulic behaviors of mixed gas, including hydrogen, which may cause containment-vessel damage. With a view of upgrading SA-evaluation methods, we intend to improve the accuracy of analyses with the computer codes for SA, employing knowledge obtained from benchmark exercise

Basic design specifications

Maximum service pressure	1.5 MPa
Maximum temperature of injection gas	973 K
Test vessel height	11.2 m
Test vessel diameter	2.5 m
Equipment of pool and jacket for cooling	
Detailed instrumentations for temperature and concentration distribution	



Large-scale containment vessel test facility (CIGMA)

Fig.2-2 Outline of the large-scale containment vessel test facility (CIGMA)

The CIGMA facility is designed to be able to simulate the behaviors of steam and hydrogen gas as well as have several measures for mitigating accidents.

on the 1F accident conducted by the OECD/NEA international cooperative project.

Moreover, we have developed aircraft-monitoring techniques using a manned helicopter to investigate the distribution of radionuclides in the atmosphere around 1F following the accident. We have performed background monitoring around the Sendai Nuclear Power Plant in response to emergency situations according to the basic disaster-management plan.

This chapter presents the results of recent research on topics including the influence of mesh shape upon temperature in computational-fluid-dynamics-code analysis of nuclear-power-plant accidents considering buoyancy flows (Topic 2-1), the ability of the SA code to predict phenomena observed in previous experiments on the coolability of molten cores in containment vessels during SAs (Topic 2-2), locally deformed structures and the strain distribution of stainless steel under high-irradiation conditions (Topic 2-3), the deterioration rate of the main components of clay buffer materials under alkaline environments during geological disposal of high-level radioactive waste (Topic 2-4), the effects of the growth of spray faults upon groundwater flow around geological-disposal systems (Topic 2-5), and a method for analyzing plutonium-isotope ratios in individual U/Pu mixed particles using alpha and mass spectrometry (Topic 2-6).

The following topic, solicited by the NSRC and related to the accident at 1F, was described in Chapter 1: evaluation of the exposure dose to the residents of Fukushima Prefecture based on measured values and consideration of behavioral patterns (Topic 1-13).

2-1 Estimating Hydrogen-Gas Behavior during Nuclear Power Plant Accidents

— Influence of Mesh Shape upon Computational Fluid Dynamics Analysis of Buoyant Flows —

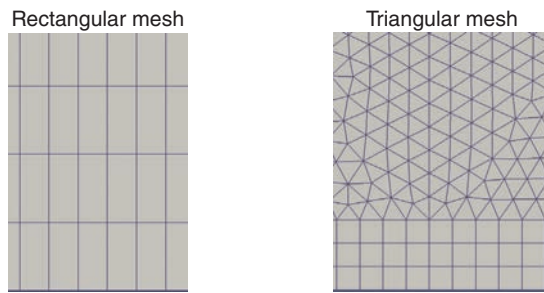


Fig.2-3 Schematic sketch of meshes

The calculation region is divided into rectangular or triangular cells.

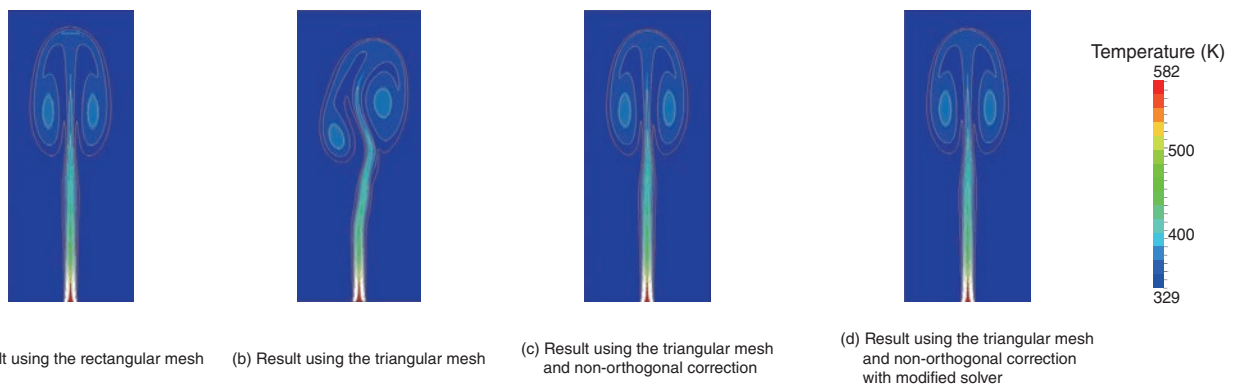


Fig.2-4 The simulation using the CFD code OpenFOAM

(a) Result using the rectangular mesh. (b) Result using the triangular mesh. (c) The result using a triangular mesh and non-orthogonal correction shows a symmetrical distribution similar to that using the rectangular mesh. (d) Calculations using the modified solver developed by JAEA proceeded more quickly than those using the existing solver.

In nuclear power plant accidents, a chemical reaction between fuel rod cladding and water leads to the generation of hydrogen gas. Hydrogen combustion may occur when hydrogen leaks into a containment vessel (CV) or a reactor building and reacts with oxygen. Therefore, accurately estimating hydrogen-gas behavior during accidents is important for securing reactor safety. Detailed analysis with computational fluid dynamics (CFD) should be performed to clarify multi-dimensional flow in CVs or reactor buildings having a large volume. The influence of buoyancy should be considered while evaluating hydrogen gas behavior because the gas is very light. In CFD simulations, a simulation area is generally divided into a small rectangular or triangular mesh. The triangular mesh is often applied to complex geometries such as CVs. However, previous researchers have indicated that the calculation accuracy with a triangular mesh is low when simulating buoyant flows.

In this research, we discuss the application of triangular meshes to a simulation of buoyant flows. The flows are analyzed by injecting hot fluid from the bottom of the 2D area while filled with cold fluid. As shown in Fig.2-3, the triangular and rectangular meshes were applied to the simulations using the CFD code OpenFOAM.

Fig.2-4 (a) shows the numerical result of temperature using the rectangular mesh with the existing solver implemented in the OpenFOAM code. This numerical result was confirmed to be a valid symmetrical distribution, which is very similar to that obtained with the fine mesh. Fig.2-4 (b) shows the asymmetrical distribution using the triangular mesh. The calculation accuracy is low for the gradient term due to the large non-orthogonality of the triangular mesh, which may cause differences between the symmetrical and asymmetrical distributions. Fig.2-4 (c) shows the symmetrical distribution obtained by the triangular mesh and a non-orthogonal (NO) correction. This correction is used to mitigate the influence of the mesh non-orthogonality. Fig.2-4 (d) shows the result obtained with the triangular mesh and the NO correction using the solver modified by JAEA. The modified solver could mitigate the influence of the mesh non-orthogonality, and calculations made with this solver were faster. We proposed a numerical method for the fast simulation of buoyant flows with the triangular mesh. In the future, we will conduct CFD analysis for complex geometries such as CVs with the application of our simulation method.

Reference

Ishigaki, M. et al., Influence of Mesh Non-Orthogonality on Numerical Simulation of Buoyant Jet Flows, Nuclear Engineering and Design, vol.314, 2017, p.326-337.

2-2 Evaluating Molten-Core-Debris Formation in Reactor Containment Vessels — Evaluation of Molten-Core Coolability in Severe Accidents —

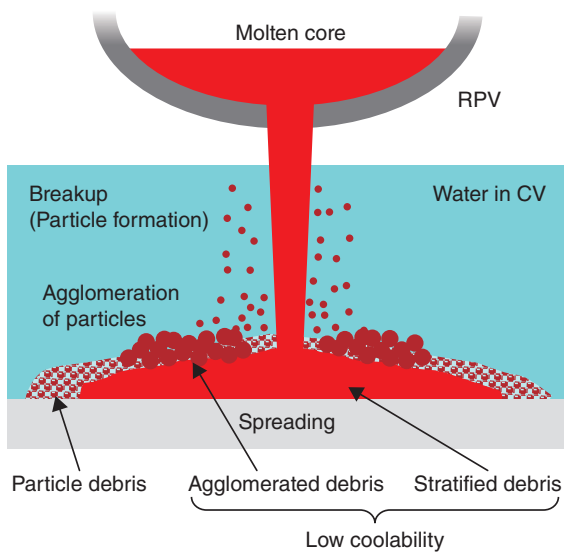


Fig.2-5 Behavior of a molten core slumping into water during a severe accident

A slumping molten core is fragmented by interaction with water and forms three types of debris: (1) “particle debris” comprising solidified particles on the floor, (2) “agglomerated debris” comprising bonded particles before solidification, and (3) “stratified debris” comprising a molten core spread and solidified on the floor without fragmentation.

In severe accidents, the integrity of the reactor containment vessel (CV) can be degraded by molten-core-concrete interaction (MCCI) following the failure of the reactor pressure vessel (RPV) and slumping of the molten core into water. To prevent and mitigate MCCIs, Japanese utilities employ the strategy of injecting water into the CV prior to RPV failure. The molten core transforms into three types of debris with different forms and coolabilities (Fig.2-5), and its spread on the floor increases its contact area with water. Therefore, the fraction of each form of debris and the area of its spread are important for debris-coolability evaluation. As these quantities are affected by parameters such as molten-core temperature, water depth, and temperature, we have been developing analytical techniques to consider these parameters and will eventually stochastically evaluate the debris coolability and effectiveness of MCCI-prevention measures considering the probability distribution of the parameters.

In this study, we enhance the capabilities of the fuel-coolant-interaction-analysis code JASMINE to calculate the debris fractions and spreading areas.

First, the diameter-distribution model of melt particles was implemented to reproduce experimental data. Some large particles with low coolability land on the floor before

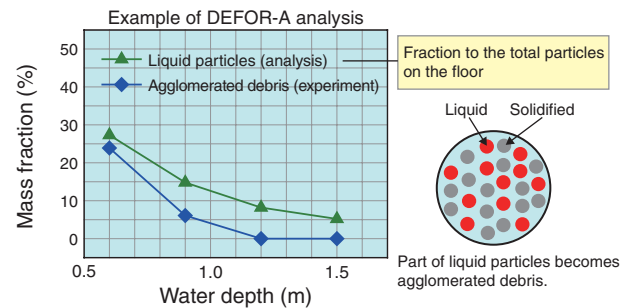


Fig.2-6 Evaluation of the agglomerated-debris fraction
A clear correlation was shown between the measured fraction of agglomerated debris and the liquid-particle fraction as estimated via JASMINE analysis.

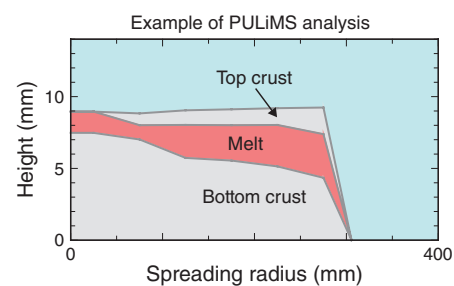


Fig.2-7 Analysis of melt spreading on the floor

The formation of crust layers at the top and bottom of the spreading melt as well as the stop of the spread was reproduced by JASMINE analysis.

solidification and can form agglomerated debris by bonding with each other. The relation between the agglomerated-debris fraction and water depth was obtained from DEFOR-A melt-slumping tests conducted by the Swedish Royal Institute of Technology (KTH). The test results demonstrate that greater water depths correspond to smaller agglomeration fractions. Analyses of tests with modified JASMINE showed that focusing upon the liquid-particle fraction was an effective means of evaluating the agglomerated-debris fraction (Fig.2-6).

Second, the hydrodynamic models of spreading and solid-surface (crust) formation were implemented to study the melt behavior on the floor. Analyses of the KTH’s PULiMS melt-spreading tests reproduced the stopping of such spreading and the formation of a three-layer structure in the solidified melt (Fig.2-7).

Techniques for evaluating the effectiveness of MCCI-prevention measures in power reactors were developed in this study although there are still issues to be solved; one example is the reproducibility of melt spreading area. In the next step, we intend to improve the melt-water heat-transfer and agglomerated-debris-formation models, among others.

This study was conducted under contract with the Secretariat of the Nuclear Regulation Authority (NRA), Japan.

Reference

Matsumoto, T. et al., Improvement of Ex-Vessel Molten Core Behavior Models for the JASMINE Code, Proceedings of 10th Korea-Japan Symposium on Nuclear Thermal Hydraulics and Safety (NTHAS10), Kyoto, Japan, 2016, paper N10P1143, 9p., in USB Flash Drive.

2-3 Refinement of Crack Growth Evaluation in the Reactor Internals of Light Water Reactors

— Analyses of Locally Deformed Structures and Strain in Highly Irradiated Stainless Steels —

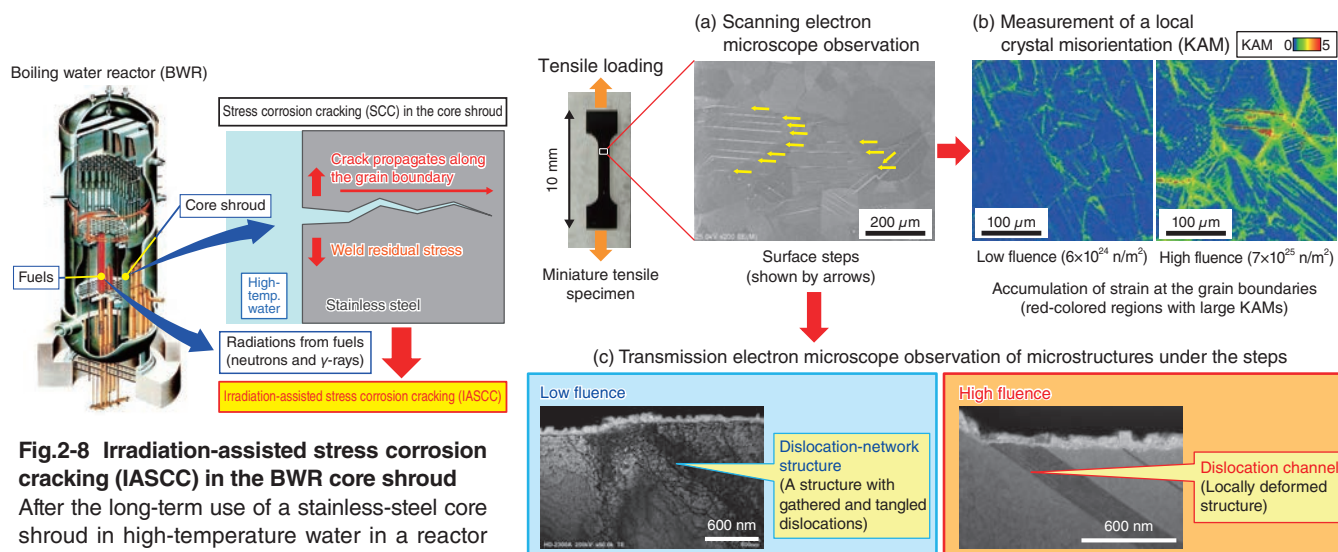


Fig.2-8 Irradiation-assisted stress corrosion cracking (IASCC) in the BWR core shroud

After the long-term use of a stainless-steel core shroud in high-temperature water in a reactor with weld residual stress, stress corrosion cracking (SCC), by which cracks propagate along grain boundaries, may occur. As SCC is enhanced by exposure to radiation from fuels, irradiation-assisted stress corrosion cracking (IASCC) may occur.

The core shroud of a boiling water reactor (BWR), which is a cylindrical reactor internal surrounding the fuel assembly, reliably supports the fuels during normal operation and serves to ensure the flow path of the water coolant. After long-term use of a core shroud with a structure composed of stainless steels connected by welding in high-temperature water in a reactor with weld residual stress, stress corrosion cracking (SCC), by which cracks propagate along the crystal grain boundaries, may occur. Moreover, as the core shroud is exposed to radiation such as neutrons and γ -rays generated from the fuels, increasing the neutron fluence to the material enhances the SCC and irradiation-assisted stress corrosion cracking (IASCC) may occur (Fig.2-8). Thus, complex factors such as materials, environment, stress, and irradiation are related to IASCC in the reactor internals, making it necessary to clarify the mechanism based on the knowledge obtained regarding each factor from test data.

To help clarify the IASCC mechanism by understanding the phenomena taking place at the crack tip, we performed a test to investigate the plastic deformation arising from the application of a load to neutron-irradiated stainless steels, focusing on the change in material properties with irradiation and stress. In the test, plastic deformation of around 2% (corresponding to the deformation at the crack tip) is applied by means of loading miniature tensile specimens fabricated from stainless steels irradiated up to around the maximum neutron fluence in the reactor internal of a BWR after 60 years of operation. Then, the deformed surface structure was observed using a scanning

Fig.2-9 Deformed structures and strain distributions on the surfaces of irradiated stainless steels after applying plastic deformation

(a) In the specimen to which plastic deformation is applied through tensile loading, linear surface steps (shown by arrows) are formed. (b) For higher fluence, the local crystal misorientation (KAM) at the grain boundaries is larger and, therefore, a more remarkable accumulation of strain is implied. (c) The microstructure under the surface step is revealed to be a dislocation-network structure under low fluence but a dislocation channel under high fluence.

electron microscope. In addition, the local crystal misorientation (KAM), which indicates changes in the crystal orientation corresponding to the amount of plastic strain, was measured and the accumulation of local strain was quantitatively evaluated. As a result, linear surface steps appeared in the specimens by deformation, as shown in Fig.2-9(a). Moreover, as a result of detailed analysis of the relation between the distribution of KAM shown in Fig.2-9(b) and the crystal grains, we confirmed that KAM had a tendency to increase with an increase in the neutron fluence, especially at the grain boundaries. These results indicate that high strain is accumulated at the grain boundaries by deformation and that this effect is enhanced under higher fluence.

We selected a region near a grain boundary with a large KAM from each specimen and observed the cross-sectional microstructures under the surface steps using a transmission electron microscope. For the crystal grain under low fluence, a dislocation-network structure induced by deformation was observed just as in an unirradiated material, whereas under high fluence, a locally deformed structure called a dislocation channel was revealed (Fig.2-9(c)). From this result, we observed that localized deformation caused more remarkable surface steps attributed to the dislocation channels under higher fluence and that this was a cause of the accumulation of strain at the grain boundaries intersecting the surface steps. We will make good use of the knowledge obtained by the present study to further refine our evaluation of crack growth.

The present study was sponsored by the Secretariat of the Nuclear Regulation Authority (NRA), Japan.

Reference

Chimi, Y. et al., Correlation between Locally Deformed Structure and Oxide Film Properties in Austenitic Stainless Steel Irradiated with Neutrons, Journal of Nuclear Materials, vol.475, 2016, p.71-80.

2-4 Deterioration Rate of Buffer Material in Geological-Disposal Sites

— Alteration Rate of Compacted Montmorillonite under Highly Alkaline Conditions —

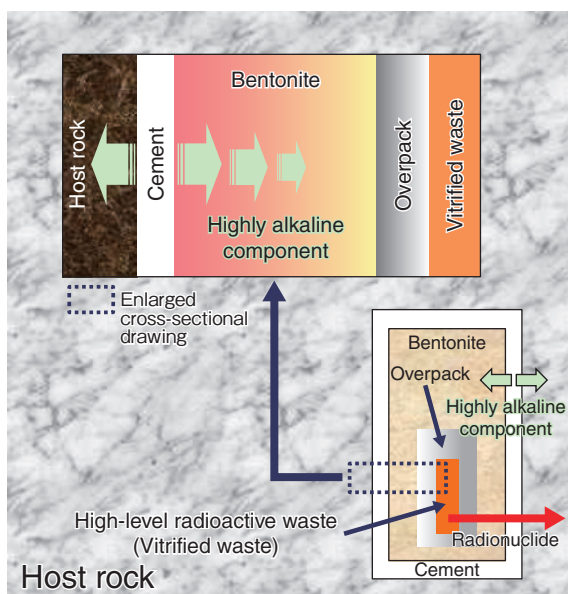


Fig.2-10 Conceptual view of the HLW-disposal system
Vitrified HLW is encapsulated in an iron container (overpack), surrounded by an engineered buffer material (bentonite), and placed in a stable host rock. Cement used for the mechanical support of shafts and drifts increases the alkalinity of the surrounding water and is likely to deteriorate the properties of the bentonite buffer over a long period.

In geological disposal system of high-level radioactive waste (HLW), vitrified waste is encapsulated in an iron container called an overpack, surrounded by an engineered bentonite-buffer material (compacted bentonite), and placed in a repository in a stable host rock, as shown in Fig.2-10. Properties of bentonite, high sorptivity and low permeability, retard outward radionuclide migration. As the retardation properties of the bentonite depend upon its montmorillonite content, the alteration of montmorillonite into other minerals induced by the highly alkaline component supplied from the cementitious materials in the system must be quantitatively evaluated in assessments of the long-term retardation properties of the system.

In our previous studies, the alteration rate of montmorillonite in compacted bentonite was experimentally formulated. However, decreases in the concentration of hydroxide ions (OH^-) by alteration of accessory minerals and its effect upon the alteration behavior of montmorillonite in compacted bentonite were not clarified.

In the present study, the alteration rate of compacted pure montmorillonite, free of accessory minerals, was experimentally investigated at temperatures of 50 °C–130 °C and a formula was proposed. Then, the alteration-rate formula of montmorillonite in compacted bentonite was compared with that of compacted montmorillonite to clarify the effect of accessory minerals upon montmorillonite alteration.

Reference

Sawaguchi T. et al., Effects of OH^- Activity and Temperature on the Dissolution Rate of Compacted Montmorillonite under Highly Alkaline Conditions, Clay Minerals, vol.51, no.2, 2016, p.267-278 [Erratum: vol.51, no.5, 2016, p.815].

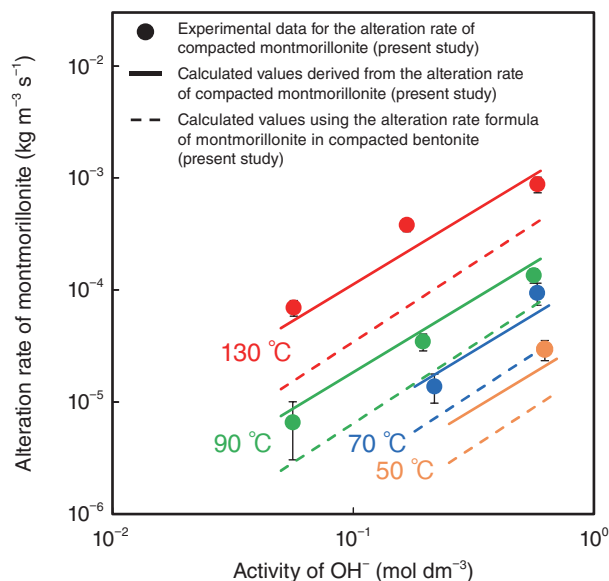


Fig.2-11 Alteration rate of montmorillonite in highly alkaline solutions

The alteration rate of montmorillonite (R_A) is approximately 2.5 times higher in compacted montmorillonite than in compacted bentonite. This result suggests that the decrease in OH^- concentration by reacting with accessory minerals in the bentonite has a great effect upon R_A and that the alteration rate of montmorillonite calculated using the previous equation ($R_A=3500 \cdot (a_{\text{OH}^-})^{1.4} \cdot \exp(-51000/RT)$; broken curves) is underestimated.

As shown in Fig.2-11, the alteration rates of compacted montmorillonite (R_A) were formulated as a function of the activity of OH^- (a_{OH^-}) and the absolute temperature (T):

$$R_A=30000 \cdot (a_{\text{OH}^-})^{1.3} \cdot \exp(-55000/RT) \text{ [kg m}^{-3} \text{ s}^{-1}\text{]},$$

where R is the gas constant. The alteration rate of montmorillonite is observed to be approximately 2.5 times higher in pure compacted montmorillonite than in compacted bentonite. This result suggests that the decrease in OH^- concentration by reacting with accessory minerals in the bentonite has a great effect upon the alteration rate of montmorillonite and that the OH^- concentration in compacted bentonite was overestimated in the previous alteration-rate formula of montmorillonite ($R_A=3500 \cdot (a_{\text{OH}^-})^{1.4} \cdot \exp(-51000/RT)$), i.e., the alteration rate of montmorillonite was underestimated.

The introduction of the alteration-rate formula derived in present study into a geochemical-calculation code under development may make it possible to evaluate the alteration of montmorillonite and accessory minerals simultaneously in compacted bentonite.

The present study was sponsored by the Secretariat of the Nuclear Regulation Authority (NRA) (formerly the Nuclear and Industrial Safety Agency, Ministry of Economy, Trade and Industry (METI), Japan).

2-5 Evaluating the Effect of Seismic Activity upon Geological Disposal

— Evaluation of the Influence of Splay-Fault Growth upon Groundwater Flow around a Geological-Disposal System —

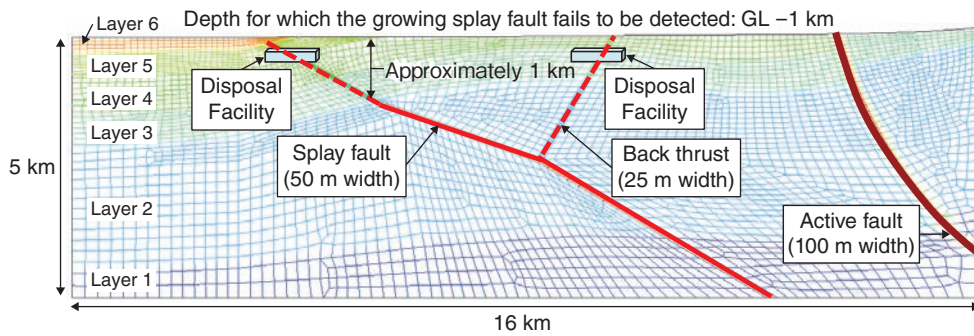


Fig.2-12 The hydrogeological model for the growth of splay faults (a splay fault and a back thrust)

We assumed that a splay fault (—) lies concealed underground deeper than a disposal facility at the time of closure of the facility. It is assumed that the growth of a splay fault and the back thrust due to subsequent seismic activities (---) will result in crossing of the disposal tunnel.

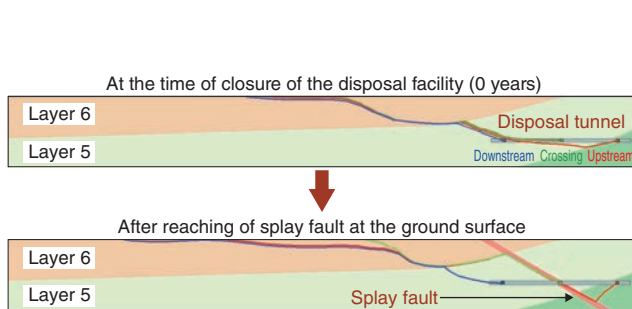


Fig.2-13 The migration paths from the disposal tunnel crossing the splay fault (GL -300 m)

Through splay-fault growth, the migration paths from both the crossing region (—) and the upstream region (—) are changed into upward-migration routes along the splay fault.

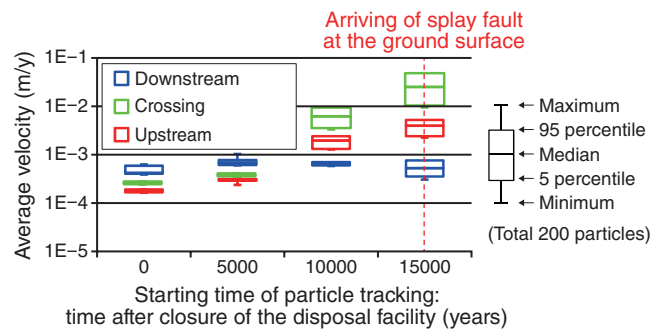


Fig.2-14 The average velocities from the disposal tunnel to the ground surface (the increment of the fault: 500 m per seismic activity)

By splay-fault growth, the average velocities from the disposal tunnel to the ground surface increase by a maximum of two orders of magnitude.

For the geological disposal of high-level radioactive waste including long-lived nuclides, the safety over hundreds of thousands of years needs to be assessed. It is required that geological and climatic-disruptive events that can affect disposal facilities considerably during this period should be avoided when selecting a site. However, it has been pointed out that some events cannot be avoided in advance due to the difficulty in predicting the future over hundreds of thousands of years. For example, it is necessary for seismic activities to avoid active faults; however, it has been pointed out that splay faults (faults derived from active faults deep underground) and back thrusts (faults which form with the opposite inclination to the splay fault) cannot be avoided in advance due to difficulties with prediction and detection. In this study, we developed a procedure for assessing the influence of the growth of splay faults (the splay fault and the buck thrust) and evaluated the effect on groundwater flow around a geological-disposal system.

To model splay faults, we investigated examples in Japan and set the conditions including the growth angle and the increment of a fault per seismic activity. Based on these conditions, we created a hydrogeological model for the growth of splay faults (Fig.2-12) and carried out unsteady two-dimensional groundwater-flow analysis. Furthermore, we assumed that there

were disposal tunnels of 1 km that crossed the splay faults, and divided these tunnels into three regions (the upstream, crossing, and downstream regions). We implemented particle-tracking analysis for 200 particles located in each region and estimated the migration path and the travel time to the ground surface of each particle while changing its starting time. From the results, we found two important effects of splay-fault growth, namely change of its path and change of the average velocity.

The migration paths from both the crossing and upstream regions are changed into upward-migration routes along the splay fault in accordance with fault growth (Fig.2-13). The average velocity from the disposal tunnel to the ground surface becomes higher than that before fault growth (maximum one/two orders of magnitude for the upstream/crossing region) (Fig.2-14). This indicates that the travel time of nuclides can be shortened by splay-fault growth. By back-thrust growth, the downward flow along the back thrust increased by one order of magnitude. This result suggests that fault growth can lead to inflow of oxidizing groundwater around the ground surface into the vicinity of a disposal tunnel, which may affect safety functions of engineering barriers.

This study includes the results of contract work funded by the Secretariat of the Nuclear Regulation Authority (NRA), Japan.

Reference

Takai, S. et al., Evaluation of Influence of Splay Fault Growth on Groundwater Flow around Geological Disposal System, Nippon Genshiryoku Gakkai Wabun Ronbunshi (Transactions of the Atomic Energy Society of Japan), vol.16, no.1, 2017, p.34-48 (in Japanese).

2-6 Determination of Plutonium-Isotope Ratios in Individual U/Pu Mixed Particles

— Novel Approach using Alpha and Mass Spectrometry for Nuclear Non-Proliferation —

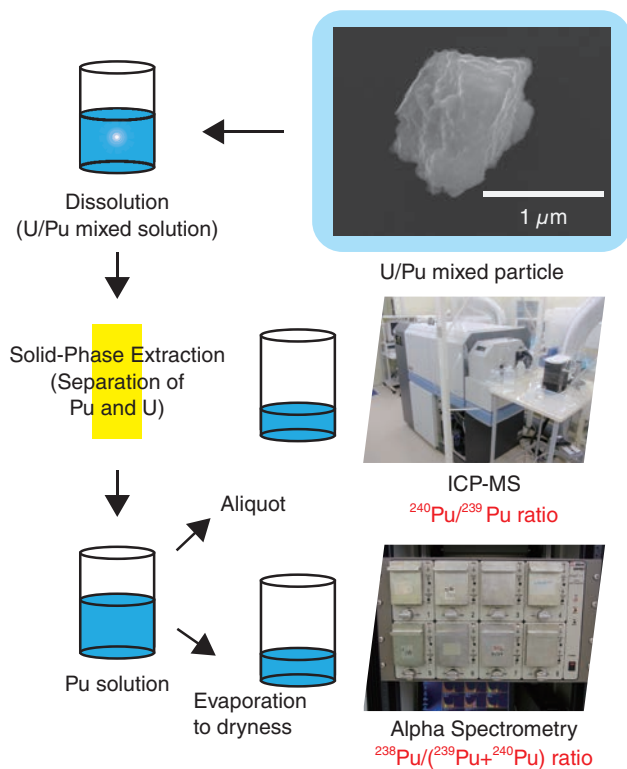


Fig.2-15 Analytical flow of Pu analysis for individual U/Pu mixed particles

A novel technique for the analysis of individual U/Pu mixed particles was developed by a combination of alpha and mass spectrometry.

Plutonium (Pu) is a key element for nuclear-fuel cycles; it is produced by neutron capture by uranium (U) in nuclear reactors and is used as U/Pu mixed-oxide (MOX) fuel after purification. On the contrary, Pu with high ^{239}Pu abundances plays an important role in the production of nuclear weapons. Therefore, undeclared nuclear activities using Pu and U should be checked and prevented. We measure U- and Pu-isotope ratios in environmental samples taken at nuclear facilities from around the world to unveil undeclared nuclear activities in cooperation with the International Atomic Energy Agency (IAEA).

The main isotopes of Pu are ^{238}Pu , ^{239}Pu , ^{240}Pu , ^{241}Pu , and ^{242}Pu . Although mass spectrometry is commonly used for isotope-ratio analysis, the determination of $^{238}\text{Pu}/^{239}\text{Pu}$ -isotope ratios in individual U/Pu mixed particles is impossible because the mass of ^{238}Pu is almost the same as that of ^{238}U . Therefore, there are no analytical techniques for measuring $^{238}\text{Pu}/^{239}\text{Pu}$ -isotope ratios in such particles. In the present study, we developed a novel technique using alpha spectrometry and inductively coupled plasma-mass spectrometry (ICP-MS) to determine Pu-isotope ratios including $^{238}\text{Pu}/^{239}\text{Pu}$.

The analytical procedure developed in this study is shown in Fig.2-15. Each U/Pu particle was isolated using a glass needle under a scanning electron microscope and dissolved

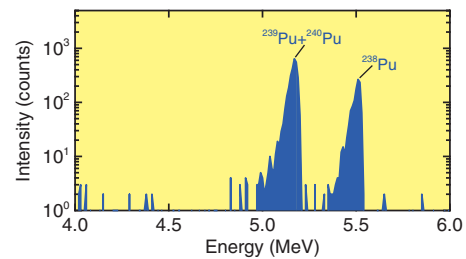


Fig.2-16 Alpha spectrum of a U/Pu mixed particle with a U/Pu ratio of 5 measured for 2000000 s
Well-separated peaks assigned to ^{238}Pu and $^{239}\text{Pu}+^{240}\text{Pu}$ were obtained in the spectrum.

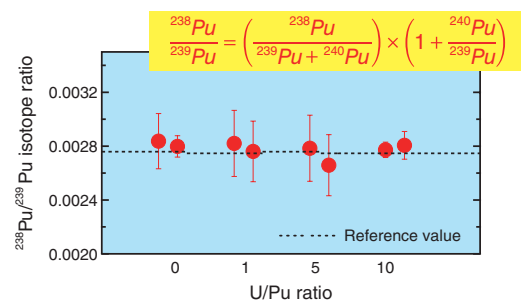


Fig.2-17 The $^{238}\text{Pu}/^{239}\text{Pu}$ isotope ratios measured for individual U/Pu mixed particles with U/Pu ratios of 0, 1, 5, and 10

The $^{238}\text{Pu}/^{239}\text{Pu}$ -isotope ratios determined with the proposed method were quite consistent with the reference values.

with acids. Pu in the sample solution was separated from U by solid-phase extraction. The $^{240}\text{Pu}/^{239}\text{Pu}$, $^{241}\text{Pu}/^{239}\text{Pu}$, and $^{242}\text{Pu}/^{239}\text{Pu}$ -isotope ratios and the $^{238}\text{Pu}/(^{239}\text{Pu}+^{240}\text{Pu})$ activity ratios in the Pu solution were determined with ICP-MS and alpha spectrometry, respectively. Finally, the $^{238}\text{Pu}/^{239}\text{Pu}$ -isotope ratios in each particle were calculated from the $^{240}\text{Pu}/^{239}\text{Pu}$ and $^{238}\text{Pu}/(^{239}\text{Pu}+^{240}\text{Pu})$ ratios.

Fig.2-16 shows an alpha spectrum of Pu extracted from a U/Pu mixed particle with a U/Pu ratio of 5. Since well-separated peaks were obtained in this spectrum, the $^{238}\text{Pu}/(^{239}\text{Pu}+^{240}\text{Pu})$ -activity ratio could be determined accurately. In addition, the $^{240}\text{Pu}/^{239}\text{Pu}$, $^{241}\text{Pu}/^{239}\text{Pu}$, and $^{242}\text{Pu}/^{239}\text{Pu}$ isotope ratios were successfully determined with ICP-MS. Fig.2-17 shows the $^{238}\text{Pu}/^{239}\text{Pu}$ isotope ratios in individual U/Pu mixed particles with the U/Pu ratios of 0, 1, 5, and 10. These values calculated from the $^{240}\text{Pu}/^{239}\text{Pu}$ isotope ratios and the $^{238}\text{Pu}/(^{239}\text{Pu}+^{240}\text{Pu})$ activity ratios were well consistent with reference values. These results indicate that the proposed method using alpha spectrometry and ICP-MS enables us to determine Pu-isotope ratios accurately for individual U/Pu mixed particles.

The present study was sponsored by the Secretariat of the Nuclear Regulation Authority (NRA), Japan.

Reference

Esaka, F. et al., Analysis of Plutonium Isotope Ratios including $^{238}\text{Pu}/^{239}\text{Pu}$ in Individual U-Pu Mixed Oxide Particles by Means of a Combination of Alpha Spectrometry and ICP-MS, *Talanta*, vol.165, 2017, p.122-127.

Advanced Science Pioneers the Future

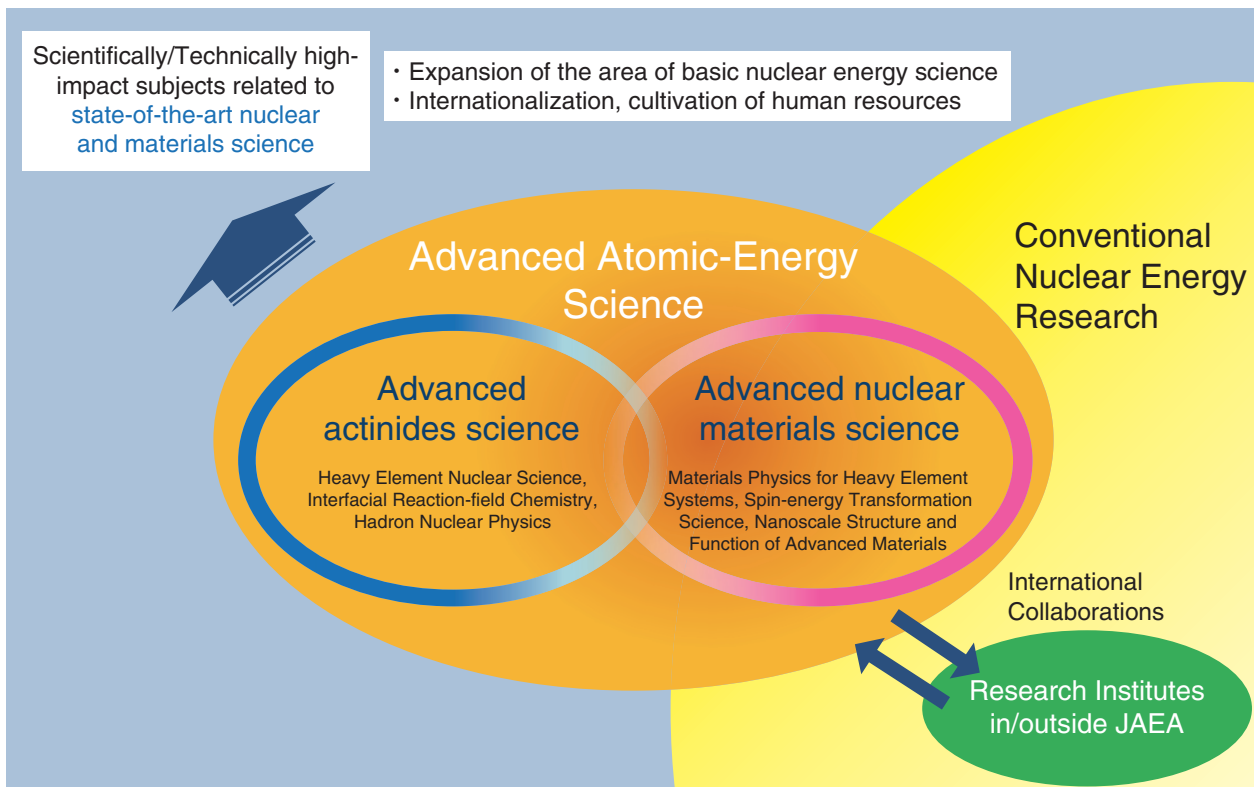


Fig.3-1 The role of advanced nuclear-scientific research

Our aim is to perform high-impact scientific and technical studies related to state-of-the-art nuclear and materials science.

Basic science supports the most nuclear-energy-related technology. In research, it is particularly crucial to respond to the new stages of nuclear-energy development into which society will be entering in the next few decades, as well as to constantly seek solutions to today's energy problems.

The role of the Advanced Science Research Center (ASRC) is to explore the unlimited potential of nuclear energy from the perspective of basic science. Through this process, we aim to open up new fields of research and further develop science and technology. In FY2015, we started our mid-term plan, focusing on two main areas: advanced actinides science and advanced nuclear-materials science (Fig.3-1). Research on the former has been conducted with the aim of creating a new concept for nuclear and heavy-element-based actinide science. For the latter, we have commenced investigation and development of new nuclear-energy-related materials. Through interactions between the two areas and collaboration with research institutes inside and outside of the Japan Atomic Energy Agency (JAEA), we have worked to cultivate new fields of nuclear-energy science (Fig.3-1).

We have made numerous highlighted achievements during FY2016. Through advanced actinides science, a new method of obtaining fission-fragment-mass distributions using multi-nucleon transfer reactions was established at the JAEA tandem accelerator (Topic 3-1). This method generates data for more

than fourteen actinide nuclei at once, including neutron-rich nuclei that have not yet been investigated. At J-PARC, we found evidence of the production of K^- -proton-proton bound states, a new type of nuclear structure through anti- K meson between light hadrons (Topic 3-2). New technology for controlling the migration of cesium from forests to living areas was developed using the natural forces of polymers and clay. We developed verification tests in Iitate village, Fukushima, as well as other locations. We expect to prevent recontamination of living areas (Chapter 1, Topic 1-20).

Substantial results have been obtained by advanced nuclear-materials science. Theoretical calculation of the magnetic order of non-magnetic ions was performed (Topic 3-3). This result would allow the existence of new magnetic materials. High-spin rotational motion generates magnetism in metals; through the Barnett effect (i.e., the production of magnetization by rotating a body), the gyroscopic g -factors of rare-earth metals were measured (Topic 3-4). We have also determined the structure of germanene, the germanium-based equivalent of graphene, on an aluminum substrate using a total-reflection high-energy positron diffraction (TRHEPD) method (Topic 3-5), and revealed it to have an asymmetric structure.

We at the ASRC believe that it is important to develop human resources with nuclear expertise and to demonstrate their abilities through nuclear basic research.

3-1 New Experimental Method for Obtaining Nuclear-Fission Data — Opening-Up Fission Studies for Neutron-Rich Nuclei —

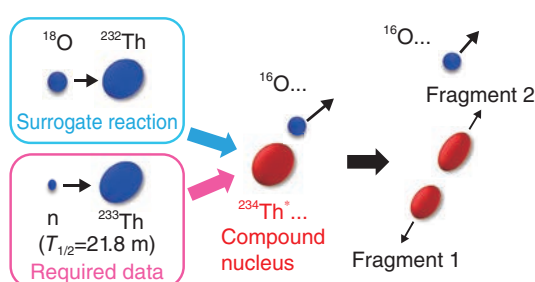


Fig.3-2 Principle of the surrogate-reaction technique

The surrogate reaction technique is a method to obtain neutron-induced fission data of specific nucleus, by populating the same compound nuclei with multi-nucleon transfer reactions and measuring its fission properties, thereby generating data which are practically impossible to take using neutron source. This illustration shows how to obtain the $n + {}^{233}\text{Th}$ data from the ${}^{18}\text{O} + {}^{232}\text{Th}$ reaction.

Long-lived minor-actinide (MA) nuclides such as americium and neptunium isotopes are produced in atomic power plants, which must be confined under control for a long period of time. The use of accelerator-driven systems (ADSs), for example, is considered one viable option for the incineration and/or transmutation of long-lived MAs into shorter-lived products through the use of high-energy-neutron-induced fission. This results in the production of many fission-product isotopes, whose yields (fission-fragment-mass distributions; FFMDs) should be well investigated. For the ADS system, the data necessary for the design broaden both in nuclides and incident neutron-energy, compared to the conventional light-water reactors. Some of the nuclides are short-lived, such that direct measurements using neutron beams are practically impossible. Furthermore, high-energy data are extremely limited, even for well-studied isotopes.

In this study, we used heavy-ion-induced multi-nucleon reactions to solve these problems. An ${}^{18}\text{O}$ beam from the JAEA tandem accelerator was used to bombard the ${}^{232}\text{Th}$ target (as shown in Fig.3-2) to generate the FFMDs for fourteen nuclides ranging from thorium to uranium, together with their incident-neutron-energy dependence up to 50 MeV, in one experiment. Good agreement with the literature data available for some nuclides served to validate this approach as a surrogate for neutron-induced fission. The surrogate-reaction method was only used in the cross-section measurement, and JAEA is the first to apply this idea to obtaining FFMDs. Another important

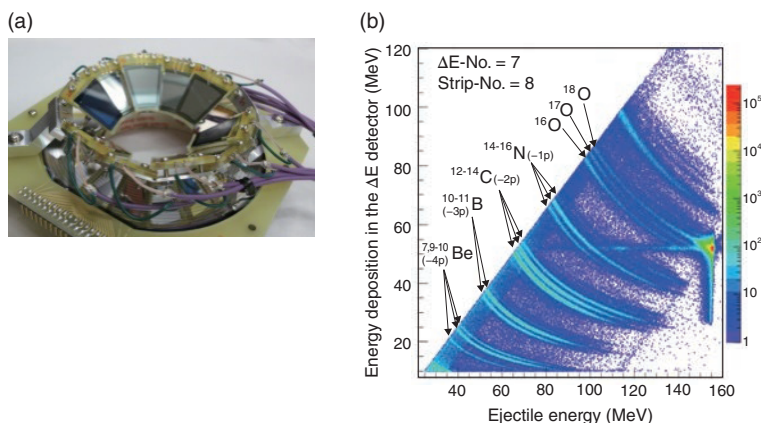


Fig.3-3 (a) Silicon charged-particle telescope (ΔE -E) and (b) result of analyzing ejectile nuclei

A charged particle deposits its partial energy into the thin-silicon ΔE layer (see photo, 220 mm²) depending upon the ejected isotopes produced by the multi-nucleon-transfer reaction. The assignment of the outgoing particle identifies the transfer channel (Fig.3-2). Data in (b), obtained in the ${}^{18}\text{O} + {}^{232}\text{Th}$ reaction, are shown on the ΔE (ordinate) vs E (abscissa) plane. Different colors indicate different yields; see the scale on the right-hand side.

feature is that the reaction allows us to access neutron-rich nuclei for fission studies, adding a new region onto the chart of nuclides.

In multi-nucleon-transfer reactions, a wide variety of excited nuclei are produced by exchanging neutrons and protons. We took advantage this process in the fission study using a technique for identifying produced nuclei on an event-by-event basis with a newly designed silicon ΔE -E detector (Fig.3-3(a)). The ejectile nucleus after the specific transfer channel was identified to determine the generated compound nuclide. This can be seen in the spectrum of Fig.3-3(b), where the different isotope lines corresponding to compound nuclei are clearly separated. We also determined the kinetic energy of the ejectile to assign an excitation energy to the compound nucleus, which is directly transformed into the incident-neutron energy. In the experiment, we also performed velocity measurements of the fission fragments to determine the fragment masses in the kinematic consideration. Through experiments using several radioactive-target materials such as U, Np, and Cm isotopes available in the JAEA tandem facility, almost all fission data required for the ADS can be obtained.

This study was partially supported by the program for “Comprehensive study of delayed-neutron yields for accurate evaluation of the kinetics of high-burn-up reactors” of the Ministry of Education, Culture, Sports, Science and Technology, Japan (MEXT).

Reference

Léguillon, R., Nishio, K. et al., Fission Fragments Mass Distributions of Nuclei Populated by the Multinucleon Transfer Channels of the ${}^{18}\text{O} + {}^{232}\text{Th}$ Reaction, Physics Letters B, vol.761, 2016, p.125-130.

3-2 A New Form of Atomic Nuclei with a “Strange Particle”

— An Antikaon and Two Nucleons Make a Bound State through the Strong Interaction —

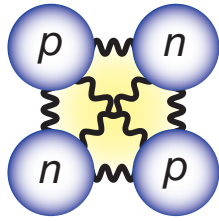


Fig.3-4 A bound state of two protons and two neutrons
An atomic nucleus is formed as a bound state of nucleons, which are attracted to each other due to the nuclear force. This figure represents the ${}^4\text{He}$ nucleus.

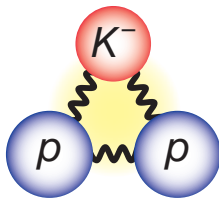


Fig.3-5 A bound state of an antikaon and two nucleons
A bound state like a typical atomic nucleus is expected to exist due to the strong interaction, which is an extension of the nuclear force. The state in this figure is called K^-pp according to its constituent particles.

Typical atomic nuclei are composed of two types of particles, protons and neutrons, as shown in Fig.3-4, and are bound due to the nuclear force between them. Because both protons and neutrons are constructed only out of up and down quarks, they resemble each other except for their electromagnetic properties. Due to this fact, we use the term “nucleon” to refer to a generic particle, whether a proton or a neutron, making up a nucleus.

Our research interest is in how the nuclear force changes if we replace one of the up or down quarks inside a nucleon with a quark of a different “flavor”, such as a strange quark. We refer to such an interaction between particles containing quarks of different flavors as the strong interaction, which is an extension of the nuclear force. Up until now, the strong interaction has been intensively studied in both theory and experiment.

It is well known that the nuclear force is attractive. However, in general, the strong interaction may be attractive or repulsive with various strengths depending on the flavors of quarks inside particles. Among many combinations of particles, that of a K^- meson (composed of strange and anti-up quarks) and protons has attracted much attention because their interaction is expected to be strongly attractive. Indeed, it has been theoretically predicted that there exists a bound state

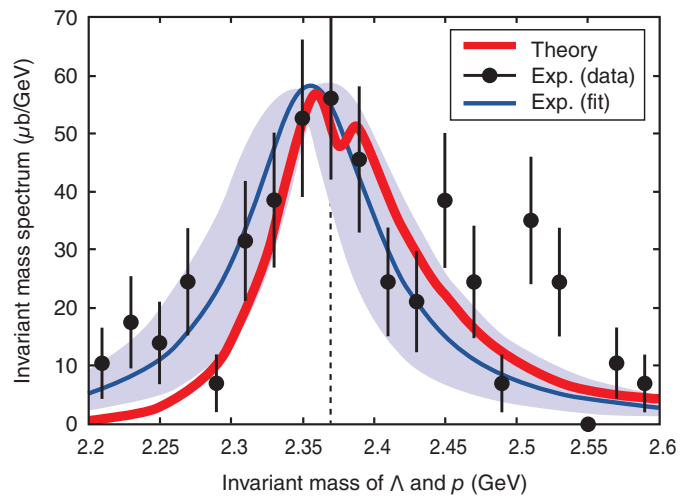


Fig.3-6 Experimental and theoretical results of the Λp invariant-mass spectrum

The invariant-mass spectrum of a Λ particle and a proton in the $K^-{}^3\text{He} \rightarrow \Lambda p n$ reaction. Experimental results (black points and the blue band) are scaled for comparison with the theoretical result (thick red line). The vertical dashed line indicates the threshold of the K^-pp system.

consisting of a K^- meson and two protons (the so-called K^-pp state, or more precisely the $\bar{K}NN$ bound state), as shown in Fig.3-5.

In order to discover this K^-pp state experimentally, we need a facility in which strange quarks are copiously generated. The Japan Proton Accelerator Research Complex (J-PARC), located at the Tokai campus of JAEA, is the best facility for searching for the K^-pp state. Using the high intensity K^- beam at the hadron hall of J-PARC, we bombarded a ${}^3\text{He}$ target with $3.4 \times 10^9 K^-$ s and observed the $K^-{}^3\text{He} \rightarrow \Lambda p n$ reaction. As a result, we found a peak structure around the K^-pp threshold (2.37 GeV) in the invariant-mass spectrum of the Λp system, shown as the black points and blue band in Fig.3-6. This peak may be a signal of the desired K^-pp bound state.

We further theoretically calculated the $K^-{}^3\text{He} \rightarrow \Lambda p n$ reaction to investigate the origin of the observed peak structure at J-PARC. Assuming that the K^-pp state is generated, we obtained the thick red line in Fig.3-6, which qualitatively agrees with the experimental result. This strongly supports the possibility that the K^-pp bound state was indeed produced in the J-PARC experiment.

This bound state is a new form of atomic nucleus composed of an antikaon (a “strange particle”) and two nucleons, bound by the strong interaction between them.

References

- Sada, Y., Tanida, K. et al., Structure near the $K^- + p + p$ Threshold in the In-Flight ${}^3\text{He}(K^-, \Lambda p)n$ Reaction, Progress of Theoretical and Experimental Physics, vol.2016, issue 5, 2016, p.051D01-1-051D01-11.
Sekihara, T. et al., On the Structure Observed in the In-Flight ${}^3\text{He}(K^-, \Lambda p)n$ Reaction at J-PARC, Progress of Theoretical and Experimental Physics, vol.2016, issue 12, 2016, p.123D03-1-123D03-27.

3-3 Magnetic Order of Non-Magnetic Ions

— Theoretical Investigation of Higher-Order Magnetic Order of Non-Kramers Ions —

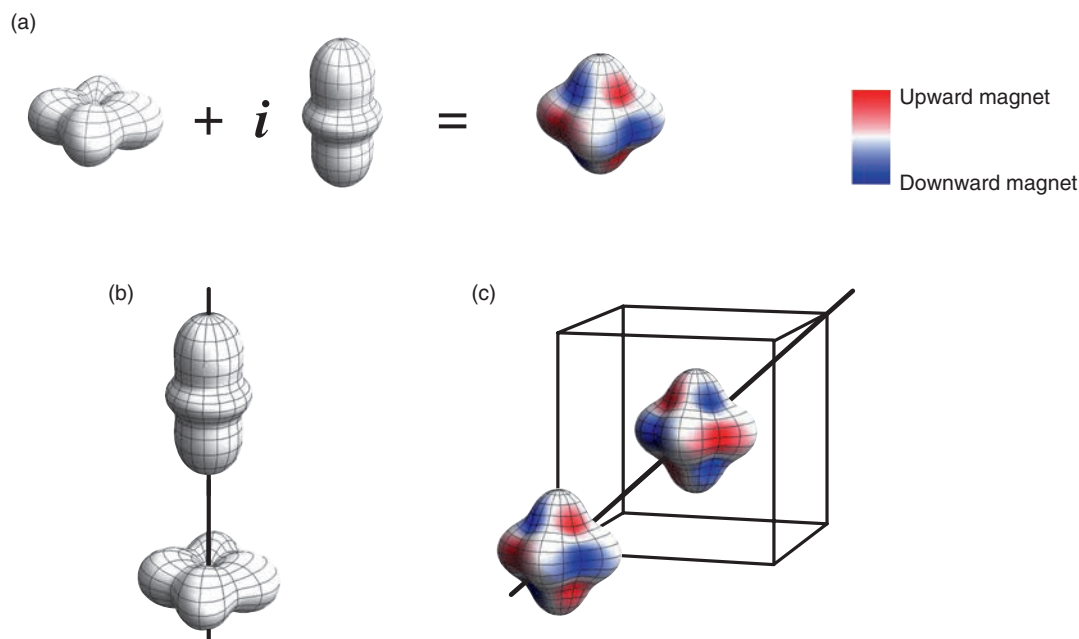


Fig.3-7 Various states made from non-magnetic states

(a) A magnetic state composed of non-magnetic states with differently shaped electron distributions. In the red and blue areas, the axes of the circulating currents are in opposite directions and the currents produce opposite magnetic fields. (b) Non-magnetic state for ions aligned along a direction of a lattice axis. (c) Magnetic state for ions aligned along a diagonal direction.

The magnetism of a material originates from its electrons, since electrons behave as tiny magnets and align in the same direction in an ordinary macroscopic magnet. This magnetic property of an electron is called spin. Thus, basic research on understanding and manipulating spins in materials is very important.

If there are two electrons in an ion, however, magnetism can be canceled out by aligning their spins in opposite directions, resulting in a non-magnetic ion. We call an ion with an odd number of electrons a Kramers ion and one with an even number of electrons a non-Kramers ion. To become a non-magnetic ion, the spins of the electrons have to cancel out. It is possible only for non-Kramers ions. Conversely, a Kramers ion, for example neodymium, is always magnetic ion and is a good candidate for use in a strong magnet.

On the other hand, non-magnetic ions cannot possess magnetism in an ordinary manner. However, surprisingly, according to quantum mechanics (which describes microscopic objects such as ions and electrons), a magnetic object can emerge from non-magnetic objects.

When we have two different non-magnetic states, the principles of quantum mechanics allow construction of a “superposed state” by adding these states with a coefficient of the imaginary unit i (Fig.3-7(a)). This state has circulating currents of the electrons, thereby reviving magnetism since a circulating current generates a magnetic field like an

electromagnet. In this state, the magnetic field produced by the currents cannot be described as a single magnet, since the direction of the axis of circulation changes depending upon position. Rather, such a state is described by a complex of magnets and is called a higher-order magnetic state.

Such higher-order magnetic states have been investigated and actually observed in some materials, but to date, only those with magnetic ions.

To investigate whether it is possible to realize such a magnetic state in non-magnetic materials, we have studied a theoretical model of non-Kramers ions with two electrons in each ion. In this model, we can compose two non-magnetic states for each ion with differently shaped electron distributions, as shown in Fig.3-7(a). In both states, the spins of the two electrons align oppositely and magnetism is canceled out. Then, we search for stable states for several kinds of lattice structures. We find that the alignment of the non-magnetic states (non-magnetic order, Fig.3-7(b)) occurs when ions align along a lattice-axis direction. On the other hand, the alignment of the magnetic states (magnetic order, Fig.3-7(c)) occurs when ions align along a diagonal direction. Thus, it is interesting to search lattices in which ions are located along diagonal directions for such an exotic magnetic state.

This work was supported by the Japan Society for the Promotion of Science (JSPS) KAKENHI Grant-in-Aid for Scientific Research (C) (No.15K05191).

Reference

Kubo, K. et al., Influence of Lattice Structure on Multipole Interactions in Γ_3 Non-Kramers Doublet Systems, Physical Review B, vol.95, issue 5, 2017, p.054425-1-054425-6.

3-4 High-Speed Rotation Turns an Ordinary Metal into a Magnet

— Exploring the Relationship between Magnetism and Rotation that Fascinated Einstein —

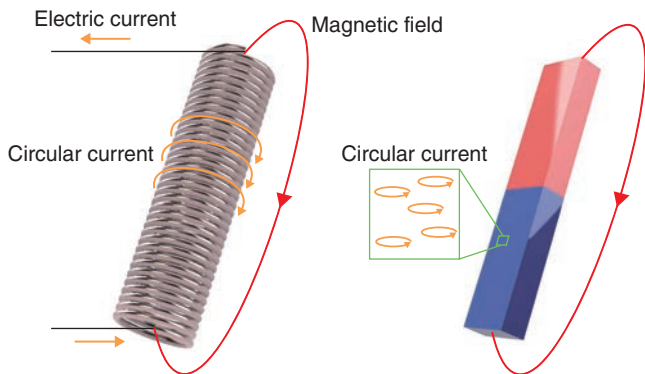


Fig.3-8 Electromagnet (left) and permanent magnet (right)
Einstein thought that a permanent magnet has small circular currents like an electromagnet.

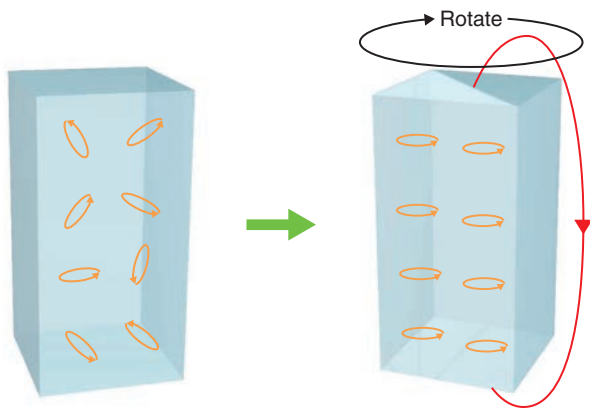


Fig.3-9 Barnett effect
Disordered circular currents are aligned as shown in the figure by rotating the body.

Magnets are roughly divided into electromagnets, which become magnets when a current flows through coils wrapped around a metal core, and permanent magnets such as iron, which show magnetic properties without a current (Fig.3-8). Einstein thought that small circular currents in metal cause the properties of a permanent magnet and therefore believed that the direction of these circular currents could be controlled by rotation of the body. Einstein proved experimentally that changing the strength of the electromagnetic field surrounding an iron specimen could cause the specimen to rotate, which is known as the Einstein-de-Haas effect. In the same year, Barnett discovered the eponymous Barnett effect, whereby the intensity of a permanent magnet changes when its body is rotated (Fig.3-9). These experiments were performed using permanent magnets such as iron, but most metal does not show permanent magnetic properties at room temperature.

What happens when rotating an ordinary metal that is not a permanent magnet? By utilizing technologies developed over the past 100 years, we devised an *in-situ* magnetization-measurement apparatus to observe the strength of magnetization in metal rotating at several thousands of

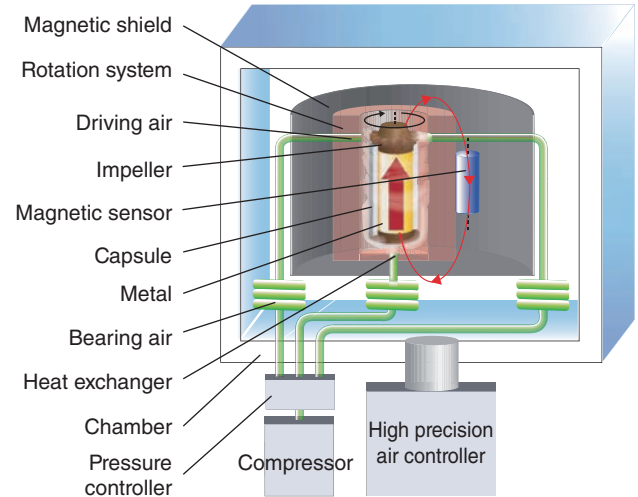


Fig.3-10 Experimental apparatus for observation of the Barnett effect

The metal specimen turns into a magnet by rotating it several thousands of times per second. The stray field arises from the magnet during the rotation. The strength of circular currents in the metal can be estimated by the stray field, which is measured with a magnetic sensor.

cycles per second, as shown in Fig.3-10. Using this apparatus, we performed experiments on gadolinium, terbium, and dysprosium, which are ordinary metals.

As a result of the experiment, we confirmed that ordinary metals turn into magnets during rotation, and that the strength of these magnets is proportional to the rotational frequency. This result indicates that circular currents can exist in any metal. Such currents can be divided into two types: orbital motion corresponding to the Earth turning around the sun, and the spin arising from the rotation of the Earth itself. We succeeded in determining the contributions of orbital motion and spin to the magnetism in each of gadolinium, terbium and dysprosium by precisely measuring the magnetic strength during rotation. We determined the strength of each circular motion in ordinary metal using mechanical rotation for the first time in the world.

This result, which provides a new way to control the magnetic properties of ordinary metal using mechanical rotation, is expected to allow nanoscale acceleration and magnetic sensors.

Reference

Ogata, Y. et al., Gyroscopic g Factor of Rare Earth Metals, Applied Physics Letters, vol.110, issue 7, 2017, p.072409-1-072409-4.

3-5 Asymmetric Structure of the New “Germanene” Material — Possible New Germanene Properties —

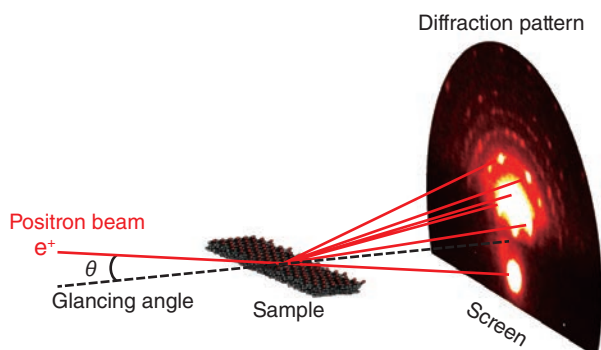


Fig.3-11 Experimental setup of total-reflection high-energy positron diffraction (TRHEPD)

The positron beam strikes the sample surface at a grazing angle and then diffracted positrons exit from the surface, carrying information about the surface atomic configuration. Since the positron beam barely penetrates the deeper bulk region, the diffracted positrons mainly contain information about the topmost surface layer. Thus, the atomic configuration of this layer can be determined accurately by means of intensity analysis of the diffracted positrons.

As expected post-graphene materials, efforts have been made to fabricate novel atomic sheets composed of heavier group-IV elements with the honeycomb structure of graphene. For instance, atomic sheets of silicon and germanium are called silicene and germanene, respectively. Owing to the expected buckling configuration due to the bonding character and the stronger spin-orbit interaction in heavier atoms, these materials are expected to provide novel spin-related properties.

Graphene can be obtained by exfoliation of graphite, which is well-known for its use as pencil lead. Since silicene and germanene lack parent materials like graphite, they have been regarded as a research target for theorists. However, research on such atomic sheets has opened up since the successful synthesis of silicene on Ag and ZrB₂ substrates in 2012.

In 2015, a uniform, large-area germanene sheet was fabricated on an Al substrate. Germanene was expected to have buckled structure due to its bonding character, which sharply contrasts with the flat structure of graphene. Therefore, there are many possible structural models for germanene because of its complex buckling configurations. Moreover, it is not easy to investigate such a material, which has a thickness of only one atomic layer. In this study, we tried to reveal the atomic configuration of germanene using a total-reflection high-energy positron diffraction (TRHEPD) technique.

Reference

Fukaya, Y. et al., Asymmetric Structure of Germanene on an Al(111) Surface Studied by Total-Reflection High-Energy Positron Diffraction, 2D Materials, vol.3, no.3, 2016, p.035019-1-035019-7.

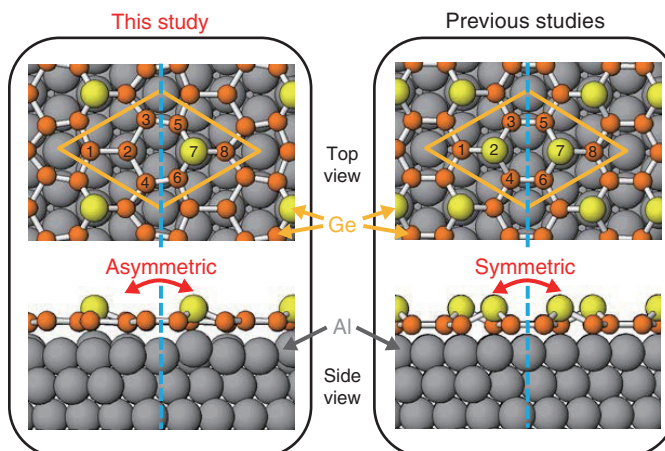


Fig.3-12 Atomic configurations of germanene determined in this study (left) and expected in the previous studies (right)

Orange and yellow circles indicate Ge atoms. Gray ones are Al atoms. To highlight a buckled configuration, the upwardly shifted Ge atoms are represented by large yellow circles. As a result, the atomic configuration determined in this study is asymmetric with respect to the blue dotted line whereas the previously reported configuration is not.

Fig.3-11 shows the experimental setup of the TRHEPD method, by which positrons, the antiparticles of electrons, are used as a probe beam. Since the positron beam has a positive charge (opposite to that of electrons), it cannot penetrate the deeper bulk region because of the strong repulsive force from the positive point charge of the nucleus. In particular, total reflection takes place at a low incidence angle; therefore, the positron beam selectively *sees* the topmost surface layer.

In previous studies, two Ge atoms (labeled 2 and 7 in the right panel of Fig.3-12) per unit cell were shifted upwards, suggesting a symmetric structure. However, the TRHEPD experiments demonstrated that the spot intensities diffracted to the left and right differ. This indicates that the atomic configuration of germanene is not symmetric. The detailed intensity analysis shows that only one Ge atom (labeled 7 in the left panel of Fig.3-12) is shifted upwards. As a result, the newly proposed structural model may have novel germanene properties.

Recently, atomically thin superconductors have been shown to exhibit higher superconducting transition temperatures as compared with those of the corresponding bulk materials. In the near future, we will fabricate such fascinating atomic sheets and investigate the atomic configuration to reveal novel properties.

An Interface Bridge between Nuclear-Energy R&D and Fundamental Research

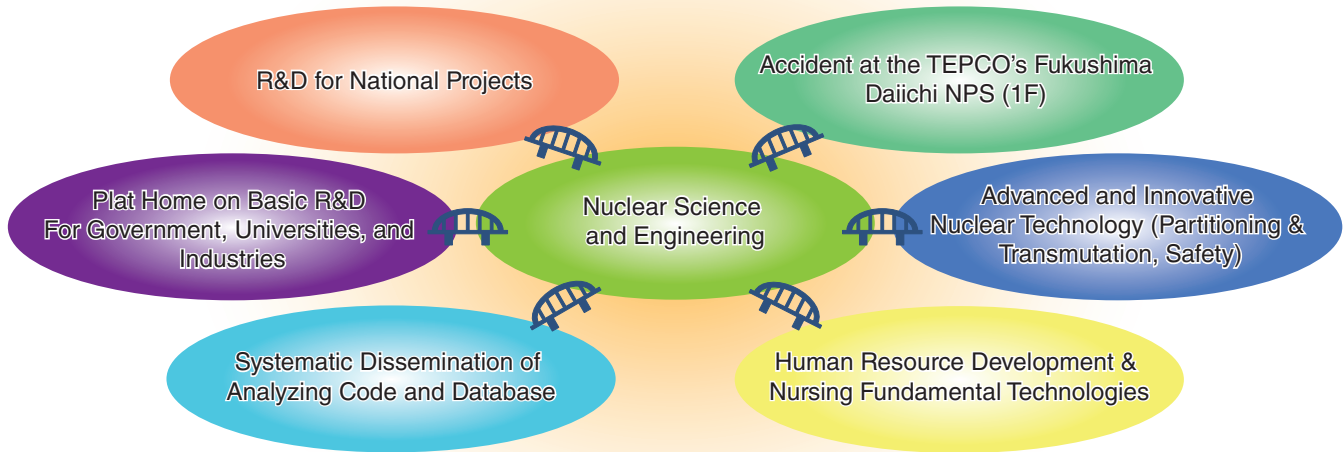


Fig.4-1 Relation between Nuclear-engineering Fundamental Research and Nuclear-energy R&D

The outputs of nuclear science and engineering research, which include databases, analytical codes, and techniques, form a knowledge base for lots of technologies in the nuclear engineering field. These are applied for research on such topics as the recovery of the Fukushima area and the safe use of light-water reactors and high-level waste management (partitioning and transmutation). They are also useful for cooperative work with universities and industries, human-resource development, and technology nursing.

The outputs of nuclear science and engineering research form a knowledge base for many technologies in the nuclear-engineering field. These include techniques for observing materials (analysis) and understanding phenomena (modeling). They have been integrated into analysis codes and databases and have been introduced to projects inside JAEA, such as research and development of fast reactors, nuclear waste treatment, safety technology, recovery from the accident at the TEPCO's Fukushima Daiichi NPS (1F), key technologies for improving reactor safety (Topic 4-1), and transmutation technologies to reduce the amount of long-lived radioactive waste (Topics 4-2, 4-3, and 4-4). Our research has also been used outside JAEA in academia and industry (Fig.4-1).

The neutron- and radiation-transport code is used in various fields such as reactor design, shielding calculation, and radiation-dose estimation. For this purpose, nuclear data are converted into a certain code format in the library, via a processing step. We have developed a nuclear-data-processing code called FRENDY (Topic 4-5).

Zirconium (Zr) has high corrosion resistance and is often used in nuclear spent-fuel-recycling facilities that employ high-temperature nitric acid. On the contrary, Zr absorbs hydrogen easily, causing it to be brittle. Moreover radiation in spent nuclear fuel (SNF) pool disintegrates water molecules into hydrogen and oxygen. Thus, it is important to understand the Zr characteristics of hydrogen absorption (Topic 4-6).

Hexagonal-crystal metals such as Zr have good characteristics as structural materials that are light and heat- and corrosion-resistant. However, they have the drawbacks of being hard to process. We have simulated the above characteristics at the atomic and molecular level to improve the alloy design of such materials (Topic 4-7).

One radioactive isotope (RI) of palladium (Pd), ^{107}Pd , is a fission product of Uranium (U) with a long half-life (6.5 million years); however, ^{107}Pd from SNF has not been measured previously due to the difficulty of doing so, and the calculated results have been used for management purposes. We have succeeded in separating ^{107}Pd from SNF and quantitatively measuring it using a pulsed laser (Topic 4-8).

In the case of a severe accident at a nuclear power plant, RI can contaminate an area of the ocean, for example the 1F case. It is important to be able to predict RI contamination, distribution, and transfer in the eastern-Asia region in the event of such an accident. We have developed a system for simulating RI diffusion in the ocean (Topic 4-9).

Neutron dosimeters and survey meters are used to control doses of workers at nuclear and accelerator facilities. These are calibrated periodically, typically using RI neutron sources. The calibration strongly depends upon the neutron-energy spectrum. We have constructed calibration fields to simulate the neutron slow-down spectrum more precisely (Topic 4-10).

4-1 Prevention of Severe-Accident Progression by Delaying Core Overheating and Melting — Development of FEMAXI-ATF Code for Accident-Tolerant Fuel-Behavior Analysis —

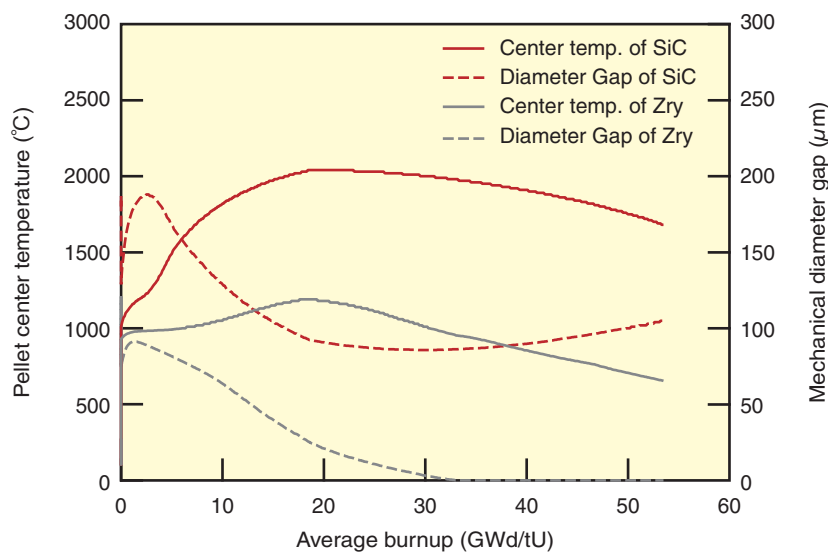


Fig.4-2 Analysis of changes in fuel-center temperature and pellet-cladding gap size using the FEMAXI-ATF code
We performed fuel-behavior analysis under typical BWR (boiling water reactor) operating conditions using the FEMAXI-ATF code. The SiC cladding shows larger swelling under irradiation than the Zircaloy cladding, which increases the gap size and consequently the fuel temperature. Though the fuel's central temperature is higher than that of Zircaloy-cladding fuel, it is sufficiently lower than the melting temperature.

Zirconium alloys (Zircalloys), which are used as fuel cladding and other core components in light-water reactors (LWRs), are readily oxidized at high temperatures. The reaction of zirconium with water or steam is accompanied by the release of hydrogen gas as well as the formation of an oxide. In addition, the reaction is highly exothermic. It is believed that the Zircaloy fuel cladding was oxidized in the heated core and that the subsequent temperature escalation due to oxidation caused core melting in the accident at the TEPCO's Fukushima Daiichi NPS (1F). It is also presumed that the reactor building was caused to explode by hydrogen generated by the leak of oxidants from the primary containment vessel. Based on lessons learned from the 1F accident, we are developing advanced fuel and core components with enhanced accident tolerance to prevent extensive core damage and hydrogen generation and to mitigate these phenomena in accidents whose severity exceeds the basis of the reactor's design.

Silicon carbide (SiC) is an attractive candidate for an accident-tolerant cladding material because of its high chemical stability and heat resistance. Since SiC is expected to be far less reactive with steam than is Zircaloy, the generation of heat and hydrogen gas would be greatly suppressed.

The material properties of SiC, such as its swelling behavior and mechanical properties, are different from those of Zircaloy. It is essential to identify the fuel-behavior difference between Zircaloy-based and SiC-based cladding not only under accident conditions but also during normal operation.

The FEMAXI-ATF code has been developed to analyze the SiC-cladding-fuel behaviors as an extended version of the LWR fuel-analysis code FEMAXI-7. The thermal, mechanical and irradiation-property models of SiC have been newly implemented in FEMAXI-7.

Triplex SiC-cladding designs combining monolithic SiC and SiC/SiC-composite layers have been proposed to provide features such as corrosion protection, improved mechanical properties, and leak-tightness. The FEMAXI-ATF code was improved to treat the triplex-cladding structure. The pseudo-ductility model for SiC/SiC composite was developed based on experimental values from the literature. SiC cladding is corroded by coolant water and wall-thinning occurs. The code was enhanced to account for the thinning behavior in the outer cladding layer.

Analysis using the FEMAXI-ATF code indicated that the SiC cladding swells more under irradiation than the Zircaloy cladding, increasing the gap size and therefore the fuel temperature (Fig.4-2). R&D on the utilization of SiC as a LWR-fuel cladding has been prioritized based on the present analysis.

A part of this study is the result of the "Development of a Technical Basis for Introducing Advanced Fuels Contributing to Safety Improvement of Current Light Water Reactors," as carried out under the Project for the "Development of a Technical Basis for Safety Improvement at Nuclear Power Plants," by the Agency for Natural Resources and Energy, the Ministry of Economy, Trade and Industry (METI), Japan in FY 2016.

Reference

Shirasu, N. et al., Fuel Behavior Analysis for Accident Tolerant Fuel with SiC Cladding using Adapted FEMAXI-7 Code, Proceedings of Water Reactor Fuel Performance Meeting (WRFP2017), Jeju Island, Korea, 2017, paper 226, 8p., in USB Flash Drive.

4-2 Efficient Partition of Nuclides in High-Level Waste — High-Efficiency Separation of Americium and Curium —

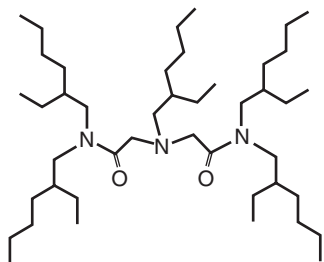


Fig.4-3 Molecular structure of ADAAM(EH)
ADAAM(EH) is a highly practical, high-performance extractant for separation of Am and Cm.

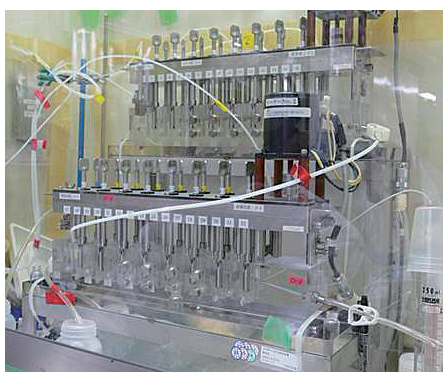


Fig.4-4 Mixer-settler extractors in a fume hood
The units comprise 8-stage extraction, 8-stage scrub, and 16-stage strip sections.

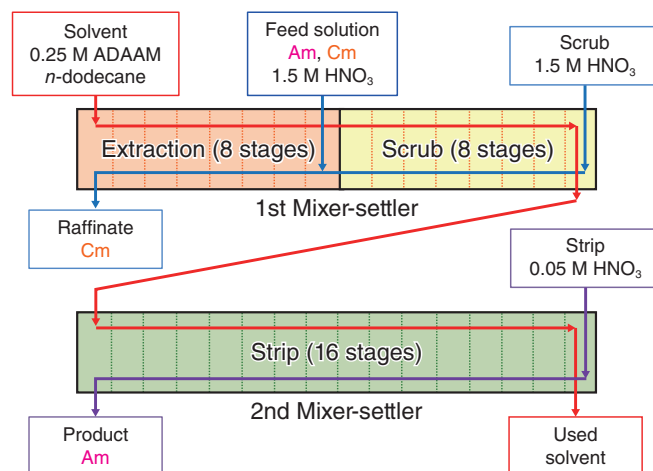


Fig.4-5 Operating conditions of two mixer-settler units
A continuous extraction and stripping test was conducted over 5 h using a multistage countercurrent mixer-settler extractor with ADAAM(EH).

Table 4-1 Fractional distribution of Am and Cm

In this test, the separation of Am and Cm was achieved with a very high yield.

Element	Product	Raffinate	Used solvent	Recovery
Am	> 99.8%	< 0.2%	< 0.2%	99.8%
Cm	9.6%	90%	< 0.2%	99.6%

We have been developing partitioning and transmutation (P&T) systems. The long-term radioactive toxicity of high-level waste (HLW) mainly depends upon minor actinides (MAs) such as americium (Am) and curium (Cm). The toxicity of MAs could be decreased by P&T. The separation of MAs from HLW is an important task for P&T. After MAs are separated from HLW, the mutual separation of Am and Cm (Am/Cm separation) can be conducted. Am and Cm can be transmuted together, although Cm produces a large amount of heat during its decay. Therefore, the removal of the pyrogenic Cm nuclide would reduce the difficulties associated with MA-fuel fabrication. However, Am/Cm separation is very challenging because the two elements have similar chemical and physical properties. Although various ligands and separation methods have been studied for Am/Cm separation, an effective approach for practical use has not yet been developed.

A highly practical reagent, called alkyl diamide amine (ADAAM(EH), Fig.4-3) has been developed. ADAAM(EH) satisfies the CHON principle (it contains only C, H, O, and N atoms), making it practical for incineration at the end of its lifecycle. Furthermore, ADAAM(EH) has high extraction

capacity, good solubility in diluents, clear and fast phase separation, fast extraction kinetics, easy synthesis, and low cost. Am/Cm separation using ADAAM(EH) has been investigated, and it was found that ADAAM(EH) has a high selectivity for Am over Cm.

A continuous, 5-h solvent-extraction and stripping test was conducted using a multistage countercurrent mixer-settler extractor ((MS), Fig.4-4). 0.25 M ADAAM(EH) in *n*-dodecane was used as the solvent. The concentrations of HNO₃ in the feed and scrub solutions were 1.5 M and 0.05 M in the strip solution, respectively. The concentrations of metal ions used in the feed solution were sub-ppb-level for Am and Cm (Fig.4-5). Am was extracted and stripped with a very high yield (Table 4-1). The feed solution was contaminated with 9.6% Cm. A decrease to 10% pyrogenic Cm would reduce difficulties in MA-fuel fabrication. By contrast, Am is removed from the Cm in the raffinate, facilitating disposal of Cm.

In the future, we will investigate the reaction mechanisms and radiation of ADAAM(EH). Additionally, a HLW HOT test will be performed to complete the separation process.

Reference

Suzuki, H. et al., High-Performance Alkyl Diamide Amine and Water-Soluble Diamide Ligand for Separating of Am(III) from Cm(III), Analytical Sciences, vol.33, no.2, 2017, p.239-242.

4-3 Reliability Evaluation of Nuclear Data Required for Core Design of Nuclear Transmutation Systems

— Verification of Trans-Uranium (TRU) Cross-Sections Based on Critical Experiments using FCA —

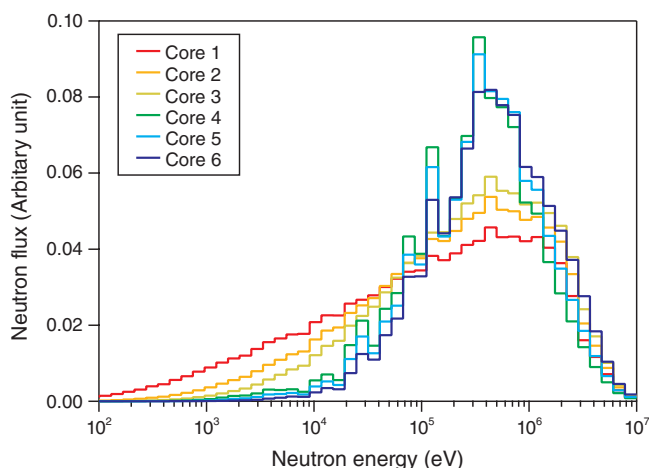


Fig.4-6 Energy distribution of neutron flux at a core center
The neutron spectrum shifts gradually from intermediate to fast as the core number increases from 1 (—) to 6 (—). This series of experiments systematically provides central-fission-rate ratios for TRU nuclides.

High-level waste (HLW) discharged from nuclear power plants contains minor actinides (MAs), such as americium (Am), neptunium (Np), and curium (Cm), which have long-lived radioactive toxicity with half-lives of up to 2 million years. Partitioning and transmutation (P&T) is a key technology for separating long-lived nuclides from the HLW and transmuting them into short-lived or stable nuclides through fission reactions. Based on nuclear transmutation, we investigate an accelerator-driven system (ADS) to minimize the environmental burden and toxic risk due to HLW.

The probability of causing nuclear fission, which is called the fission cross-section, depends on the energies of incident neutrons. In particular, the fission cross-sections of MAs are important nuclear data required for the core design of nuclear-transmutation systems. To evaluate the reliability of these nuclear data, it is effective to compare the calculated value using nuclear data with experimental values measured using critical assemblies.

Using the fast critical assembly (FCA), fission-rate ratios for trans-uranium (TRU) elements including MAs were measured in several experimental cores. Each core consisted of a simple combination of fuel and diluent materials such as graphite or stainless steel, in which neutrons lose energy through collisions.

Reference

Fukushima, M. et al., Analyses with Latest Major Nuclear Data Libraries of the Fission Rate Ratios for Several TRU Nuclides in the FCA-IX Experiments, Journal of Nuclear Science and Technology, vol.54, issue 7, 2017, p.795-805.

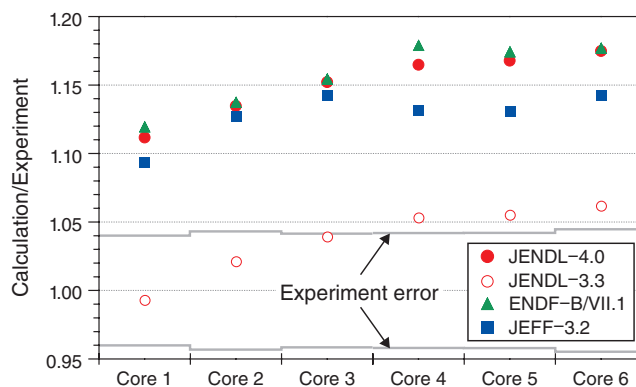


Fig.4-7 An example of a comparison between experimental and calculated values for the fission-rate ratio of ^{244}Cm to ^{239}Pu

Solid marks show results in the latest major nuclear-data-libraries of JENDL-4.0 (●), ENDF/B-VII.1 (▲), and JEFF-3.2 (■). The open circle (○) indicates the result according to JENDL-3.3 (old version).

The neutron spectra at the central core shift gradually by varying the combination of loaded fuel and diluent, as shown in Fig.4-6. To widely utilize experimental data to validate the fission cross-sections of TRU, we developed benchmark models and analyzed them using the Japanese Evaluated Nuclear Data Library (JENDL) developed at JAEA, as well as the latest foreign nuclear-data-libraries, ENDF/B-VII.1 (US) and JEFF-3.2 (Europe).

For the fission-rate ratios of ^{237}Np to ^{239}Pu , the calculation values from all libraries were found to be in good agreement with experimental values. As for the fission-rate ratios of ^{241}Am and ^{243}Am to ^{239}Pu , all libraries slightly underestimated the experimental values. On the other hand, analyses of the fission-rate ratios of ^{244}Cm to ^{239}Pu showed that the latest libraries including JENDL-4.0 resulted in obvious overestimations by more than 10%, while the calculations by JENDL-3.3 (old version) were almost consistent with experimental values (Fig.4-7). Furthermore, the overestimated fission-rate ratios of ^{244}Cm were revealed to be caused by the larger fission cross-sections of ^{244}Cm around 1 MeV.

The TRU data measured using FCA are expected help improve the accuracy of fission cross-sections of TRU by taking advantage of their unique characteristics with systematically changed neutron spectra.

4-4 Real-Time Measurement of Heavy-Liquid-Metal Flow under a Severe Environment — Development of an Ultrasonic Flowmeter for a Lead-Bismuth Target —

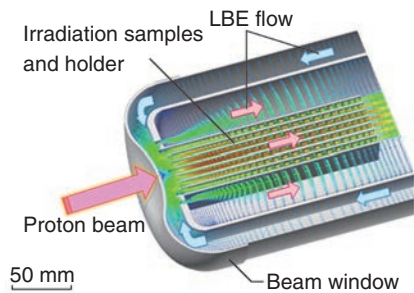


Fig.4-8 Schematic of a lead-bismuth-eutectic (LBE) target vessel

The target vessel has a double-tube structure. Candidate structural materials of ADS are loaded into the inner tube for irradiation tests.

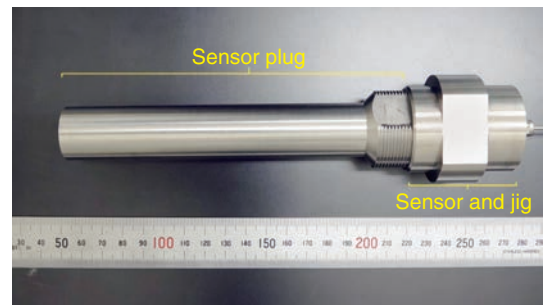


Fig.4-9 Exterior of ultrasonic sensor for LBE-flowrate measurement

This sensor provides sufficient heat resistance (<500 °C) and radiation resistance (<10 MGy) to be applicable to severe environments, such as those during operation of the LBE target.

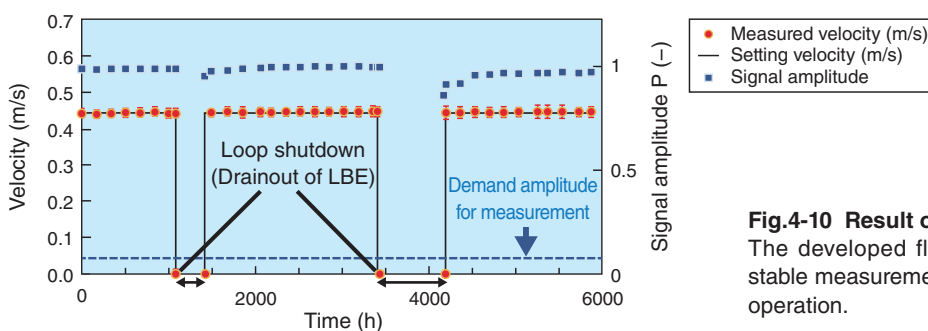


Fig.4-10 Result of the LBE-flow-measurement test
The developed flowmeter demonstrated sufficiently stable measurement under the condition of LBE target operation.

Spent nuclear fuel contains long-lived high-level radioactive materials that are highly toxic to humans and the environment. We have performed various R&D activities towards an accelerator-driven system (ADS) for transmuting long-lived nuclides into short-lived or stable ones using neutrons generated in a spallation target. In an ADS, the spallation target provides neutrons generated via spallation reactions induced by bombarding intense high-energy-proton beams onto a heavy material such as lead. Construction of an ADS target test facility (TEF-T) falls within our scope as a step preceding construction of a demonstrative ADS for performing a post-irradiation-examination program of several candidate ADS materials such as T91 and type 316SS. A lead-bismuth-eutectic (LBE) alloy spallation target (Fig.4-8) is installed in the TEF-T and irradiated by a 400-MeV, 250-kW pulsed proton beam. The flowrate of LBE should be controlled with an accuracy less than 10% because it affects the safety of the LBE target and the temperature of the irradiation field. Since LBE is strongly corrosive to materials under high-temperature environment, it is too difficult to measure the flowrate of LBE stably over a long period. To overcome this issue, we focused on the ultrasonic transparency of opaque metallic materials and developed an ultrasonic-flowmeter based on the measurement technology for a sodium-cooled fast reactor. This technology employed the propagation-time difference of an ultrasonic burst signal to derive a mean velocity along a signal path. Since this method does not require suspended particles, it is a more practical instrument that can prevent contamination of an LBE. The

resultant flowmeter provided stable output under the flowing-LBE environment for long operating periods.

Lead zirconate titanate (PZT) is a typical piezoelectric element for emitting an ultrasonic signal. Since its maximum applicable temperature is about 365 °C, it is difficult to use PZT at the operational temperature of an LBE target (350–450 °C). Furthermore, PZT is weak in a radiation environment; therefore, we developed an ultrasonic sensor (Fig.4-9) using lithium niobate (LiNbO₃). The permittivity of LiNbO₃ is smaller by one order of magnitude or more than that of PZT, while it has a high temperature resistance of more than 1000 °C and a high radiation resistance. As a countermeasure against a small permittivity, a liquid-immersion plug ensuring wettability with LBE was provided on the front surface of the sensor to solve the typical problem that inhibited signal propagation at the solid-liquid boundary. We also applied a linear signal path to realize efficient signal exchange, achieving a reception signal with an intensity of about 50% of that of the transmission signal.

As a result of application tests performed in an experimental LBE loop shown in Fig.4-10, we succeeded in monitoring the LBE flowrate with a satisfactory stability (error: 3% or less) under the operating conditions assumed for the TEF-T target (flow velocity: 0.37 m/s; operation time: about 4500 h). We decided to apply the ultrasonic flowmeter to TEF-T. In the future, we will acquire more data with the present flowmeter by performing simulation tests such as coolant-flow-reduction events to further improve the safety of LBE target.

Reference

Obayashi, H. et al., Development of Plug-in Type Ultrasonic Flowmeter for Lead-Bismuth Spallation Target System, Proceedings of 11th International Topical Meeting on Nuclear Reactor Thermal Hydraulics, Operation and Safety (NUTHOS-11), Gyeongju, Korea, 2016, paper N11P0107, 10p., in USB Flash Drive.

4-5 Interface of Nuclear Data and Transport Codes

— Development of Nuclear Data Processing System FRENDY —

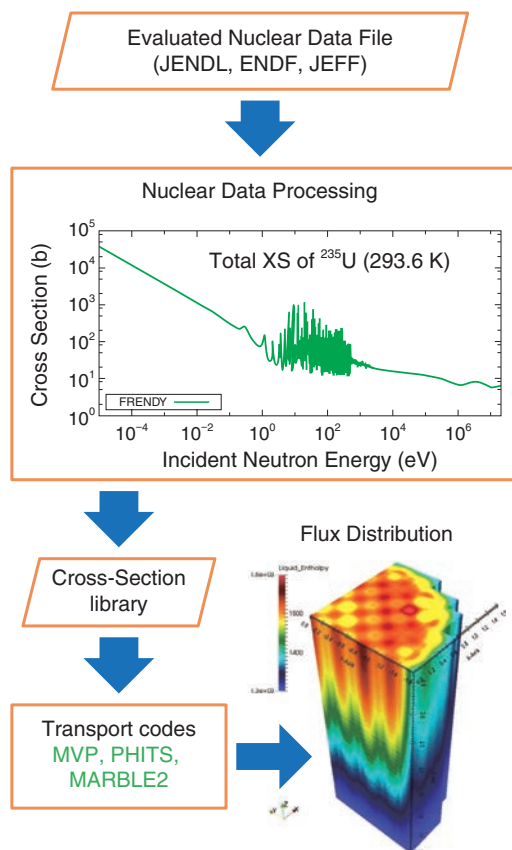


Fig.4-11 Overview of Nuclear Data Processing

To handle the nuclear data file using particle transport codes, the nuclear data file must be processed (i.e., linearized, Doppler broadened and so on).

We provide an evaluated nuclear data file, JENDL, and many particle transport codes, e.g., MVP, PHITS, and MARBLE2. These codes cannot read the nuclear data file directly and a cross section data library, which is generated by the nuclear data processing system, is required, as shown in Fig.4-11. The nuclear data processing system is not just a converter. It performs many processes, e.g., reconstruction of the resonance region, linearization, Doppler broadening, and calculation of the probability table in the unresolved resonance region.

The NJOY code of LANL has been widely used throughout the world including Japan for several decades. However, it is sometimes unable to process the newly released JENDL correctly, and this problem cannot be resolved in a timely manner. Therefore, expertise on particle transport codes, as well as the nuclear data, has been desired in the domestic nuclear data processing system, since it serves as an indispensable interface between nuclear data files and particle transport codes.

We started developing the new nuclear data processing

Table 4-2 Comparison of k-effective results for benchmark experiments processed by FRENDY and NJOY

Comparing the k-effective values using the cross section library processed by FRENDY and by NJOY, the large differences are not observed.

Exp. No. of ICSBEP*	FRENDY	NJOY	Relative Dif.
HMF05-01	0.97241	0.97267	-0.03%
HMI06-01	0.99358	0.99370	-0.01%
HMM01-01	1.07812	1.07824	-0.01%
HMT06-01	0.99409	0.99388	0.02%
HCI05-07	0.98970	0.98971	0.00%
ICI01-18	0.97242	0.97227	0.02%
ICT02-01	1.00369	1.00351	0.02%
LCT01-01	0.99965	0.99949	0.02%
PMF01-01	0.99904	0.99887	0.02%
PMF05-01	0.99697	0.99718	-0.02%
UCT01-01	1.00315	1.00329	-0.01%
UMF04-01	0.99865	0.99842	0.02%

*ICSBEP (International Criticality Safety Benchmark Evaluation Project), which is managed by the OECD / NEA, contains the details of critical experiments conducted in the world.

system FRENDY (FRom Evaluated Nuclear Data librarY to any application) to satisfy these expectations. Several foreign institutes have also implemented similar projects, but FRENDY is one of the most advanced systems in the world.

FRENDY uses the same processing method adopted in NJOY, because the implementation of the conventional method is an important step in the development of the new system. For verification, we compared the processing results of FRENDY with those of NJOY. Table 4-2 indicates that the processing results of FRENDY are in good agreement with those of NJOY.

To improve processing, we investigated all processing methods used in FRENDY and found several problems with the conventional technique. To overcome these problems, we introduced a new nuclear data processing method. Investigation of the impact upon the neutronics calculation is now in progress. Development of FRENDY and advancement of nuclear data processing will contribute to improving the prediction accuracy of particle transport codes.

Reference

Tada, K. et al., Development and Verification of a New Nuclear Data Processing System FRENDY, Journal of Nuclear Science and Technology, vol.54, issue 7, 2017, p.806-817.

4-6 Research on the Material-Degradation Behavior by Radiolytic-Hydrogen Absorption — Hydrogen-Absorption Behavior on Zirconium under γ -ray Irradiation —

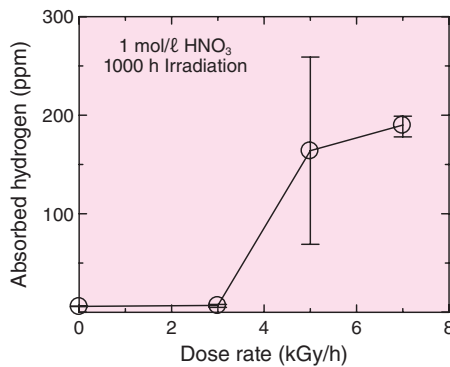


Fig.4-12 Effect of dose rate upon hydrogen absorption for Zr

Hydrogen absorption increased with γ -ray dose rate.

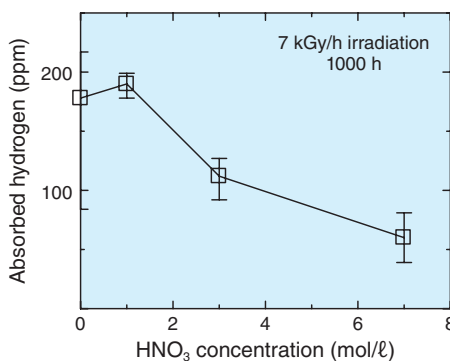


Fig.4-13 Effect of HNO₃ concentration upon hydrogen absorption for Zr

Hydrogen absorption decreased with HNO₃ concentration.

In spent-nuclear-fuel-reprocessing plants, high-concentration nitric-acid solutions (HNO₃) at high temperature are used to dissolve spent fuel. Because zirconium (Zr) has excellent corrosion resistance in such an environment, it has been used as a structural material in spent-nuclear-fuel-reprocessing equipment.

On the other hand, it is known that Zr can easily absorb hydrogen and then become brittle. Additionally, so-called radiolytic hydrogen is generated from the reprocessing solutions under irradiation.

Therefore, it is important to understand radiolytic-hydrogen-absorption behavior to predict plant-equipment deterioration. However, there is no information on the radiolytic-hydrogen-absorption behavior on Zr in HNO₃. Moreover, the present state of the absorbed hydrogen in Zr is not clear.

To elucidate radiolytic-hydrogen-absorption behavior on Zr in HNO₃, we conducted an immersion test for Zr in HNO₃ with Co-60 γ -ray irradiation for up to 1000 h.

After an immersion test, the average hydrogen concentration in Zr was increased up to 40 times (Fig.4-12). Additionally, the average hydrogen concentration decreased with the concentration of nitric-acid solutions after immersion

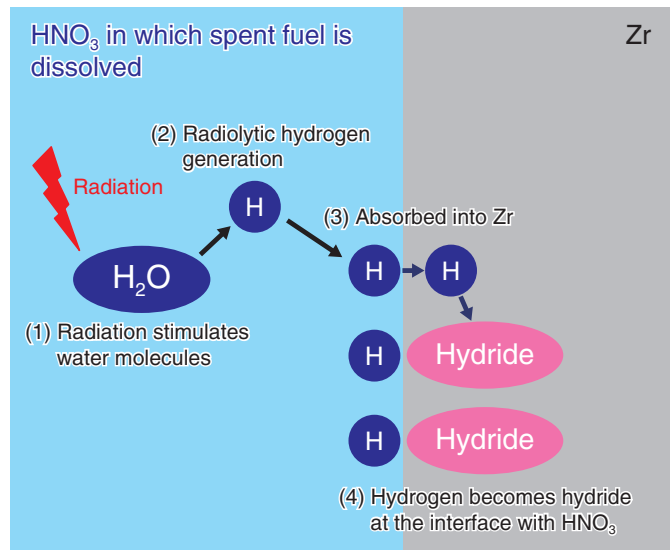


Fig.4-14 Schematic view of radiolytic hydrogen-absorption behavior

From this research result, we clarified that absorbed radiolytic hydrogen becomes hydrides in Zr on the Zr surface in contact with HNO₃.

tests (Fig.4-13).

From the measurement results of hydrogen-penetration depth in Zr following immersion tests, concentrations of hydrogen on the Zr surfaces in contact with HNO₃ were observed. The results of crystalline analysis showed that the hydrogen presented as hydride in Zr.

These results show that the absorbed hydrogen quickly becomes hydride because Zr easily generates hydride. It also suggests that the absorbed hydrogen must pass through the hydride layer before Zr metal after the hydride has been formed.

In this research, we elucidated the fact that Zr can absorb radiolytic hydrogen in HNO₃ and clarified that the distribution and morphology of the absorbed hydrogen (Fig.4-14).

These new findings can be used to estimate hydrogen absorption and predict hydrogen embrittlement in long-term operation of reprocessing plants. We intend to contribute to securing the structural integrity of reprocessing plants through our research activities.

The present study was sponsored by the Nuclear Regulation Authority (NRA), Japan.

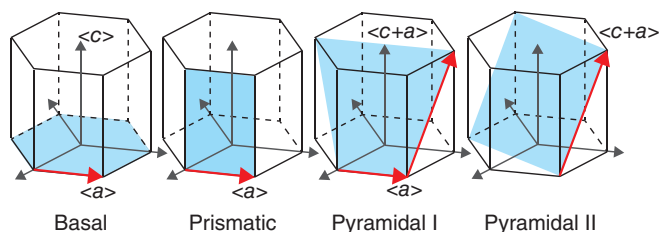
Reference

Ishijima, Y. et al., Hydrogen Absorption Behavior on Zirconium under γ -Radiolysis of Nitric Acid Solution, Nippon Genshiryoku Gakkai Wabun Ronbunshi (Transactions of the Atomic Energy Society of Japan), vol.16, no.2, 2017, p.100-106 (in Japanese).

4-7 Predicting Mechanical Properties of Alloys

— Computational Approach for Modeling the Strengthening/Softening Mechanism —

(a) Slip system in HCP metals



(b) Stacking-fault energy

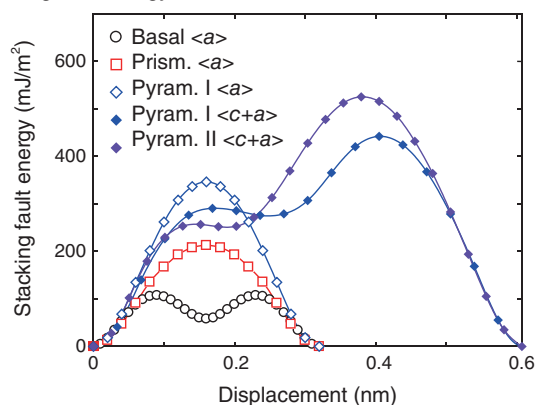


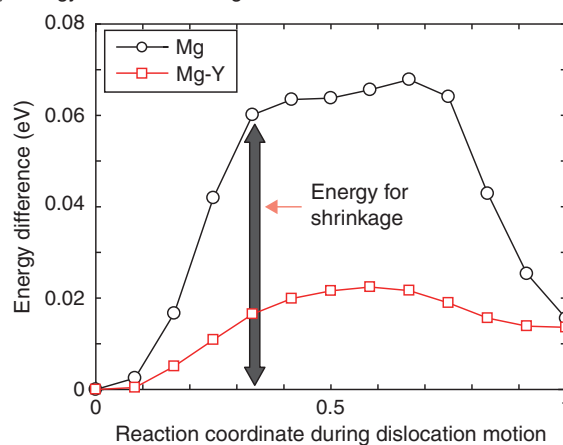
Fig.4-15 Crystallographic structure of HCP metals: (a) slip plane and (b) stacking-fault energy

HCP metals have various slip planes. Potential slip directions are shown by red arrows for each plane. The energy differences, defined as stacking-fault energies, are shown in (b). Basal slip is expected to be the primary slip system.

Hexagonal close-packed (HCP) metals such as magnesium (Mg), titanium (Ti), and zirconium (Zr) exhibit excellent material properties including a lightweight structure, heat resistance, and corrosion resistance. Widespread application, however, has been limited because of a key weakness stemming from their HCP crystal structure. Unlike iron or aluminum, HCP metals have various slip planes, causing anisotropic plastic deformation. This makes it more important to improve the formability through plastic working. Solution strengthening is a well-known approach to tailoring the mechanical properties of structural alloys. Ultimately, the properties of the dislocation/solute interaction are rooted in the electronic structure of the alloy. A computational approach to predicting the effect of alloying upon mechanical properties plays a crucial role in non-empirical alloy design.

Here, we introduce an electronic-structure-based approach to understand the dislocation-solute interaction. Fig.4-15 shows possible slip planes in HCP metals and energy difference along

(a) Energy difference during dislocation motion



(b) Dislocation-core structures

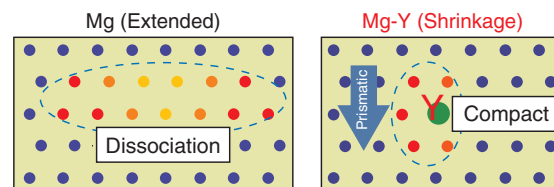


Fig.4-16 Effect of alloying elements upon dislocation motion

(a) Energy difference during the motion of dislocations in the prismatic plane and (b) dislocation-core structures in pure Mg and Mg-Y alloys. The energy barrier for prismatic slip is reduced by the Y solution due to the strong electronic interaction.

a red arrow. The energy difference is defined as a stacking-fault energy that determines the dislocation-core structure and motion. Fig.4-15(b) shows that energy along $\langle a \rangle$ in the basal plane is extremely low, while those values in the non-basal planes are high. Reducing energy difference in the prismatic plane is a potential approach to improving plastic anisotropy.

Subsequently, we have constructed a dislocation-quadrupole model in a periodic cell and evaluated energy difference during motion in the prismatic plane, as shown in Fig.4-16(a). yttrium (Y) solute definitely reduces the energy barrier for dislocation motion in the prismatic plane. The transition states of dislocation-core structure during the motion are shown in Fig.4-16(b). Interestingly, the dissociated dislocation in pure Mg tends to shrink due to the strong electronic interaction with Y, which promotes dislocation motion on non-basal planes and reduces plastic anisotropy. Computational models based on atomistic simulations are expected to be an effective approach for new-alloy design.

Reference

Tsuru, T. et al., Effect of Solute Atoms on Dislocation Motion in Mg: An Electronic Structure Perspective, Scientific Reports, vol.5, 2015, p.8793-1-8793-8.

4-8 Quantitation of the Difficult-to-Measure Nuclide Palladium-107

— Measurement of Palladium Obtained by Laser Irradiation of Spent Nuclear Fuel —

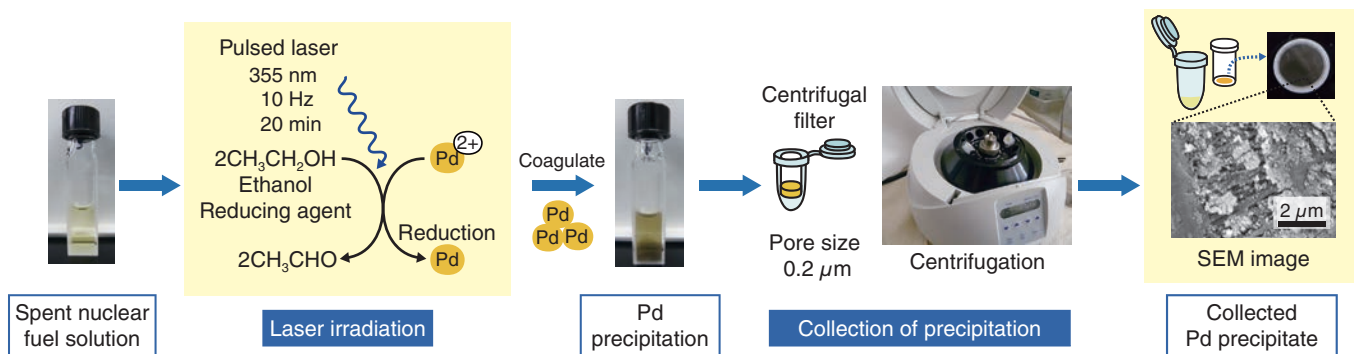


Fig.4-17 Separation mechanism of high-purity Pd by laser irradiation and its operating procedure

Laser irradiation induces reduction of a Pd ion, changing it from a divalent cation (Pd^{2+}) to a non-charged form. The reduced Pd atoms coagulate with each other to form a precipitate, allowing Pd to be easily recovered. This technique enables operators to maintain a safe distance from highly radioactive samples, leading to minimum radiation exposure.

Table 4-3 Contamination rates of major constituents of spent nuclear fuel in Pd precipitate

Almost no elements that initially existed in the spent nuclear-fuel sample were found in the Pd precipitate prepared by laser irradiation. Accurate quantitation of ^{107}Pd can only be achieved with such high-purity Pd.

Element	Sr	Cs	Ba	Ru	Rh	U	Np	Pu	Am
Contamination (%) [*]	<0.001	<0.001	0.001	<0.001	<0.001	0.004	<0.001	<0.001	<0.001

^{*}Contamination (%) = (Weight of element found in Pd precipitate) / (Weight of Pd precipitate) × 100

Palladium-107 (^{107}Pd), which is one of the radionuclides generated by nuclear fission of uranium, is found in spent nuclear fuel. Due to its extremely long half-life of about 6.5×10^6 years, ^{107}Pd can be potentially harmful to human body over a long period of time. The long-term risks involved in ^{107}Pd radiation are basically estimated based on the ^{107}Pd content in spent nuclear fuel. However, predicted values provided through theoretical calculation have been used instead of the measured content of ^{107}Pd because of the lack of published information concerning ^{107}Pd quantitation.

Accurate measurement of ^{107}Pd can only be achieved by a separation technique which allows recovery of high-purity Pd from spent nuclear fuel. Chromatographic separation using adsorbent-packed columns, which is the most commonly applied technique, is inevitably associated with numerous operational steps, making it hard to complete the separation in a short time. Additionally, continuous work with highly radioactive samples, such as a spent nuclear-fuel solution, causes undesirable radiation exposure to workers.

The separation technique developed in this study enables selective recovery of Pd by a simple operation, leading to the world's first successful quantitation of ^{107}Pd in spent nuclear

fuel. Precipitation of Pd is induced by irradiation by a pulsed laser of wavelength 355 nm (Fig.4-17). The precipitation reaction is completed in 20 minutes in a closed vessel and operators can keep their distance from a sample during irradiation. This can help minimize the contamination of laboratory facilities and radiation exposure to workers during irradiation.

The resulting Pd precipitate was dissolved with aqua regia (a mixture of nitric acid and hydrochloric acids) and measured by inductively coupled plasma-mass spectrometry. Almost none of the elements initially present were detected in the precipitate (Table 4-3) and Pd was recovered with a purity above 99.9%. With the perfect removal of all interfering components, ^{107}Pd in spent nuclear fuel was accurately measured.

Application of the developed technique to other samples, for example, high-level radioactive waste (HLW), is expected. We are trying to expand the versatility of our technique for application to HLW, which has a complicated chemical composition. We will make continuous efforts to establish highly reliable safety assessment of HLW disposal by offering accurate measurements of ^{107}Pd .

Reference

Asai, S. et al., Determination of ^{107}Pd in Pd Recovered by Laser-Induced Photoreduction with Inductively Coupled Plasma Mass Spectrometry, Analytical Chemistry, vol.88, issue 24, 2016, p.12227-12233.

4-9 Forecast of Radionuclide Dispersion in the Ocean

— Development of an Emergency-Assessment System for Marine-Environmental Radioactivity —

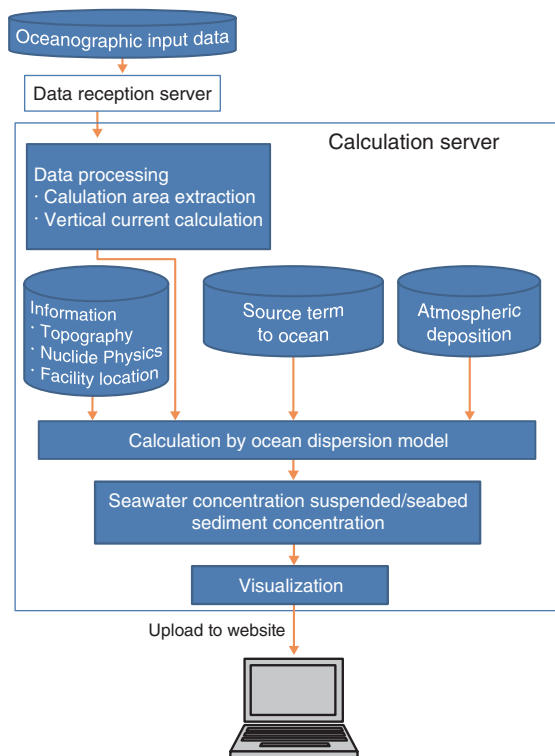


Fig.4-18 System configuration and processing flow

It takes about 3 hours to receive the online forecast data on oceanic-flow fields from the Japan Meteorological Agency, execute prediction calculations up to 30 days using the ocean-dispersion model, and visualize the calculation results.

If radioactive substances are released into the environment due to an accident at a nuclear facility, they can enter the ocean via the atmosphere or land, causing marine pollution. Ascertaining the pollution situation of the marine environment and considering emergency measures is important not only for Japan, but all across East Asia, where the number of nuclear-power plants has recently increased.

Taking this situation into consideration, we have developed the Short-Term Emergency-Assessment system of Marine-Environmental Radioactivity (STEAMER) to immediately predict the radionuclide concentration around Japan in the case of a nuclear accident (Fig.4-18). STEAMER forecasts the radionuclide concentration in the ocean and sea-bottom sediment for 30 days using an ocean-dispersion model developed by JAEA based on online forecast data for oceanic flow fields from the Japan Meteorological Agency and information concerning radionuclide-release into the ocean. It is possible to estimate the distribution of radionuclides after

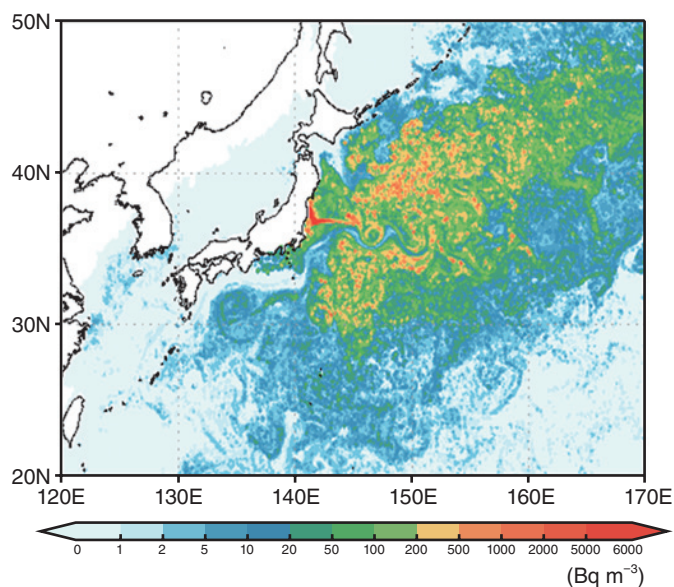


Fig.4-19 Exemplary calculation of radionuclide dispersion in the ocean due to the accident at the TEPCO's Fukushima Daiichi NPS (1F)

Calculation results of the sea-surface concentration of Cs-137. Results show that airborne Cs-137 mainly spread northeastward, whereas Cs-137 was released directly from 1F into the ocean and transported eastward.

release from nuclear sites in East Asian countries including Japan and any sea region around Japan. Coupling STEAMER with an emergency-atmospheric-dispersion-prediction system, such as the Worldwide version of the System for Prediction of Environmental Emergency Dose Information (WSPEEDI) enables comprehensive environmental-pollution predictions both in the air and the ocean (Fig.4-19). The stability and robustness of the system has been validated by test operation since September 2014.

It is possible to use STEAMER for the design of oceanic-emergency countermeasures against nuclear accidents and detailed post-accident assessment, such as setting up an emergency-ocean-monitoring area based on the predicted pollution distribution, estimating the source term of oceanic release from a facility through reverse analysis of ocean-monitoring data, and prohibiting fishing and sailing based on detailed assessment.

Reference

Kobayashi, T. et al., Development of a Short-Term Emergency Assessment System of the Marine Environmental Radioactivity around Japan, Journal of Nuclear Science and Technology, vol.54, issue 5, 2017, p.609-616.

4-10 Development of Neutron Calibration Fields for Improving the Reliability of Neutron-Dose Estimation

— Moderated Neutron Calibration Fields Considering Energy Distributions in Actual Workplaces —

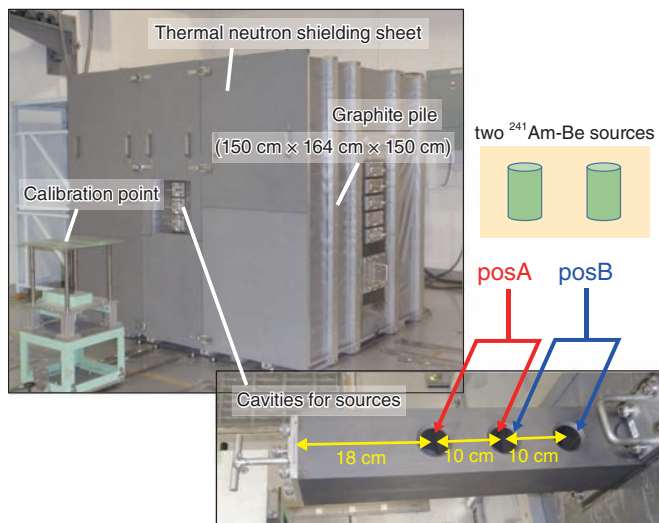


Fig.4-20 Overview of the graphite-moderated neutron calibration fields

Neutrons released from $^{241}\text{Am-Be}$ RI sources are moderated by elastic scattering in the graphite pile and emitted from the surface of the pile with various energies. The neutron energy distribution of the field is variable under changes of the positions of two $^{241}\text{Am-Be}$ sources (posA and posB).

In facilities such as nuclear reactors or accelerators where neutron radiation is frequently used, neutron survey meters and personal dosimeters are widely used for radiation protection for workers. Neutron dosimeters are generally calibrated in the field produced by ^{252}Cf or $^{241}\text{Am-Be}$ radioisotope (RI) neutron sources at regular intervals. However, neutron energy distributions produced from RI sources are localized around an energy range of a few MeV, and differ significantly from those observed in actual workplaces in most cases. Therefore, dosimeters often over- or underestimate neutron dose in the workplace because their response strongly depends on the energy distribution of the neutron field to be measured. To solve this problem, moderated neutron calibration fields that simulate the neutron energy distribution in actual workplaces by combining neutron sources and appropriate moderators are required. A more reliable evaluation of neutron dose in workplaces is possible using neutron dosimeters calibrated in fields whose neutron energy distribution is similar to that in workplaces.

At JAEA's Facility of Radiation Standards (FRS), we have developed novel neutron calibration fields using a graphite moderator and $^{241}\text{Am-Be}$ sources (Fig.4-20). The graphite pile is also used for the thermal-neutron calibration field in FRS. While a ^{252}Cf source is installed in the cavity at the center of the pile for the thermal-neutron field, two $^{241}\text{Am-Be}$ neutron sources are installed in cavities located at the shallower position

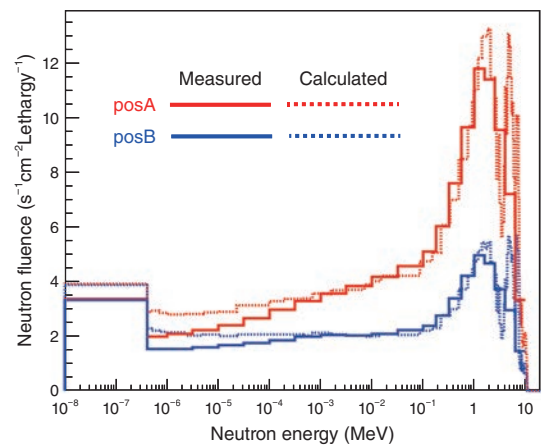


Fig.4-21 Neutron energy distributions at the calibration point

Neutron energy distributions at the calibration point were evaluated with Monte-Carlo calculations and measurements using a neutron spectrometer. Continuous-energy distributions from thermal-neutron energy to several MeV, with fluence-averaged energies of 0.84 MeV (posA) and 0.60 MeV (posB), were given.

inside the graphite pile for moderated neutron fields, so as to yield epi-thermal neutrons (1 eV to a few 100 keV) which are not yet thermalized. The neutron energy distribution is variable by changing the positions of two neutron sources (posA and posB, as in Fig.4-20). Furthermore, the thermal neutron-shielding sheet including gadolinium is put on the surface of the graphite pile to decrease the number of thermal neutrons at the calibration point.

The neutron energy distributions of the fields were evaluated by Monte-Carlo calculations and measurements using a neutron spectrometer, as shown in Fig.4-21. As seen at workplaces in nuclear reactors or fuel-reprocessing facilities, continuous-energy distributions were given over a wide energy range from thermal- neutron energy to several MeV. The fluence-averaged energies were given as 0.84 MeV for posA and 0.60 MeV for posB. The reference ambient-dose-equivalent rate $H^*(10)$ and personal-dose-equivalent rate $H_p(10)$ were determined based on measurement of the neutron energy distribution. The given dose-equivalent rates, 20–50 $\mu\text{Sv/h}$, were confirmed to be sufficient for calibration of neutron dosimeters.

Currently, new moderated neutron calibration fields are available for calibration of neutron dosimeters or performance testing of neutron-measuring instruments, as well as for external users in the framework of shared use of JAEA facilities.

Reference

Nishino, S. et al., Development of the Graphite-Moderated Neutron Calibration Fields using $^{241}\text{Am-Be}$ Sources in JAEA-FRS, Journal of Radiation Protection and Research, vol.41, no.3, 2016, p.211-215.

Contributing to Developments in Science and Technology, and Academic Research using Neutron and Synchrotron Radiation

In accordance with the *Science and Technology Basic Plan* formulated by the Government of Japan, we aim to contribute to the advance of science and technology and the promotion of industry in Japan through the production of innovative results using neutron and synchrotron radiation. We are making use of the high-intensity proton accelerator at the Japan Proton Accelerator Research Complex (J-PARC) and the JAEA synchrotron-radiation beamlines at Super Photon ring-8 GeV (SPring-8), upgrading neutron facilities and devices, and pursuing world-leading research in fields such as nuclear energy and materials sciences utilizing neutron and synchrotron radiation.

(1) Research and development at J-PARC

J-PARC comprises a series of three proton accelerators, namely a linear accelerator (LINAC), a 3-GeV rapid-cycling synchrotron (RCS), and a 50-GeV synchrotron, as well as three experimental facilities. The facilities include the Materials and Life Science Experimental Facility (MLF) for a wide range of research fields using neutron and/or muon beams, the Hadron Experimental Facility for nuclear and particle-physics experiments using K-mesons and other particles, and the Neutrino Experimental Facility for the T2K-particle physics experiments using neutrinos. All these experimental facilities are open to users from across the globe.

In FY2016 at the MLF, the user program for seven scheduled run cycles (154 days) was successfully accomplished at 150–200 kW with an availability over 90%. Both the experimental programs and international programs for training future researchers (such as the Neutron & Muon School) were conducted at 19 neutron instruments and 2 muon beamlines. At the RADEN neutron instrument (Fig.5-1), the two-dimensional distribution of microstructure in a steel sample was quantitatively visualized by analyzing the data obtained with a time-of-flight neutron Bragg-edge transmission-imaging technique. The experimental result was in good agreement with those obtained by neutron and electron-backscatter diffraction, yielding better quality than that obtained via conventional neutron radiography. In this chapter, the following two outcomes from MLF are introduced: (1) successful magnetic-structure analysis of a material containing rare-earth elements with strong neutron absorption in combination with a single-crystal neutron-diffraction measurement conducted at the neutron instrument SENJU (Fig.5-1) (Topic 5-1) and (2) determining the applicability of polarized-neutron scattering under grazing-incidence geometry for studying magnetic properties of layered systems (Topic 5-2).

At the accelerators, successive tests and component

improvements were conducted to realize stable operation with a 1-MW beam. At the LINAC, the ion source achieved stable operation with an extraction-beam current of 40 mA for approximately 1350 h. At the 3-GeV RCS, the cause of beam instability preventing a high-output intensity was investigated through numerical analyses and accelerator studies, demonstrating that beam stabilization in the latter half of the acceleration period was important (Topic 5-3).

(2) Applied neutron and synchrotron-radiation research and development

The Materials Sciences Research Center aims to create innovative results and seed research in a wide range of scientific, technological, and academic fields by developing and improving applied neutron and synchrotron-radiation tools for advanced structural and functional analysis.

In FY2016, we have developed the world's fastest neutron-diffraction texture-measurement method at iMATERIA at the J-PARC MLF (Fig.5-1) for neutron sciences (Topic 5-4). This result is expected to contribute to research and development leading to lighter-weight automobiles. The nanoscopic structure of hydrogel nanoparticles expected to be used as carriers to deliver drugs into the body was revealed by a small-angle neutron-scattering method (Topic 5-5). In synchrotron-radiation sciences, we have studied the stainless steel SUS304 with excellent mechanical properties using SPring-8 high-intensity synchrotron radiation to discover a new nanosized crystalline phase (Topic 5-6). The results of this research are expected to lead to elucidation of the mechanism of embrittlement of stainless steel by hydrogen in the future. We applied soft X-ray angle-resolved photoelectron spectroscopy (Fig.5-2) to uranium compounds coexisting with magnetism and superconductivity and clarified the electronic state of matter (Topic 5-7). This is expected to be useful for future material development.

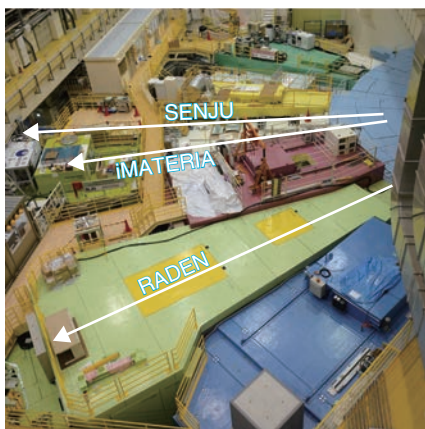


Fig.5-1 Neutron instruments in experimental hall No.2 of MLF
The outcomes of the three neutron instruments indicated by white lines are introduced in this section.

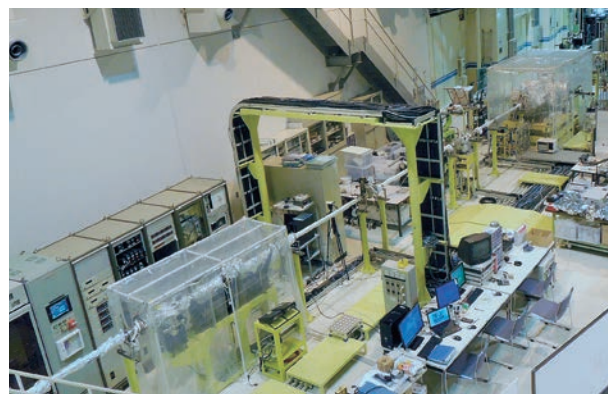


Fig.5-2 SPring-8 BL23SU used in Topic 5-7
BL23SU is a soft X-ray beam line utilized in research on applications to surface chemistry, biophysical spectroscopy, and solid-state physics.

5-1 Magnetic-Structure Analysis of a Highly Neutron-Absorbent Material with Pulsed-Neutron Diffraction — Magnetic Structure of EuGa_4 Studied by Single-Crystal Neutron Diffraction —

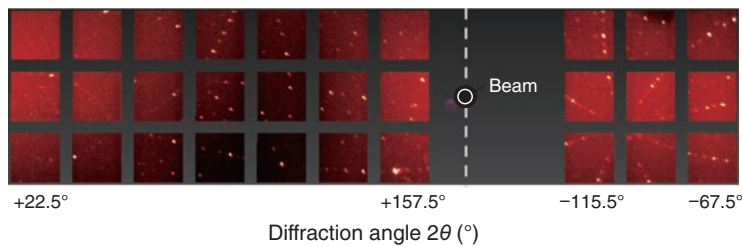


Fig.5-3 Neutron-diffraction pattern from an EuGa_4 single crystal
Diffraction spots were observed clearly though the shadow due to the high neutron-absorption ratio of Eu.

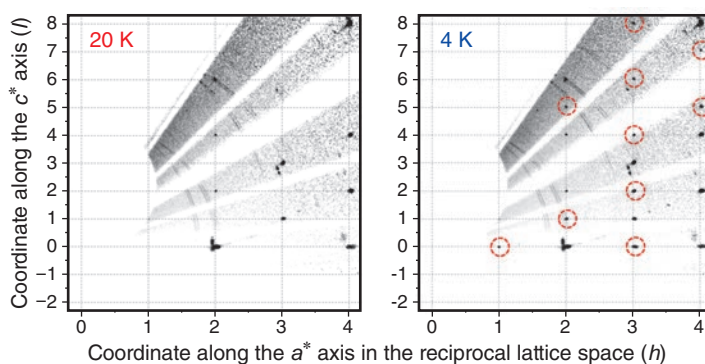


Fig.5-4 Neutron-diffraction intensities on particular planes at 20 K and 4 K
Magnetic reflections (red-dotted circles) were observed below 16 K, which is the magnetic-transition temperature.

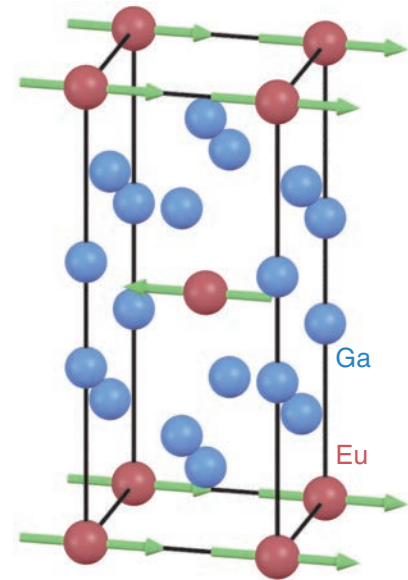


Fig.5-5 Crystal and magnetic structures of EuGa_4 at 4 K based on analysis of pulsed-neutron-diffraction data
Eu atoms, Ga atoms, and magnetic moments are shown by red circles, blue circles, and green arrows, respectively.

Magnetic-structure analysis by single-crystal neutron diffraction is an essential tool for studying the magnetic properties of materials. However, analysis of materials containing rare-earth elements such as Europium (Eu), Samarium (Sm), and Gadolinium (Gd) is not easy. As these elements show extremely high neutron absorption and non-monotonic neutron-energy dependence of absorption, the correct diffraction intensity cannot be obtained directly from the measured data. A correction method for such data is required.

In the present study, we developed an absorption-correction method for the single-crystal neutron-diffraction data from materials with high and complicated neutron absorption. By adopting this method for analyzing the high-quality neutron-diffraction data measured using the Extreme Environment Single Crystal Neutron Diffractometer SENJU, the magnetic structure of EuGa_4 was successfully obtained.

Fig.5-3 shows the diffraction pattern from the EuGa_4 single crystal measured by the detectors of SENJU. Although a shadow appeared due to the high neutron absorptivity of the sample, each diffraction spot was clearly observed. In general,

the arrangements of the atoms and spins in materials can be obtained from the intensities of the spots. However, in the present case, the intensities extracted from the data must be corrected to suppress the effect of absorption before quantitative analysis of the structures. Therefore, an intensity correction based on the neutron-energy dependence of absorption for elements in the nuclear database was adopted for this analysis. The positions of the diffraction spots are as important as their intensities. Fig.5-4 shows the intensity distribution in the particular plane that reflects the tetragonal crystal lattice of EuGa_4 . The possible spin arrangements can be estimated from the positions of the spots appearing below 16 K, the ordering temperature of the spins in EuGa_4 . From these data, we conclude that the spins in EuGa_4 are arranged alternately, as shown in Fig.5-5, and that the magnitude of the magnetic moment is ideal for divalent Eu.

We will develop the present analytical method of neutron-diffraction data more extensively, together with instruments for understanding the structure and properties of rare-earth compounds.

Reference

Kawasaki, T. et al., Magnetic Structure of Divalent Europium Compound EuGa_4 Studied by Single-Crystal Time-of-Flight Neutron Diffraction, Journal of the Physical Society of Japan, vol.85, no.11, 2016, p.114711-1-114711-5.

5-2 Towards a Comprehensive Understanding of the Unique Magnetic Properties of Layered Systems

— An Application of Polarized Neutron Scattering under Grazing-Incidence Geometry to Analysis of In-Plane Magnetic Structure —

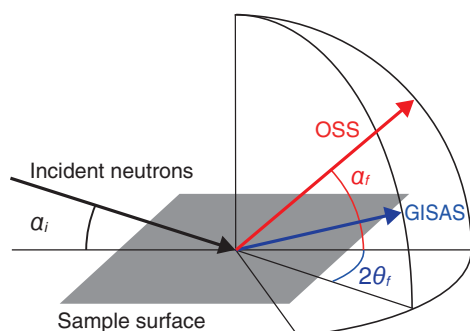


Fig.5-6 Scattering geometry of polarized neutron off-specular scattering (OSS) and grazing-incidence small-angle scattering (GISAS) measurements

The OSS measures the intensity dependence on the exit angle α_f , whereas GISAS is performed at an angle of $2\theta_i$. The data analysis provides the in-plane correlation length. Since the accessible length scale differs between them, the accuracy of the obtained parameter can be improved by the complementary measurements of the OSS and GISAS.

Layered magnetic structures exhibit interesting and important magnetic properties such as exchange coupling between layers, giant magnetoresistance, and tunnel magnetoresistance, none of which are present in the bulk. These anomalous magnetic properties basically arise from the size of the structure in the out-of-plane and/or in-plane directions reduced to the nm range. It is not possible to obtain information on the size of the structure and orientation of spins in magnetic multilayers through direct observation of the surface, although it is important to elucidate the mechanism and to offer the possibility of new applications.

Polarized neutron scattering under a grazing-incidence geometry (Fig.5-6) is a unique and non-destructive technique for observing the correlations of small magnetic objects in a layered system. It is expected to clarify the mechanism behind the magnetic properties mentioned above. In order to demonstrate this, polarized neutron off-specular scattering (OSS) and grazing-incidence small-angle scattering (GISAS) measurements were performed for the Fe/Si multilayers used for the spin-polarization of a neutron beam. The measurement was performed on the D17 polarized neutron reflectometer and the D33 small-angle diffractometer at the high-flux reactor in the Institut Laue Langevin. Soft magnetic properties play a critical role in determining the performance of the neutron polarizing multilayers as they need to display high polarization efficiencies under low external magnetic fields to meet a variety of research demands. The magnetic layers fabricated using the sputtering technique are nanocrystalline with a size less than the ferromagnetic exchange length (≈ 20 nm) where the exchange interaction between neighboring spins becomes dominant over the local anisotropies of randomly oriented grains. Hence, it should be possible to explain its magnetic behavior, which differs from that of the bulk, using the random anisotropy model.

Reference

Maruyama, R. et al., Study of the In-Plane Magnetic Structure of a Layered System using Polarized Neutron Scattering under Grazing Incidence Geometry, Nuclear Instruments and Methods in Physics Research A, vol.819, 2016, p.37-53.

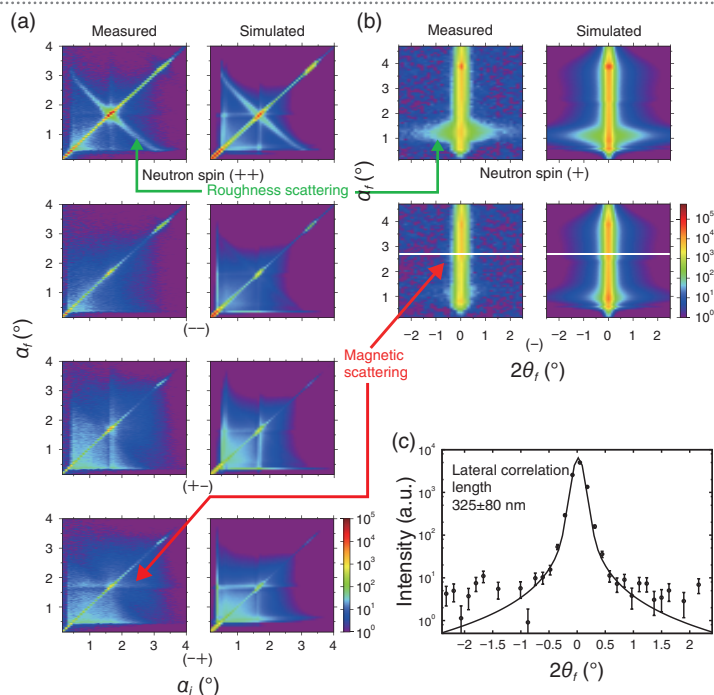


Fig.5-7 Polarized neutron scattering images of the Fe/Si multilayer of 30 bilayers with a thickness of 10 nm

(a) OSS and (b) GISAS images and (c) intensity profiles along the white lines of the GISAS image.

The OSS and GISAS data, shown in Figs.5-7(a) and 5-7(b), provide complementary information on the lengths of areas where the spins are aligned to the same direction, since the accessible length scales of the in-plane structures differ between them. The measured data were analyzed by the simulation according to the framework of the distorted wave Born approximation (DWBA), where the scattering due to the in-plane magnetic structure is assumed to be a small perturbation of the reflection and refraction occurring at the multilayer interfaces. Analysis with the DWBA reasonably explains the measured data. The obtained lateral correlation lengths corresponding to half the length of the area with a uniform orientation of the spins were determined by comparison of the measured profile with the simulated one (Fig.5-7(c)).

This study demonstrated that complementary measurements with the OSS and GISAS are suitable for investigating the in-plane structure of layered systems with a length scale ranging from nm to μm . The obtained lateral correlation length was much larger than the in-plane grain size. This shows that the exchange interaction gives rise to the formation of areas comprising a large number of grains, where the spins are aligned to the same direction. Hence, the obtained result is in good agreement with the random anisotropy model. This model predicts that reduction in grain size and uniform uniaxial anisotropy will result in soft magnetic properties. This allows the possibility of further improvement to the Fe/Si multilayer as a neutron polarization device. Polarized neutron scattering under a grazing-incidence geometry is expected to be a powerful tool not only for basic research related to the unique magnetic properties of layered systems, but also for industrial developments such as magnetic data-storage devices of which the areal density is becoming ever higher.

5-3 Realization of High-Intensity Proton Beams

— Beam-Instability Issues and the Measure at the 3-GeV RCS in J-PARC —

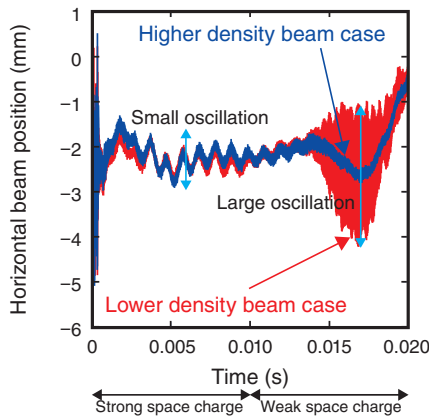


Fig.5-8 Measurement results of beam positions at the RCS
A bunch compression of only 2% makes an unstable beam (red) into a stabilized one (blue) by increasing the beam-current density.

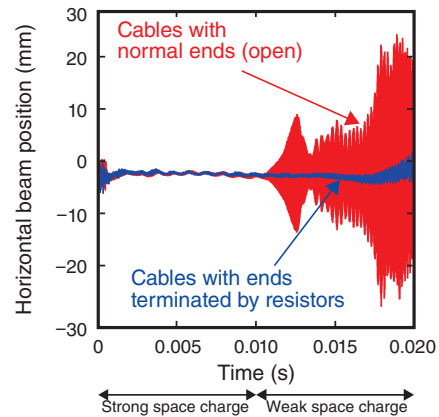


Fig.5-10 Dependence of beam positions upon terminal conditions
Termination of the cables' ends with resistors improves the unstable beam (red) into a stabilized one (blue).

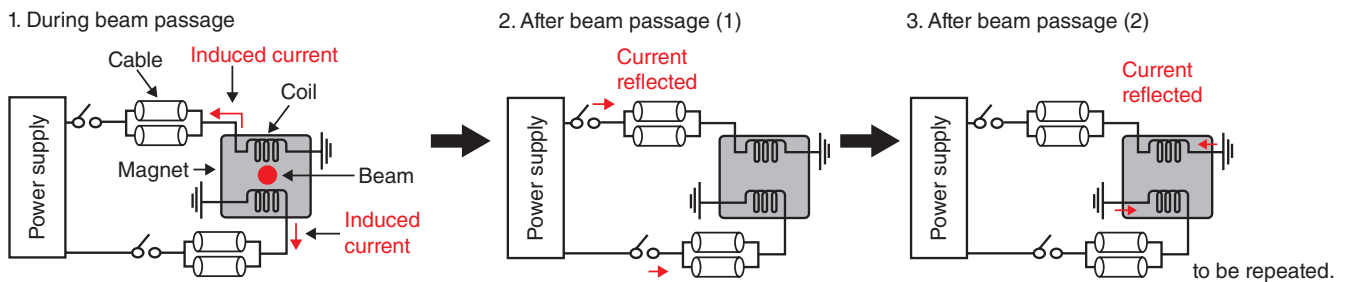


Fig.5-9 Schematic of beam-induced currents after a beam passes through the kicker magnet
Beam-induced currents are superposed every time the beams pass through the kicker, because the power supply is switched off during the ramping time.

Over the past decades, the power frontier of proton accelerators has been advanced up to the 1-MW level; such high-intensity beams largely tend to oscillate transversely, making it quite difficult to accelerate the beam. This is the so called beam-instability issues; such instabilities are excited by the interaction between the beam and the chamber walls, or the devices in synchrotrons. Recently, we have developed two new beam-stabilization schemes against beam-instabilities.

Fig.5-8 shows measurement results for the 750-kW beam at the 3-GeV Rapid Cycling Synchrotron (RCS) in J-PARC. The oscillation after 0.010 s on the red line represents the beam instability.

The RCS is equipped with kicker magnets, which extract the 3-GeV beam by exciting a pulsed magnetic field with a 300 ns rising time. The magnets are installed in vacuum, and so tend to make the beam unstable during the ramping time. We have developed a new theory, and predicted that the beam-induced current on the kicker cables should be the dominant source of beam instability (Fig.5-9). Accordingly, we have demonstrated

stabilization of the unstable beam by terminating the ends of the kicker cables with resistors, i.e., by suppressing the beam-induced currents (Fig.5-10). Furthermore, we have successfully stabilized the beam instability by avoiding the resonance condition between the beam-oscillation frequency and the reciprocating frequency of the beam-induced current in the cables, without modification of the kicker cables' ends.

Our theory also predicts that the higher-energy beams tend to be unstable, due to mitigation of the space-charge-damping effect. As indicated by the red lines in Figs.5-8 and 5-10, the beam instability occurs at high energy, as expected. Finally, we successfully stabilize the high-intensity beam even after a ramping time of 0.010 s by compressing the beam length, i.e., by enhancing the space-charge-damping effects (the blue line of Fig.5-8).

These new schemes play an important role in establishing the beam-operation parameters toward the realization of a 1-MW-output beam power at the RCS.

Reference

Shobuda, Y. et al., Theoretical Elucidation of Space Charge Effects on the Coupled-Bunch Instability at the 3 GeV Rapid Cycling Synchrotron at the Japan Proton Accelerator Research Complex, Progress of Theoretical and Experimental Physics, vol.2017, issue 1, 2017, p.013G01-1-013G01-39.

5-4 Exploring the Structural Materials Frontier using Neutron Diffraction

— Development of the Bulk Texture Measurement Technique at the Rapidest Level —

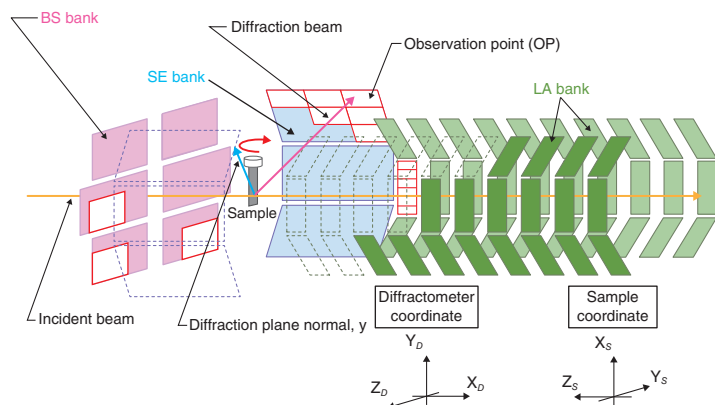


Fig.5-11 Schematic illustration of texture measurement at iMATERIA

Neutron observation points (red frame) are divided from various neutron detectors (color squares), where the neutron diffraction patterns are collected independently. BS bank: back scattering banks; SE bank: sample environmental banks; LA bank: low angle banks.

Metallic material composed of fine crystal grains with various orientations usually possesses some specific orientation distribution deviating from the random distribution of a powder sample, due to the plastic deformation and/or heat treatment. The deviation extents and distribution densities (i.e., texture) have an evident influence upon the mechanical strength and plastic deformation of engineering materials. Therefore, precise and reliable texture measurement is essential for the development of high-value materials for many specific purposes, and rapid texture measurement instruments and related analytical techniques are required.

Conventional X-ray diffraction texture measurement only involves local information about materials near the surface within a depth of several tens of micrometers; the bulk textures related to macroscopic mechanical properties are not easy to obtain. Thanks to the high penetrability of neutrons, much more extensive bulk-texture measurements are becoming available through simple neutron experiments for reliable prediction of bulk mechanical properties.

During the angle-dispersive neutron diffraction texture measurement using a monochromatic neutron source, the diffracted neutrons towards numerous stereographic orientations are measured by a neutron detector with small angular coverage, such that at least several hundred sample rotations are necessary over a long period to collect enough information for texture calculation.

During time-of-flight neutron diffraction, the polychromatic neutrons can be recorded sensitively according to different wavelengths through monitoring their arrival times from the neutron source through the sample to various neutron observation points, such that the corresponding time-of-flight

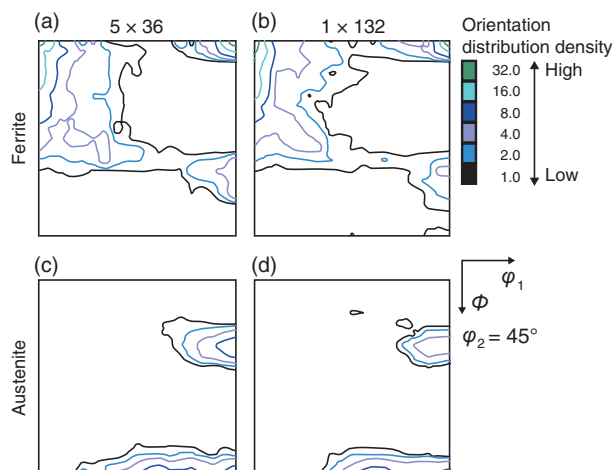


Fig.5-12 $\phi_2 = 45^\circ$ sections of orientation distribution functions (ODF (ϕ_1, ϕ, ϕ_2)) of ferrite and austenite

(a) & (c): using a conventional method with 36 observation points through five sample rotations; (b) & (d): using 132 observation points without any sample rotation. The obtained austenite and ferrite ODFs are consistent in two cases.

neutron diffraction pattern can be obtained. For the IBARAKI Materials Design Diffractometer (iMATERIA, Fig.5-11) at the Japan Proton Accelerator Research Complex (J-PARC), there are 132 observation points for collecting neutron-diffraction patterns independently. Through simultaneous Rietveld texture analysis of 132 diffraction patterns with the Materials Analysis Using Diffraction (MAUD) software, both the bulk averaged texture and the phase volume fractions of materials can be determined by a simple irradiation without any sample rotation. For the austenite-ferrite duplex stainless steel sheet, it is difficult to determine the precise phase fraction using X-ray diffraction because of strong texture. At iMATERIA, 10 minutes is sufficient for simple radiation of the above steel sample, and its phase fraction and bulk textures were determined simultaneously; this represents the rapidest measurement level ever achieved in the world (Fig.5-12).

Considering that the neutron beam flux at J-PARC is increasing, the measurement time for bulk textures per sample may decline to less than 1 minute in the near future. Therefore, iMATERIA has become a powerful neutron diffractometer for frontier materials R&D activities. For example, its rapid texture measurement is expected to enable it to monitor real-time change in bulk textures and phase volume fractions during rapid plastic deformation and/or rapid heating of engineering materials. This technology is also expected to be useful in texture-optimization researches of advanced electromagnetic steel sheets for high performance electric motors, and next-generation ultrahigh strength multiphase steel sheets for automobile body lightening.

This research was accomplished as a collaborative study among Ibaraki University, Ibaraki Prefectural Government, Japan Atomic Energy Agency and Nippon Yakin Kogyo Co., Ltd.

Reference

Onuki, Y., Xu, P. G. et al., Rapid Measurement Scheme for Texture in Cubic Metallic Materials using Time-of-Flight Neutron Diffraction at iMATERIA, Journal of Applied Crystallography, vol.49, part 5, 2016, p.1579-1584.

5-5 Nanoscopic-Structural Investigation of Nanoparticles for Drug-Delivery Carriers

— Small-Angle Neutron Scattering Reveals the Internal Structure of Nanogels —

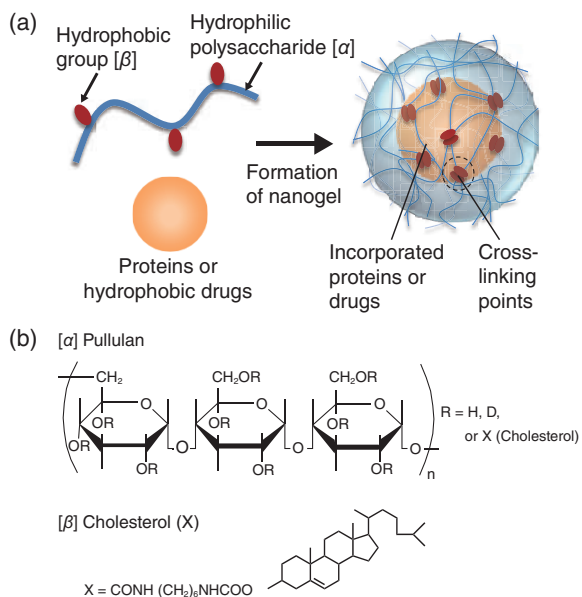


Fig.5-13 Formation of nanogels

(a) Schematic of a nanogel that is formed by self-associating partially hydrophobic modified polysaccharides. Nanogels are able to load proteins or drugs. (b) Chemical structures of pullulan and cholesterol.

Cholesterol-bearing pullulans spontaneously form stable nanogels of about 30 nm in diameter in aqueous solution due to hydrophobic interactions between cholesterol molecules (Fig.5-13). Because such nanogels possess a high loading capacity for proteins and drugs mainly through the hydrophobic interaction, they have been applied in drug-delivery systems. Although the spatial distribution of cross-linking points in the nanogels is closely related to their properties, no clear nanoscopic information has been obtained so far due to the complex structure with multiple components. This study aims to investigate the structure of the nanogels by means of contrast-variation small-angle neutron scattering (SANS), which enables us to determine the quantitative complex structure at the nanometer scale.

Small-angle scattering is a powerful technique that uses elastic-neutron scattering at a small scattering angle to study nano- to macro-structures (Fig.5-14(a)). The neutron-scattering length varies considerably between two isotopes; thus, the contrast-variation technique can be easily applied

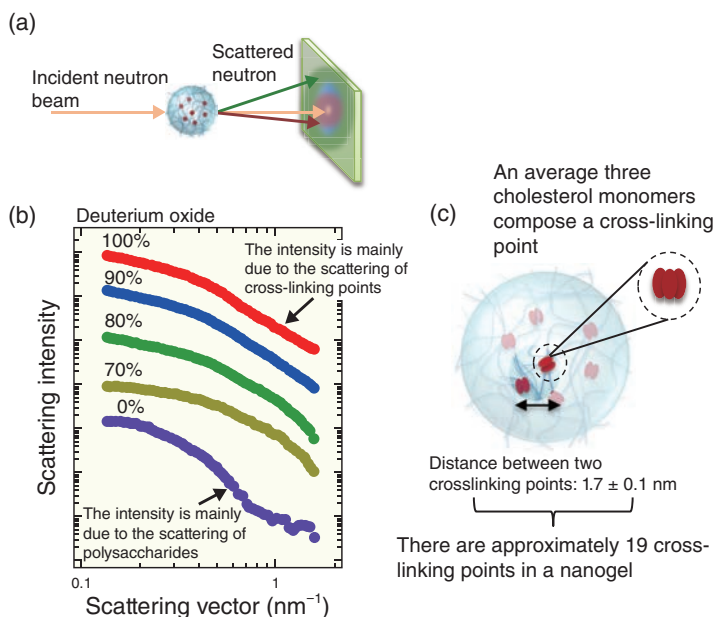


Fig.5-14 Small-angle neutron scattering of nanogels

(a) Schematic of a small-angle neutron-scattering (SANS) experiment. (b) Scattering intensities of nanogels dispersed in water with deuterium-oxide (D_2O) fractions of 100%, 90%, 80%, 70%, and 0%. (c) Nanoscopic structure of a nanogel revealed by neutron-scattering analysis.

with neutrons by utilizing the difference in nuclear scattering arising from hydrogen/deuterium replacement in the system.

Fig.5-14(b) shows the scattering intensities of the nanogels dispersed in water with D_2O fractions of 100%, 90%, 80%, 70%, and 0%. The scattering intensities vary with the D_2O fraction in the water; this is characteristic of multicomponent systems because the contrast-matching points for pullulan and cholesterol against water are different. The partial-scattering functions for each component were individually extracted, after which the pullulan-network structure and the cholesterol distribution in the nanogels were evaluated. From our analyses, it was observed that the cross-linking points are formed by aggregation of trimer-cholesterol molecules, and that there are 19 cross-linking points in a nanogel.

The SANS experiments were performed using a time-of-flight diffractometer, TAIKAN at J-PARC, Japan. This study was supported partially by the Japan Society for the Promotion of Science (JSPS) KAKENHI Grant-in-Aid for Young Scientists (B) (No.25790087).

Reference

Sekine, Y. et al., Nanoscopic Structural Investigation of Physically Cross-Linked Nanogels Formed from Self-Associating Polymers, *The Journal of Physical Chemistry B*, vol.120, issue 46, 2016, p.11996-12002.

5-6 Aiming for the Development of Stronger Stainless Steel

— First Observation of an Intermediate ϵ -phase at Room Temperature using High-Intensity Synchrotron Radiation —

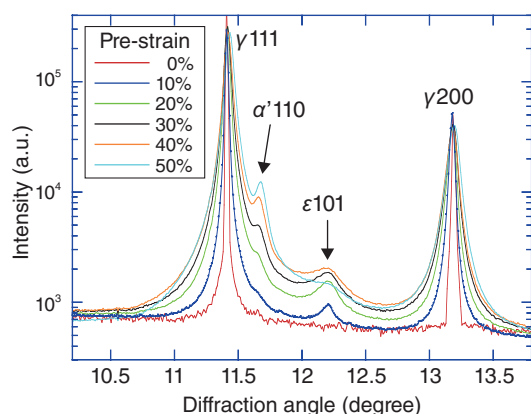


Fig.5-15 X-ray-diffraction profiles of pre-strained SUS304 specimens

As the value of pre-strain increases, the ϵ phase is observed to be generated and to increase, while the α' phase increases with a delay.

Stainless steel is an alloy steel containing mainly γ iron, at least 10.5% chromium, and a small quantity of alloying elements such as Ni. SUS is a designation of stainless steel, and a representative type known as SUS304 is standardized as having a Japanese Industrial Standards (JIS) containing 18% Cr and 8% Ni. As SUS304 has a well-balanced corrosion resistance and ductility and excellent mechanical properties, it is widely used in kitchens, home appliances, automobiles, railroad cars, reactor shrouds, and so on. It is known that, as the crystal structure changes, it becomes stronger, and the elongation also increases as a force is exerted upon SUS304. In order to improve characteristics such as breakability and ease of processing, it is very important to clarify the process of crystal-structure change.

The crystalline structure of SUS304 is known to change into an α' -phase body-centered cubic structure, starting with defects and dislocations occurring in the γ phase of the face-centered cubic structure. In previous studies, transmission electron microscopy has been reported to show that a hexagonal close-packed structure called the ϵ phase appears as an intermediate phase between the γ and α' phases. However, the ϵ phase has been observed only below room temperature and it has been speculated not to appear at higher temperatures.

In this study, we investigated the generation of the ϵ phase at room temperature using the synchrotron-radiation-diffraction method. The experiment was carried out at the BL02B1 beamline of the large synchrotron-radiation facility SPring-8. Fig.5-15 shows the obtained X-ray-diffraction data. As the value of pre-strain increases, the generation and increase of the peak intensity of the ϵ phase was observed. Furthermore, it was observed that the α' phase increased with the increase of the ϵ

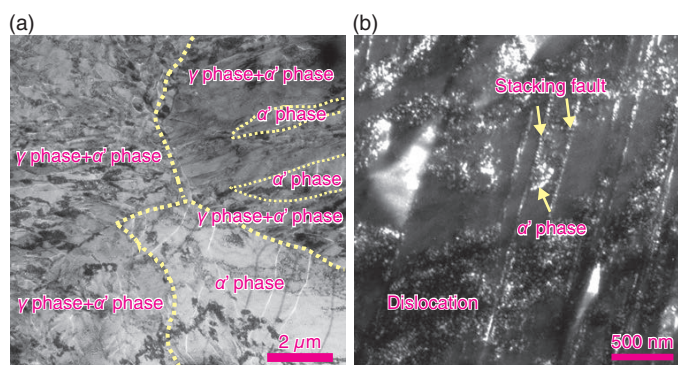


Fig.5-16 Lorentz-transmission electron-microscopy photograph of an SUS304 specimen (elongation: 20%)

(a) Fresnel image: A ferromagnetic α' phase is generated near the grain boundaries of two $\gamma + \alpha'$ phases indicated by a dotted line. (b) Foucault image: The ferromagnetic α' phase appears white and nano-sized-dot contrast is observed around stacking faults and dislocations.

phase. Using a high-intensity light source generated at SPring-8, the ϵ phase could be clearly observed, though the number of crystals in the ϵ phase is extremely small compared to those in the γ or α' phases. Unlike previous reports, this result shows that the ϵ phase is generated even at room temperature. This suggests that the γ phase was changed into an α' phase via the intermediate ϵ phase.

Therefore, to clarify the formation process of the α' phase, we observed the structure at the microscale using a Lorentz transmission electron microscope. Note that the α' phase has ferromagnetic properties and can be distinguished from the non-magnetic γ and ϵ phases by this technique. When observing the pre-strained specimen under 20% elongation, the α' phase was found to exist along the defect of the γ phase, as shown in Fig.5-16. This result suggests that the α' phase starts with stacking faults and dislocations and develops from there.

From these measurements, the ϵ phase was found to be formed near the twin boundary of the γ phase and to transform into the α' phase through one newly discovered process of induced martensitic transformation at room temperature. We are currently investigating these properties in detail because these phases may be the origin of the properties of stainless steel.

In addition, in practical usage, SUS304 has a major problem in that the tensile ductility decreases, making the material brittle when hydrogen is added to it. Our recent studies have shown that hydrogen embrittlement occurs via the formation of a high density of ϵ -phase material at room temperature. The results of this study are expected to lead to elucidation of the mechanism of embrittlement in stainless steel by hydrogen, as well as the proposal and development of materials for use in hydrogen-rich environments.

Reference

Hatano, M., Shobu, T. et al., Presence of ϵ -Martensite as an Intermediate Phase during the Strain-Induced Transformation of SUS304 Stainless Steel, Philosophical Magazine Letters, vol.96, issue 6, 2016, p.220-227.

5-7 Electronic Structure of Actinide Compounds Studied by Synchrotron Radiation

— Electronic Structures of Uranium Compounds that Show the Coexistence of Superconductivity and Magnetism —

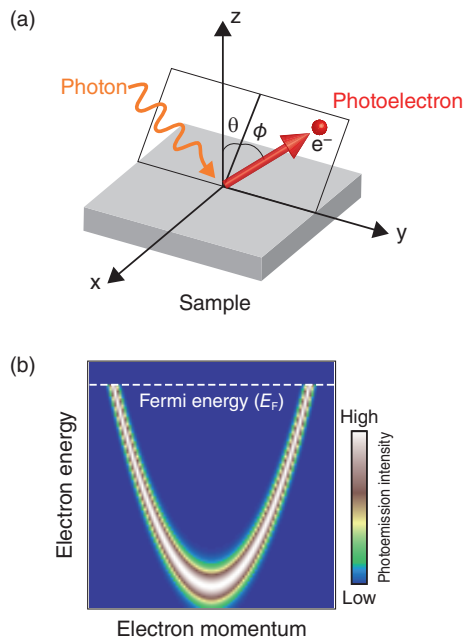


Fig.5-17 Schematic diagram of angle-resolved photoelectron spectroscopy

(a) Measurement configuration of angle-resolved photoelectron spectroscopy. Photons are emitted onto the sample surface and the energy and angular dependence of the emitted photoelectrons are measured. (b) Angle-resolved photoemission spectra. The momentum on the horizontal axis is a function of the photoelectron-emission angle. The highest photoelectron energy corresponds to the Fermi level.

Actinide compounds such as those of uranium show complicated physical properties such as various magnetic and superconductive behaviors and share a characteristic position among strongly correlated electron systems. In particular, superconductivity often coexists with magnetic order in uranium compounds, making them important for understanding how this coexistence occurs. These unique physical properties of uranium compounds are attributed to the nature of U 5f electrons, which show both itinerant and localized properties due to the electron-correlation effect, but a unified understanding has not yet been achieved.

SPring-8 BL23SU can handle radioactive materials such as uranium compounds, and it is the only environment in the soft-X-ray region. Soft-X-ray angle-resolved photoelectron spectroscopy can reveal bulk-electronic structure and be used to observe physical quantities such as band structure and the Fermi surface, which characterize the electronic state of matter. Fig.5-17 shows a schematic of angle-resolved photoelectron spectroscopy. By measuring the kinetic energy and angular distribution of the emitted photoelectrons, experimentally deriving the band dispersion and shape of the Fermi surface is possible. We have elucidated the electronic states of many uranium compounds.

References

- Fujimori, S. et al., Electronic Structures of Uranium Compounds Studied by Soft X-Ray Photoelectron Spectroscopy, *Journal of the Physical Society of Japan*, vol.85, no.6, 2016, p.062001-1-062001-33.
- Fujimori, S., Band Structures of 4f and 5f Materials Studied by Angle-Resolved Photoelectron Spectroscopy, *Journal of Physics: Condensed Matter*, vol.28, no.15, 2016, p.153002-1-153002-31.

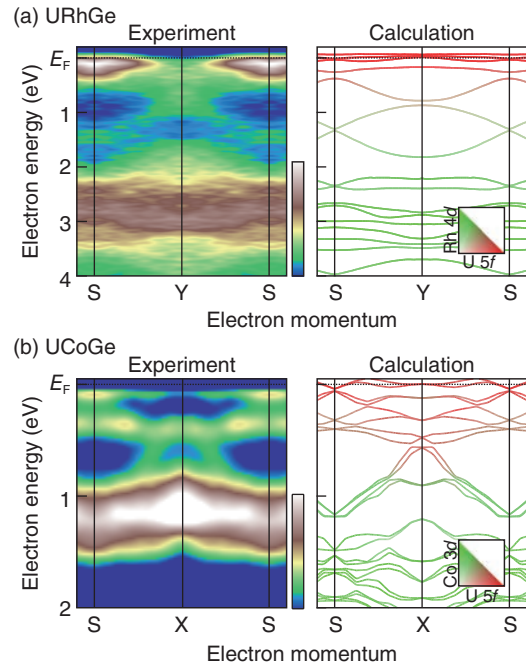


Fig.5-18 Comparison of the band structures and Fermi surfaces of (a) URhGe and (b) UCoGe

The horizontal axis is the electronic momentum; the color of the experimental-spectrum map is the intensity of the photoelectrons and the color coding of bands (red and green) shows the contributions from the orbitals of uranium and transition-metal atoms.

In this study, we compare the band structure obtained by soft-X-ray angle-resolved photoemission spectroscopy to the band-calculation results for uranium compounds with coexisting superconductivity and magnetism. Some uranium compounds are attracting attention due to the coexistence of ferromagnetism and superconductivity, which have been considered contradictory properties. Fig.5-18 shows a comparison between the experimentally determined band structures of (a) URhGe and (b) UCoGe and the band-calculation result. Experiments show that the overall band structures of these compounds can be explained by band calculation; on the other hand, when considering the structure near the Fermi level (which determines the electroconductive properties of substances) the agreement between the experiment and the calculation becomes worse. These results indicate that U 5f electrons, which are responsible for superconductivity and ferromagnetism, basically have an itinerant nature but an electronic-correlation effect. This result is not only fundamental information for understanding the electronic state of uranium compounds, it is also useful for considering models of the coexistence of magnetism and superconductivity.

Research and Development of HTGR, Hydrogen Production, and Heat Application Technologies

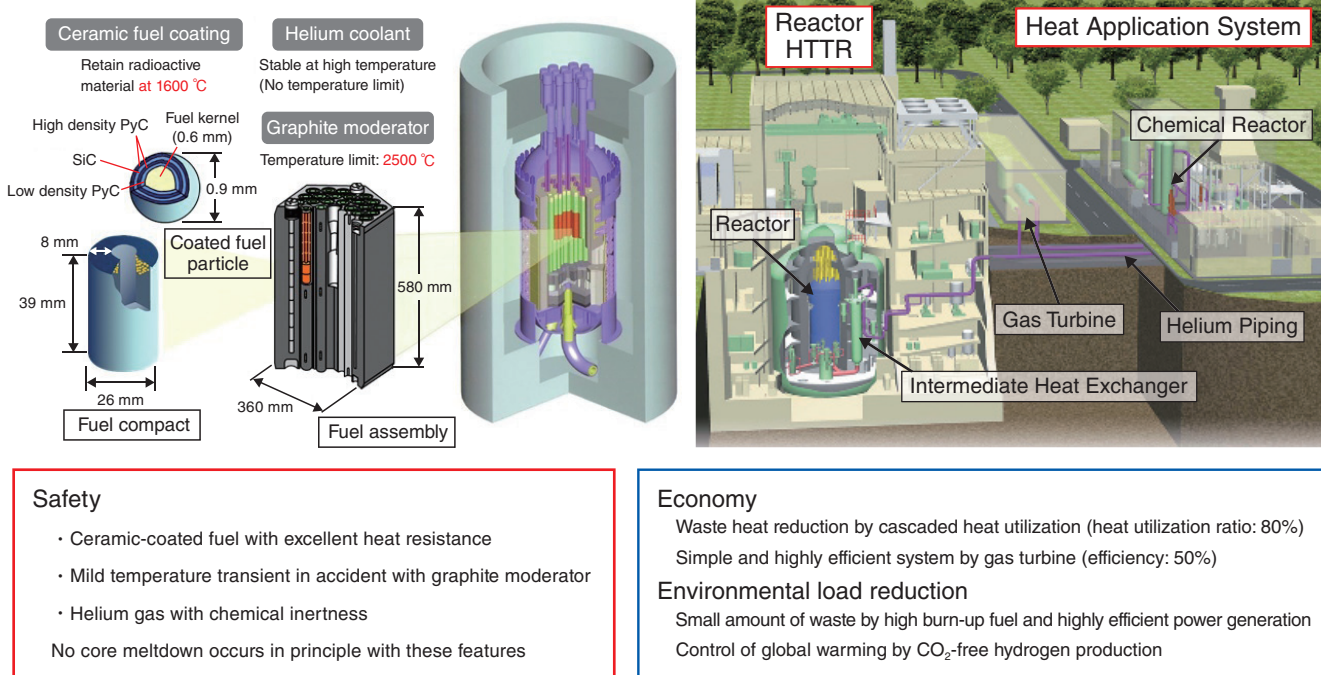


Fig.6-1 Features of HTGR

HTGR is a He gas-cooled and graphite-moderated thermal-neutron reactor with excellent inherent safety features; it can meet various heat application requirements such as hydrogen production and power generation. Its features are strongly expected to regain the public's trust in nuclear power.

To remedy the fragility of our country's energy-supply-demand structure arising from excessive dependence on fossil-fuel resources from abroad while simultaneously reducing greenhouse-gas emissions in response to global warming, Japan's basic philosophy is to advance nuclear-energy utilization on the premise of ensuring safety. We expect to use nuclear energy not only for power generation but also for various heat applications. "The Strategic Energy Plan" and "The Growth Strategy 2017", decided by the cabinet, list promotion of research and development of a High Temperature Gas-cooled Reactor (HTGR) as a national policy because such reactors have excellent inherent safety characteristics and meet the energy demand for various industries. Reflecting on this social situation, the HTGR forum is developing strategies for commercializing HTGRs and deploying Japanese HTGR technologies overseas.

An HTGR can supply heat at a temperature of 950 °C using fuel particles coated with ceramics, graphite-core material, and inert helium and can be designed as a meltdown-proof reactor in the case of any severe accident. The High Temperature engineering Test Reactor (HTTR) was constructed using the most advanced HTGR technologies developed in Japan, including coated-fuel-particle-fabrication technology with excellent fission-product-retaining performance and large-scale graphite-fabrication technology with high strength and irradiation resistance; it generated a temperature of 950 °C in 2004 for the first time in the world and demonstrated a stable

supply of heat over a 50-day operational period at 950 °C in 2010. We have demonstrated that even if the reactor-cooling system shuts down and the reactor scram fails, the reactor itself naturally shuts down and remains in a stable condition.

HTGR has excellent features that allow it to respond to the needs of various industries, such as highly efficient power generation with a helium-gas-turbine system, hydrogen production (Fig.6-1), and seawater desalination using waste heat from a gas-turbine system.

In this study, we promote the design of the HTTR-cogeneration system toward demonstrating nuclear-heat applications (Topic 6-1), propose an innovative heat exchanger as an essential component of the HTGR heat-application system (Topic 6-2), and verify the thermal-load responsibility using an inventory-control method in which the coolant pressure is controlled to manage the reactor power (Topic 6-3). We also research core design using highly oxidation-resistant fuel (Topic 6-4). In the field of heat-application research, we also conduct thermochemical hydrogen-production tests of the innovative iodine-sulfur process at a continuous-hydrogen-production-test facility made of industrial materials (Topic 6-5). Moreover, we develop a temperature-measurement technique using melt wire to estimate the core temperature of the HTTR (Topic 6-6).

We are preparing to resume operation of the HTTR by conducting a conformity review on new regulatory requirements issued by the NRA after the Great East Japan Earthquake.

6-1 Toward a Demonstration of the HTGR Cogeneration System

— Completion of Component Design and Preliminary Safety Assessment for the HTTR-GT/H₂ Plant —

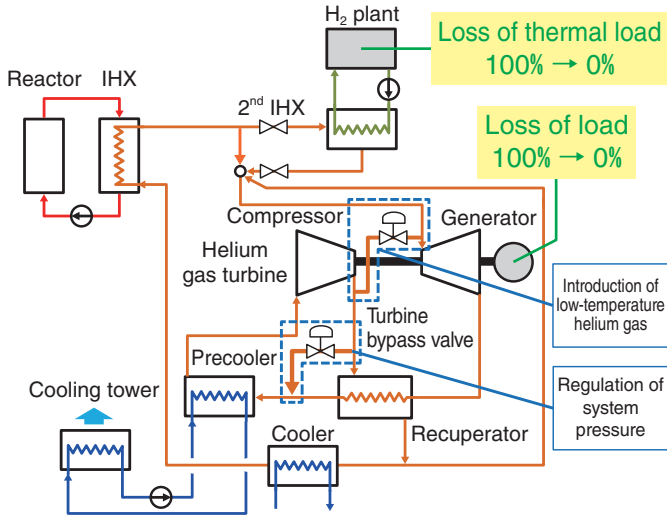


Fig.6-2 Mitigation system for the HTTR-GT/H₂ plant

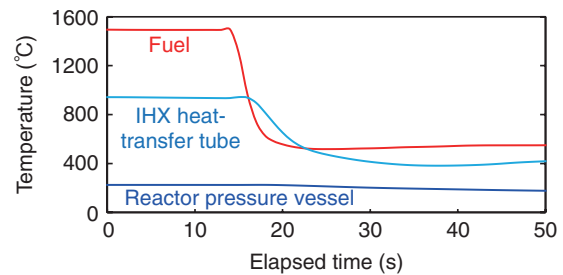
System pressure is regulated to suppress turbine over-speed during loss of generator load. Low-temperature helium gas is introduced to the turbine inlet to mitigate the temperature increase in reactor coolant against loss of thermal load in an H₂ plant.

High Temperature Gas-cooled Reactors (HTGRs) are expected to extend the use of nuclear energy for heat applications such as hydrogen (H₂) production owing to their inherently safe characteristics and high-temperature heat-supply capabilities. We are planning a demonstration program for carbon-dioxide-emission-free cogeneration of electricity and H₂ using the High Temperature engineering Test Reactor (HTTR).

The program aims to demonstrate heat-application technologies for HTGR and to obtain a first-of-a-kind license for coupling chemical plants to nuclear reactors. We have been conducting system and component design for the HTTR gas-turbine cogeneration plant (HTTR-GT/H₂ plant) since 2015. As a result, we have completed pre-licensing of the basic design with a power output of 1 MW and a H₂-production rate of 30 Nm³/h.

In addition, we have performed preliminary analysis to ensure reactor safety during abnormal events in the heat-application system. First, we selected two new events—loss of generator load and loss of thermal load in an H₂ plant—which must be evaluated under coupling of a helium-gas turbine and an H₂ plant to the HTTR. Then, the plant dynamics of selected events are evaluated by RELAP5 code, a system-analysis code. We employed the same mitigation systems as commercial HTGR-

(a) Loss of generator load



(b) Loss of thermal load in H₂ plant

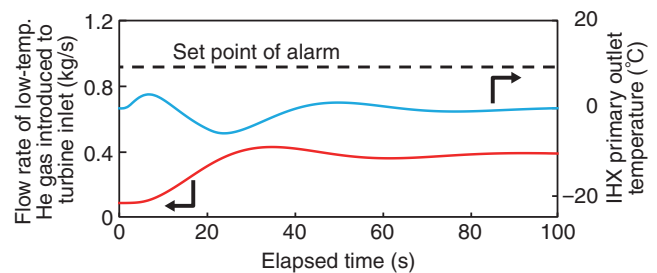


Fig.6-3 Plant dynamics of HTTR-GT/H₂ plant

The integrity of the plant and stable operation of the reactor can be maintained by the same mitigation systems used in commercial HTGR cogeneration systems.

cogeneration systems for demonstration of system-design technologies. As for the loss of generator load, a turbine-bypass control valve is devised to suppress turbine over-speed by regulating system pressure. Regarding the loss of the thermal load in an H₂ plant, a turbine-inlet-temperature-control valve is installed to introduce low-temperature helium gas from compressor inlet to the turbine inlet to suppress the temperature increase in the reactor coolant (Fig.6-2).

The simulation results demonstrate that loss of the generator load does not impact the temperature of fuel or the reactor-coolant-pressure boundary and that the integrity of the plant is maintained even if control-system failure is assumed and conservative conditions for measurement errors and operational fluctuations based on the HTTR design are applied. In addition, the results demonstrate that the transients did not trip the alarm and that stable operation of reactors can be achieved during loss-of-thermal-load events in H₂ plants (Fig.6-3).

Toward the realization of the HTTR demonstration test, it is important to share construction cost with foreign entities utilizing international collaboration. A further direction of study is to investigate a detailed test plan with countries interested in the demonstration program.

Reference

Sato, H. et al., System Analysis for HTTR-GT/H₂ Plant - Safety Analysis of HTTR for Coupling Helium Gas Turbine and H₂ Plant -, JAEA-Technology 2017-020, 2017, 23p. (in Japanese).

6-2 Development of High-Temperature Equipment for Heat Utilization of a High-Temperature Gas Furnace — Proposal for a Low-Cost, Long-Lived Intermediate Heat Exchanger —

Table 6-1 Design condition of a 0.7-MW 2nd IHX assuming HTTR-GT/H₂

By setting the operating pressure higher on the secondary side than on the tertiary side, it is possible to prevent the gas on the tertiary side from flowing into the secondary side when the heat-exchanger tube breaks. The tertiary-side-outlet temperature is 840 °C, making it possible to use high-temperature heat.

	Secondary side	Tertiary side
Helium gas flow rate (kg/s)	2.57	0.389
Inlet temperature (°C)	885	493
Outlet temperature (°C)	832	840
Inlet pressure (MPa)	4.19	4.07
Logarithmic temperature difference (°C)	146	
Tube outer diameter (mm)	-	45
Number of tubes	-	10
Helical coil diameter (mm)	-	1140

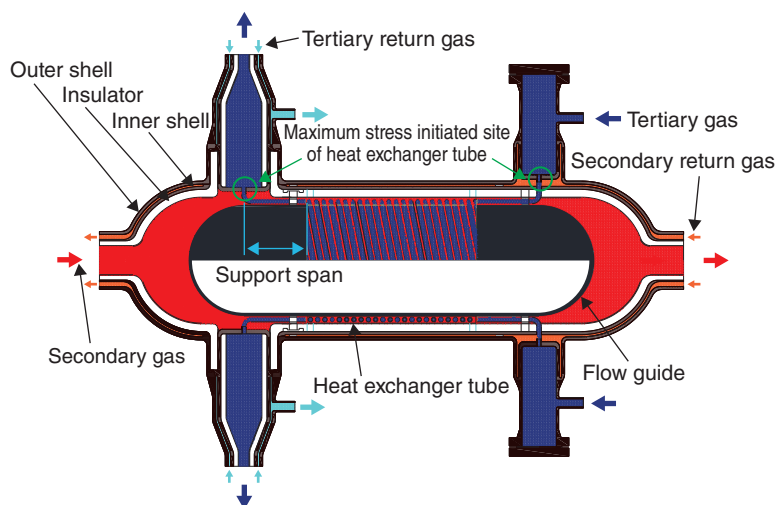


Fig.6-4 Conceptual diagram of a 0.7-MW 2nd IHX assuming HTTR-GT/H₂
This structure can reduce the primary stress of the heat-exchanger tube to which the maximum stress is given, as compared with a conventional vertical-type IHX, by reducing the center pipe and simplifying the multiple-container structure. The design satisfies the allowable stress corresponding to an operational lifetime of 40 years. It also enables the cost to be reduced by reducing the quantity of material.

Toward the development of high-temperature equipment for thermal utilization of High Temperature Gas-cooled Reactors (HTGRs), an intermediate heat exchanger (IHX) and a gas turbine are installed in series to supply heat to a hydrogen-production facility. In this manner, a gas-turbine high-temperature-reactor system (GTHTR300C) capable of efficiently supplying heat to hydrogen production and power generation has been researched and developed. For demonstration purposes, a hydrogen-production system (HTTR-GT/H₂) using iodine-sulfur process (IS process) with power generation by a helium-gas turbine connected to the High Temperature engineering Test Reactor (HTTR) is designed and studied. IHXs are important equipment for high-temperature-gas-furnace-heat utilization. As they are used under high-temperature environments, equipment having high-temperature creep strengths are required to ensure structural integrity, running the risk of an increased manufacturing cost. Therefore, we propose a structural concept for a horizontal-type IHX for the purpose of improving creep strength and cost and evaluate these quantities for GTHTR300C.

The exchange-heat condition of the second IHX designed for HTTR-GT/H₂ (the intermediate heat exchanger between the secondary and tertiary helium) is 0.7 MW. To prevent the tertiary-system gas from entering the secondary-system side, the pressure on the secondary-system side is set 0.12-MPa higher (Table 6-1). The horizontal-type second IHX is composed of inner and outer shells, a flow guide, a heat-exchanger tube, and so on. In the case of the horizontal-type IHX, a center pipe is not needed to support the heat-exchanger tube and therefore acts only as a flow guide. Thus, it is possible to reduce the quantity of material while ensuring the same aseismic strength as a vertical-type IHX.

In the horizontal-type second IHX (Fig.6-4), secondary-system gas (➔) flows through the inner shell, while tertiary-

system gas (➔) flows through the heat-exchanger tube. Secondary gas (➔) then returns from the helium-gas turbine flowing between the outer and inner shells, while tertiary gas (➔) returns from the hydrogen-production facility. Inside the inner shell, heat exchange occurs between the secondary- and tertiary-system gases, and the return gas of decreased temperature flows into the space between the outer and inner shells. Thus, the cooling effect on the outer shell side can be improved, and the thermal stress of the whole device can be reduced.

Stress calculation was performed using the general-purpose finite-element-method-based structural-analysis program ABAQUS. In addition, except at the center pipe, in the creep-life evaluation of the horizontal second IHX with reduced support stress of the heat-exchanger tube, the support span of the heat-exchanger tube necessary to withstand creep rupture of the material was shortened from 1.4 m for the vertical-type to 0.9 m. Thus, the maximum initiated stress in the heat-exchanger tube was 4.3 MPa in the vertical-type, but 1.9 MPa in the horizontal-type. Finally, a value that satisfies the allowable stress (2.6 MPa) corresponding to the cumulative-creep-damage coefficient corresponding to continuous operation for 40 years has been achieved, as compared with a designated life of 20 years for the vertical-type. For lifespan evaluation, it is thought to be necessary to verify the effectiveness of the design by acquiring creep data over a long period.

Based on the above evaluation, physical-quantity assessment of the horizontal-type IHX with an exchange heat of 170 MW at GTHTR300C was performed. Compared with the vertical-type, the weight of the material was found to be drastically reduced, and material-cost estimates are reduced by 30%.

Based on these results, the horizontal second IHX will be studied in detail in the future.

Reference

Yan, X., Iwatsuki, J. et al., HTTR-GT/H₂ Test Plant – System Design, Proceedings of 8th International Topical Meeting on High Temperature Reactor Technology (HTR 2016), Las Vegas, Nevada, USA, 2016, p.827-836, in CD-ROM.

6-3 Toward Practical Load-Following Operation of HTGRs Connected to Heat-Application Systems

— Elucidation of Thermal-Load-Fluctuation Absorption at Various Coolant Pressures —

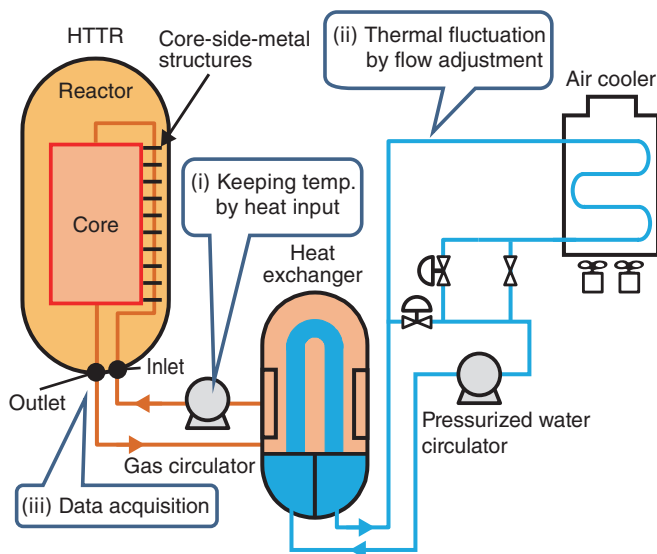


Fig.6-5 Confirmation test of thermal-load-fluctuation absorption against coolant pressure

By varying the pressurized-water temperature through the air cooler from the condition keeping the reactor-inlet-coolant temperature constant at different coolant pressures through heat input from the gas circulator, the reactor-inlet-coolant temperature was decreased by approximately 30 °C and the influence of coolant pressure upon thermal-load-fluctuation absorption was investigated.

When installing High Temperature Gas-cooled Reactors (HTGRs) connected to hydrogen-production facilities or gas-turbine power-generation systems in isolated locations or developing countries without electric power grids, load-following operation that adjusts the reactor power is required according to heat-utilization demand from the viewpoint of improving economic efficiency. Under load-following operation, the reactor power is adjusted by keeping the reactor-outlet-coolant temperature constant and controlling the mass-flow-rate (inventory) of the coolant by adjusting the coolant pressure. As a result, improving the plant economy by controlling the power according to the demand for hydrogen and electric power is possible.

On the contrary, heat-utilization technologies such as hydrogen-production systems are installed as general industrial systems, not nuclear-reactor systems, in order to improve economic efficiency. Therefore, even when the temperature fluctuation (thermal load) assumed at the abnormal condition in the heat-utilization system propagates to the reactor inlet, it is necessary to indicate that the reactor power and reactor-outlet-coolant temperature do not exceed operational limits. In past studies, it has been found that in the state of high coolant pressure during rated operation, this thermal load is absorbed and suppressed by a heat-transfer-promoting effect due to irregularities in the core-side-metal structures (thermal-load-fluctuation absorption) and that the core-side-metal structures work as buffer for the thermal load to prevent sudden

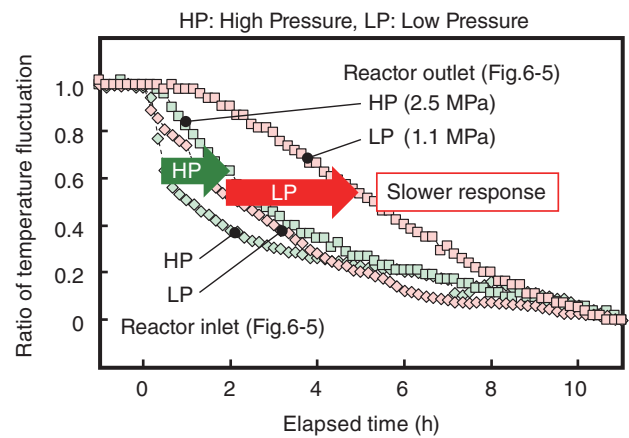


Fig.6-6 Effect of coolant pressure upon thermal-load-fluctuation absorption

The green and red data points show the results of the high- and low-pressure tests, respectively. The response of the reactor-outlet-coolant temperature to fluctuation in the inlet-coolant temperature was found to be slower at low pressure than that at high pressure. Fluctuation was difficult to transfer at low pressure and thermal-load-fluctuation absorption was excellent in this region.

temperature changes in the core. Thus, the reactor-power adjustment against temperature fluctuation of the core works smoothly, and the reactor power and outlet-coolant temperature are stabilized. However, since the heat-transfer coefficient decreases at low coolant pressure under inventory control, it is necessary to check whether the same mechanism works effectively.

In the case of the lower coolant pressure under inventory control, based on previous findings that (1) the temperature fluctuation of the core-side-metal structures becomes slow due to a decrease in the heat-transfer coefficient of the coolant and (2) the heat capacity of the coolant decreases due to a decrease in the mass-flow rate, improving the temperature followability of the coolant to the structures, we predicted that the fluctuation of the reactor-outlet-coolant temperature should become slower than that of higher coolant pressure. Then, to confirm this prediction, test data on thermal-load-fluctuation absorptivity of the reactor were acquired using the High Temperature engineering Test Reactor (HTTR) under different coolant pressures (1.1 and 2.5 MPa), with heat input from the gas circulator; the reactor-inlet-coolant temperature was decreased by approximately 30 °C (Fig.6-5).

As a result of the test, we confirmed that the thermal-load-fluctuation absorptivity at low pressure is superior to that at high pressure (Fig.6-6). Toward realization of load-following operation of HTGRs, the load-fluctuation absorptivity under different coolant pressures was clarified.

Reference

Inaba, Y. et al., Nuclear Heat Supply Fluctuation Tests by Non-Nuclear Heating with HTTR, Journal of Nuclear Engineering and Radiation Science, vol.2, issue 4, 2016, p.041001-1-041001-7.

6-4 Safety Enhancement of High-Temperature Gas-Cooled Reactors

— Nuclear and Thermal Design of an Oxidation-Resistant Fuel-Loaded Reactor Core —

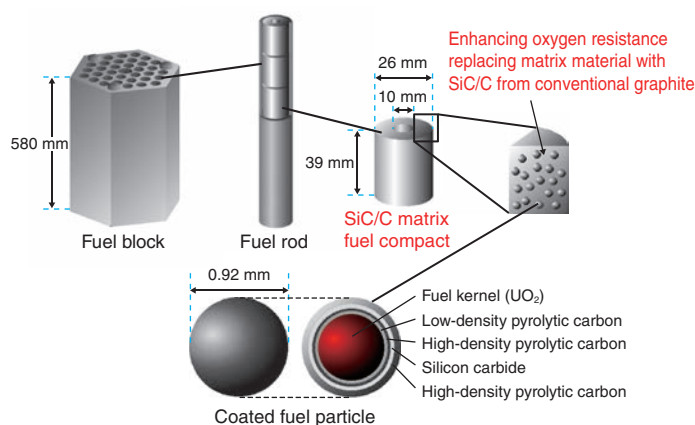


Fig.6-7 HTGR-fuel example with enhanced oxidation resistance
A conventional fuel compact is fabricated by sintering coated-fuel particles, which consist of fuel kernels coated with ceramic layers, with a graphite matrix. The oxidation resistance of the fuel compact is enhanced by replacing the matrix material with a compound of silicon and graphite (SiC/C).

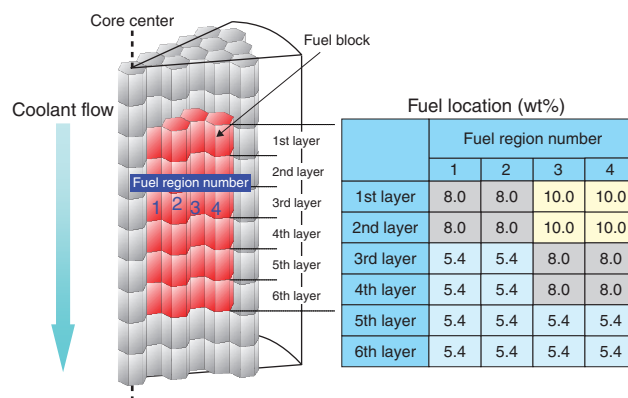


Fig.6-8 Fuel location to optimize power distribution
Higher-enrichment fuel is placed at the upper region, where the coolant temperature is low, and at the outer region, where neutron flux is low. Owing to this fuel location, the fuel temperature is uniform in the reactor core and consequently the maximum fuel temperature is suppressed.

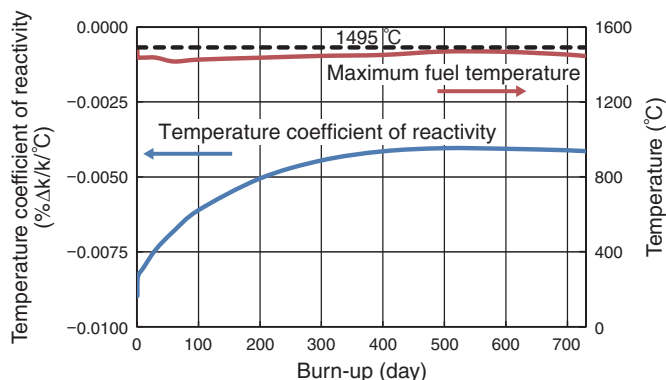


Fig.6-9 Calculation results for the temperature coefficient of reactivity and the maximum fuel temperature
The fuel temperature was confirmed to be lower than the limit of 1495 °C and the temperature coefficient of reactivity had a negative value during the burn-up period.

We are developing an oxidation-resistant fuel (SiC/C-matrix-fuel compact, Fig.6-7), which promises to enhance the safety of High Temperature Gas-cooled Reactors (HTGRs) by maintaining its integrity under air ingress. Such an ingress is considered as a characteristic accident due to pipe rupture, with a large amount of air (beyond any projections) entering into the reactor core. To introduce the SiC/C matrix-fuel compact to the HTGRs, the nuclear and thermal feasibility of the reactor core should be confirmed in addition to establishing fuel-fabrication technology. Nuclear and thermal design was performed for the SiC/C-matrix-fuel-compact-loaded HTGR based on the conceptual design of HTR50S so as to achieve the same performance, namely a 50-MW thermal power and 730-day (2-year) burn-up period.

The most important issues facing the nuclear and thermal design of HTR50S are determination of fuel specifications (such as the degree of enrichment needed for the required period of operation) and optimization of the power distribution to suppress the fuel temperature below the limit during the burn-up period. Silicon, which is included in the SiC/C matrix, more easily yields neutron-capture reactions than graphite and almost fails to moderate neutrons. Owing to these nuclear characteristics, the reactivity of the reactor core decreases

when the fuel-compact-matrix material is replaced with SiC/C from conventional graphite. To compensate for the reactivity decrease, the average fuel enrichment was determined to be 1.1wt% higher than the original HTR50S. Optimization of the power distribution was performed using three kinds of fuel enrichment as with the original HTGR50S, and the fuel location was determined as shown in Fig.6-8.

The excess reactivity and power distribution were calculated by performing burn-up calculations with the whole-core model, and the fuel temperature was calculated using the power-distribution results. It was confirmed that the reactor core has enough excess reactivity to operate for 730 days with 50 MW of thermal power, and the fuel temperature is kept below the limit during the burn-up period (Fig.6-9). Additionally, the shutdown margin was confirmed to be larger than 1%Δk/k and it was observed that the reactor could be safely stopped. The temperature coefficient of reactivity was found to have a negative value, leading to a self-stabilizing characteristic. Based on the above results, the nuclear and thermal feasibility of the SiC/C-matrix-fuel-compact-loaded HTGR were confirmed.

The present study was sponsored by the Ministry of Education, Culture, Sports, Science and Technology, Japan (MEXT).

Reference

Aihara, J., Goto, M. et al., Nuclear Thermal Design of High Temperature Gas-Cooled Reactor with SiC/C Mixed Matrix Fuel Compacts, Proceedings of 8th International Topical Meeting on High Temperature Reactor Technology (HTR 2016), Las Vegas, Nevada, USA, 2016, p.814-822, in CD-ROM.

6-5 R&D on CO₂-Free H₂ Production by the IS Process

— Progress from Lab Stage to Industrial-Material-Facility Stage —

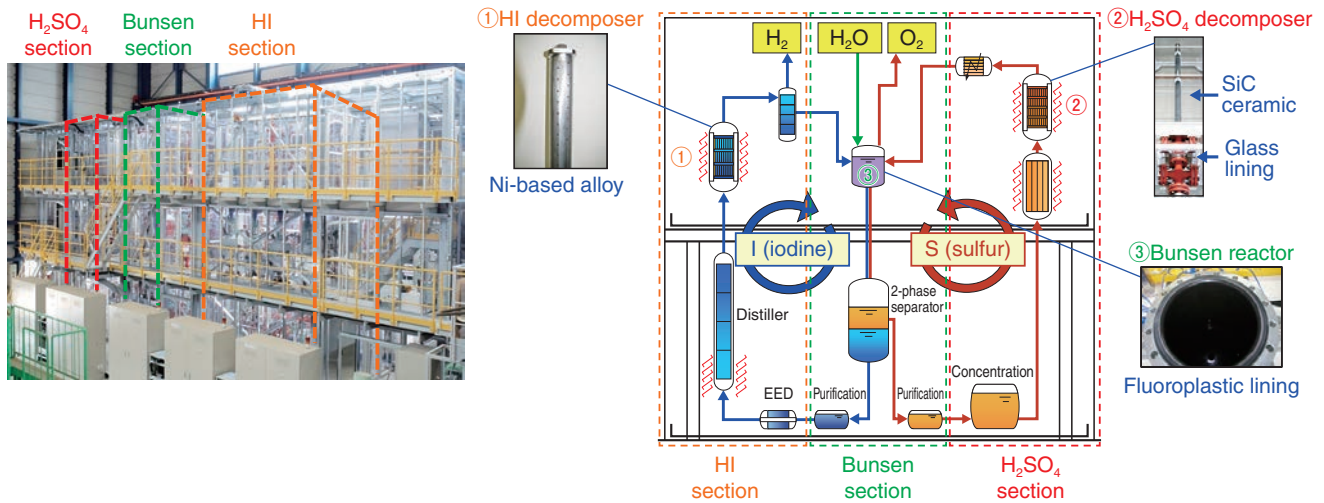


Fig.6-10 Continuous-H₂-production test facility
 (Left) Photo of the facility: Size, 18.5 m (W) × 5.0 m (D) × 8.1 m (H). (Right) Structure and reactor components: Materials used for liquid-phase components not shown in the figure include impervious graphite for electro-electrolysis (EED) HI concentrators and heat exchangers, as well as fluoroplastic- and glass-linings for other components and lines.

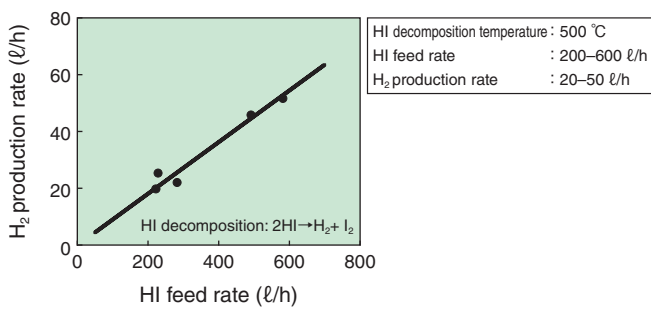


Fig.6-11 Effect of HI feed upon H₂ production in a HI decomposer

The H₂-production rate is controllable by changing the HI-feed rate because the one is proportional to the other. Reprint from Takegami, H. et al., 2016 Annual Meeting of AESJ, 2N23 (in Japanese), (partly modified)

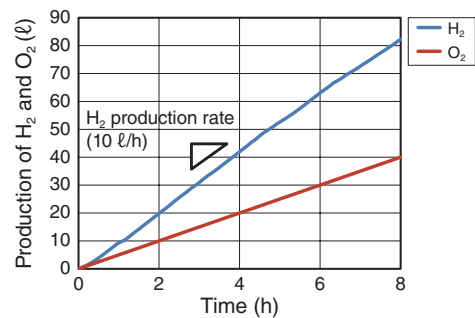


Fig.6-12 Total H₂ and O₂ production in a process demonstration

H₂O is decomposed at a constant rate and H₂- and O₂-production rates are balanced by considering a constant gradient and H₂/O₂-production ratio that is constant at 2.

We have performed R&D on thermochemical hydrogen (H₂)-production using iodine-sulfur (IS) process as an application of High Temperature Gas-cooled Reactor (HTGR) heat. The IS process consists of Bunsen reaction to produce hydrogen iodide (HI) and sulfuric acid (H₂SO₄), HI decomposition to produce H₂, and H₂SO₄ decomposition to produce oxygen (O₂). Overall, H₂O is decomposed into H₂ and O₂. The IS process is expected to offer CO₂-free H₂ production because carbon is neither in the material nor in the energy source.

We succeeded in conducting a one-week continuous H₂ production using a lab-scale facility in FY2004. Components in the facility was made of glass. Corrosion- and heat-resistant components of industrial materials are required for commercialization because large-scale structures cannot be made of glass.

We constructed a test facility in FY2013 by applying

corrosion- and heat-resistant materials to the whole process (left in Fig.6-10). Reactors were developed and integrated into each section (right in Fig.6-10). The designed H₂-production rate was 100 l/h. The functionality of individual sections was verified in FY2015. Process-rate control in reactors, such as control of H₂ production by HI feeding (Fig.6-11), and phase separation (such as HI distillation) were verified. Then, a demonstration was performed by coupling the 3 sections. An 8-h continuous H₂ production at 10 l/h was achieved in February 2016 (Fig.6-12). By checking the facilities after operations and performing operational-data analysis, we found that clogging prevention and Bunsen-solution-composition control were important for longer-term operation.

We plan to improve the facility based on these findings for longer-term operations to verify the technology and integrity of the facility.

Reference

Kasahara, S. et al., Current R&D Status of Thermochemical Water Splitting Iodine-Sulfur Process in Japan Atomic Energy Agency, International Journal of Hydrogen Energy, vol.42, issue 19, 2017, p.13477-13485.

6-6 Clarifying the Core Temperature in High-Temperature Gas-Cooled Reactors

— Development of Measurement Technology Based on Melt Wires for Control-Rod Temperature to Estimate Core Temperature —

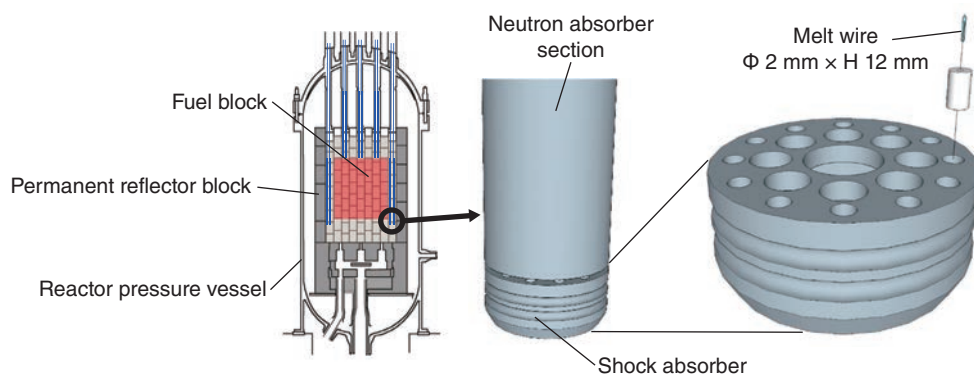


Fig.6-13 Melt wires in the control rod

Melt wires are installed in holes in the shock absorbers of the control rods. Twelve types of metallic wire with melting points from approximately 400 °C to 1000 °C were selected.

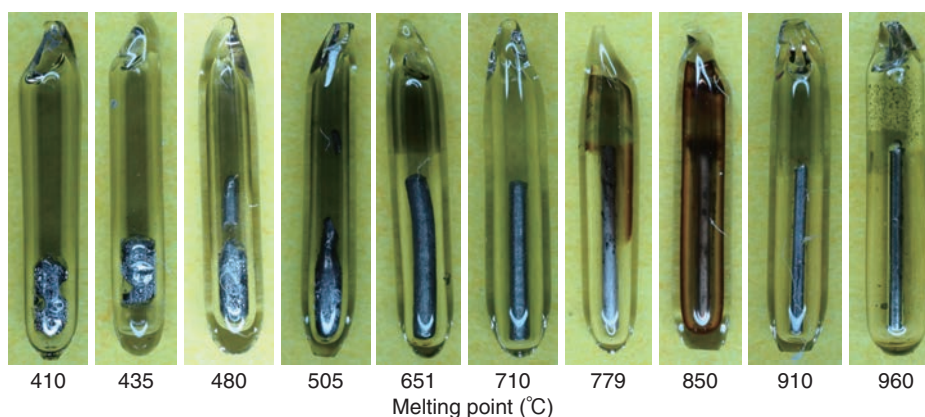


Fig.6-14 Observational results of melt wires

Melt wires having a melting point of 505 °C or less were melted, while wires having a melting point of 651 °C or higher were unmelted.

To improve the design of High Temperature Gas-cooled Reactors (HTGRs), measuring the temperatures of actual reactor cores is necessary to reduce uncertainties in the design analysis. However, measurements of core temperatures are difficult to perform because there are problems with the installation, durability, and corrosion of instrumentation under a super-reducing atmosphere.

In the High Temperature engineering Test Reactor (HTTR), actual measurement data were required because the temperatures of fuel, control-rod cladding, and the heat-transfer tubes of intermediate heat exchangers are close to their design limits. Temperature measurement of control-rod cladding is especially important.

Control rods, which are the only metallic components in the fuel region, are periodically removed from the reactor and maintained. The installation and removal of melt wires can be carried out during such inspections. Melt wires with different melting points were selected due to their excellent features with extremely low risk of failure and high accuracy, and installed in the shock absorber at the lowest tip of the control rod to measure its maximum temperature.

In Germany's experimental pebble-bed-type HTGR (AVR), the maximum temperature of the core was measured by melt wires, but information concerning measurement position was

not recorded. Meanwhile, the data measured by HTTR can be adequately used to improve design technology because measurement position can be identified and accurately controlled (Fig.6-13).

To avoid damage to the control rod by overheating, a two-step control-rod-insertion method was adopted in the HTTR. The control rod used in the highest-temperature case was selected for the measurement as the first step. Twelve types of melt wires with melting points ranging from approximately 400 °C to 1000 °C were installed in this control rod. The melt-wire observations obtained by CCD camera are shown in Fig.6-14. It was found that the maximum temperature at the measuring position of the control rod is in the range of 505 °C to 651 °C.

On the contrary, the results of thermal-conductivity analysis show that the maximum temperature of the control rod is approximately 800 °C. The maximum fuel temperature of HTTR is numerically predicted to have a margin of approximately 200 °C based on its hot-spot factor. Therefore, the actual measurement result of the control-rod temperature can be used for more reasonable design to reduce the margin.

In the future, we plan to improve our fuel-temperature-evaluation method by clarifying the temperature distribution of the core, and to establish an international standard of HTGR design by measuring the temperatures of other control rods.

Reference

Hamamoto, S. et al., Development of Temperature Measurement Technology for Control Rod using Melt Wire in High Temperature Engineering Test Reactor (HTTR), JAEA-Technology 2017-012, 2017, 20p. (in Japanese).

Research and Development of Fast Reactor Cycle Technology

Fast reactor (FR) cycle technology, as shown in Fig.7-1, is an innovative technology with the potential to dramatically enhance the utilization efficiency of uranium resources, as is required for the long-term use of nuclear energy. We are aiming to innovate in numerous ways to make FR cycle technology acceptable to society. The FR cycle technology must be able to maximally reduce the risk of nuclear disasters such as that at the TEPCO's Fukushima Daiichi NPS, which released large amounts of radioactive substances. For this purpose, we will create a safety enhancement concept that incorporates measures to prevent severe accidents and mitigate the impact in the design on the wide assumption of causes leading to severe accidents, including natural disasters.

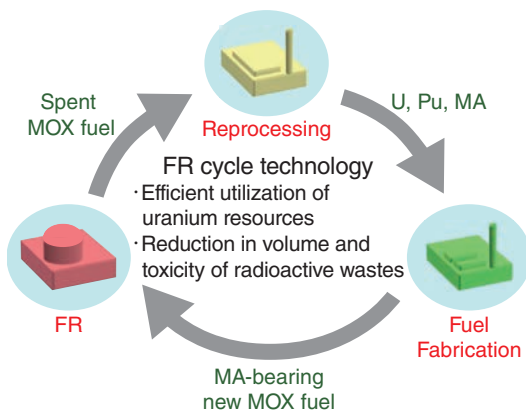


Fig.7-1 Fast reactor cycle technology

In fast reactor (FR) cycle technology, uranium, plutonium, etc., which are extracted from spent fuels, will be reused in FRs, while generating electricity by the reactors.

FR cycle technology is capable of drastically shortening the period required to sufficiently reduce the radiotoxicity of high-level radioactive waste by partitioning long-lived nuclides when reprocessing, shortening the lifetime of the nuclides by transmutation in an FR. For that reason, we aim at innovation in nuclear energy systems by developing a technology for partitioning and transmutation of Minor Actinides (MAs) from long-lived nuclides in the FR cycle.

In FY2016, we conducted an international standardization of the safety design criteria of FRs in the Generation IV International Forum (GIF) framework and experimental studies on severe accident measures which should be incorporated into design (Fig.7-2), etc. Furthermore, in collaboration with France, we conducted joint design and evaluation of ASTRID (Advanced Sodium Technological Reactor for Industrial Demonstration), which is being developed in France; we also conducted information exchange, analysis code development, planning of testing, etc. on reactor technology, safety, and fuel as part of the ASTRID research and development (R&D) cooperation. In the fields of fuel reprocessing and fuel fabrication technology, basic technology development and small-scale MA cycle tests (SmART Cycle research), etc. were conducted.

This chapter presents the following R&D activities toward an enhanced FR safety concept. We proposed a method of evaluating leaks prior to breaking of FR pipes to sophisticate

structural integrity evaluation technology for FRs (Topic 7-1). To develop a thermal-hydraulic evaluation method, we built a three-dimensional simulation model and compared its analysis results with experimental results (Topic 7-2). In the field of maintenance and repair technology for sodium-cooled FRs, the development of inspection technology for structures immersed in opaque sodium was carried out using ultrasonic waves (Topic 7-3). Using data from natural circulation tests with the Prototype Fast Breeder Reactor Monju, validation of an analytical model of the core region was performed in terms of thermal hydraulics when the core was cooled by the natural circulation of sodium after a shut-down (Topic 7-4).

Towards the development of a reprocessing technology for FR fuel, sludge cleaning method in a centrifugal contactor was developed, pursuing sophistication in the process of separating and recovering nuclear materials (Topic 7-5).

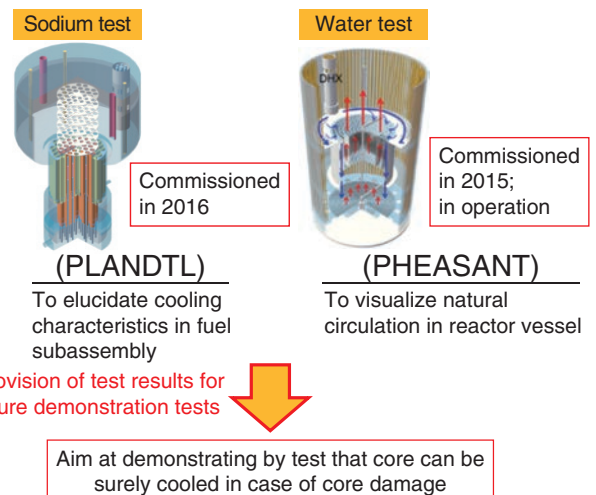


Fig.7-2 Example of research and development (R&D) activity for severe accident measures

Experimental studies using water and sodium testing facilities are now ongoing to evaluate the cooling characteristics of various decay heat removal systems in the case of core damage.

We are engaged in bilateral cooperation, mainly with the United States and France, as well as multilateral cooperation such as GIF in order to conduct the R&D on FR cycle technology effectively and efficiently (Fig.7-3). In addition, we are making efforts to develop base technologies and human resources in cooperation with universities and research institutions.



Fig.7-3 International cooperation in FR cycle development
International cooperation in the development of FR cycle technology is being carried out with partners who can create synergistic effects utilizing bi- and multilateral cooperation frameworks.

7-1 Sophisticated Structural-Integrity Assessment of Fast-Reactor Components

— A Proposal of Procedure for Assessing Leaks before Breakage of Fast-Reactor Pipes —

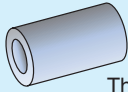
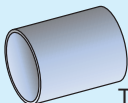
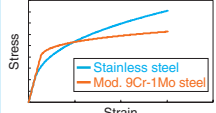
	LWR	SFR
Geometry	 Thick	 Thin
Loads	Primary	Secondary
Material characteristics		

Fig.7-4 SFR-pipe features

An LBB-assessment procedure accounting for SFR-pipe features such as thin-wall geometry, material characteristics, among others, is required.

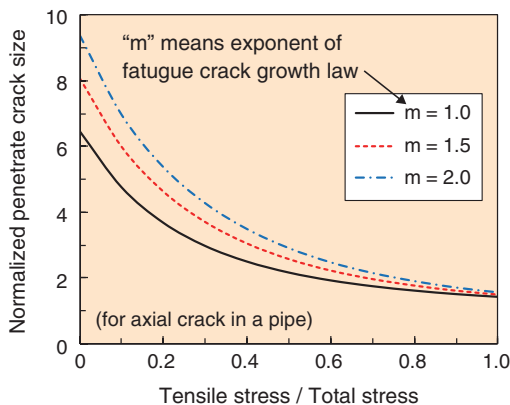


Fig.7-6 Penetrating-crack-size diagram

For users' convenience, penetrating-crack-size diagrams are prepared.

The pipe geometry of a sodium-cooled fast reactor (SFR) has thin walls and a large diameter compared to that of a light-water reactor (LWR). The pipe material, modified 9Cr-1Mo steel, has a relatively high yield strength and low ductility compared to conventional austenitic stainless steels, as shown in Fig.7-4. In addition, the secondary stress caused by thermal expansion is predominant in SFR. Accounting for these features, a rational leak-before-break (LBB)-assessment guideline is proposed and will be published to provide a technical basis for substitution of volumetric tests by continuous leak-monitoring during in-service inspections.

LBB is based on the concept that it is possible to deal properly and safely with cracks by detecting leakage of internal fluid from a penetrating defect before catastrophic failure occurs.

First, an LBB-assessment flowchart for the SFR components

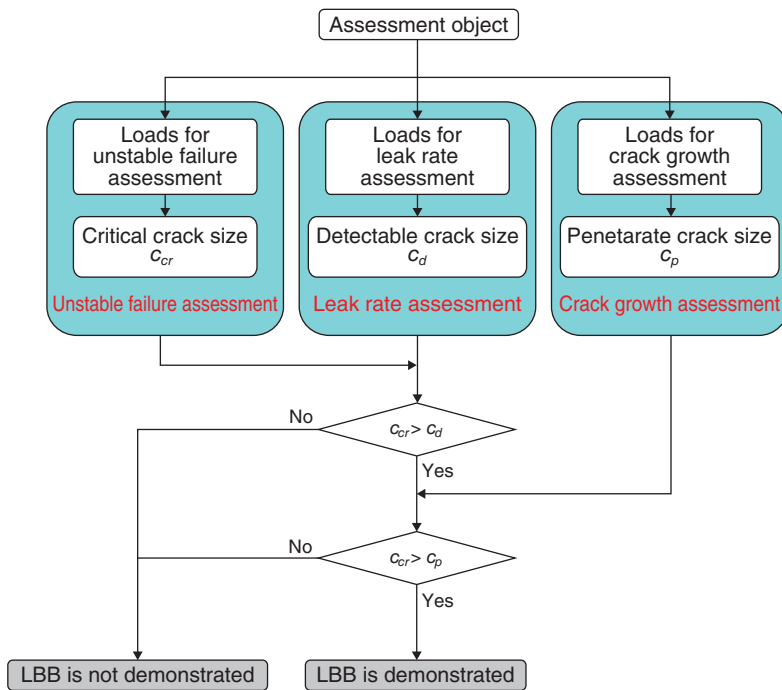


Fig.7-5 Provisional LBB-assessment flowchart

If the critical crack size is larger than the detectable or penetrating crack sizes, we conclude that LBB is demonstrated. Unstable-failure and leak-rate assessment takes SFR pipe features into account. In crack-growth assessment, a user can calculate the penetrating-crack size using the diagram, as shown in Fig.7-6.

was proposed, as shown in Fig.7-5. Secondly, taking the SFR-pipe features into account, evaluation methods for calculating the critical-crack size, the detectable-crack size, and the penetrating-crack size were developed and incorporated into LBB assessment. Confirming that the penetrating-crack size depends almost exclusively upon material characteristics and loading conditions, evaluation diagrams were prepared for users' convenience, as shown in Fig.7-6. Furthermore, adequate-safety margins were recommended for reasonable and conservative evaluations. As a non-mandatory appendix, some material characteristics that can be used in evaluations are also illustrated for easy use of the methods.

To publish the developed LBB-assessment procedure as a guideline officially authorized by the Japan Society of Mechanical Engineers (JSME), JAEA will make a technical contribution.

Reference

Wakai, T. et al., Demonstration of Leak-Before-Break in Japan Sodium Cooled Fast Reactor (JSFR) Pipes, Nuclear Engineering and Design, vol.269, 2014, p.88-96.

7-2 Development of a Thermal-Hydraulic-Evaluation Method for a Straight-Tube Steam Generator

— Establishing a Three-Dimensional Simulation Model and Comparing it with Test Data —

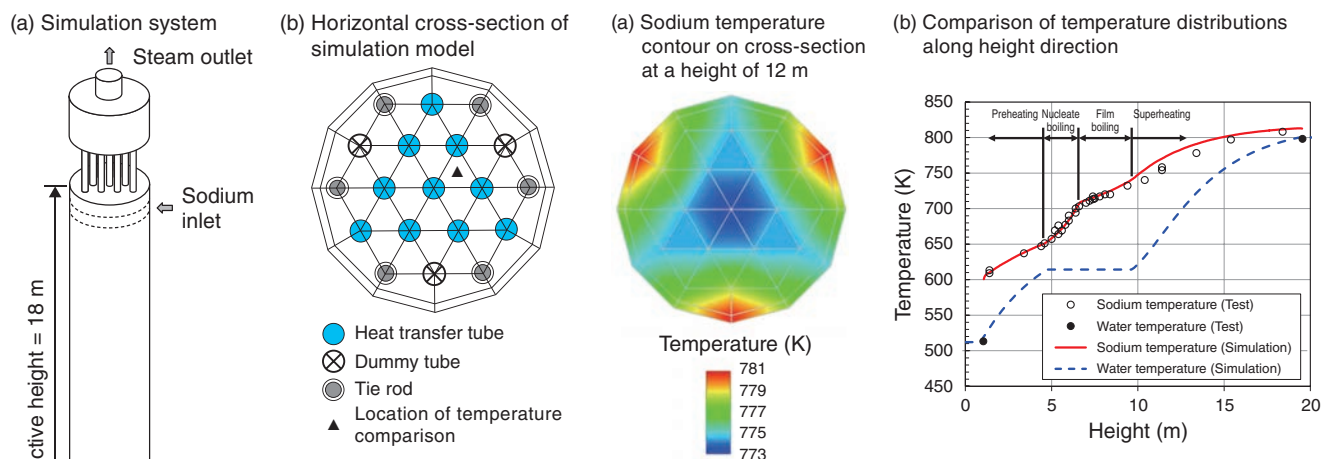


Fig.7-7 Simulation model for an SG test

A three-dimensional simulation model was generated for fundamental validation of TSG with a 1-MWt SG test in which the heat-transfer characteristics of a double-walled straight tube were observed.

A double-walled straight-tube steam generator (SG) has been studied to attain high reliability and thermal capacity in sodium-cooled fast reactors. In a straight-tube SG, many heat-transfer tubes are arranged inside a cylindrical container. The water in the tubes is heated by hot sodium outside the tubes, and steam is generated. It is necessary to evaluate the temperature deviation in view of tube buckling due to thermal-expansion mismatches among tubes. The temperature deviation is caused by the nonuniform sodium flow inside the tube bundle or a lack of heat transfer near the blocked tube where flaws are detected. However, local-temperature rise could not be predicted by the previous two-dimensional simulation method with an axisymmetric assumption. For this reason, it was necessary to develop a new evaluation method capable of accurately predicting the three-dimensional temperature distribution in the SG.

In the present study, a three-dimensional thermal-hydraulic-analysis code for steam generators (TSG) was developed; this code couples the three-dimensional simulation of sodium with multi-channel-simulation of water. Specifically, a porous-body model that considered a reduction of fluid volume due to heat-transfer tubes was adopted to analyze the three-dimensional flow of sodium, and a multi-channel-simulation model was adopted to analyze steam–water two-phase flow in these heat-transfer tubes. Furthermore, a data-transfer method was

Fig.7-8 Simulation results of the SG test

(a) The circumferential-nonuniform-temperature distribution was evaluated by the three-dimensional method of TSG; this property was impossible to simulate with the previous two-dimensional method with an axisymmetric assumption. (b) The simulated sodium-temperature distribution along the height direction was consistent with the test data, and the capability of calculating the two-phase flow inside heat-transfer tubes (preheating, nucleate boiling, film boiling, and superheating) was confirmed.

developed for thermal coupling between sodium and water. To validate the TSG code, the existing SG tests were analyzed and its results were compared with the test data.

The test equipment is a 1-MWt double-walled straight-tube SG comprising 10 heat-transfer tubes, 3 dummy tubes without water in them, and 6 tie rods for maintaining the components. Fig.7-7(a) shows the simulation system and Fig.7-7(b) shows the horizontal cross-section of the simulation model. As shown in Fig.7-8(a), the sodium temperature on the outer side (where tie rods and dummy tubes exist) is higher than that at the central part (where heat-transfer tubes exist). Accordingly, the nonuniform-temperature distribution has been well captured by TSG. In Fig.7-8(b), the simulated sodium-temperature distribution along the height direction is consistent with the test data, and the influence of different heat-transfer coefficients corresponding to the flow-boiling regimes inside the heat-transfer tube (preheating, nucleate boiling, film boiling, and superheating) on the temperature distribution was confirmed. From these results, TSG was found to be applicable for analyzing three-dimensional thermal hydraulics in SG.

We plan to conduct further validation analyses and perform three-dimensional asymmetric-temperature evaluations for large-sized straight-tube SGs and structural-integrity analyses of heat-transfer tubes.

Reference

Yoshikawa, R. et al., Development of Sodium-Water Coupled Thermal-Hydraulics Simulation Code for Sodium-Heated Straight Tube Steam Generator of Fast Reactors, Proceedings of 11th International Topical Meeting on Nuclear Reactor Thermal Hydraulics, Operation and Safety (NUTHOS-11), Gyeongju, Korea, 2016, N11P0418, 12p., in USB Flash Drive.

7-3 Improvement of Maintenance Technology for Sodium-Cooled Fast Reactors — Development of a Visual-Inspection Device under Opaque Sodium —

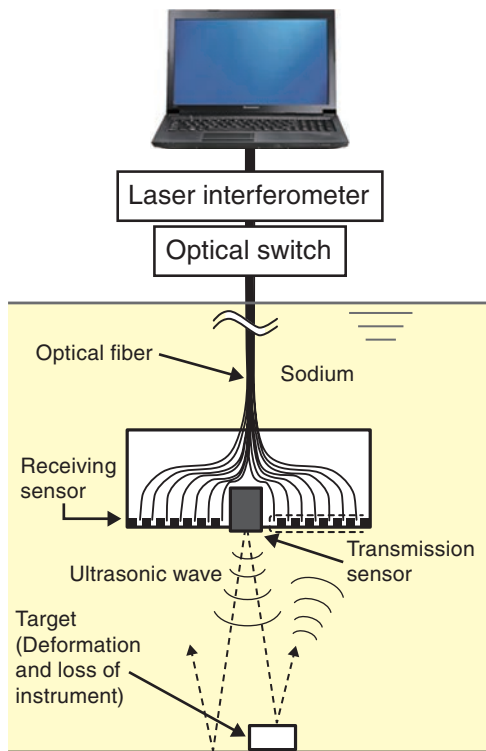


Fig.7-9 Composition of USV

USV detects the distance from the target using the delay between the transmission and reception times.

As a fundamental engineering task towards commercialization of fast-reactor-cycle technology, we have developed an under-sodium viewer (USV) for inspection in opaque-liquid-metal coolant.

The USV system will be operated at regular inspection times during commercial use. The USV is required to be able to perform quick inspections in order to conduct an efficient regular inspection. Therefore, we aim to develop a USV that can be used to conduct inspections from a 1-m distance and reduce the measurement time.

Fig.7-9 shows a schematic of the USV. A transmission sensor that includes a piezo element transmits an ultrasonic wave, which is received by receiving sensors located around the transmission sensor. The USV detects the distance from the target using the delay between the transmission and reception times. The USV can image a target using the time-delays at many receiving sensors. The USV in this study adopts an optical-receiving system that measures the vibration displacement of a diaphragm using a laser as a receiving sensor. The advantages of the optical-receiving system are low loss in signal convection and a high directivity angle leading to high resolution. The piezo element diameter was enlarged to

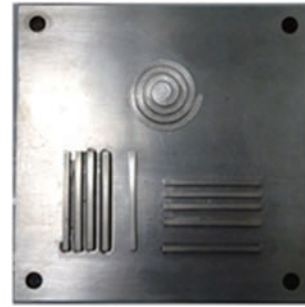


Fig.7-10 Photograph of an imaging target

The width of each line is 3 mm, and the distances between them are 3, 5, and 10 mm in the line target. The width of each line is 4 mm and the distance is 2 mm in height between each thread in the spiral target.

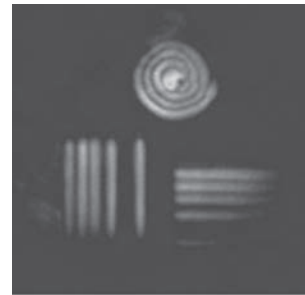


Fig.7-11 Result of an imaging experiment in water

The image obtained by the new USV sensors is clear from a distance of 800 mm.

increase the signal intensity with the aim of detecting signals at a distance of 1 m. It is important to reduce the dependence on signal processing, for example, the averaging procedure, with the aim of reducing the measurement time. Therefore, we improved the damping performance of the transmission sensor and reduced the noise in the receiving one. An imaging experiment was conducted using the new transmission and receiving sensors.

Fig.7-10 shows a photograph of the imaging target. The width of each line is 3 mm, and the distances between them are 3, 5, and 10 mm in the line target. The width of each line is 4 mm and the distance is 2 mm in height between each thread in the spiral target. Fig.7-11 shows the result of the imaging experiment in water from a distance of 800 mm. As shown in the Fig.7-11, the line and spiral targets can be clearly imaged. In the future, we will conduct imaging experiments in sodium to improve the transmission and receiving sensors to image the target more clearly.

This document includes part of the results of the “Technical development program on a commercialized FBR plant,” entrusted to the Japan Atomic Energy Agency (JAEA) by the Ministry of Economy, Trade and Industry, Japan (METI).

Reference

Aizawa, K. et al., Development of Under Sodium Viewer for Next Generation Sodium-Cooled Fast Reactors, Proceedings of International Conference on Fast Reactors and Related Fuel Cycles: Next Generation Nuclear Systems for Sustainable Development (FR17), Yekaterinburg, Russia, 2017, 9p., in USB Flash Drive.

7-4 Progress in Reactor Modeling during Natural-Circulation Cooling — Validation of a Reactor Analytical Model using Measured Data —

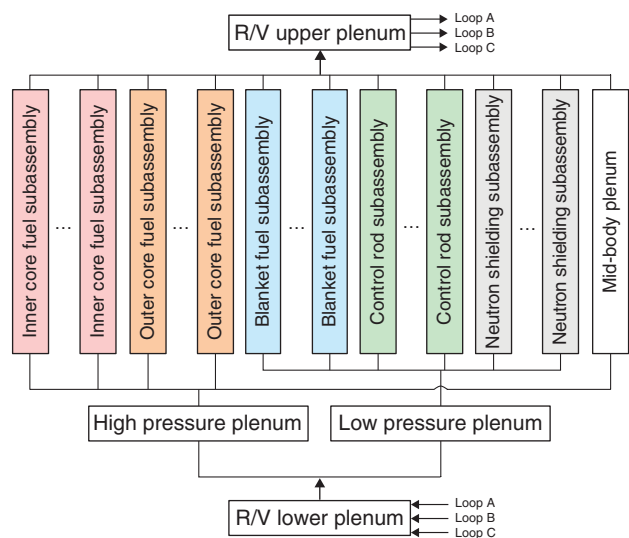


Fig.7-12 Whole core model

This analytical model can simulate heat transfer among core elements such as the core fuel subassembly and can calculate their temperatures and flow rates. Core fuel subassemblies are connected to the high-pressure plenum, whereas others are connected to the low-pressure plenum in the Monju Reactor.

After the accident at the TEPCO's Fukushima Daiichi NPS, new regulatory requirements considering severe accidents (SAs) were established. Therefore, strengthening plant against natural disasters and preparing safety measures against SAs such as long-term station blackouts (SBOs) are of critical importance. In the event of an SBO, the experimental fast reactor Joyo and the prototype fast-breeder reactor Monju employ decay-heat removal from the core into atmosphere through air coolers using natural circulation of sodium coolant, which requires no power supply.

This decay-heat removal by a fully natural circulation system is adopted in the design of the Japan Sodium-cooled Fast Reactor. As the driving force of coolant is the only buoyancy in natural circulation, the coolant-flow rate is very small. Therefore, two phenomena, namely radial-heat transfer and flow redistribution among core elements such as core subassemblies, become dominant during natural circulation and dynamically change the temperature and flow rate into each core element.

Therefore, a whole-core model considering the heat-transfer effect among subassemblies and flow redistribution has been developed to predict their behavior for each core element (Fig.7-12). The two effects in this model were already validated by test results of natural circulation at the sodium test loop, PLANDTL, and the experimental fast reactor, Joyo. In this study, we comprehensively validated that the whole-core model

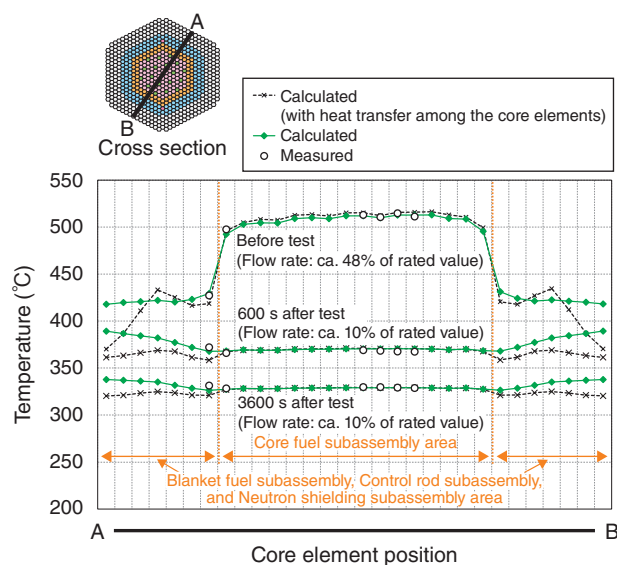


Fig.7-13 Comparison between the analytical result and the measured data

This figure shows the temperature distribution of the core-element outlet on the cross section shown in the figure. The outermost layer of the neutron shielding subassembly is adiabatic under the analytical condition. The analytical results agree well with measured values at each time.

could be applied for MONJU by comparing with the result of the plant-trip test at 40% power. An empirical formula based on the data obtained for a flow rate ranging from low to rated flow rate was applied to the pressure model of each core element.

The measured temperature distribution in the core-element outlet on the cross section at time periods of 600 s and 3600 s after the plant trip with a 10% flow rate differed from the distribution before the plant trip. The temperature of the innermost layer of the blanket fuel subassembly area with almost no heat is higher than that of the core fuel subassembly. The calculated temperature distributions of the core-element outlet agree well with those measured at each time (Fig.7-13). The temperatures of the blanket fuel subassembly, the control rod subassembly, and the neutron shielding subassembly area with almost no heat differ significantly from those without heat-transfer among subassemblies. We observed that heat transfer from core fuel assemblies had significant effects to the temperature distribution and confirmed that the whole-core model can simulate heat transfer among core elements such as the core fuel subassembly; we also calculated the temperature distribution correctly in flow conditions of more than 10%.

Hence, this model can evaluate the plant behavior of a large reactor during natural circulation using an empirical formula based on the data for the low-flow-rate condition.

Reference

Mori, T. et al., Validation and Applicability of Reactor Core Modeling in a Plant Dynamics Code during Station Blackout, Proceedings of 2017 International Congress on Advances in Nuclear Power Plants (ICAPP 2017), Fukui and Kyoto, Japan, 2017, paper 17409, 9p., in DVD-ROM.

7-5 Advancing the Separation Process for Spent Nuclear Fuel Reprocessing — Development of a Sludge-Cleaning Method in a Centrifugal Contactor —

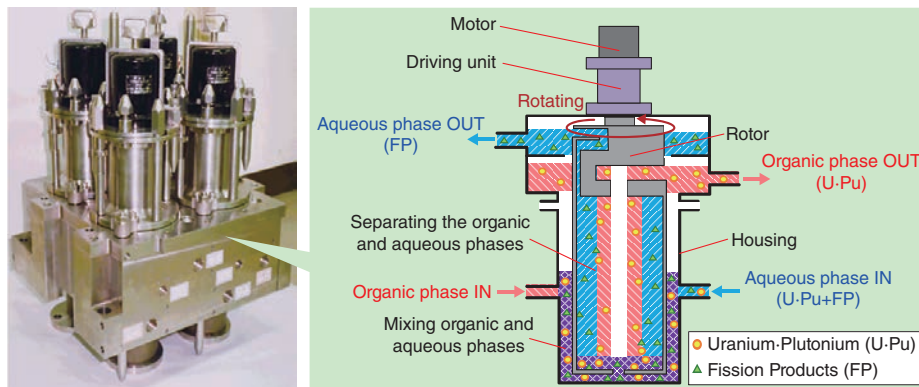


Fig.7-14 Schematic of a centrifugal contactor

A centrifugal contactor comprises a motor, driving unit, rotor, and housing. Aqueous-phase and organic-phase are mixed in the annular area (between the rotor and the housing), and then the mixed phase is separated in the rotor.

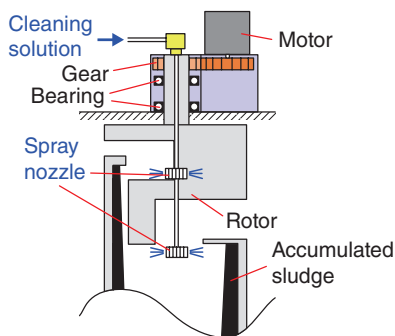


Fig.7-15 Addition of the spray nozzle

We introduced the spray nozzle to the rotor to more efficiently clean the sludge accumulated there.

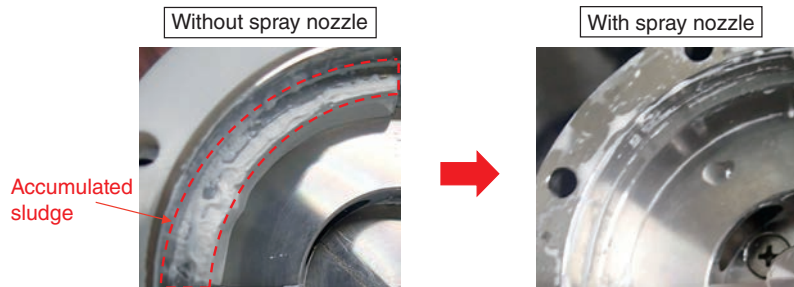


Fig.7-16 Effect of spray nozzle upon cleaning performance (upper rotor)

The sludge accumulated in the upper rotor could not be cleaned without the spray nozzle (left); in contrary, it could be significantly cleaned by introducing a spray nozzle (right).

We have been developing a centrifugal contactor for the solvent extraction process in spent nuclear fuel reprocessing (Fig.7-14).

A centrifugal contactor allows mixing of aqueous and organic phases in the annular area and separates them in a rotor using its strong centrifugal force. This characteristic reduces the residence time of the mixed solution compared to other apparatuses, e.g., mixer settlers, or pulsed columns, thereby preventing solvent degradation.

The centrifugal contactor has been used in the purification stage of reprocessing plants; however, it has not been used in the extraction stage for uranium and plutonium due to the sludge that is contained as fine particles or insoluble residue in the feed solution.

It is difficult to remove sludge perfectly from the process solution; therefore, we experimentally evaluated the sludge accumulation behavior in the centrifugal contactor and its influence on phase separation and extraction performance.

The result showed that the sludge was accumulated only in the rotor and decreased the separation performance.

As it is necessary to keep the centrifugal contactor clean for stable operation, we tried to introduce a spray nozzle for efficient cleaning. We embodied the structure of the spray nozzle in the centrifugal contactor by surveying the relation between its structure and the cleaning performance (Fig.7-15). This centrifugal contactor supplies the cleaning solution from the top of the rotor, which decreases the risk of radioactive-solution leakage and makes maintenance easier.

This new centrifugal contactor could perfectly clean the accumulated sludge with 20% of the cleaning solution and time needed by conventional centrifugal contactors (Fig.7-16).

Through this study, we could establish an efficient cleaning method for sludge accumulated in the centrifugal contactor.

The present study was sponsored by the Ministry of Economy, Trade and Industry, Japan (METI).

Reference

Sakamoto, A. et al., Effect of Sludge Behavior on Performance of Centrifugal Contactor, *Procedia Chemistry*, vol.21, 2016, p.495-502.

Decommissioning of Nuclear Facilities and Radioactive Waste Management

Five old nuclear-power plants in Japan have been slated for decommissioning. Extensive decommissioning of nuclear facilities will start in the near future. For safe and appropriate nuclear-facility decommissioning and radioactive waste management, introducing new technologies and knowledge and promoting the development of technologies for advanced safety and cost reduction is necessary. We have been comprehensively developing technologies for safe and effective dismantling of nuclear facilities for minimization and stabilization of radioactive wastes and for radioactive waste disposal. Our disposal-project is intended to cover low-level radioactive wastes from research facilities at universities and private organizations, as well as from JAEA's own facilities (Fig.8-1).

The technological development achievements in this fiscal year include

- An equivalent-model method for correcting density and

source localization using multiple γ rays with different energies at the Ningyo-toge Environmental Engineering Center (Topic 8-1)

- Comparison of the activation/burn-up calculation with sampled-chemical analysis of the composition ratios of 17 candidate nuclides for safety assessment of waste disposal from post-irradiation test facilities; this research serves as a technique for verifying radioactivity concentrations in wastes (Topic 8-2)

In addition to the above, the following R&D results concerning the response to the accident at the TEPCO's Fukushima Daiichi NPS were summarized in Chapter 1.

- Investigation of the influence of sea-water and concrete components on nuclear-fuel-reprocessing-equipment materials (Topic 1-6)
- Development of a portable small α -ray position detector (Topic 1-8)

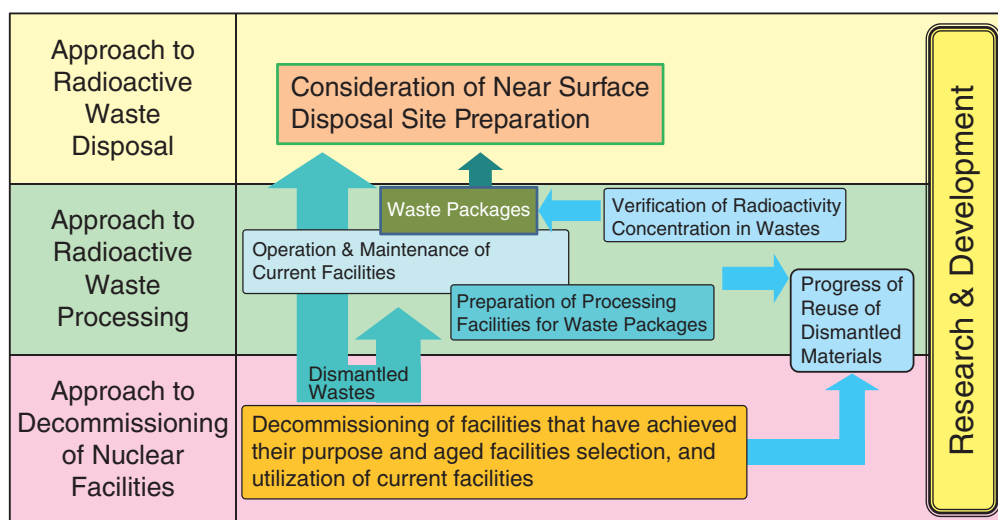


Fig.8-1 Outline of low-level radioactive waste management

Systematic promotion of developing technologies for decommissioning nuclear facilities and managing radioactive waste from generation through to disposal.

R&D to Improve Geological Disposal Technology and Reliability in Japan

Geological disposal is an option for long-term isolation of high-level radioactive waste (HLW) produced during nuclear-power generation from human environments. This is a critical issue with which the present generation must sensibly deal, and it will remain crucial in the future regardless of any revision of the national nuclear-energy policy.

In Japan, spent fuel from power reactors is reprocessed to extract reusable uranium and plutonium for power generation. The highly active liquid waste separated from the spent fuel during chemical reprocessing is solidified into a stable glass form. Under the Japanese disposal concept, vitrified wastes are then encapsulated in a thick steel overpack surrounded by highly compacted bentonite and placed in a stable geological environment at a depth of more than 300 m below the surface (Fig.8-2).

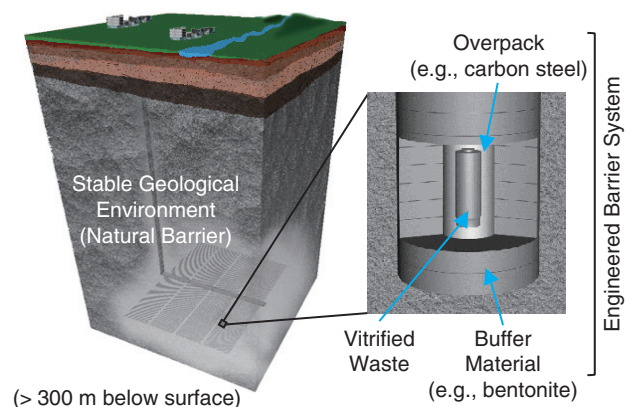


Fig.8-2 Schematic view of the basic concept for geological disposal of high-level radioactive waste in Japan

Implementing geological disposal of HLW is a long-term project that will last over 100 years. The project begins with site selection and continues to repository construction and operation, which will be followed by backfill for repository closure. It is, thus, of great importance to proceed efficiently with the project as a national responsibility by continuously improving its sound technical basis and applying these attitudes to implementation, regulatory activities, and most importantly enhancement of public confidence. To this end, we have made and will continue to make steady progress towards R&D in various fields, including geoscience, repository engineering, and safety assessment, with the aim of improving the technologies used for reliable geological disposal in Japan.

Underground Scientific Research

At present, our R&D is focused specifically on projects at two underground research laboratories (URLs). One at Mizunami, which researches crystalline rocks, and the other at Horonobe, which researches sedimentary formation (Fig.8-3).

Various techniques and methodologies for investigating geological characteristics have been developed, and research on understanding long-term hydrological and/or mass-transport behavior has been conducted at URLs (Topics 8-3, 8-4, and 8-6). R&D on engineered barrier systems using underground

galleries has started at Horonobe (Topic 8-5).

In addition, there are ongoing studies on tectonics, volcanic and faulting activities, and the like, to evaluate the long-term stability of geological environments in Japan. As a base technology for these studies, the development of dating techniques using advanced equipment for isotope geology and geochronology are ongoing at the Toki Research Institute of Isotope Geology and Geochronology (TRIGGER) (Topic 8-7).

Research and Development on Geological Disposal Technologies

In parallel with such geoscientific efforts, we are conducting an extensive study on repository design and safety assessment of the disposal system at the Nuclear Fuel Cycle Engineering Laboratories in Tokai based on experiments and models of the long-term evolution of the disposal system and radionuclide migration (Topics 8-8 and 8-9). These studies exploit data and information that were obtained at both URLs.

The prototype knowledge-management system that was developed in 2010 is being improved and managed steadily. Furthermore, the results of the R&D activities have been summarized as a web-based report (CoolRep), which is available on JAEA's public website (CoolRep: <http://kms1.jaea.go.jp/CoolRep/index.html>).

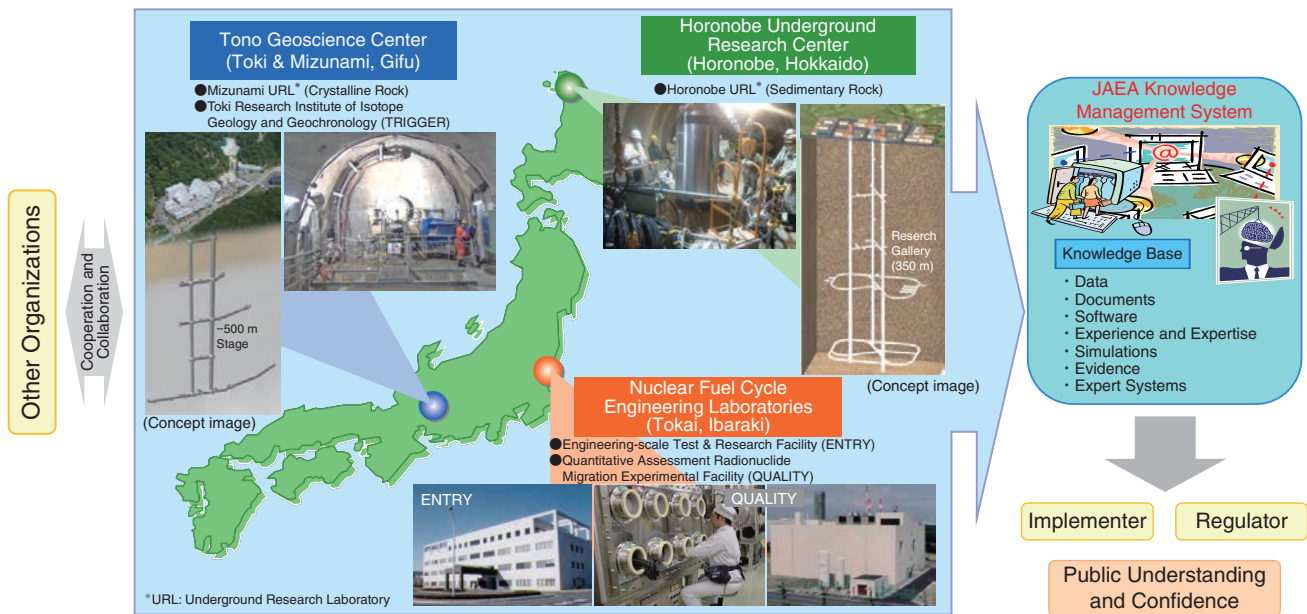


Fig.8-3 Structure of JAEA R&D activities

Improvement of Safety and Technologies of Fuel Reprocessing

The Tokai Reprocessing Plant promotes high-level radioactive-liquid-waste vitrification and Pu-solution solidification to MOX powder to reduce the risk to this facility caused by radioactive material stored in the solution state. The Pu solution completed solidification to MOX powder in July 2016. Vitrification of the high-level radioactive-liquid waste is planned to be completed by the 2028 Japan fiscal year. We are steadily promoting this process with a primary focus on safety. We have also developed advanced vitrification technologies as well as solidification technologies for low-level radioactive-liquid waste. Development of our solidification technologies, nitric-acid-decomposition treatment, and new-cement solidification techniques are ongoing.

The remaining nuclear material to be processed in this facility is still subject to International Atomic Energy Agency (IAEA) and Nuclear Regulation Authority (NRA) inspection, despite our risk-reducing activities. Performance improvement of the non-destructive assay (NDA) technique for plutonium-nitrate solution was conducted by joint research with Los Alamos National Laboratory in the United States.

In this research, we can confirm accurate and rapid evaluation of the amount of plutonium in a solution sample using three types of neutron-coincidence-counting techniques (Topic 8-10).

In addition to the above, we attempt to understand the properties of residues generated by reprocessing irradiated fast-reactor fuel (Topic 8-11).

8-1 Quantifying the Radioactivity of Waste Products

— Accuracy Improvement of a Quantitative Method Focused on Scattering γ -rays —

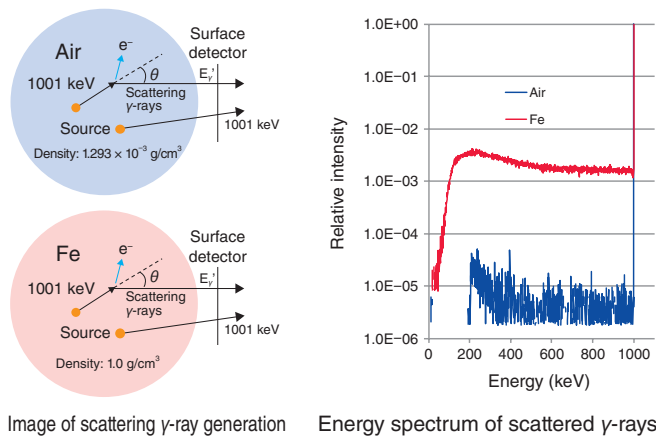


Fig.8-4 Simulation of γ -ray scattering

1001-keV γ -rays scattered from U progeny nuclides were determined using the transportation-calculation code MCNP. The shielding materials are composed of iron and air. The γ -ray spectra shielded with these components were calculated and compared with one another. Using scattered γ -rays over a wide range, the accuracy of the radioactivity determination was improved.

Dismantled materials generated from nuclear facilities are reused or disposed in repository sites. Confirmation of their radioactivity is required.

If confirmation of the clearance level of metal samples with complicated shapes were possible, the amount of waste could be reduced.

Even if wastes have complicated shapes, their radioactivity concentration can be measured by γ -ray measurement, since γ -rays have strong material-penetrating power.

Uranium (U) has a low γ -ray-emission rate. Therefore, increasing measurement efficiency is necessary. Semiconductor detectors have high resolution but low detection efficiency; hence, measurements with such detectors take a long time. To shorten the measurement time, it is reasonable to use a highly efficient NaI detector.

The shielding of γ -rays differs depending on the density of materials and the source localization. If the radioactivity concentration is evaluated by assuming that the density and source distribution of samples are homogenous, large errors will occur. For this reason, we estimated the attenuation due to the distance between the source and detector using measured values for two γ -rays (a, b) with different energies.

Let us consider the attenuation factor, X_{geometry} . Here, let r be the distance from the source to the detector and μ_a, μ_b be the linear-attenuation coefficients of different energies of two γ -rays; the γ -ray counting rate, n_a , can be shown as $n_a \sim e^{-\mu_a r} / r^2$.

Reference

Yokoyama, K. et al., Verification of a Quantitative Method of Uranium238 in the Radioactive Waste using Photon Occurred by Compton Effect, Radioisotopes, vol.64, no.11, 2015, p.687-696 (in Japanese).

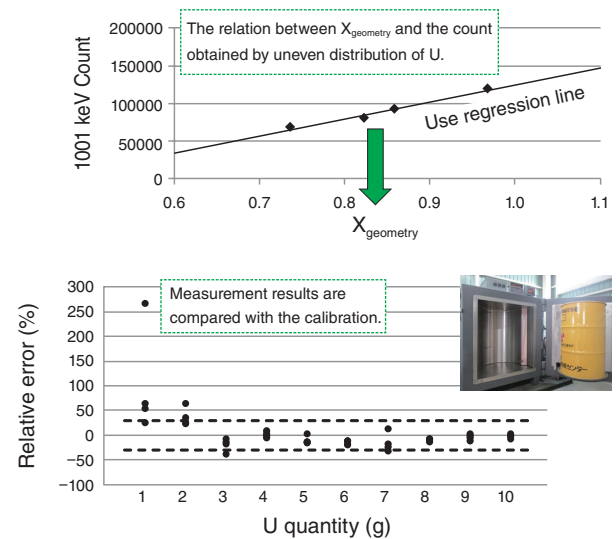


Fig.8-5 Relative error in radioactivity determination

U (1–10 g) was placed in a simulated drum (200 kg). Two NaI detectors (3 × 5 × 16 inch) were used for measurement over a period of 1800 s. If the acceptable relative error is approximately $\pm 30\%$, the lower limit of quantification was approximately 0.4 Bq/g, which is independent of the distribution of U sources. It seems that the radioactivity concentration below 1.0 Bq/g can be quantified, even if the error is included.

In this case, 'r' in $\ln(n_a/n_b) \sim -(\mu_a - \mu_b)r$ can be shown by the logarithm of the ratio of the counting rate. When the density distribution of the sample is regarded as homogeneous, the influence of different positions of sources is mainly expressed as $1/r^2$. When $-\ln(n_a/n_b)$ is substituted for 'r', the X_{geometry} can be expressed as follows (equivalent-model method):

$$X_{\text{geometry}} = \frac{1}{(\ln(1/(n_a/n_b)))^2}$$

It is possible to replace the average distance between multiple source positions and detectors with one equivalent distance. A calibration curve is represented by the regression line calculated from X_{geometry} and a counting rate of 1001 keV is obtained from a certain known amount of U. Comparing the plot obtained by measuring samples with the calibration curve, the U amount can be measured.

Though γ -rays of 1001 keV and 766 keV have been used for evaluation, the lower limit of quantitation of radioactivity was approximately 4 to 5 Bq/g (approximately 40 g of U) because of their low emission limits. Hence, we improved the accuracy of low-level radioactivity determination using scattered γ -rays with high counting rate (Fig.8-4). We tested our method with a simulated drum of 1.0 Bq/g or less using a commercially available device (Fig.8-5). In spite of the uneven distribution of the source, we were able to obtain a lower limit of quantification (below 1.0 Bq/g) required for the evaluation of the clearance level.

8-2 Radioactivity-Confirmation Method for the Disposal of Low-Level Waste

— Evaluation Method to Determine the Radioactivity Concentration in Radioactive Waste Generated from Post-Irradiation Examination Facilities —

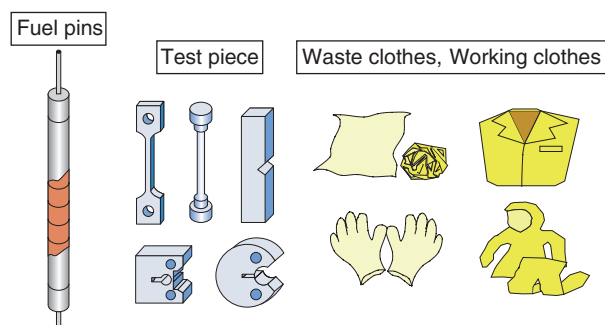


Fig.8-6 Example of waste generated from post-irradiation examination facilities

Irradiation fuel, materials irradiated in a nuclear reactor, waste, and working clothes used in examinations were selected as sample materials.



Fig.8-7 Sample of combustible wastes

Rubber gloves were gathered as a waste sample from waste housed in containers.

A technique for evaluating the radioactivity concentration must be developed to enable the disposal of waste products generated from research, industrial, and medical facilities. The waste generated from post-irradiation-examination (PIE) facilities (Fig.8-6) includes a large number of radionuclides from irradiation fuel and materials irradiated in a nuclear reactor. Therefore, establishing methods to reasonably confirm these nuclides is necessary. We calculated the radioactivity-concentration ratio (nuclide-composition ratio) of nuclides in irradiation fuel and irradiated materials based on burn-up calculations; we also devised a method for evaluating the radioactivity of waste using this nuclide-composition ratio. In this study, the analytical nuclide-composition-ratio value was considered against the value theoretically calculated.

Seventeen nuclides (^3H , ^{14}C , ^{60}Co , ^{63}Ni , ^{90}Sr , ^{99}Tc , ^{137}Cs , ^{154}Eu , ^{234}U , ^{235}U , ^{238}U , ^{238}Pu , ^{239}Pu , ^{240}Pu , ^{241}Pu , ^{241}Am , and ^{244}Cm) were selected as evaluation-target-candidate nuclides for the burial disposal of radioactive waste of PIE facilities in this study. For such nuclides, the nuclide-composition ratio for

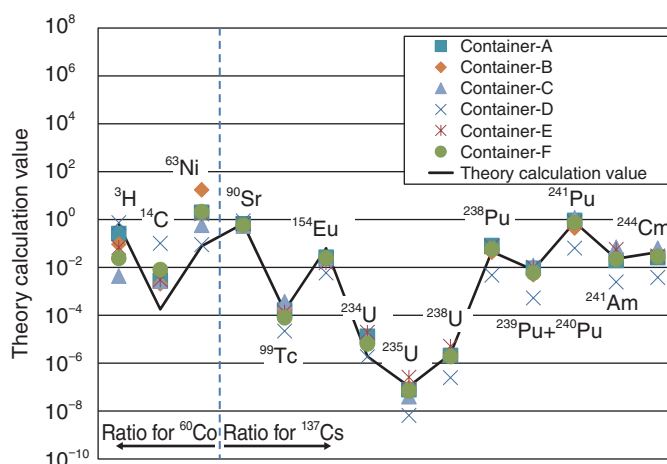


Fig.8-8 Comparison of the nuclide-composition ratios of analytical and theoretically calculated values

For ^{90}Sr , ^{99}Tc , ^{154}Eu , ^{234}U , ^{235}U , ^{238}U , ^{238}Pu , $^{239}\text{Pu}+^{240}\text{Pu}$, ^{241}Pu , ^{241}Am , and ^{244}Cm , the analytical value of the nuclide-composition ratio accorded with that obtained by theory. Differences were seen in the ratios of ^{14}C and ^{63}Ni ; this suggests that considering the contribution of radioactive cladding in a refrigerant and the influence of different elementary compositions of materials is necessary. Each waste sample taken from a container A–F comprised polluted waste from one type of irradiation fuel or irradiated material. The theoretical nuclide-composition ratio was determined by burn-up calculation.

^{60}Co or ^{137}Cs was calculated based on the result of chemical analysis of a sample of combustible wastes (Fig.8-7) generated from PIE facilities. On the other hand, the theoretical nuclide-composition ratio using the burn-up calculation was determined based on the irradiation condition of the materials in question.

It was observed that the theoretical nuclide-composition ratios of ^{90}Sr , ^{99}Tc , ^{154}Eu , ^{234}U , ^{235}U , ^{238}U , ^{238}Pu , $^{239}\text{Pu}+^{240}\text{Pu}$, ^{241}Pu , ^{241}Am , and ^{244}Cm occurring in the fuel agreed well with their analytical values (Fig.8-8). On the contrary, for ^{14}C and ^{63}Ni , which were corrosion products of materials, a difference was seen between the analytical and experimental nuclide-composition ratios. We believe that this result suggests the necessity of considering the contribution of radioactive cladding in a refrigerant and the influence of differences in the elementary compositions of materials.

We are presently examining the influence of the above factors upon the nuclide composition of irradiation fuel and irradiated materials with the aim of improving this method.

Reference

Tsui, T. et al., Study on the Evaluation Method to Determine the Radioactivity Concentration in Radioactive Waste Generated from Post-Irradiation Examination Facilities – Part 2 –, JAEA-Technology 2017-010, 2017, 75p. (in Japanese).

8-3 Understanding the Self-Sealing Function of the Underground Environment

— Study of the Long-Term Behavior of Hydrogeological Structures Related to Faulting —

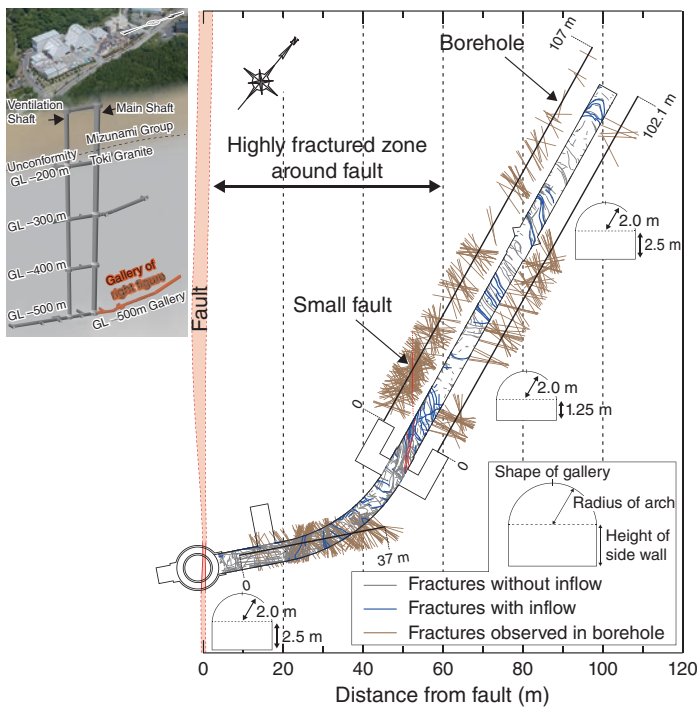


Fig.8-9 Fracture distribution at the GL -500 m gallery and layout of the Mizunami Underground Research Laboratory
Fractures with groundwater inflow comprise approximately 10% of all known fractures (146 of 2002 fractures) at the GL -500 m level. A highly fractured zone extends approximately 60 m from the fault.

Understanding long-term groundwater flow is critical to assess the safety of geological disposal of high-level radioactive waste (HLW). Fractures in crystalline rock, such as granite, function as pathways for groundwater flow. Characteristics of fractures have the potential to change due to faulting and/or formation of fracture fillings. The dynamic behavior of hydrogeological structures around faults has therefore been studied at 500 m below ground level (GL) in the Mizunami Underground Research Laboratory (Fig.8-9).

Detailed borehole and gallery-wall investigations indicate that there are three stages in the development of hydrogeological structures (Fig.8-10). The first stage is characterized by the formation of relatively large primary fractures after the temperature of the granite pluton has decreased through the ductile-brittle transition and is subjected to brittle-deformation conditions. Collectively, these primary fractures act as the primary pathway for groundwater. The second stage is associated with faulting of the pluton and formation of a damage zone containing relatively small fractures, which act to increase

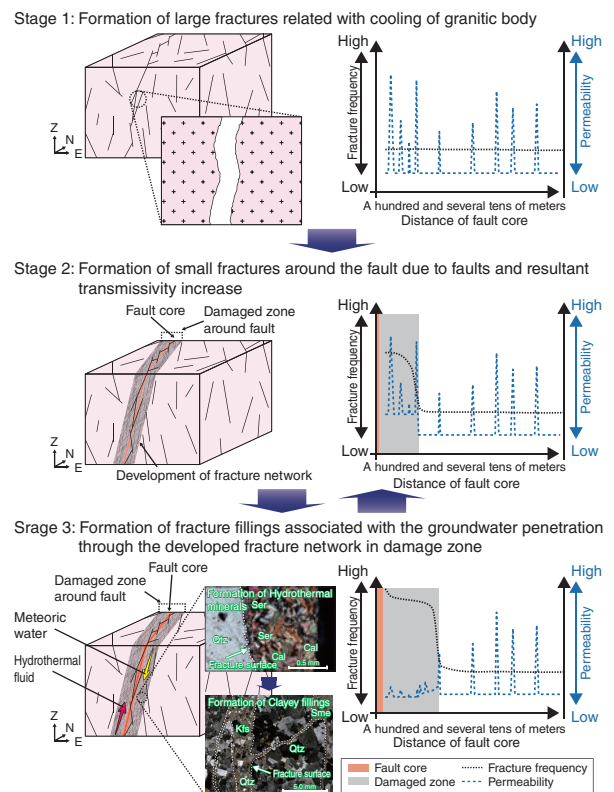


Fig.8-10 Long-term behavior of hydrogeological structures around faults

The permeability of the damage zone is increased by faulting but decreased by precipitating and injecting minerals to close and/or seal fractures by penetration of reactive groundwater and fault reactivation.

the hydraulic permeability. The third stage is marked by a decrease in the hydraulic permeability of the damage zone caused by the precipitation of secondary minerals, typically including sericite, chlorite, and calcite, from the infiltration of reactive groundwater. As much as 90% of fractures can be sealed in this manner. Additionally, unconsolidated clayey fillings, which are formed by injected under high-pressure pore water associate with fault reactivation, can act as a natural grout material. These fillings are a unique feature of active orogenic fields found in the Japanese islands.

The underground environment has the potential to decrease the hydraulic permeability of fractures and faults in the long term by a natural “self-sealing function”. Processes that contribute to this function include the precipitation of minerals from infiltrating reactive groundwater and the injection of material under high pressures associated with fault reactivation. These processes are considered favorable for the geological disposal of HLW in the active orogenic fields of the Japanese islands.

Reference

Ishibashi, M. et al., Long Term Behavior of Hydrogeological Structures Associated with Faulting: An Example from the Deep Crystalline Rock in the Mizunami URL, Central Japan, Engineering Geology, vol.208, 2016, p.114-127.

8-4 Micropores Retarding Mass Transport in Granitic Rock — Visualization and Observation of Matrix-Diffusion Pathways —

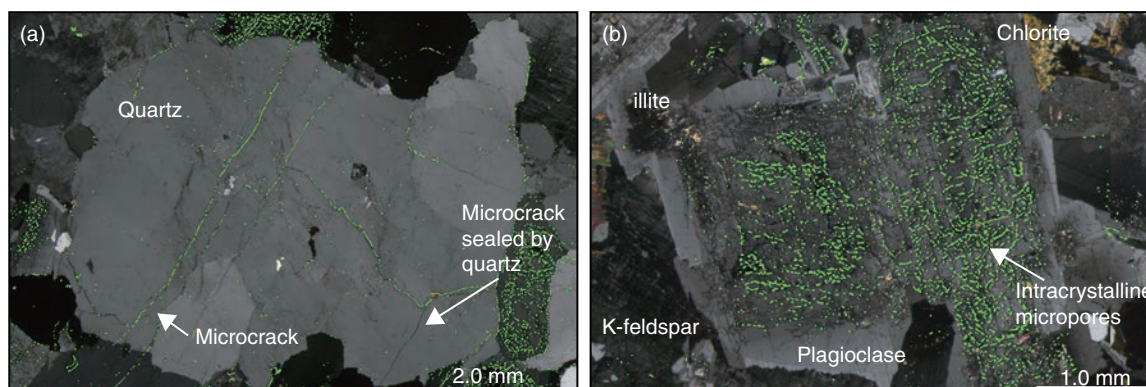


Fig.8-11 Mode of occurrences of micropores in granitic rock

Green color delimits (a) microcracks in quartz and (b) micropores in a plagioclase crystal, as observed by fluorescence microscopy.

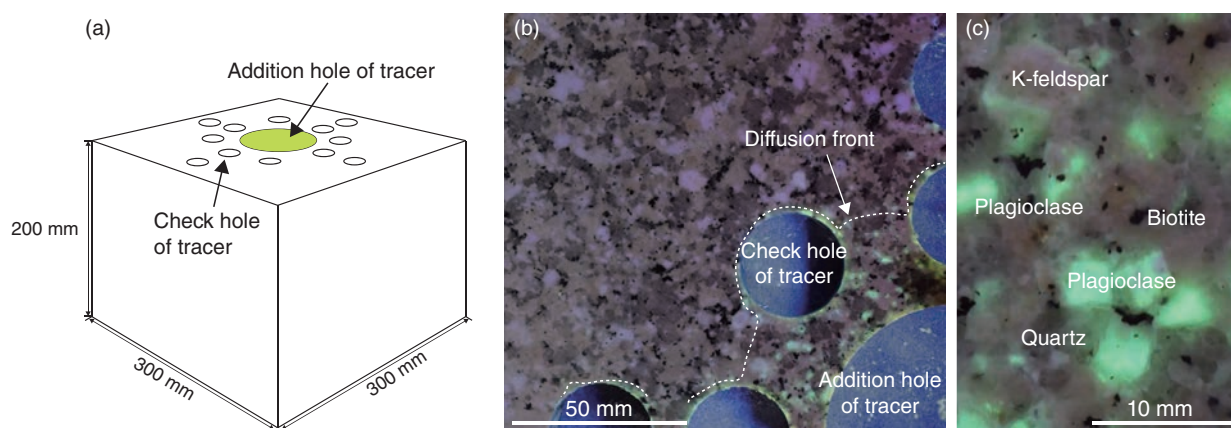


Fig.8-12 Result of a diffusion test using a rock-block scale

(a and b) Diffusion of tracer material (pale green) into intact rock is confirmed by a rock-block-scale diffusion test. (c) Tracer materials mainly observed in the plagioclase.

Dissolved matter in groundwater is transported through fractures in crystalline granite rocks and is largely retarded by diffusion into the micropores of the rock matrix, a process known as matrix diffusion. An important aspect of understanding matrix diffusion is the distribution and connectivity of the micropores, which act as diffusion pathways. Matrix diffusion and high retardation factors are advanced in granitic rocks that have been altered by weathering and hydrothermal circulation, causing increased distribution and connectivity of the micropores. Despite their prominence, however, few matrix-diffusion studies have investigated unaltered granitic rocks. A method based on fluorescence microscopy has therefore been developed to visualize and characterize micropores in crystals (Fig.8-11) and matrix diffusion through a rock-block scale diffusion test using unaltered samples of Toki granite from JAEA's Mizunami URL (Fig.8-12).

To identify the distribution of micropores using fluorescence microscopy, a fragment of rock ground to a thickness of approximately 0.03 mm was attached to glasses with bonds

including fluorescent agents. As a result, microcracks were observed in quartz (Fig.8-11(a)) and intracrystalline micropores were observed in plagioclases and the cleavage planes of biotite (Fig.8-11(b)). In addition, the proportions of micropore in plagioclase demonstrated a higher value than other crystals. The formation of micropores in plagioclase is caused by the reaction of plagioclase with fluids in the final stages of granitic-rock cooling, a process known as deuteritic alteration, which is widespread in Japanese granites. In the rock-block-scale diffusion test, tracer materials were mainly observed in plagioclases (Fig.8-12(c)); therefore, the intracrystalline micropores in plagioclase act as the dominant matrix-diffusion pathways.

The micropores in plagioclase, caused by deuteritic alteration, acted as the dominant matrix-diffusion pathways in Toki granite. This mechanism of matrix diffusion will be further tested and may prove to be of general applicability given the widespread occurrence of deuteritic alteration of plagioclase in the granitic rocks of Japan.

Reference

Ishibashi, M. et al., Characteristics of Micro Transfer Paths and Diffusion Phenomena in the Matrix of Deep Crystalline Rock, Genshiryoku Bakkundo Kenkyu (Journal of Nuclear Fuel Cycle and Environment), vol.23, no.2, 2016, p.121-130 (in Japanese).

8–5 Demonstration of Geological Disposal Technology in a Real Underground Environment

— Technological Development for an In situ Experiment to Confirm the Performance of an Engineered Barrier System at the Horonobe Underground Research Laboratory (URL) —

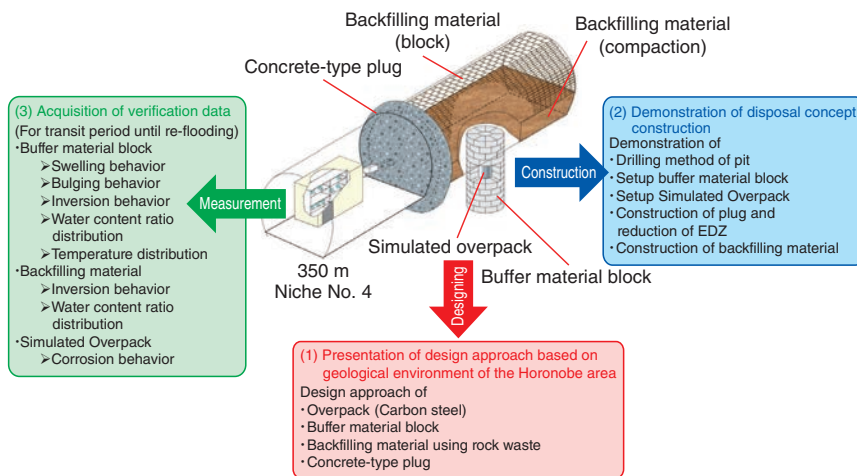


Fig.8-13 Proposal and operational content of the EBS experiment

In the EBS test, buffer material blocks and a simulated overpack of realistic size, weight, and heat generation were placed in a test pit. The vertical emplacement concept of the engineered barrier system is based upon the H12 report (JNC, 1999).

Disposal of high-level radioactive waste (HLW) in Japan will likely be in a purpose-built repository buried deep in the geosphere. The scientific and technical basis for ensuring repository performance in the long term have been written into the *Second progress report on research and development for the geological disposal of HLW in Japan*, referred to as the H12 report (JNC, 1999). Many of the requirements, however, have not yet been tested under full-scale, in situ conditions. At the 350-m depth of the Horonobe URL, full-scale, *in situ* experiments are therefore being conducted to confirm the scientific and technical basis of the engineered barrier system (EBS test) of a HLW repository (Fig.8-13). The objectives of the EBS test are (1) presentation of design methods for an engineered barrier system using the underground environment of Horonobe URL as an example, (2) construction of the HLW disposal concept as described in the H12 report, and (3) acquisition of verification data of coupled thermal–hydraulic–mechanical–chemical (THMC) processes that will affect the long-term performance of the bentonite buffer. In the EBS test, the design method was taken from the H12 report and applied to the geological-sedimentary soft-rock characteristics of the Horonobe URL. In particular, the applicability of the design method was tested through the development and production of a drilling machine for the large-diameter pit required for the vertical-emplacement concept, the production of buffer material block and backfilling material, and the implementation of updates in the design methods as needed.

The rotary-excavation method of fixing the excavating



Fig.8-14 Drilling machine for a large-diameter pit

A disposal pit 2.4 m in diameter and 4.5 m in depth was successfully drilled using this machine.



Fig.8-15 Production of a backfilling material block

Preparation of 30 × 30 × 10-cm³ backfilling material blocks for manual installation, with each block weighing approximately 16 kg. These blocks were manufactured by compression molding with the 80-t pressing machine visible in the background.

machine to the bottom of the gallery is described in the H12 report as being suitable for drilling a pit in soft sedimentary rock. In the current EBS test, a self-propelled large-diameter excavator was developed and produced (Fig.8-14), combining casing drilling and auger excavation and allowing continuous drilling of a disposal pit in a soft sedimentary rock. Through this experiment, the applicability of the excavator to drilling a full-scale disposal pit in situ in a soft sedimentary rock at 350-m depth was confirmed.

Backfilling of the disposal tunnels in a HLW repository will reuse a large amount of the rock waste that was produced in excavating these tunnels. In the EBS test, the backfilling material of bentonite and actual waste rock from the construction of the Horonobe URL was specifically mixed and found to have satisfactory performance requirements, including low water permeability. Backfilling of the EBS-test gallery using this material was successfully completed (Fig.8-15). The technology required to backfill the disposal tunnel with the machine was not developed in the current EBS test, but will be in the future.

The current-design method of the EBS of an HLW repository located in soft sedimentary rock was satisfactorily demonstrated through the EBS test. The EBS test continues to acquire verification data concerning THMC processes operating in a full-scale, in situ experiment, which will be used to underpin the development of predictive THMC models. The EBS test will be dismantled in the future when further analyses are conducted to further improve the design method.

Reference

Nakayama, M. et al., The In-Situ Experiment for Performance Confirmation of Engineered Barrier System at Horonobe Underground Research Laboratory – Production of Casing Drilling Machine for Large Diameter Pit, Simulated Overpack, Buffer Material Blocks and Backfilling Materials –, JAEA-Research 2016-010, 2016, 57p. (in Japanese).

8-6 Investigation of the Fault Distribution in Sedimentary Rocks

— Relationship between Faults Oriented Parallel and Oblique to Bedding in Neogene Massive Siliceous Mudstones —

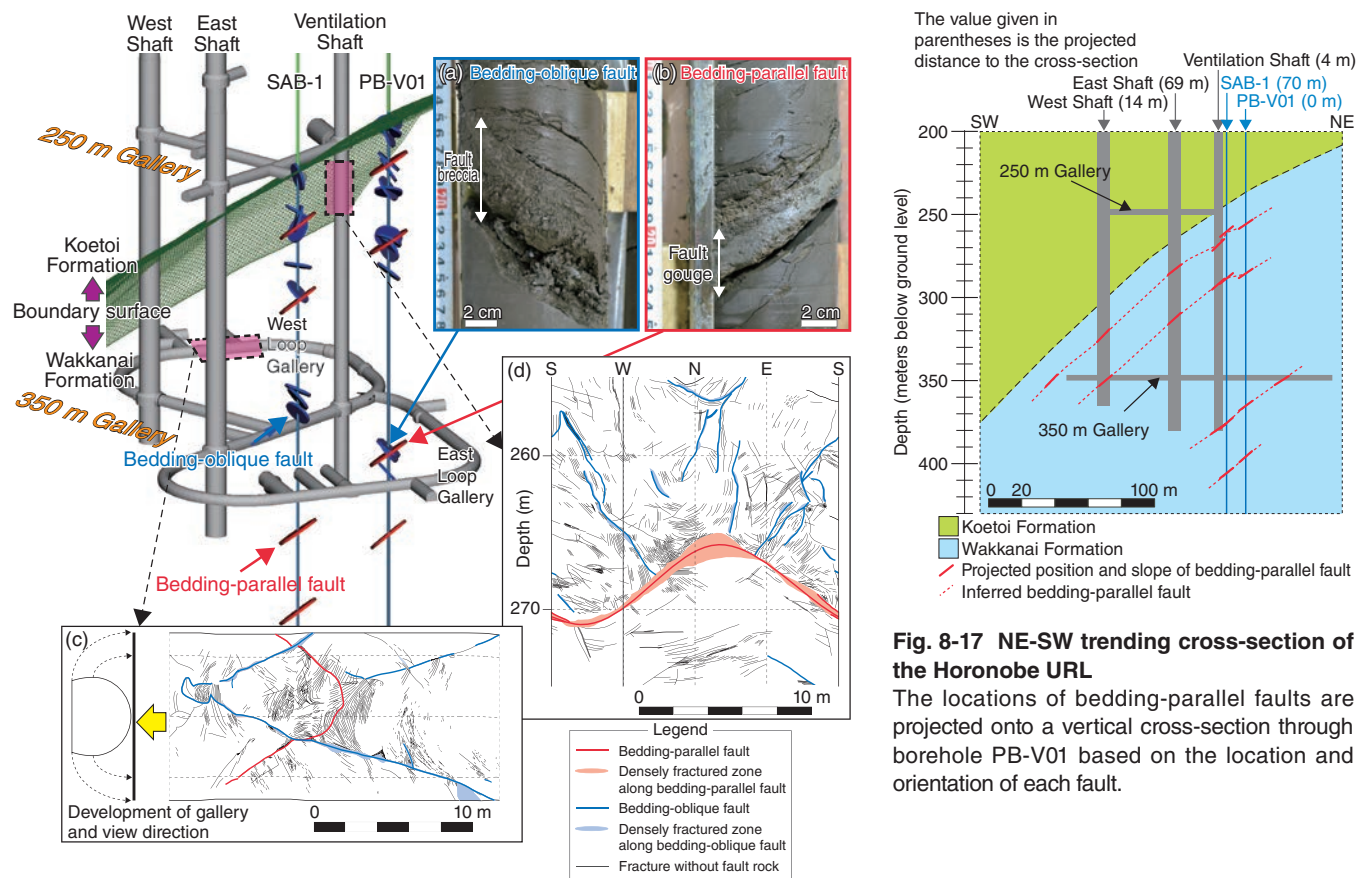


Fig.8-16 Horonobe URL site and faults observed in pilot boreholes SAB-1 and PB-V01

- (a) Sample of a bedding-oblique fault observed at a 363.17-m depth in borehole PB-V01.
 (b) Sample of a bedding-parallel fault observed at a 365.20-m depth in borehole PB-V01.
 (c) Map showing fractures on the gallery wall of the 350-m West Loop Gallery.
 (d) Map showing fractures on the Ventilation-Shaft wall at depths of 255 to 275 m.

The development of a 3D model that identifies the location, distribution, and relationship of geological structures is important for the design and long-term safety assessment of a repository for the geological disposal of high-level radioactive waste (HLW). The reliability of the model can be improved by identifying faults and fractures from fracture logging of boreholes and fracture mapping on the walls of shafts and galleries as they are excavated.

The deeper parts of the Horonobe Underground Research Laboratory (URL) are located in the Wakkanai Formation, which comprises Neogene massive siliceous mudstones (Fig.8-16). At the Horonobe URL, which is located on the western limb of an anticline, the contact between the Wakkanai and Koetoi formations strikes NW–SE and dips moderately to the west. A number of bedding-oblique faults containing fault breccia (Fig.8-16(a)) and four bedding-parallel faults containing fault gouges (Fig.8-16(b)) have been observed in the Wakkanai Formation from two pilot boreholes

(PB-V01 and SAB-1). A bedding-oblique fault that displaced a bedding-parallel fault was observed in the 350-m West Loop Gallery (Fig.8-16(c)) and is consistent with previous assignments of bedding-oblique faults that have formed following bedding-parallel faults. However, bedding-oblique faults were observed in the Ventilation Shaft at depths of 265–271 m that terminate near the bedding-parallel faults (Fig.8-16(d)). Based on the location and orientation of bedding-parallel faults as observed in the boreholes and galleries, four bedding-parallel faults could be identified from depths of 260–410 m (Fig.8-17). We therefore suggest here that the first formed bedding-parallel faults affect the propagation of the latter-stage bedding-oblique faults.

The data collected by fracture mapping on the gallery walls are helpful for greater understanding of the location, distribution, and relations between the bedding-parallel and bedding-oblique faults identified at the Horonobe URL. This helps to improve the reliability of 3D models developed for geological structures.

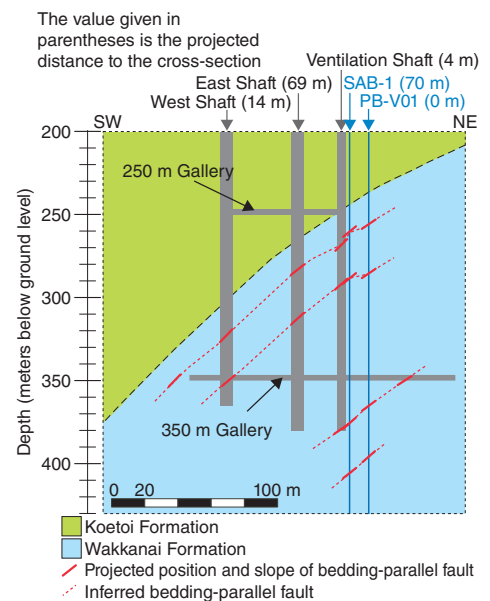


Fig. 8-17 NE-SW trending cross-section of the Horonobe URL

The locations of bedding-parallel faults are projected onto a vertical cross-section through borehole PB-V01 based on the location and orientation of each fault.

Reference

Hayano, A. et al., Relationship between Faults Oriented Parallel and Oblique to Bedding in Neogene Massive Siliceous Mudstones at The Horonobe Underground Research Laboratory, Japan, IOP Conference Series: Earth and Environmental Science, vol.44, 2016, p.022004-1-022004-8.

8-7 Dating of Minerals in Rocks

— Technical Development of a Rapid CHIME Dating Procedure —

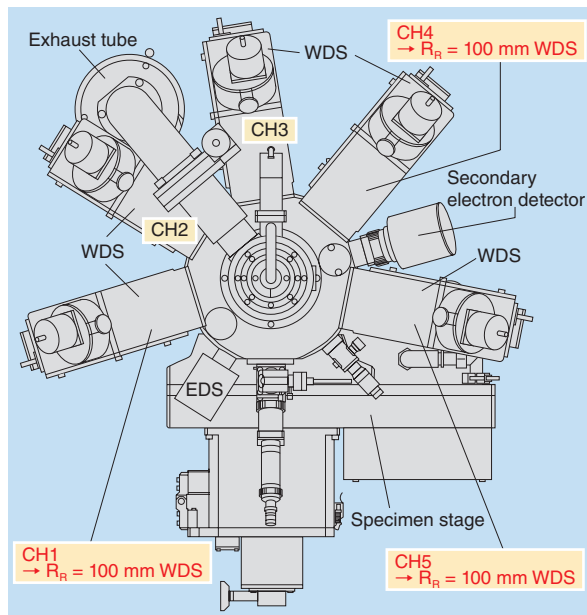


Fig.8-18 Overview of EPMA analysis (modified from a product catalog of JEOL Ltd.)

The EPMA at the Tono Geoscience Center has two conventional $R_R = 140$ mm wavelength-dispersive spectrometers (WDSs) (CH2 and CH3) and three relatively new $R_R = 100$ mm WDSs (CH1, CH4, and CH5).

By dating minerals in sediments, we can know when they were formed and from where the minerals were sourced. The history of minerals offers us some geological and tectonic information, for example, concerning formation and building of the mountains that sourced the minerals. This approach is called “provenance analysis” and is a very effective technique for determining long-term changes in the geological environment from past to present for geological disposal of high-level radioactive waste. A problem exists, however, in that a large number of mineral analyses are required for this purpose.

The chemical Th-U-total Pb isochron method (CHIME; Suzuki and Adachi, 1991) is a radiometric dating method for minerals. Radioactive thorium (Th) and uranium (U) decay into a series of other elements before finally converting into lead (Pb). An advantage of the CHIME dating method is that it does not require isotopic-ratio analysis. Instead, the age of a mineral can be estimated from the concentrations of Th, U, and Pb measured using an electron probe microanalyzer (EPMA). In EPMA analysis, electron bombardment generates X-rays in the sample to be analyzed. From the wavelength and intensity of the lines in the X-ray spectrum, the elements present may be identified and their concentrations estimated.

In the current study, the CHIME dating procedure is

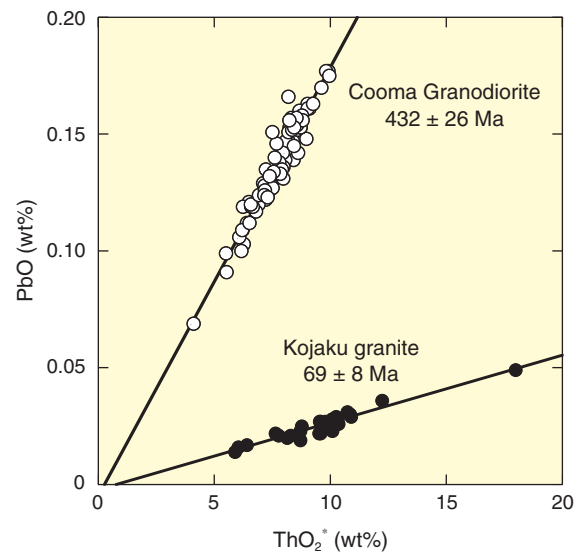


Fig.8-19 Rapid CHIME dating of monazites

The rapid CHIME dating procedure was applied to monazites from Cooma Granodiorite in Australia (432.8 ± 3.5 Ma; Williams, 2001) and Kojaku granite (68.5 ± 0.7 Ma; Sueoka et al., 2016) from the Tsuruga Peninsula of Japan. The age values in this study corresponded with those of previous studies within the error range. (ThO_2^* : measured ThO_2 plus ThO_2 equivalent to measured UO_2)

advanced by the first-time use of a wavelength-dispersive spectrometer (WDS) with a Rowland circle (R_R) of 100 mm (Fig.8-18). The use of an $R_R = 100$ mm WDS is beneficial in that it requires less than half the time needed for the conventional CHIME dating procedure and so is better suited to the large number of mineral analyses that are required. The disadvantage of $R_R = 100$ mm WDS is a reduced spectral resolution, which represents the functional ability of WDS to distinguish two X-rays when their wavelengths are close to each other. This problem was overcome by calculating an “interference correction,” which eliminates the influence of interfering X-rays. The interference correction was calculated based on the analytical data of natural monazite, a natural mineral containing Th and U. The disadvantage of $R_R = 100$ mm WDS is a reduction in spectral resolution, which was overcome by calculating a new “interference correction” based on the analytical data of monazite, thereby eliminating the influence of interfering X-rays.

The reliability of this advanced CHIME dating procedure was confirmed by dating of monazites separated from rocks that had been previously dated using other methods (Fig.8-19). This advanced CHIME dating procedure, therefore, offers a practical, rapid, and reliable means of dating minerals.

Reference

Shimizu, M. et al., CHIME Monazite Dating: Pb Analysis on an $R_R=100$ mm Spectrometer and Correction of Interferences between Th, U, and Pb with Natural Monazite, *Journal of Mineralogical and Petrological Sciences*, vol.112, no.2, 2017, p.88-96.

8-8 Mechanistic Modeling of Nuclide Migration in Rock

— Clay-Based Modeling Approaches for Diffusion and Sorption in Mudstone —

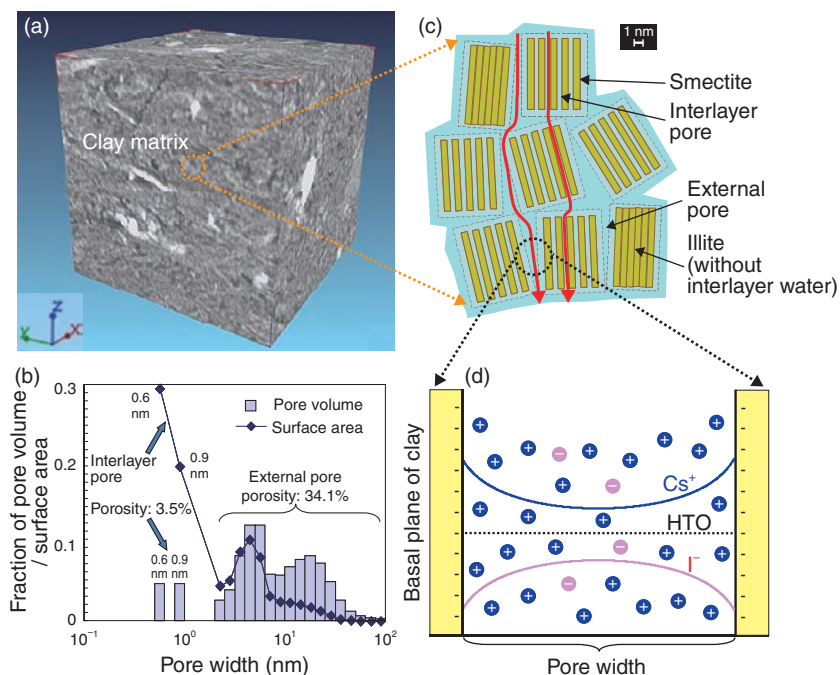


Fig. 8-20 Conceptual images of a clay-based diffusion model
 (a) 3D image of a rock matrix obtained by X-ray CT; (b) pore-size distribution by mercury porosimetry; (c and d) simplified sketches of the clay matrix and EDL in a nanoscale pore.

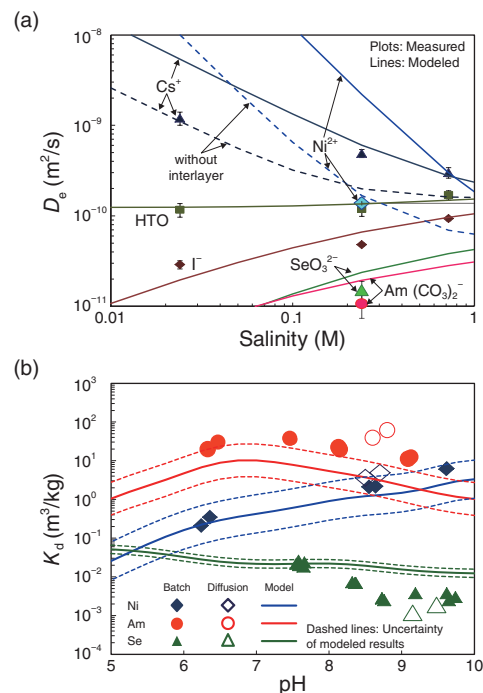


Fig.8-21 Comparison between measured and modeled results of Ni, Am, and Se
 (a) D_e vs. pore-water salinity; (b) K_d vs. pH.

Diffusion and sorption of radionuclides (RNs) in rocks are key processes for the safe geological disposal of radioactive waste. To set reliable parameters for various geological and geochemical conditions relevant to safety assessment, understanding diffusion and sorption processes and developing mechanistic models is necessary. A clay-based modeling approach that assumes key contributions of clay minerals has been developed to describe the diffusion and sorption behavior of simple ions (Cs^+ , I^-) in the mudstone from the Horonobe underground research laboratory (URL) in previous studies. The present study focuses upon experimental and numerical investigation of the diffusion and sorption of more complex species including Ni(II), Am(III), and Se(IV) in the mudstone from the Horonobe URL.

Effective diffusivities (D_e) measured by through-diffusion experiments indicated cation excess and anion exclusion effects and were interpreted by the clay-based modeling approach. The diffusion behaviors were assumed to be dominated by nanoscale pores in the homogeneously dispersed clay matrix, based on mineral and pore distributions by nano-focus X-ray CT and mercury porosimetry (Figs.8-20(a) and (b)). The clay matrix comprises non-swelling illite without interlayer water and swelling smectite with interlayer water (Fig.8-20(c)). The diffusion model based on the electrical double layer (EDL) describing the relative ionic concentrations and viscoelectric

effects at the negatively charged clay surface is connected to a simplified homogeneous-pore model with the size distribution (Fig.8-20(d)). The dominant species under the test conditions are estimated to be Ni^{2+} , $\text{Am}(\text{CO}_3)_2^-$, and SeO_3^{2-} . The diffusion model can qualitatively express D_e trends including cation excess and anion exclusion effects ($\text{Cs}^+ > \text{Ni}^{2+} > \text{HTO} > \text{I}^- > \text{SeO}_3^{2-} > \text{Am}(\text{CO}_3)_2^-$), as well as the salinity dependences (Fig.8-21(a)). As shown by dashed lines in Fig.8-21(a), interlayer pores contribute significantly to cation diffusion, and the disparity between the modeled and measured D_e values of cations may indicate that the contributions of the interlayer pores vary according to cations and salinity conditions.

Distribution coefficients (K_d) measured by batch sorption experiments were consistent with those obtained by diffusion tests and were calculated by the sorption model using site capacities determined from the clay contents and model parameters (i.e., ion exchange and surface complexation). Trends in K_d predicted by the sorption model, considering the additive contributions of illite and smectite, demonstrate reasonable agreement with measurements as a function of pH (Fig.8-21(b)).

From these results, electrostatic interactions in nanoscale pores and sorption reactions at clay surfaces control the diffusion and sorption of various RNs. The clay-based modeling approach can be applied to predicting the diffusion and sorption behaviors of various RNs with complex chemistry in mudstone.

Reference

Tachi, Y. et al., Clay-Based Modeling Approach to Diffusion and Sorption in the Argillaceous Rock from the Horonobe URL: Application to Ni(II), Am(III), and Se(IV), The Clay Minerals Society Workshop Lectures Series, vol.21, chapter 19, 2016, p.241-250.

8-9 Evaluation of the Long-Term Mechanical Behavior of a TRU Waste Repository

— Development of a Mechanical Analysis Method Considering the Chemical Evolution of Engineered Barrier Materials —

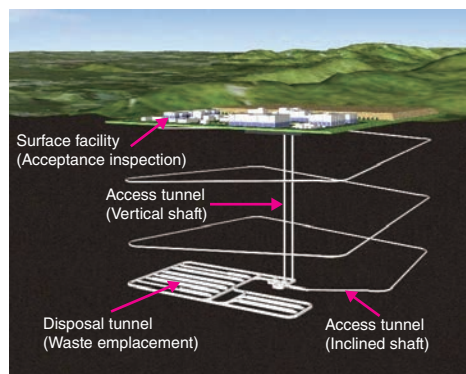


Fig.8-22 Concept of the TRU waste repository

The upper figure shows a conceptual view of TRU waste repository and the lower figure shows a cross-section of the TRU waste disposal tunnel with buffer material.

Radioactive waste generated in the reprocessing of spent fuel from nuclear power plants and in the fabrication of mixed oxide fuel, excluding high level radioactive waste, is referred to as TRU waste in Japan because it contains transuranic elements. Disposal of highly radioactive TRU wastes is to be done in a purpose built repository located in stable host rock at depths exceeding 300 meters so as to isolate them from the biosphere for a long period. The repository itself will be constructed from concrete and cement mortar (cementitious materials) and compacted bentonite will be used as a buffer material to encapsulate the TRU wastes (Fig.8-22). To perform a safety assessment of TRU waste disposal, the long-term evolution of the repository from the viewpoint of the events and the processes affecting chemistry, dynamics, and hydrology must be evaluated. It is important, for example, to determine the buffer material thickness required to minimize groundwater flow and retard radionuclide migration. A mechanical analysis method was, therefore, developed to evaluate the long-term evolution of a TRU waste repository considering both the mechanical and chemical properties of engineered barrier materials.

Important events and processes were selected by consideration of the construction, operation, and post-closure phases of the

Table 8-1 Events and processes considered in the evaluation model
Events and processes incorporated into the analytical method are shown.

Phase	Phase Incorporated events and processes
Construction and operation (~ ca.100 years)	<ul style="list-style-type: none"> Stress changes of host rock by excavation Creep of host rock Support of host rock by concrete lining/support Compaction of buffer due to emplacement of structure framework and TRU waste Swelling of buffer
Post-closure	<ul style="list-style-type: none"> Creep of host rock Decrease in strength of concrete lining/support by leaching Decrease in swelling capacity of buffer by ion exchanging and dissolution of smectite Preliminary and secondary consolidation of buffer Strength decrease of TRU waste, cement mortar filler, and structure framework by leaching

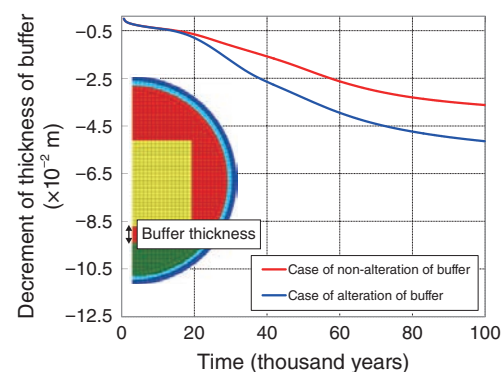


Fig.8-23 Calculated results using the developed analytical method

Time dependencies of the decrement of buffer thickness in the lower repository position are shown. Alteration of the buffer by Ca exchange and dissolution were considered.

repository (Table 8-1), which were then incorporated into the mechanical analysis method. During the post-closure phase, percolating groundwaters will saturate the repository and start to dissolve the more soluble Ca-bearing cementitious material components. The mechanical strength of the cementitious materials will, therefore, decrease and the percolating groundwater will become hyperalkaline. Hyperalkaline percolating groundwater would adversely affect the bentonite buffer, causing conversion from a Na-type to a Ca-type, with an associated loss of plasticity, swelling, and swelling capacity, and an increase in dissolution and degradation. The mechanical analysis method developed here was used to investigate the change in the buffer material thickness caused by hyperalkaline percolating groundwater on a timeframe of up to 100 thousand years (Fig.8-23). It was observed that hyperalkaline percolating groundwater only contributes to the degradation of approximately 2 cm of buffer material thickness after 100 thousand years.

In the future, as a means of conducting a more comprehensive study, a mechanical analysis of the repository that reflects a better constrained numerical analysis of the chemical evolution will be performed.

Reference

Mihara, M. et al., Long-Term Mechanical Analysis Code Considering Chemical Alteration for a TRU Waste Geological Repository, Genshiryoku Bakkundo Kenkyu (Journal of Nuclear Fuel Cycle and Environment), vol.24, no.1, 2017, p.15-26 (in Japanese).

8-10 Improvement of the Uncertainty and Rapidity of the Measurement Technique for a Plutonium Nitrate Solution Sample — Improvement of Neutron Nondestructive Assay —

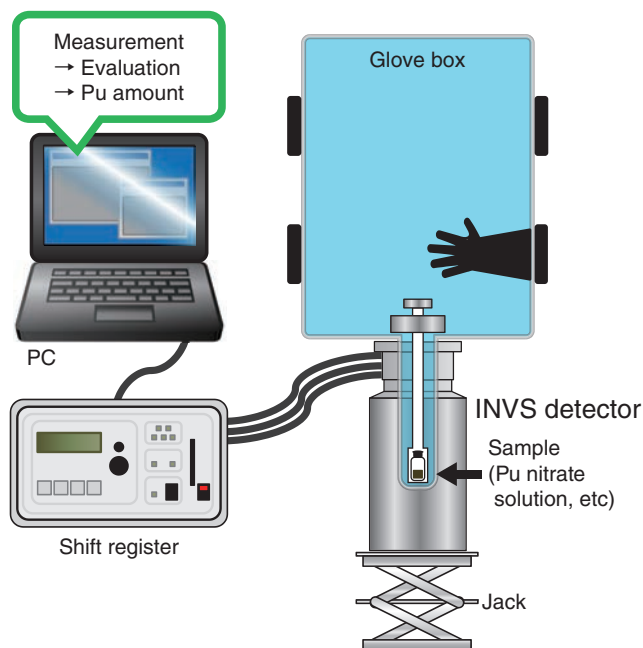


Fig.8-24 Composition of the glove box and equipment for the INVS system

The inventory sample verification system (INVS) is a neutron counter with ^3He proportional detectors. It is used for measurement and evaluation of the amount of Pu using a shift register and dedicated software.

Plutonium (Pu) nitrate solution, which is recovered from spent fuels for light-water reactors and so on, is stored in the Tokai Reprocessing Plant. Since the solution is treated as a direct-use material (i.e., a nuclear material that can be directly used for manufacturing nuclear explosives), verification activities are being conducted by the Nuclear Regulation Authority and the International Atomic Energy Agency.

The inventory sample verification system (INVS), which is shown in Fig.8-24, is a neutron nondestructive assay detector for Pu contained in mixed-oxide (MOX) powder and Pu nitrate solution, and has been used to verify the correctness of our declarations by inspection. We studied the INVS to improve the uncertainty of our measurements to within 1% for Pu nitrate solution, the same level as that of destructive assay.

First, we confirmed detector parameters (high voltage and response profile, among others). Then, we optimized the necessary parameters for calibration (efficiency and coincidence neutron fraction without multiplication, among others) using a fabricated MOX pellet source which the neutron source is Pu, just as in actual samples. Then, we determined necessary calibration curves for the passive calibration curve method and the known- α method.

To choose a proper calibration method, the measurement results of actual samples were evaluated by the three different neutron coincidence techniques (i.e., techniques based on

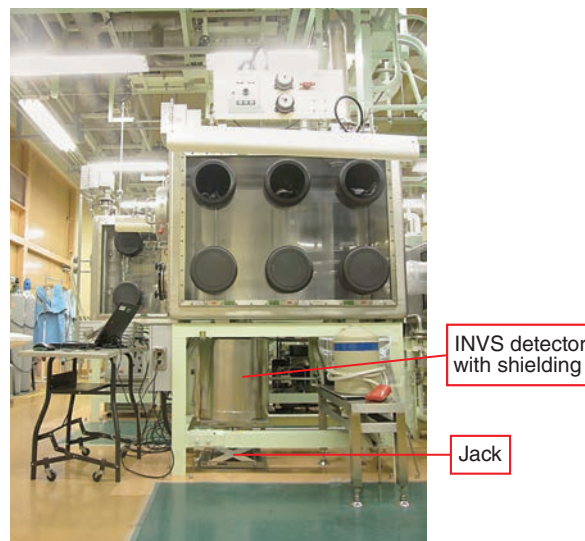


Fig.8-25 The composition of the glove box and the INVS with shielding

A photograph of the glove box and the INVS with shielding made of high-density polyethylene.

counting coincidence neutrons from fission reactions) which include the passive calibration curve method, the known- α method (using the defined ratio of fission neutrons), and the multiplicity method (using triple neutrons from fission reactions). Since the application of both the known- α method and the multiplicity method to solution samples is uncommon, we expect to gain new information by this study.

The evaluation results of about one-day measurements using the passive calibration curve method and the known- α method achieved uncertainties of 1%; however, the results of the multiplicity method showed an uncertainty of approximately 2%. Therefore, we installed new shielding to reduce the effect of background neutrons to improve the uncertainty (Fig.8-25). The application of the shielding improved the uncertainty, especially of the known- α method results; the passive calibration curve and known- α methods both achieved uncertainties of 1% with measurement times within one hour. As a result of shielding, the multiplicity method was found to have difficulty achieving an uncertainty of 1%; however, the passive calibration curve method and the known- α method should be used as measurement techniques with good uncertainty and rapidity.

Our research was accomplished as the collaborative study with Los Alamos National Laboratories to improve nuclear material accountancy in Tokai Reprocessing Plant.

Reference

Swinhoe, M., Makino, R. et al., Improvement of INVS Measurement Uncertainty for Pu and U-Pu Nitrate Solution, LA-UR-17-23474, 2017, 28p.

8-11 Understanding the Characteristics of Insoluble Sludge in the Reprocessing of Fast Reactor Fuels

— Evaluating the Characteristics of Insoluble Sludge from the Dissolution of Irradiated Fast Reactor Fuel —

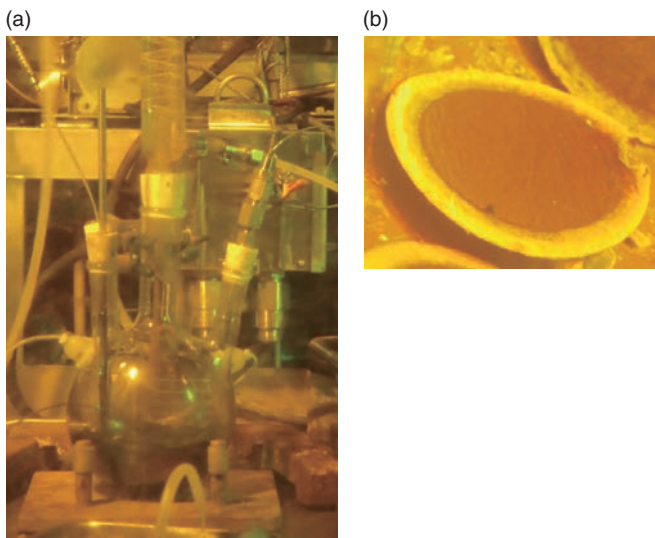


Fig.8-26 (a) Appearance of dissolving fuels and (b) filtrated residues

Handling of irradiated fuels in concrete cells is carried out by remote manipulation. Experiments were on the same scale as the laboratory, using 300 ml of nitric acid for dissolution; then, sludge was filtrated with a glass filter.

Spent fuels which are irradiated by a nuclear reactor (irradiated fuels) are reprocessed to recover uranium (U) and plutonium (Pu). During reprocessing, fuels are dissolved with nitric acid, but insoluble matter (sludge) such as precipitation or residue remains. If sludge goes into the subsequent process together with the dissolved solution, it may cause equipment failure or block the pipe. Therefore, understanding the characteristics of insoluble sludge and its formation in process is important. In particular, the composition of the fast reactor fuel differs from that of the light-water reactor (LWR) fuel that has been used conventionally; the characteristics of the sludge also change, but sufficient information has yet to be obtained.

Evaluation of the characteristics of sludge formed by dissolving fuels irradiated at the “JOYO” experimental fast reactor was carried on at Chemical Processing Facility (CPF). Irradiated fuel pins from “JOYO” were sheared into 1.5-cm segments and then dissolved by heated nitric acid in a glass flask. Most of the nuclear-fuel materials (U and Pu) and fission products (FPs) were dissolved into the solution, but a small part of the insoluble sludge remained. This sludge was recovered by suction filtration (Fig.8-26).

The elemental compositions of sludge samples recovered under several dissolution conditions were determined. Molybdenum (Mo), technetium (Tc), platinum-group elements

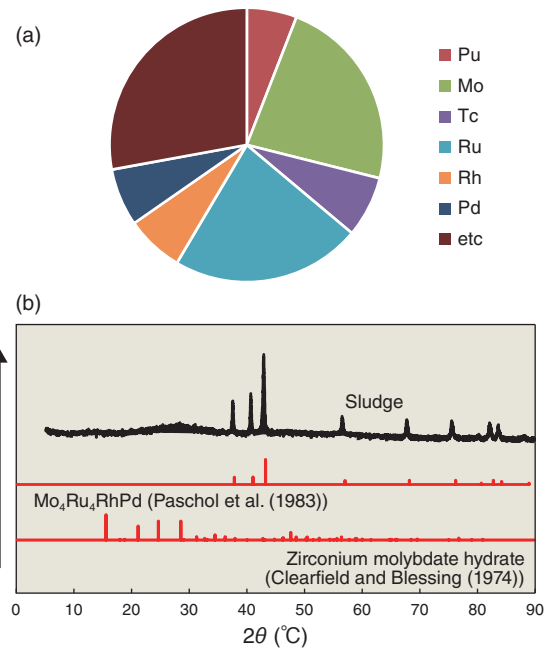


Fig.8-27 (a) Chemical compositions of sludge and (b) X-ray diffraction patterns

(a) The weight percentage of elements contained in one sludge sample. In the legend, quantified elements are shown; “etc.” includes all other elements. (b) The patterns of X-ray diffraction. For comparison, the reported values of the two compounds of interest are also shown.

(ruthenium (Ru), rhodium (Rh), and palladium (Pd)), and Pu were included (Fig.8-27(a)). Differences in fuel-dissolution conditions (fuel types, nitric acid concentration, among others) did not significantly affect sludge composition.

X-ray diffraction patterns are shown in Fig.8-27(b). The sludge pattern agrees well with that reported for $\text{Mo}_4\text{Ru}_4\text{RhPd}$ alloy. Technetium is also contained in the sludge, suggesting that the alloy analyzed here is $\text{Mo}_4\text{Ru}_{3.7}\text{Rh}_{1.1}\text{Pd}_{1.1}\text{Tc}_{1.2}$.

Research on sludge formed during reprocessing of LWR fuel showed that it contains a large amount of zirconium molybdate hydrate in addition to $\text{Mo}_4\text{Ru}_4\text{RhPd}$ alloy. Zirconium molybdate hydrate is a compound that precipitates when the solution is heated. There are very fine particles which are difficult to filter; therefore, it is necessary to suppress the formation. However, Zirconium was not detected from the sludge analyzed in this study, and no peak of Zirconium molybdate hydrate was observed. It can be assumed that much of the Mo was alloyed and caused a low Mo concentration of the dissolved solution; therefore, Zirconium molybdate hydrate did not precipitate. The characteristics of sludge from LWR and fast reactor fuels were found to be different; we will continue evaluating further sludge for the development of fast reactor fuel reprocessing.

Reference

Aihara, H. et al., Characterization of the Insoluble Sludge from the Dissolution of Irradiated Fast Breeder Reactor Fuel, *Procedia Chemistry*, vol.21, 2016, p.279-284.

Computational Science for Nuclear Research and Development

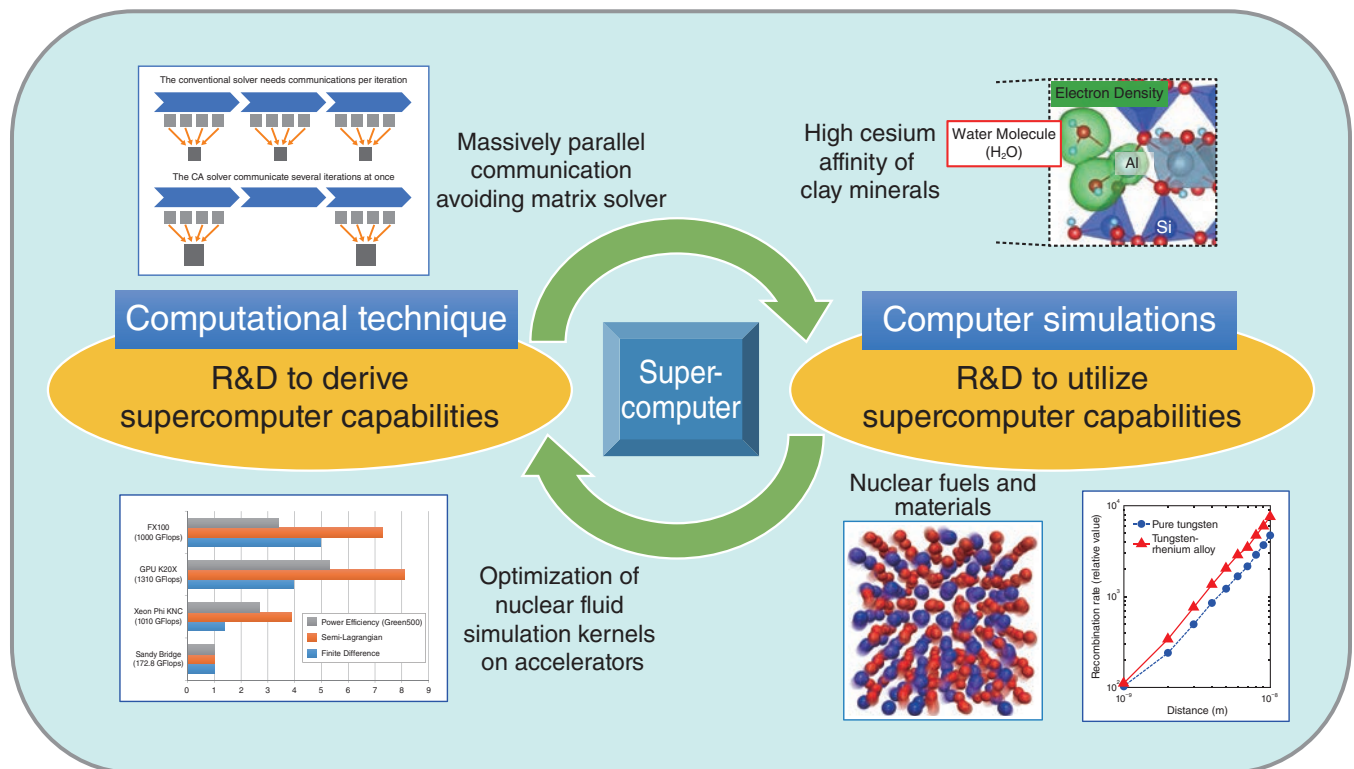


Fig.9-1 Research & Development (R&D) at the Center for Computational Science and e-systems

We are promoting computational science in the nuclear-energy-research field, with our two pillars being R&D to derive supercomputer capabilities and R&D to utilize supercomputer capabilities.

We are performing research and development of computational science and technology with the aim of analyzing the various issues required for solving the problems generated by the accident at the TEPCO's Fukushima Daiichi NPS (1F), and for research and development of future nuclear power systems as shown in Fig.9-1. Here, we will present four main topics.

The Center is developing advanced calculation technology to maximize supercomputer capacity. In a state-of-the-art supercomputer, network communication between computing devices has become a bottleneck for deciding the processing speed of the overall calculation; however, we have succeeded in developing a communication-oriented solver that greatly reduces communications processing (Topic 9-1). To make full use of accelerators that speed up the numerical-calculation method in the field of nuclear power, various calculation methods have been studied and the main part of the calculation code for nuclear fluid has been successfully optimized for accelerators (Topic 9-2). These results will lead improvement of R&D capabilities not only in the nuclear field, but also in the computational-science field as a whole.

In addition, we are conducting R&D using supercomputers; one such topic involves using high-precision calculation

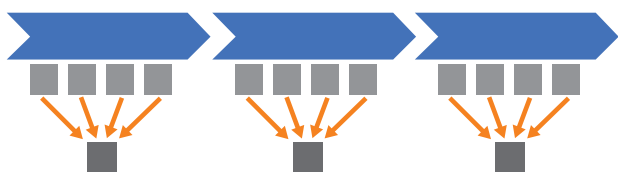
methods to examine the characteristics of radioactive cesium related to fuel and materials in nuclear power plants and 1F-accident countermeasures based in first principles from the level of electrons. We have also revealed the peculiar behavior of thorium dioxide, a next-generation nuclear fuel, at high temperature through molecular-dynamics simulation based on first-principles calculation (Topic 9-3). In tungsten alloy, which is a candidate to be the inner-wall material of a fusion reactor, simulation of lattice-defect migration based on first-principles calculation was performed to clarify why the addition of rhenium improves the irradiation resistance of tungsten (Topic 9-4). In addition, the results related to investigating the cause of clay minerals with a high ability to adsorb radioactive cesium are also obtained (Chapter 1, Topic 1-19).

We received the "ISC 2016 HPC in Asia Poster Award" with RIKEN on June 22nd, 2016, for research and development of advanced calculation technology. We also organized workshops entitled "Efforts of Computational Science for Recovery from the Fukushima Accident" on February 14th, 2017. In addition, we are undertaking activities to disseminate computational science and technology.

9-1 Acceleration-Flow Analysis in a Nuclear Reactor

— Development of Massively Parallel Communication-Avoiding Matrix Solvers —

(a) The conventional solver communicates each iteration individually



(b) The CA solver communicates several iterations at once

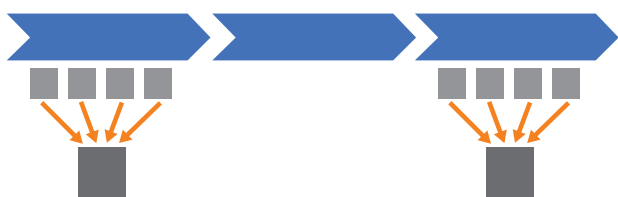


Fig.9-2 Representations of calculation and communication by the conventional and CA solvers

(a) shows the conventional solver, which needs communications indicated by arrows between the processors for each iteration. (b) shows the CA solver, which can communicate data from several iterations at once and reduce communications.

We promote the development of a multiphase thermal-hydraulic computational fluid dynamics (CFD) code for analyzing the relocation of molten materials in nuclear reactors during severe accidents. Current supercomputers can simulate the melt-relocation behavior of several fuel assemblies. However, to analyze a severe accident for the whole reactor-pressure vessel, we need exa-scale computers that can perform calculations more than 100 times faster than current supercomputers.

Current supercomputers are based on distributed-memory parallelism with tens of thousands of computers connected by a network. In order to make full use of the supercomputers' performance, it is necessary to communicate the calculated data and synchronize the steps of processing; however, the communication cost is a bottleneck in exa-scale computers. In multiphase CFD code, the matrix solver for the pressure equation accounts for most of the computational cost. Since the communicational cost of the conventional solver is relatively large, the communication bottleneck becomes obvious in large-scale parallel computation. We developed the communication-avoiding (CA) matrix solver to resolve this issue and further enable large-scale CFD code analysis.

The conventional matrix solver uses the conjugate-gradient (CG) method, an iterative technique. The CG method solves a large-scale matrix problem by calculating the residual of the approximate solution and modifying the solution. The conventional solver requires inner-product operations with

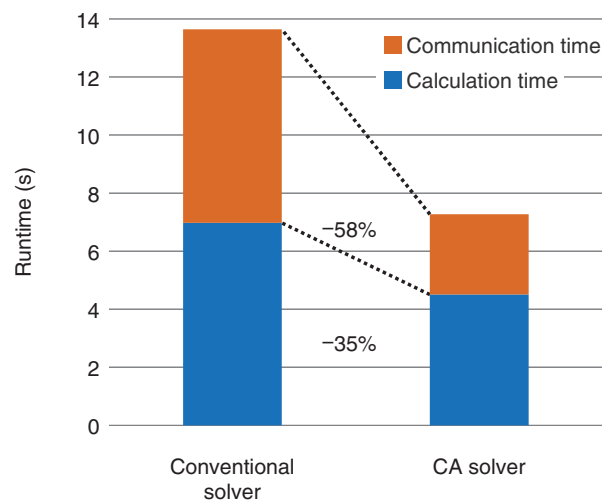


Fig.9-3 Parallel-performance comparison of the conventional and CA solvers

This figure shows the runtime of matrix calculation of the Poisson equation ($800 \times 500 \times 3540$ lattice) on the K computer with 30000 nodes. With the CA solver, the communication time, which occupied about half of the whole time of the conventional solver, is greatly reduced and the performance is roughly doubled.

global communications, which collect data calculated by tens of thousands of computers per iteration (Fig.9-2(a)).

However, by communicating the data required for inner-product calculation only once for several iterations by changing the algorithm that is mathematically equivalent to the conventional solver, the CA solver can reduce the number of collective communications and synchronizations to a fraction of that of the conventional solver (Fig.9-2(b)). Despite this algorithm change causing the computational cost to become larger, the CA algorithm is suitable because the communication cost is significantly higher than the computational cost in massively parallel processing. We evaluated our CA solver's performance on the K computer, which is the representative supercomputer in Japan. Because of the tens of thousands of computers involved in massively parallel processing, the communication cost manifested in the conventional solver was greatly reduced. In addition, the changed algorithm decreased the number of memory accesses, accelerating the calculation time and doubling the total performance (Fig.9-3).

We will develop the CA solver for a general matrix library and provide it to the community. The present study was sponsored by the Ministry of Education, Culture, Sports, Science and Technology (MEXT), Japan, Post-K Priority Issue 6, "Accelerated Development of Innovative Clean Energy Systems".

Reference

Mayumi, A. et al., Left-Preconditioned Communication-Avoiding Conjugate Gradient Methods for Multiphase CFD Simulations on the K Computer, Proceedings of 7th Workshop on Latest Advances in Scalable Algorithms for Large-Scale Systems (ScalA 2016), Salt Lake City, Utah, USA, 2016, p.17-24.

9-2 Development of a Low-Power-Consumption Computing Technology Based on Accelerators — Optimization of Nuclear-Fluid-Simulation Kernels on Accelerators —

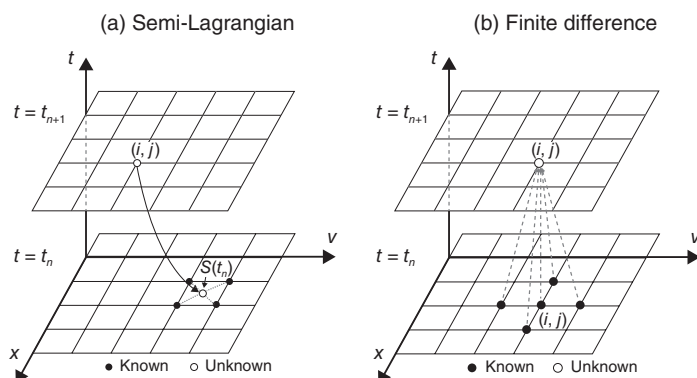


Fig.9-4 Numerical schemes of fluid-simulation kernels

Memory-access patterns in the time development of a convection operator using (a) semi-Lagrangian and (b) finite-difference schemes. Here, t and (x, v) show time and space, respectively. The semi-Lagrangian scheme traces the development of the solution by data access along streamlines, whereas the finite-difference scheme develops the solution via regular data access.

Higher computing performance is needed to improve nuclear-fluid simulations, such as analyses of severe accidents and the environmental dynamics of radioactive substances, and applying them to real problems. The development of exascale supercomputer is ongoing worldwide, and in Japan, the Post-K computer, which will succeed the K-computer, is being developed. One critical issue for such exascale supercomputers is low-power-consumption computing technology, which enables a performance more than two orders of magnitude higher than current supercomputers with similar power consumption. On the hardware side, accelerators have been developed, and both requirements on low power consumption and improved computing performance have been satisfied by suppressing the processor frequency and accumulating many computing cores within a processor. However, on the software side, it is not clear if conventional numerical schemes can be efficiently processed on such accelerators. In this work, we optimized the computing kernels of nuclear-fluid-simulation codes on accelerators and evaluated their computing performances.

We optimized convection-operator kernels based on the finite-difference and semi-Lagrangian schemes, which are representative schemes in fluid simulations, using graphical processing units (GPUs) and two kinds of many-core processors, namely Xeon Phi and FX100. GPUs have many computing cores designed for graphics processing, while many-core processors are based on conventional CPUs. The finite-difference scheme has regular memory access, and the semi-Lagrangian scheme traces the solution along streamlines,

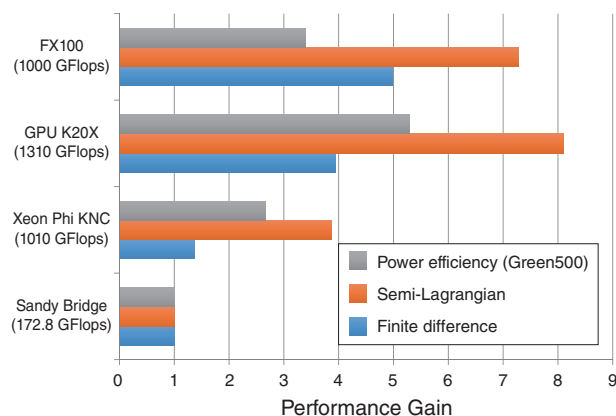


Fig.9-5 Performance comparisons of fluid-simulation kernels on accelerators

Power efficiency and performance ratios of the semi-Lagrangian and finite-difference schemes on accelerators (FX100/GPU/XeonPhi), as normalized by those on a CPU (Sandy Bridge). The power efficiency is based upon computation speed (Flops) per unit power consumption in a matrix-computation benchmark called Green500.

which become random-memory access (Fig.9-4). Although the above accelerators have 3–5 times higher computing performance per unit power consumption than conventional CPUs, they have complicated hierarchical memory structures for supplying data to many computing cores. Therefore, adapting the memory-access patterns to hierarchical memory structures based upon an understanding of both the memory structures and the physical properties of the convection operator is the key to optimization.

It is found that FX100 can attain high computing performance without special optimization, as it is based on a shared in-processor memory, similar to that of conventional CPUs. On the other hand, on Xeon Phi, which is based on a distributed in-processor memory on each core, optimizing data access and computation patterns for the distributed memory improves computing performance by approximately 1.3 times, and on GPUs, an optimized algorithm that fully utilizes a texture memory for graphic processing leads to approximately 1.9 times higher computing performance. Thanks to the above optimization techniques, the finite-difference and semi-Lagrangian kernels are respectively accelerated up to 5 and 8 times compared with conventional CPUs (Fig.9-5), and the use of accelerators to attain low-power-consumption computing capability has been demonstrated.

This research was supported by the Ministry of Education, Culture, Sports, Science and Technology (MEXT), Japan, Post-K Priority Issue 6, “Accelerated Development of Innovative Clean Energy Systems”.

Reference

Asahi, Y., Idomura, Y. et al., Optimization of Fusion Kernels on Accelerators with Indirect or Strided Memory Access Patterns, IEEE Transactions on Parallel and Distributed Systems, vol.28, no.7, 2017, p.1974-1987.

9-3 High-Temperature Properties of Nuclear-Fuel Materials

— First-Principles Molecular-Dynamics Simulation of Thorium Dioxide —

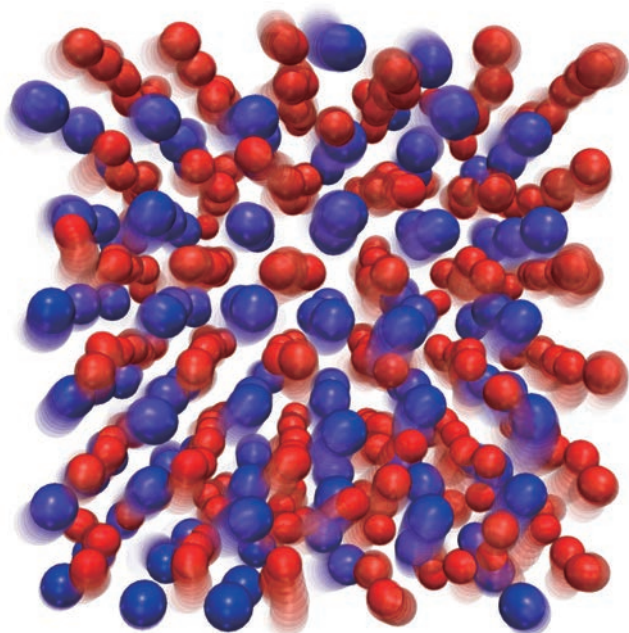


Fig.9-6 Atomic motions in a crystal of thorium dioxide
Motions of 108 thorium atoms (●) and 216 oxygen atoms (●) at high temperature (3500 K) are indicated. One can see that the positions of atoms are disordered at temperatures almost as high as the melting point, though atoms are ordered at low temperature. Moreover, the lighter the oxygen atoms are, the more significantly they move.

In developing safer and more efficient nuclear fuels, it is crucial to understand their high-temperature properties. However, it is not easy to reproduce extreme situations inside nuclear reactors in laboratories for the purposes of measuring various nuclear-fuel properties. Thus, it is expected that numerical simulations will help experimenters to evaluate the thermophysical properties of fuels.

While thorium dioxide is a candidate next-generation fuel, its high-temperature properties, which are important in severe-accident analysis, have yet to be investigated in detail. In most actinide dioxides, anomalous behaviors are known to be observed at high temperature slightly below their melting point. For example, the enthalpy of uranium dioxide increases drastically above 2500 K, whereas it increases slowly below 2500 K. Though similar phenomena have been predicted in the case of thorium dioxide, the drastic change in the enthalpy increment has not been observed clearly due to the low accuracy of the experiments.

We explored the high-temperature behavior of thorium dioxide using first-principles molecular-dynamics simulations. Such simulation is a method to analyze the motions of

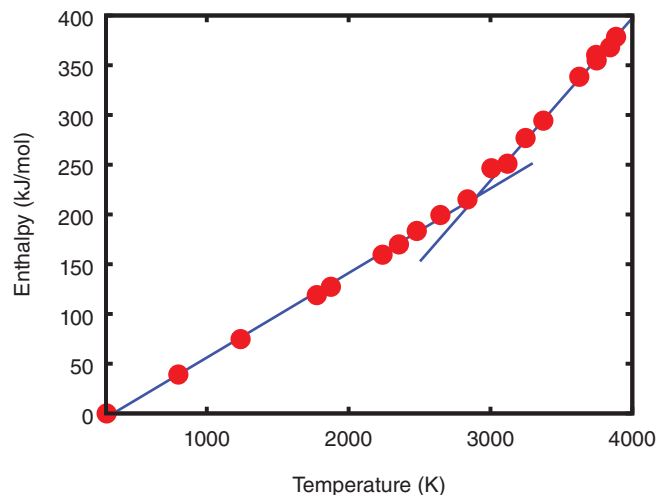


Fig.9-7 Temperature dependence of the enthalpy of thorium dioxide

Red dots (●) indicate the calculated enthalpy. Blue lines are guides to the eye. Drastic change in the slope is observed around 3000 K.

atoms with atomic forces calculated from the fundamental interactions of nuclei and electrons. According to this method, high-accuracy calculations are possible without empirical parameters. We evaluated the relationship between the enthalpy of thorium dioxide and temperature by numerical simulations using supercomputers, where we prepared a calculation cell of a thorium-dioxide crystal with 324 atoms (Fig.9-6). As shown in Fig.9-7, we discovered a drastic increment of enthalpy above 3000 K; the calculated transition temperature of thorium dioxide is 500-K larger than that of uranium dioxide. We found that the drastic changes in enthalpy were blurred in experiments, though this was clear in our calculations due to their high accuracy. Moreover, we also found that, above 3000 K, oxygen atoms moved almost freely as atoms in liquid do. These motions were revealed to cause drastic changes in enthalpy.

Thus, numerical simulations enable us to evaluate various properties of materials, some of which are difficult to measure by experiment. By doing so, we hope to contribute to the development of safer nuclear fuels.

Reference

Nakamura, H. et al., High-Temperature Properties of Thorium Dioxide: A First-Principles Molecular Dynamics Study, *Journal of Nuclear Materials*, vol.478, 2016, p.56-60.

9-4 Solving the Mystery of Irradiation-Resistant Alloys

— Simulation of Interstitial Atoms' Migration Based on First-Principles Calculation —

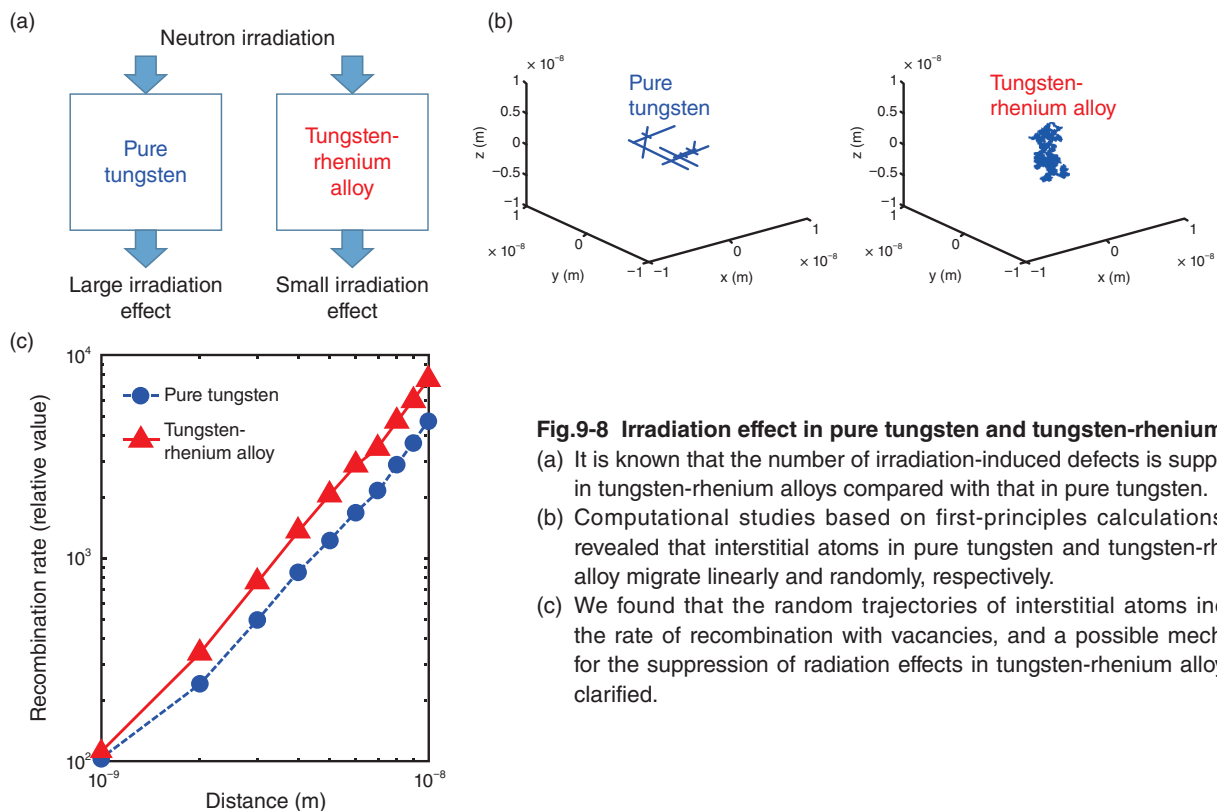


Fig.9-8 Irradiation effect in pure tungsten and tungsten-rhenium alloy

- (a) It is known that the number of irradiation-induced defects is suppressed in tungsten-rhenium alloys compared with that in pure tungsten.
- (b) Computational studies based on first-principles calculations have revealed that interstitial atoms in pure tungsten and tungsten-rhenium alloy migrate linearly and randomly, respectively.
- (c) We found that the random trajectories of interstitial atoms increase the rate of recombination with vacancies, and a possible mechanism for the suppression of radiation effects in tungsten-rhenium alloys was clarified.

Nuclear-energy generation originates with a nuclear fission or fusion chain reaction through neutrons. The degradation of the structural materials of these reactors through the neutron irradiation is inevitable; however, such degradation must be minimized to achieve safe and economical operation. In particular, plasma-facing walls are exposed to high-energy neutron irradiation in addition to high-temperature plasma, and they are used in extreme environments. Tungsten, which is a refractory metal, is the prime candidate for use as such walls in future fusion reactors.

Prior to recent detailed studies, it had been believed that tungsten would not easily absorb hydrogen isotopes such as deuterium, which is a nuclear-fusion-reactor fuel; this property would be beneficial if tungsten were to be used as a plasma-facing material. However, it is now known that tungsten does absorb hydrogen isotopes at atomic-sized holes that are generated by neutron irradiation. Such absorption of fuel inside the wall is not favorable from either economy- or safety-related points of view. It is however known that the irradiation effects are suppressed in tungsten-rhenium alloys compared with pure tungsten (Fig.9-8(a)), but the mechanism of this favorable effect is not known. We also know that rhenium atoms inside tungsten become aggregated and make materials more brittle, which is an unfavorable effect. For the reasons above, we wondered if rhenium could be substituted

by other elements to achieve a favorable effect, and we needed to know the mechanism of this effect.

Under fast-neutron irradiation, some atoms at lattice sites are displaced and are inserted at interstitial positions, leaving vacancies behind. Suppression of irradiation effects means that displaced atoms tend to recombine with vacancies also generated by irradiation. In this study, we thoroughly investigated the migration and recombination of displaced atoms in pure tungsten and tungsten-rhenium alloy using density-functional-theory-based first-principles calculations. We found that interstitial atoms in pure tungsten migrate one-dimensionally, while those in the alloy migrate randomly (Fig.9-8(b)). Fig.9-8(c) shows how this difference propagates to the difference in the recombination rate, i.e., the probability of an interstitial atom recombining with a vacancy located within a given distance. Notice that the probability is larger in alloys than in pure tungsten. This suggests that random migration of interstitials reduces irradiation effects; various experimental evidence that we have obtained so far has supported this notion. In the future, we would like to search for new radiation-resistant alloys based on the current results.

This work is supported by the Japan Society for the Promotion of Science (JSPS) KAKENHI Grant-in-Aid for Scientific Research (C) (No.15K06672).

Reference

Suzudo, T. et al., Suppression of Radiation-Induced Point Defects by Rhenium and Osmium Interstitials in Tungsten, Scientific Reports, vol.6, 2016, p36738-1-36738-6.

Development of Technology and Human Capacity Building in the Nuclear Nonproliferation and Nuclear Security Fields to Support the Peaceful Use of Nuclear Energy

The Integrated Support Center for Nuclear Nonproliferation and Nuclear Security (ISCN) has been conducting the following activities on technology and human capacity development related to nuclear nonproliferation and security. In these activities, the ISCN is cooperating with relevant domestic and overseas organizations (Fig.10-1).

Technology Development for Japanese and International Applications

We have been developing technologies that strengthen nuclear nonproliferation and security in accordance with domestic and international trends. For instance, the nondestructive assay technology to quantify the nuclear materials in fuel debris at the TEPCO's Fukushima Daiichi NPS has been developing. We are also examining safeguards technologies for the possible direct disposal of spent fuel. We have been developing some basic technologies for nuclear measurement and nuclear detection, e.g. detection technology for nuclear materials contained in heavy shielded containers using nuclear resonance fluorescence analysis, nondestructive assay technology to measure various types of nuclear materials including high-radiation materials, monitoring technology for plutonium solutions containing fission products. Furthermore, we have been improving the accuracy and expediting the analysis of nuclear forensics technologies. We organized the international symposium on the future direction of nuclear forensics R&D in June 2017. At this symposium, we shared information on the needs on R&D and current status in each country, and increased public awareness of nuclear forensics.

Support for Government Policy Formulation Based on Our Technology Expertise

We researched the synergy effects on non-proliferation (safeguards) and nuclear security measures at nuclear-fuel cycle facilities. To enhance and promote both safeguards and nuclear security (collectively called 2Ss), we conducted an international trend survey on synergy effects. Various measurement and surveillance technologies, safeguarding equipment and information might be

utilized for 2Ss purposes in future nuclear-fuel cycle facilities.

Support for Human Capacity Development

Based on the commitments of the Japanese government made at the Nuclear Security Summit in April 2010, we have supported human capacity development, especially among Asian states, since April 2011. The aim is to strengthen nuclear security in these countries. Until March 2017, approximately 3276 participants have benefitted from our seminars and training courses on nuclear security and safeguards, which we have held within and outside of Japan. The USA and Japanese governments have lauded the ISCN for its contribution to human development in the Asian region.

International Contributions Based on Our Expertise and Experience

To establish a global verification regime for nuclear tests, we have provisionally operated the facilities of the international monitoring system of the Comprehensive Nuclear-Test-Ban Treaty (CTBT), and a national data center. After the 5th nuclear test conducted by North Korea in September of 2016, JAEA analyzed and evaluated the data observed at the CTBT radionuclide monitoring stations, and reported the results to the national government and other agencies in a timely manner. In this way, we contributed to the national government's evaluation based on the CTBT national operation system in Japan. In Topic 10-1, we discuss how medical radioisotope production facilities affect our observations of radioxenon isotopes (which are effective detection-indicators of underground nuclear tests).

Support for JAEA's Transportation and Duties of Research Reactor Fuels

Our research and development centers comply with proper nuclear transportation. In particular, we have coordinated the procurement of fresh fuels for our research reactors, and the disposal of spent fuels. Through these activities, we have contributed to the Global Threat Reduction Initiative, which aims to strengthen global nuclear security by promoting the systematic return of highly enriched uranium to the USA.

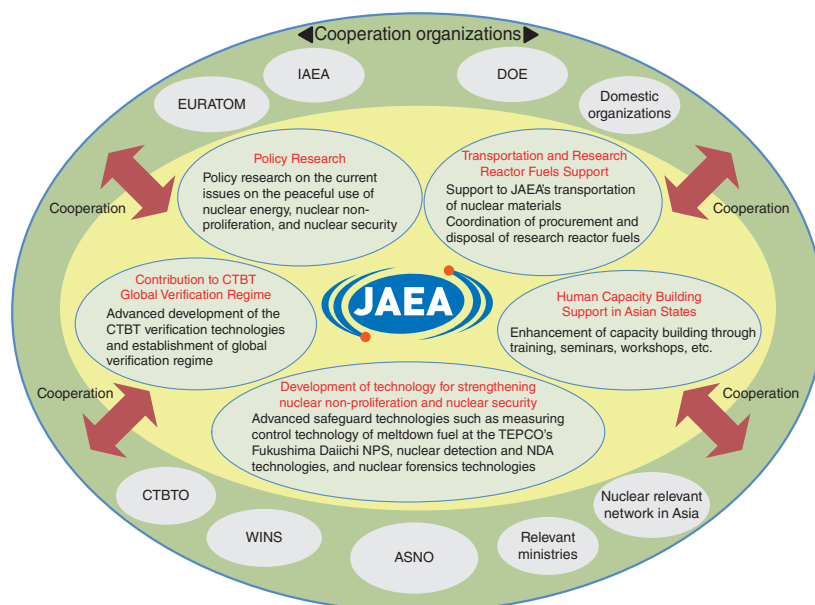


Fig.10-1 JAEA activities in developing science and technology for nuclear nonproliferation and nuclear security

We have been playing an active role in international organizations such as the International Atomic Energy Agency (IAEA), developing technologies in each member country and ensuring transparency. We are also continuing a project on human capacity development support, which contributes to capacity building in Asian countries.

10-1 Toward Enhancement of Monitoring Capability for Nuclear Tests

— Evaluating the Impact of MIPF on Observational Results at CTBT Radionuclide Stations —

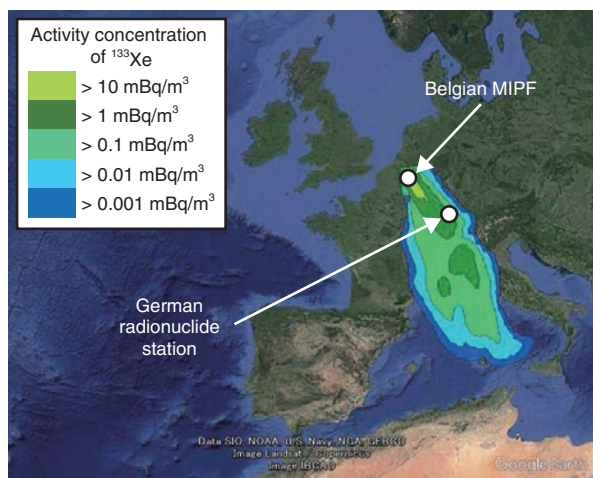


Fig.10-2 Atmospheric dispersion simulation of Xenon-133 (^{133}Xe) emitted from a Belgian medical radioisotope production facility (MIPF)

As part of the study, we simulated the atmospheric dispersion of ^{133}Xe emitted from a stack at the MIPF of the Institute for Radioelements (IRE) in Belgium using the stack monitoring data. The emitted ^{133}Xe reaches the German radionuclide station. (An atmospheric transport modelling (ATM) analysis software (HYSPLIT) developed by the National Oceanic and Atmospheric Administration (NOAA) was used.)

Although the Comprehensive Nuclear-Test-Ban Treaty (CTBT) that bans nuclear tests in any space has not yet entered into force, approximately 85% of the international monitoring system of nuclear testing, comprising 337 monitoring facilities worldwide, has established and operated provisional measures.

Among the relevant radionuclides to be monitored by the CTBT is radioxenon, which is generated in large amounts by a nuclear test. Because noble gases are chemically inert, radioxenon is more likely than other radionuclides to seep to the surface after an underground nuclear test. Therefore, radioxenon is an important detection-indicator of an underground nuclear test. Radioxenon is observed at 30 radionuclide stations worldwide (as of May 2017), including the Takasaki station in Japan, under the international monitoring system. Previous observation results showed that the radioxenon isotope ^{133}Xe is frequently detected with high activity concentrations at some stations. MIPFs are considered as the dominant emission sources of ^{133}Xe , as they produce radioisotopes for nuclear medical examinations by nuclear fission reactions. To discriminate whether the observed ^{133}Xe originates from civil nuclear facilities or nuclear testing, one must evaluate the impact of the ^{133}Xe emitted from MIPFs on the observational

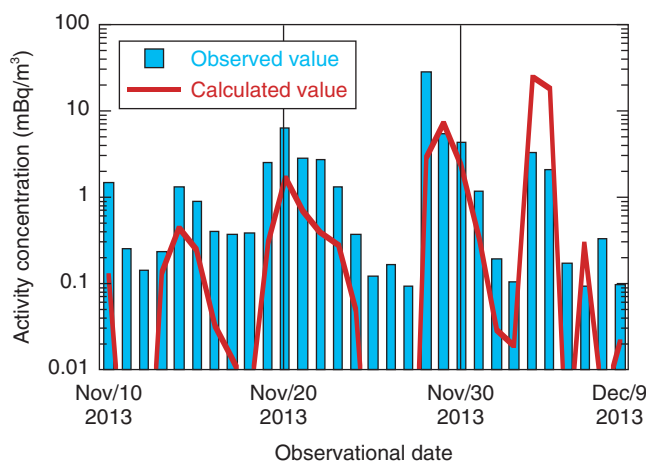


Fig.10-3 Comparison of ^{133}Xe activity concentrations observed at the German radionuclide station and calculated in simulations by the JAEA

When the observed ^{133}Xe activity concentrations at the German radionuclide station were high, the values calculated in simulations by the JAEA were also high. This correlation confirms that the MIPF of the IRE in Belgium is a dominant emission source of the ^{133}Xe observed at the German radionuclide station during this period.

results at radionuclide stations.

The impact of MIPFs was investigated in an ATM simulation analysis. Implemented in 2015, this project involved seven nations, including us and the CTBT Organization (CTBTO). In the ATM simulations, we analyzed and evaluated the activity concentration of ^{133}Xe arriving at the German radionuclide station using the stack monitoring data (acquired from November 10th to December 9th, 2013) of the MIPF of the IRE in Belgium. Figs.10-2 and 10-3 show an ATM simulation result and a comparison between the observed and simulated results at the station, respectively. The observed and calculated values on days of high ^{133}Xe activity concentration were well correlated, confirming that the MIPF of the IRE was a dominant emission source of ^{133}Xe . Conversely, on some days (when the observed ^{133}Xe activity concentration was low), the MIPF of the IRE was an unlikely emission source of ^{133}Xe .

We are continuing our ^{133}Xe observations in cooperation with the CTBTO and with specialized institutions in other countries. By evaluating the impact of emissions from civil nuclear facilities on the observational results, we hope to enhance the capability of monitoring nuclear-test emissions.

Reference

Eslinger, P. W., Kijima, Y. et al., International Challenge to Predict the Impact of Radioxenon Releases from Medical Isotope Production on a Comprehensive Nuclear Test Ban Treaty Sampling Station, *Journal of Environmental Radioactivity*, vol.157, 2016, p.41-51.

To make the technologies, patents and other research results, and facilities and equipment of the Japan Atomic Energy Agency (JAEA) widely available to society, we are promoting activities in three areas: “academia-industry collaboration”, “utilization of intellectual property”, and “facility usage”. We are also creating a database of patents and intellectual property information held by the JAEA. The following table is a list of intellectual property (patents in foreign countries) in the fiscal year 2016.

Intellectual Property Held by JAEA Patent Information

Title	Department	R&D Institutes and Centers	Publication Number	Date of Registration
1 UK				
Continuous collection method of particle component in aqueous solution and apparatus therefor	Advanced Science Research Center, Sector of Nuclear Science Research	Nuclear Science Research Institute	2364758	Jun. 29, 2016
Nano particle-dispersed high-performance liquid fluid, production method and device for that fluid, method of detecting leakage of that fluid	Advanced Fast Reactor Cycle System Research and Development Center, Sector of Fast Reactor Research and Development	Oarai Research and Development Center	1780254	Feb. 8, 2017
2 France				
Continuous collection method of particle component in aqueous solution and apparatus therefor	Advanced Science Research Center, Sector of Nuclear Science Research	Nuclear Science Research Institute	2364758	Jun. 29, 2016
Electromagnetic flowmeter	Advanced Fast Reactor Cycle System Research and Development Center, Sector of Fast Reactor Research and Development	Oarai Research and Development Center	601973	Nov. 25, 2016
Nano particle-dispersed high-performance liquid fluid, production method and device for that fluid, method of detecting leakage of that fluid	Advanced Fast Reactor Cycle System Research and Development Center, Sector of Fast Reactor Research and Development	Oarai Research and Development Center	1780254	Feb. 8, 2017
3 Germany				
Continuous collection method of particle component in aqueous solution and apparatus therefor	Advanced Science Research Center, Sector of Nuclear Science Research	Nuclear Science Research Institute	2364758	Jun. 29, 2016
Nano particle-dispersed high-performance liquid fluid, production method and device for that fluid, method of detecting leakage of that fluid	Advanced Fast Reactor Cycle System Research and Development Center, Sector of Fast Reactor Research and Development	Oarai Research and Development Center	1780254	Feb. 8, 2017

About the Design of the Cover

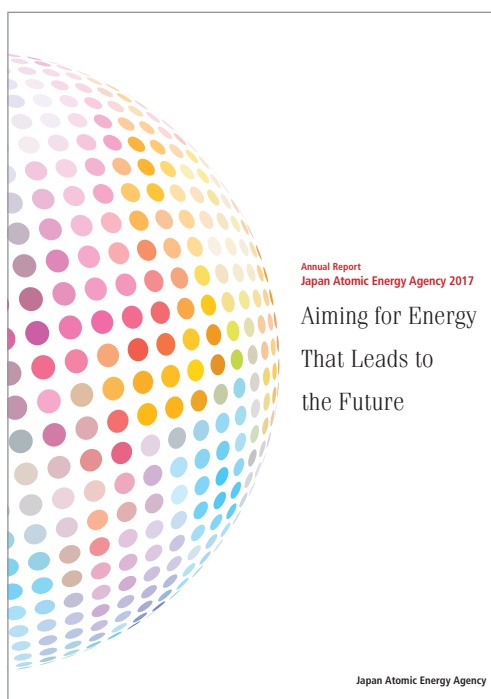
The cover is designed with white hexagons similar to the pattern in a tortoise shell, an ancient Japanese symbol of people's wish for longer lives. Coincidentally, this shape is the same as that of core fuel assemblies for both the prototype fast breeder reactor "MONJU" and the high-temperature engineering test reactor "HTTR".

The images on the cover show results of the air cooling simulation for simplified debris (top left) and drilling machine for large diameter pit (bottom right).

The top left image shows the simulation results of the heat transfer between the simplified debris and the gas phase induced by the natural convection. Fuel debris is simplified as the plate and half sphere shape and is considered the decay heat as the heat generation (Chapter 1, Topic 1-5, p.15).

The bottom right image shows the drilling machine for large diameter pit, which was developed and produced in order to excavate a pit for EBS test at Horonobe URL. The machine combines casing drilling and auger excavation, and allows continuous drilling of a disposal pit in a soft sedimentary rock (Chapter 8, Topic 8-5, p.82).





About the activity status of the whole agency
including CSR, see the annual report
Japan Atomic Energy Agency 2017

JAEA R&D Review 2017-18

Published by

Japan Atomic Energy Agency in January 2018

Editorial Board

Chief editor: Hideaki Mineo

Editors: Junya Sumita, Tomoaki Suzudo, Ayako Okubo, Shinichi Noguchi,
Tadafumi Niizato, Takeshi Takeda, Shinichi Shamoto, Takamasa Mori,
Terufumi Yokota, Shoji Takada, Taiju Shibata, Hiroshi Takada, Takashi Takata,
Yoshikazu Yamada, Masanori Ando, Kazuhiko Sato, Chie Oda

This publication is issued by Japan Atomic Energy Agency (JAEA) on a yearly basis. Inquiries about availability and/or copyright of the contents in this publication should be addressed to Institutional Repository Section, Intellectual Resources Management and R&D Collaboration Department, Japan Atomic Energy Agency (JAEA).

Address: 2-4 Shirakata, Tokai-mura, Naka-gun, Ibaraki-ken 319-1195, Japan

Phone: +81-29-282-6387, **Facsimile:** +81-29-282-5920, **e-mail:** ird-seika_shi@jaea.go.jp

All Rights Reserved by JAEA ©2018